TEEMU SALO

3D Printing and Stretchable Electronics

Tampere University Dissertations 969

Tampere University Dissertations 969

TEEMU SALO

3D Printing and Stretchable Electronics

ACADEMIC DISSERTATION
To be presented, with the permission of
the Faculty of Information Technology and Communication Sciences
of Tampere University,
for public discussion in the auditorium TB109
of the Tietotalo, Korkeakoulunkatu 1, Tampere,
on 28 March 2024, at 12 o'clock.

ACADEMIC DISSERTATION
Tampere University, Faculty of Information Technology and Communication Sciences
Finland

Responsible supervisor and Custos	Professor Jukka Vanhala Tampere University Finland	
Pre-examiners	Professor Elina Ilén Universitat Politècnica de Catalunya Spain	Professor Fernando Seoane University of Borås Sweden
Opponent	Research Professor Jussi Hiltunen VTT Finland	

The originality of this thesis has been checked using the Turnitin Originality Check service.

Copyright ©2024 author

Cover design: Roihu Inc.

ISBN 978-952-03-3322-5 (print)
ISBN 978-952-03-3323-2 (pdf)
ISSN 2489-9860 (print)
ISSN 2490-0028 (pdf)
http://urn.fi/URN:ISBN:978-952-03-3323-2

Carbon dioxide emissions from printing Tampere University dissertations have been compensated.

PunaMusta Oy – Yliopistopaino
Joensuu 2024

PREFACE

This work was carried out at the Personal Electronics Group (PEG) at Tampere University in Kankaanpää unit and Hervanta campus. The research was done in the projects SOFT3L (funded by European Union Regional Development Fund, Satakunta Regional Council, and City of Kankaanpää), Elastronics (funded by Business Finland), and REEL (funded by Academy of Finland). I would also thank Fraunhofer IZM for the research exchange period.

I would like to thank my supervisor Prof. Jukka Vanhala for his support and guidance on this journey. In 2017, I would not have guessed how vast adventure from his "By the way are you interested" invitation to do the M.Sc. thesis about stretchable electronics in Kankaanpää would have become. Nevertheless, I would like to thank Assoc. Prof. Mikko Kanerva for getting me started in my Doctoral studies. Correspondingly, I would like to express my gratitude to Prof. Matti Mäntysalo for rooting me in the long home straight of my Doctoral studies.

I'm grateful to all my co-authors. I would like to thank Clothing+ team, JCI Kankaanpää, and people at Kankaanpää School of Fine Arts. Also, I would like to thank Ph.D. Thomas Löher and the rest of the Berlin gang for the guidance in Fraunhofer IZM and Berlin city life during the research exchange period. Without the help of co-workers and friends this would not have been possible – sincerely thank you M.Sc. Aki Halme, M.Sc. Emma Kaappa, D.Sc. Donato Di Vito, D.Sc. Riikka Mikkonen, D.Sc. Milad Mosallaei, M.Sc. Karem Lozano Montero, D. Sc. Jari Keskinen, M.Sc. Hanna Christophliemk, B.Sc. Juhani Lahtinen, M.Sc. Fu, B.Sc. Janett Hilgenfeld, and B.Sc. Remmi Calvo Guzman.

Thank you to my family and friends for having my back during this long pilgrimage. And my soon-to-be wife Lottaliisa Salmi. How I could have done this without you.

Tampere 02.01.2024

Teemu Salo

ABSTRACT

Stretchable electronics are electronic systems that comply with dimensional changes of the substrate without the loss of functionality. Stretchable electronic technologies are developed for the manufacturing of wearable electronics, which require soft and elastic substrates. Thus, stretchable electronics have normally (I) a deformable thermoplastic polyurethane (TPU) substrate, (II) rigid printed circuit board (PCB) module islands, and (III) stretchable interconnections between the islands. In the system, the mechanical and electrical features have a linkage, where the electrical performance is affected by the mechanical difference of the components.

In this thesis, manufacturing methods are researched to control and decrease the mechanical differences in stretchable electronics. The joining of rigid and stretchable substrates with structural and non-structural adhesives is studied with peel tests. Also, TPU 3D printing on the TPU substrate is explored to optimize shaped stretchable interconnections. The 3D printing is further adapted for the stretchable 3D-printed interconnections and sensors. Finally, the interconnection deformations close to the islands are studied in hybrid stretchable circuit board (SCB) technology.

The results show that the structural adhesives are incapable of complying with the elongation of TPU substrate, which induces irregular peeling. With the non-structural adhesive, the adhesive stretches, producing stable peeling. In the case of small and local interconnection supports, the adhesives are replaced by 3D printing directly molten TPU plastic on the screen-printed TPU substrate. The good adhesion of ~ 1,9 N/mm allows the supports to increase the safe elongation of interconnections by ~ 27%. Moreover, the 3D printing of TPU is usable for stretchable 3D printed structures. Unlike with current conductive 3D printing materials, permeable carbon fiber nonwovens enable stretchable and conductive composites. Thin ~ 53 μm fiber layer deforms evenly with cyclic 50 % elongation, and thick > 150 μm fiber layers have the best resistance results 4 Ω□. Lastly, with various protective structures, the interconnection transition area close to the SCB islands is used to stabilize the samples at 10 % and 20 % cyclic elongation.

Demonstrated new manufacturing methods advance stretchable electronics by balancing the mechanical differences of the system, which increases the stretchability and integration level of stretchable systems. More durable and smaller systems build a foundation for indistinguishable structural electronics and maintainable wearable electronics for casual use, military, sports, and healthcare sectors.

CONTENTS

1 INTRODUCTION 13
  1.1 Aim and scope of the thesis 14
  1.2 Structure of the thesis 15
  1.3 The author's contribution 16

2 MAIN COMPONENTS IN STRETCHABLE ELECTRONICS 17
  2.1 Substrates 19
    2.1.1 Rigid substrates 21
    2.1.2 Flexible substrates 22
    2.1.3 Stretchable substrates 24
    2.1.4 Textile substrates 25
  2.2 Module islands and joining methods 26
    2.2.1 Adhesion 28
    2.2.2 Bonding methods 29
    2.2.3 Stress concentration effect of the module 33
  2.3 Stretchable interconnections 35
    2.3.1 Rigid shaped copper foil interconnections 38
    2.3.2 Rigid printed interconnections 40
    2.3.3 Deformable printed interconnections 41
    2.3.4 Fiber-based interconnections 42
    2.3.5 Failure mechanisms of stretchable interconnections on a deformable substrate 43
  2.4 3D printing of stretchable electronics 45
    2.4.1 FFF 3D-printing method 45
    2.4.2 Structure and stretchability of FFF 3D-printed objects 48
    2.4.3 Electronics prepared by FFF 49
    2.4.4 Electronics prepared by other 3D-printing techniques 51
    2.4.5 Stretchable electronics prepared by FFF 51
    2.4.6 Stretchable electronics prepared by other 3D-printing techniques 52

3 RESULTS 54
  3.1 Rigid modules on deformable substrates 55
    3.1.1 Joining rigid islands on deformable substrate 56
    3.1.2 Controlling the stress concentration around the rigid islands 58
  3.2 Stretchable interconnections on a deformable substrate 60
    3.2.1 Locally reinforced interconnections via 3D printing 60
  3.3 3D printed structures in wearable electronics 62
    3.3.1 Stretchable 3D-printed structures for wearable electronics 62

4 DISCUSSION 65
4.1 Compatible attachment of rigid islands on a deformable substrate 65
4.2 Relevance of stiffness to the stretchability of interconnections 66
4.3 Possibilities of 3D-printing in stretchable electronics 69

5 CONCLUSIONS AND FUTURE WORK 70
5.1 Conclusions 70
5.2 Future work 72

REFERENCES 73

List of Figures

Figure 1. The main components in stretchable electronics and examples of their use together or in pairs. Functional tattoo image by Mika Kanerva / University of Tampere. 18

Figure 2. Four integration levels of stretchable electronics. The single device level (I), the circuit level (II), the stretchable system level (III), and the wearable application level (IV). Adapted from a packaging hierarchy of electronic systems [44]........ 19

Figure 3. Deformations in stretchable wearable electronics: a) no deformation, b flexing, c) stretching, d) compression, and e) twisting. 20

Figure 4. Substrates of wearable electronics: a) rigid FR4 substrate, b flexible PI substrate, c) stretchable TPU substrate, and d) 3D-printed substrate [53]........ 21

Figure 5. Bonding methods in wearable electronics: a) snap-fit joint, b) soldering, c) ACF, d) direct 3D printed plastic on textile, e) 3D printed fastener, and f) conventional snap buttons. 30

Figure 6. Role of the stress concentration at the failure of straight copper element: a) the elongation of the undamaged copper element, and b) the elongation of snapped copper element [158]. 34

Figure 7. Manufacturing technologies of stretchable interconnections, a) laser direct imaging [167], b) Dimatix DMP-2850 inkjet-printer [168], c) screen-printing [18], and d) circular knitting machine [169]. 36

Figure 8. Stretchable interconnection examples: a) stretchable electronics system consisting copper meanders, made with SCB method [16], b) temperature sensor plaster, which consists inkjet-printed graphene/PEDOT:PSS temperature sensor between screen-printed silver ink interconnections [39], c) knitted interconnections and electrode from conductive silver coated yarn, and d) dispensed stretchable conductive ink interconnections in a 3D-printed board........ 37

Figure 9. The side etching phenomenon of the meander-shaped copper foil interconnections. 39

Figure 10. Example failures of different stretchable interconnection materials: a) shaped copper foil structures, and b) straight screen-printed silver interconnections. 44

Figure 11. Ultimaker S5 3D-printer and the critical parts that affect the FFF process: a) Ultimaker S5 3D-printer, b) filament spool, c) feeding system, d) print core that includes a heat sink, heater block, and nozzle, e) building plate, and f) chamber. 46

Figure 12. The screenshot from Ultimaker Cura slicer software (version 5.2.2), where the general structure of the 3D-printed module is shown: a) the bottom of the module, where the red line is the outer wall, the green line is the inner wall, and the yellow lines are the bottom areas, b) the middle of the module, where orange lines are the infill areas with 80 % infill ratio, and c) the top of the module. 48

Figure 13. The four major areas of the Thesis with the overlapping pie chart, which marks the dealt areas in Publications I–IV. 54

Figure 14. Deformations and damages of cyclic test samples: a) bending of protective structures, b) snapped protective structures because of fatigue damage, c) torn holes between snapped protective structures, and d) failed printed lines in the transition area of the sample. Adapted from [158] 59

Figure 15. Resistance curves of the 20 % elongated cyclic test samples: a) the resistance of stable copper–printed silver transition area, b) the resistance of unstable transition area, c) the resistance of the printed interconnection without protective structure rupture, and d) the resistance of the interconnection with a rupture of protective structure. [158] 59

Figure 16. Directly 3D-printed plastics on the TPU film: a) average maximum bond strength of the sample series, and b) TPU 260 °C peel test sample before snapping of the film, which reveals the melted surface of the film. Adapted from [147] 61

Figure 17. The transition area of screen-printed meanders, which deformations are modified differently by directly 3D-printed supports: a) plain sample without supports, b) straight supports between the meanders, c) straight supports outside the meanders, and d) curved supports inside the meanders. Adapted from [147] 62

Figure 18. Raw data comparison of 3D-printed cyclic test samples with 30 % elongation: a) the sample with 1 thin CFC layer, which provides the systematic resistance variation between 600 Ω – 800 Ω, and b) the sample with a thick CFC layer laminated from 3 thin CFCs show varying resistance results between 350 Ω – 1250 Ω. Adapted from [46] 64

Figure 19. DIC results of 3D-printed samples with 2, 3, or 1 layers of thin CFC: a) in 20% elongation, and b) in 50% elongation. Adapted from [46] ... 64

List of Tables

Table 1. Used NCAs with between rigid and deformable substrates. [137] ... 56

Table 2. Identified failure mechanisms of the peel test samples. In embedded figures, green resembles the rigid FR4 and PLA substrates, light blue resembles the deformable TPU substrate (which was peeled from the rigid substrates), and dark blue resembles the adhesive layer. [137] ... 57

LIST OF SYMBOLS AND ABBREVIATIONS

2D	Two-dimensional
3D	Three-dimensional
ACA	Anisotropic conductive adhesives
ACF	Anisotropic conductive adhesive film
AM	Additive manufacturing
CA	Cyanoacrylate
CFC	Carbon fiber cloth
CTE	Coefficient of thermal expansion
DIW	Direct ink writing
ECG	Electrocardiography
ED	Electrodeposited copper
EMG	Electromyography
FEA	Finite element analysis
FFF	Fused-filament fabrication
FTIR	Fourier-transform infrared spectroscopy
IC	Integrated circuit
LED	Light-emitting diode
MJF	Multi-jet fusion
MJP	Multi-jet printing
NCA	Non-conductive adhesive
PCB	Printed circuit board
PDMS	Polydimethylsiloxane
PI	Polyimide
PLA	Polylactic acid
PSA	Pressure-sensitive adhesive
PU	Polyurethane
RA	Rolled and annealed copper
SCB	Stretchable circuit board
SLA	Stereolithography
SMD	Surface-mounted device
SOC	System-on-chip
Tg	Glass transition temperature
TPU	Thermoplastic polyurethane
UV	Ultraviolet

ORIGINAL PUBLICATIONS

Publication I	Salo T., Halme A., Kanerva M., and Vanhala J. “Bond strength and failure mechanisms of nonconductive adhesives for stretchable electronics,” IEEE Trans. Compon. Packaging. Manuf., vol. 10, no. 5, pp. 770–778, 2020.
Publication II	Salo T., Halme A., Lahtinen J., and Vanhala J. “Enhanced stretchable electronics made by fused-filament fabrication,” Flex. Print. Electron., vol. 5, no. 4, p. 045001, 2020.
Publication III	Salo T., Di Vito D., Halme A., and Vanhala J. “Electromechanical properties of 3D-printed stretchable carbon fiber composites,” Micromachines, vol. 13, no. 10, p. 1732, 2022.
Publication IV	Salo T., Werft L., Scenev V., Adams B., Di Vito D., Halme A., Scenev V., Walter H., Löher T., and Vanhala J. “Mechanical properties of structured copper and printed silver hybrid stretchable electronic systems,” Flex. Print. Electron., vol. 8, no. 2, p. 025019, 2023.

1 INTRODUCTION

Stretchable electronics can be described as electronic systems that provide same electrical properties as traditional rigid electronics, but with the ability to comply with complex mechanical deformations [1]. Stretchable electronics are used in a growing sector of wearable electronics, where stretchable electronics are applied on clothing or skin for better comfort, higher functionality, and new applications [2]. The "intelligence" of wearable stretchable electronics is still widely based on traditional electronics components, which have progressed from single transistors in the 1950s, through early integrated circuits (ICs) in the 1960s to current system-on-chip (SOC) components with over a billion transistors [3]. The miniaturization has enabled the development of the modern society with systems like e.g. a smartphone which has revolutionized our communication, entertainment and mobility [4].

The miniaturization of electronics has brought the idea that electronics can be integrated with apparel. Eyeglasses, watches, and other small objects are natural carriers for rigid electronics, and for larger and more complex systems, clothes can be enhanced with electronics [5]. Mechanically complex textiles have been already manufactured since the invention of the Jacquard looms around 1801, and with current digital manufacturing methods and miniaturized electronics, electrically sophisticated textiles with integrated electronics have been fabricated [6], [7]. For more intelligent and interactive systems, wearable electronics are made stretchable with various technologies, which include conductive yarns, conductive inks, and laminated film with electronic features [8]–[10].

The stretchability of an electronics system is possible by dividing traditional rigid electronics into small module islands, which are spread over a deformable substrate. The islands are combined by interconnections that are made stretchable by varying shapes and materials of the interconnections [11]. Also, the islands are fixed mechanically and electrically on the deformable substrate with different joining methods [12]–[14]. The build-up decisions of stretchable electronics are mainly affected by the final requirements of the wearables and available manufacturing methods [5].

The most prominent subtractive technology is the stretchable circuit board (SCB) technology, which uses a modified printed circuit board (PCB) manufacturing method to manufacture stretchable electronics [15]. The technology complements rigid and flexible substrates with deformable ones, enabling the stretchability of the system [16]. The stretchability of conventionally used flexible materials, such as copper and polyimide film (PI), is allowed by shaping them as 2-dimensional (2D) springs [17].

Additive manufacturing (AM) includes various fabrication methods, where screen-printing, inkjet printing, and other printing methods are used for planar 2D designs [18], [19]. More complex three-dimensional (3D) designs are done with 3D-printing methods, which have already emerged in the 1980s. However, 3D printing has come more common after the expiration of patents in the 2010s [20], and already, the 3D-printing has changed the way to mass-produce certain complex metal parts [21]. The 3D-printing has a huge potential in the manufacturing of functional plastic parts and electronics [22], [23], which opens the development of 3D-printed stretchable electronics.

1.1 Aim and scope of the thesis

The development of next-generation stretchable electronics is highly dependent on new manufacturing methods. The long-term aim is to make stretchable electronics systems more robust and merge them into everyday wearables, which require a higher integration level of components. The higher integration level highlights dissimilar properties of electronics, plastics, and textiles, which hinder new applications. The different properties originate from different materials, product requirements, and manufacturing methods, which need to be considered and optimized for new stretchable and wearable electronics. In this work, 3D printing, screen-printing, lamination, SCB, and gluing are used to prepare hybrid structures, which can be used to improve the durability and integration level of stretchable systems.

In this thesis, the foremost research question is, how to create electronic systems, which are stretchable, reliable, and manufacturable with current technologies. The main goal is approached by finding the answers to the following research questions:

(1) How do different non-conductive adhesives perform in the stretchable electronics joint?

(2) What 3D printing methods and designs can be used to affect the elongation of the stretchable printed interconnections?

(3) How does integrating carbon-based long staple fiber cloth impact the mechanical and electrical properties of the stretchable 3D-printed matrix?

(4) How to control the amount of stress in the transition area of SCB modules with different protective structures?

1.2 Structure of the thesis

This thesis consists of five chapters, which draw together and summarize the research work in four peer-reviewed journal publications. Chapter 1 introduces the topic of the thesis, the aim and scope of the thesis, the research questions, the structure of the thesis, and the contribution of the authors. Chapter 2 deals extensively with the main three components of stretchable electronics; the deformable substrates, the rigid PCB islands with their joining methods, and the stretchable interconnections. Chapter 2 also reviews the 3D-printing methods of electronics and stretchable electronics. Chapter 3 shows the major results, while Chapter 4 presents further analyses of the outcomes. Finally, Chapter 5 concludes the thesis and summarizes the findings.

1.3 The author's contribution

Publication I. The author was the main contributor and fabricated the samples. The author, A. Halme, and J. Vanhala conceptualized the research. M. Kanerva and the author designed the peel test setup and analyzed the peel test results. O. Orell assisted with the tensile tester. S. Siljander assisted to implement the FTIR analyses, which results were analyzed together by S. Siljander, M. Kanerva, and the author. A. Halme, M. Kanerva, and J. Vanhala participated in writing and further improving of the manuscript.

Publication II. The author was the main contributor and designed the experiment and fabrication of the samples. J. Lahtinen assisted in the fabrication of the samples and conducted the T-peel tests. The author screen-printed the tensile test samples. The resistance measurement system of the tensile test samples was designed by A. Halme and the author, after which J. Lahtinen and the author executed the tensile tests. The author, A. Halme, and J. Vanhala prepared the original and revised manuscripts.

Publication III. The author was the main contributor and designed the experiment and fabrication of the samples. The author and D. Di Vito executed the cyclic testing. The simultaneous resistance measurement of cyclic tests and the analysis of resistance results were done by A. Halme and the author. D. Di Vito prepared the FE analysis and evaluated the FE analysis results. All the authors prepared the original and revised manuscript.

Publication IV. The author was the main contributor and designed the experiment with T. Löher and J. Vanhala. Evelyn Wegner supported the SCB manufacturing process of the tensile and cyclic test samples. M. Luukko assisted the author with screen-printing and tensile tests of the tensile sample series. V. Scenev supported the screen-printing of cyclic test samples, and H. Walter assisted with the cyclic test machine. L. Werft designed, and B. Adams built and improved the resistance measurement device, which was used with the cyclic test samples. The author and L. Werft performed the cyclic tests. A. Halme participated in the analysis of electrical measurements of the samples. D. Di Vito prepared FE analysis and evaluated the FE analysis results. The author, T. Löher and J. Vanhala investigated the test results. The author, T. Löher, D. Di Vito, and J. Vanhala prepared the original and revised manuscript.

2 MAIN COMPONENTS IN STRETCHABLE ELECTRONICS

Wearable electronics is a rapidly developing technology that enables a wide range of applications in fields such as glucose level and electrocardiography (ECG) monitoring [24], [25], improving learning experiences with augmented reality [26], [27], and evaluating body movement in sports [28], [29]. Rigid gadgets, such as smartwatches, virtual reality glasses, rings [30], and buttons [31], enable the improvement of the daily life of users. Still, for new applications and better comfortability, stretchable wearable electronics can be integrated into clothing, which leads to a more conformal interface between the electronics and the human body. For example, phototherapy devices [32], and clothes with temperature, heart rate, and respiration sensing can be prepared [33].

The structure of the stretchable electronics can be divided into three core components (Figure 1): (1) deformable substrates, (2) PCB module islands, and (3) stretchable interconnections between the module islands. The deformable substrates provide mechanical support, flexibility, and stretchability to the system, where various textile and plastic materials are used. The module islands contain powerful and miniaturized off-the-shelf electronics components, which perform different functions, such as sensing, data processing, and energy storage. The stretchable interconnections electrically link the module islands while enduring deformations of the substrate. The interconnections are fabricated with multiple methods, for example, by printing, photolithography, and knitting, from which the screen-printed silver ink interconnections are shown in Figure 1. The different materials and manufacturing processes affect the mechanical and electrical properties of the stretchable system. [11], [34], [35]

Stretchable electronics for wearable applications require the use of the above mentioned three components, which are optimized for functionality and deformability. Still, in Figure 1, some applications can be prepared by using only two components. Wearable gadgets [36], Internet of Things modules [37], and near-field communication tags [38], are integrated with plastics or textiles to enable the wearability of the miniaturized electronics. Fully printed electronic components on deformable substrates can contain stretchable or flexible electronics for temperature

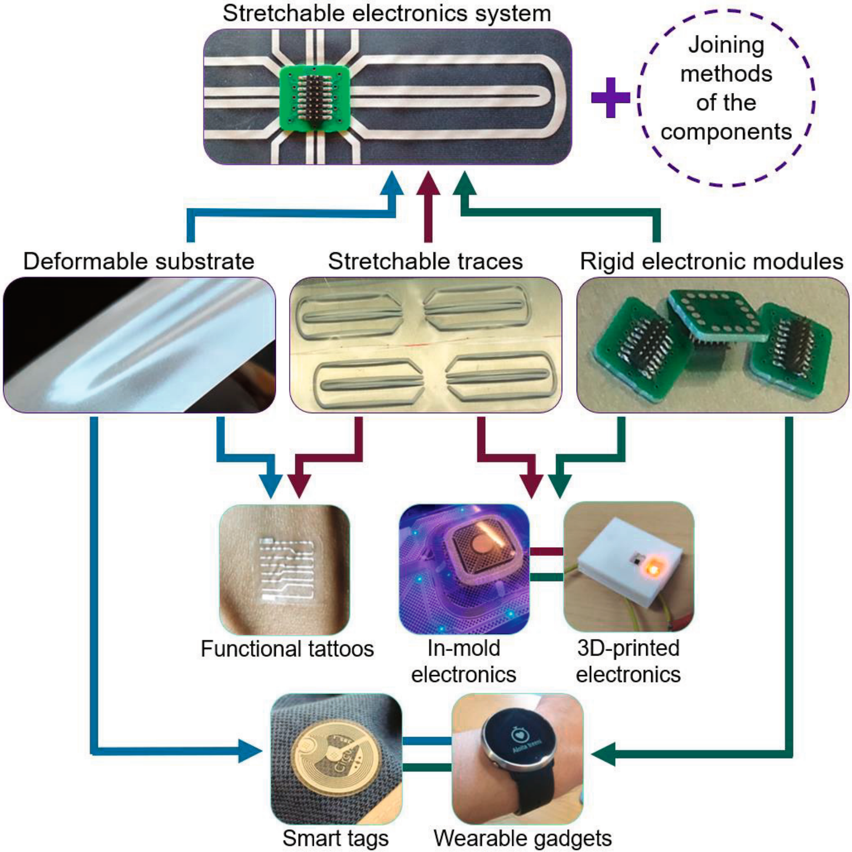

Figure 1. The main components in stretchable electronics and examples of their use together or in pairs. Functional tattoo image by Mika Kanerva / University of Tampere.

sensing [39], ECG monitoring [25], and energy storage applications [40]. In-mould electronics benefits from off-the-shelf electronics and stretchable interconnections, which sustain the thermoforming process of thermoplastic polymer films [41], [42]. An object to contain electronics and interconnections can be also prepared with 3D printing, such as fused-filament fabrication (FFF), which enables higher complexity and user-specified mass customization [20], [43].

Adapted from conventional electronics, the overall structure of wearable electronics can be divided into four integration levels: I) single device level, II) circuit level, III) stretchable system level, and IV) wearable application level (Figure 2) [44]. The first integration level (I) contains single devices, such as sensors, interconnections, and antennas, which can be fabricated by multiple methods [18], [45], [46]. At the second integration level (II), devices are combined into circuits for

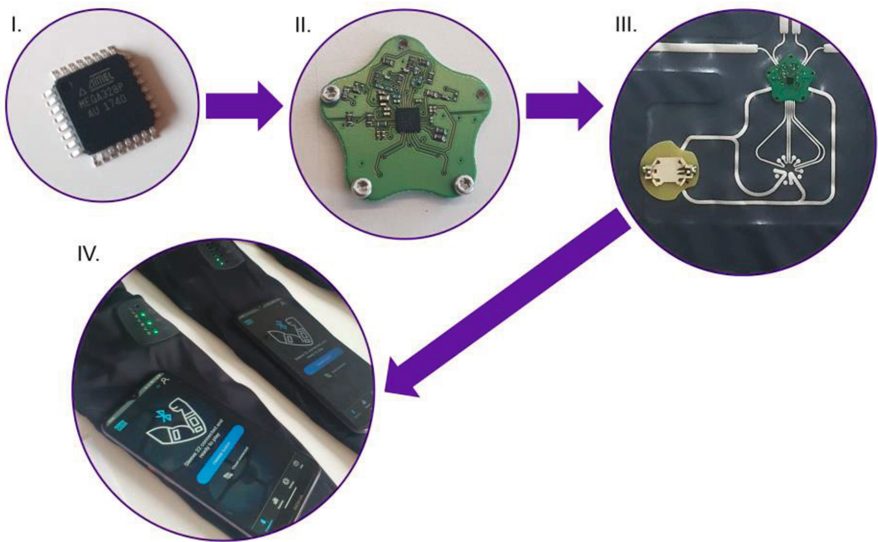

Figure 2. Four integration levels of stretchable electronics. The single device level (I), the circuit level (II), the stretchable system level (III), and the wearable application level (IV). Adapted from a packaging hierarchy of electronic systems [44].

determined functional purposes. The circuits can be traditional rigid or flexible PCB modules, or deformable build-ups fabricated by using stretchable interconnections and deformable substrates [11], [12]. At the third integration level (III), circuits are combined into stretchable systems, which have multiple features. For instance, the system can consist of sensors, accelerometers, wireless modules, and batteries [33], [47]. The highest fourth integration level (IV) is the wearable application level, which can contain one or more stretchable systems which are controlled via mobile phone or other external control devices. For instance, ECG, electromyography (EMG), respiration, and other sensor data are collected into the cloud for further analysis and real-time evaluation [48].

2.1 Substrates

Stretchable electronics systems can comply with deformations and are often used in wearable electronics, either directly applied on skin [12], [49] or laminated on a textile substrate [11]. Substrates in the stretchable system can be categorized by their mechanical properties to the rigid, flexible, and stretchable substrates, which undergo different mechanical deformations (Figure 3). The stable and

nondeformable rigid substrates do not deform. The flexible substrates are also inherently rigid, but their thinness enables different degrees of bending, and with additional shaping, can stretch, compress, and twist [11]. Stretchable substrates are fundamentally highly elastic, and they can comply with all kinds of deformations [46].

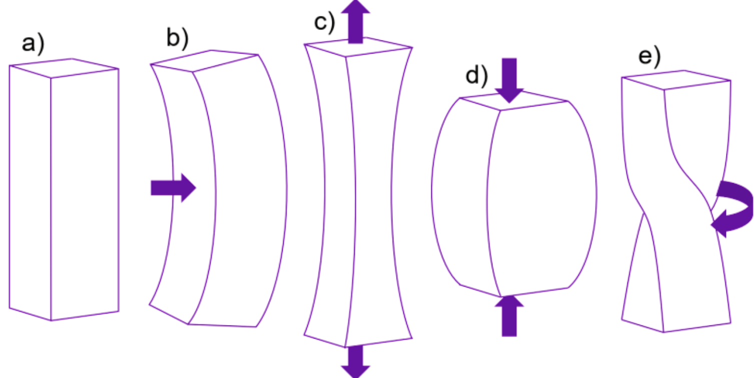

Figure 3. Deformations in stretchable wearable electronics: a) no deformation, b flexing, c) stretching, d) compression, and e) twisting.

The substrates are used alone and combined for different functions (Figure 4), for instance, rigid substrates are carriers for electronic components (Figure 4a). The flexible substrates are used for multiple purposes, where unshaped flexible circuit boards (FCBs) are carriers for electronics, and meander-shaped flexible films act as encapsulation and reinforcement of stretchable interconnections (Figure 4b). The stretchable substrates from deformable materials enable the stretchable system by combining elastically the non-stretchable areas together (Figure 4c). [11], [12]. To some extent, the homogenous mechanical properties apply to some stretchable electronics substrates. With weaving [50], knitting [51], molding [52], and 3D-printing [53], mechanically heterogeneous substrates can be fabricated (Figure 4d) For example, thickness, density, and structure affect the deformability of the substrates [51], [53], [54].

In addition to the mechanical properties, the usage of the substrates is also affected by other critical features of electronic systems. Such properties can be, for instance, thermal conductivity [55], electrical conductivity [56], biodegradability [57], transparency [58], chemical resistance [59], surface energy [60], surface roughness [61], comfort [62], and washability [9]. Currently, the substrates are optimized for their original applications, for example, the properties of rigid FR4 substrate for PCB

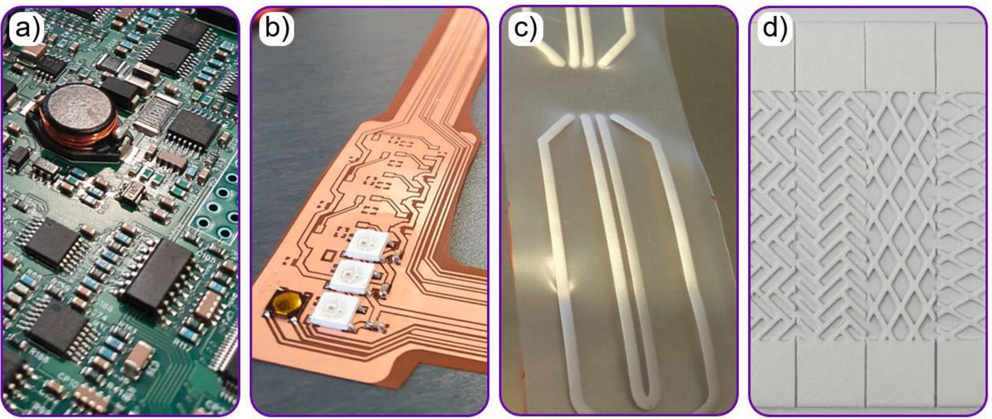

Figure 4. Substrates of wearable electronics: a) rigid FR4 substrate, b flexible PI substrate, c) stretchable TPU substrate, and d) 3D-printed substrate [53].

manufacturing are determined by the electronics industry. The overall optimization of currently used substrate materials for stretchable electronics is not ready, and by developing the manufacturing methods, the compatibility and integration level of substrate materials can be increased. However, in this work, the properties mainly dealt with the mechanical, electrical, and adhesion.

2.1.1 Rigid substrates

Rigid substrates are widely used in conventional electronics. The most used substrate in electronics is a glass fiber-reinforced epoxy laminate FR4, which abbreviation stands for the flame-retardant value of the board, standardized by the National Electrical Manufacturers Association [63]. The thermomechanical and electrical properties of the FR4 boards are focused to improve the durability of the boards, such as coefficient of thermal expansion (CTE), glass transition temperature (Tg), Young's modulus, and relative permittivity [63]–[65]. The boards are laminated with a copper foil layer, encapsulation layer, and other stacked FR4 layers. The failures generally occur as a cracking of the copper layer, solder joint, vias, or delamination of stacked layers [65], [66]. The manufacturing steps of the boards include etching of the copper layer, soldering, drilling, and other processes, which expose the boards to harsh chemical, thermal, and mechanical stresses.

The FR4 designation includes different kinds of boards. Different epoxy resins are used, and chemical composition, and type and amount of fillers affect the Tg of the resins [63]. The epoxy resins are thermoset plastics that burn before the melting

of the polymer matrix, but still, at elevated temperatures above Tg, the polymer matrix softens. The epoxy matrix is stabilized with woven glass fiber textiles, which are generally made from electrical grade glass fiber filaments that have high strength and electrical resistivity [65], [67]. The density of the woven fabrics varies, which is used in the modification of stiffness and CTE of the boards [63].

The boards are available in different thicknesses, where the thickness of the FR4 board depends on the dimensions of the woven glass fabric and epoxy matrix. The typical thickness of the board with a copper layer on both sides is 1,6 mm. When more copper layers are needed in order to route all interconnections between components, a stack of thin copper coated FR4 boards and thin so called prepreg sheets can be stacked together to form e.g. 12 layer PCB typically used in computer motherboards and smartphones. Generally, 18 μm or 35 thick μm copper foils and 10 μm – 25 μm thick solder mask layers are used. [68]

Recently, the environmental impact of composite boards for electronics has been considered, and more environment-friendly boards have been studied by replacing the epoxy matrix and glass fibers with biodegradable ones. By using other manufacturing processes, the epoxy can be changed to lignin [69] and polylactic acid (PLA) [57], which are usable in low-temperature applications. The glass fibers are replaced with PLA and natural fibers of flax, hemp, jute, and sisal [64], [70]. Notably, the flax and PLA mixture fabric with a flame retardant treatment can endure a flammability test designed for PCBs, but the flame retardant decreases the strength of the fabric by 66 % – 90 % [70].

Also, interesting applications have been done by 3D-printing methods, which allow the fabrication of 3D substrates [71] and structural electronics where the substrate, encapsulation, and the object itself are merged [72]. Several companies offer commercial manufacturing processes for 3D-printed electronics, which are discussed more in Chapter 2.4.

2.1.2 Flexible substrates

The flexible substrates are typically flexible polymer films that can be categorized between the rigid and the stretchable substrates – they are hard with a high Young's modulus, thus their elastic stretchability is limited. Because of thinness and spring-like 2D designs, they can bend and stretch tens of percent [11], [73]. PI is the most used material for films [74]. The name stands for polymers that have imide functional groups, and they are synthesized from two components, diamine and dianhydride

monomers. Modifying these two components, PIs with different properties are made [74]. The PI films have been used in electronic applications because of their high thermal stability, good mechanical and electrical properties, and relatively low relative permittivity [75], [76]. The properties enable thin and flexible but still durable films, and for example, Kapton PI films (by DuPont) are available in 7,5 μm – 125 μm thicknesses [77]. Moreover, PI films can be made inherently conductive by embedding conductive graphene, silver nanowires, or other conductive particles inside the film [58], [78]. The disadvantages of PI films are their high cost and typical brownish color, which limit their use.

As cheaper polymers, polyesters, such as polyethylene terephthalate (PET) films have been used in electronics applications. PET has lower temperature resistance than PI, but with modifications, the temperature resistance can be improved [79]. Still, PET films are less used with traditional electronics, and are more favorable in printed electronics. Low-temperature solders and conductive inks, coatings, and adhesives enable the use of PET films, where high transparency of the film allows new applications in screens and other optoelectronic devices [56], [79], [80]. The PET films are also recyclable with current technologies, decreasing the environmental impact of PET-based flexible electronics [81].

The environmental aspects have been also considered more broadly. Partially biobased PI films have been developed by replacing another component of PI with a bio-based chemical [82]–[84]. Also, paper and PLA have been used as flexible substrates in printed electronics [57], [85], [86].

The flexible substrate materials have been also applied for 3D printing processes. PI-based ink has been dispensed for simple 3D structures [87], and a soluble polyamic acid, the precursor polymer of PI, has been used to prepare 3D structures via the stereolithography (SLA) 3D printing method [88]. Moreover, PET filaments have been widely used in FFF, which can be prepared from recycled PET [89]–[91].

Thinness is the major property that affects the flexibility of the substrate, but nevertheless, flexibility is a sum of many parameters. The substrate is only one component in the flexible electronics system, which also includes adhesive layers, conductive copper layers, and cover layers, which all need to be flexible as such and in the build-up [92]. The property of one layer in the build-up can affect the flexibility of the system, for example, the grain direction of the copper layer can stiffen the flexible system anisotropically [93].

In wearable applications, worn electronics can bend, stretch, compress, or twist during their use [1]. Conventionally used flexible electronics can comply the bending, but with cutting or with other shaping methods (Figure 8a in Chapter 2.3) , they can

also comply the other deformations [17], [94]. The flexible system with different 2D shapes enables hybrid flexible electronics, where the component areas are flexible, and the interconnections between the component areas are stretchable.

2.1.3 Stretchable substrates

Stretchable substrates are carriers of electronic components, which can deform intricately under external stresses. Polymer-based stretchable films are widely used in stretchable electronics, where thermoplastic polyurethane (TPU) and polydimethylsiloxane (PDMS) are the most common films.

TPU is a block copolymer synthesized from isocyanate monomers with polyols, which segmented structure form hard crystallized segments and soft amorphous segments allow stretchability. The soft segments are formed from polyols, which chemical composition is varied for different properties. Polyols with ether bonds provide hydrolysis and low-temperature resistances, and polyols with ester bonds provide abrasion and high-temperature resistances. [73] The rigid crystalline segments are formed during the polymerization of TPU, which is formed in lamellae structures, and further in μm-scale spherulites [95]. The rigid segments act as a pinpoint of the soft segments, which together form an elastic copolymer matrix. Melting and re-crystallizing of the rigid segments make possible the thermoplastic nature of the copolymer. [73] The relation between rigid and soft segment content affects the elastic properties of the TPU [96]. In addition to the two main components, glycols can be added as chain extenders or cross-linkers to modify the thermal stability and mechanical strength of TPU [73].

TPU has its advantages and disadvantages in stretchable electronics. TPU has good abrasion and tearing resistances, and oil and ozone resistances. A typical hardness of TPU is between Shore A 65 and Shore D 50, and the maximum elongation is between 200 % – 1000 %. [73] The softening range of TPU films is 150 °C – 200 °C, and they are available in 25 μm – 1000 μm thicknesses [97]. TPU film has high surface energy, which improves the printability and lamination properties of the film. [73] However, TPU film has limited ultraviolet (UV)-stability, and there is a trade-off between good hydrolysis and thermoformability properties [97].

PDMS is a widely used thermoset silicone, which is cast and cured for different applications. Before curing, the liquid form of PDMS enables versatile use of the material [60], [98]. PDMS is synthesized from dimethyldichlorosilane, which after

cross-linking forms a polymer backbone where silicon and oxygen atoms sequences are repeated. PDMS can be further mechanically reinforced with fillers, such as silica or carbon black. Different curing methods and reactions have been used in the preparation of different types of PDMS, and in stretchable electronics, one or two-component low-temperature vulcanizing is commonly used. This kind of curing is based on a catalyst reaction or air moisture, which can be realized in low temperatures at the expense of longer curing time. [73]

The stable cross-linked polymer structure of PDMS has many advantages. PDMS has good chemical, ozone, and UV-resistances. It is transparent and biocompatible. The hardness of different silicones varies between Shore A 5 – Shore A 85, and the maximum elongation is between 100 % – 1200 %. The limiting factor of PDMS is the inert nature of the films, which makes surface pre-treatments mandatory before printing. Also, low tearing resistance and incompatibleness with a thermoforming process limit the use of PDMS. [73]

Furthermore, the deformable TPU and PDMS polymers have been applied in 3D printing. TPU has been widely used in FFF in which hardness varies between Shore A 60 – Shore A 95 [99]. PDMS is used in direct ink writing (DIW), where the extruded PDMS can be immediately cured via heat. For instance, conductive inks can be printed and encapsulated inside PDMS substrates [22], or liquid metals can be printed with PDMS for stretchable 3D structures [100].

2.1.4 Textile substrates

Textiles are multi-level substrates for electronics, where electronic components are integrated into fibers, yarns, and fabrics. Interconnections in textiles are prepared with conductive fibers, for example, steel filaments [101], silver-coated yarns [102], and carbon fiber yarns [103] are used in knitted and woven structures. Also, miniaturized surface-mounted devices (SMDs), such as light-emitting diodes (LEDs), ICs, and sensors are integrated in the fibers [7], [104]. Stretchable electronics systems built on TPU substrates are laminated on fabrics, where material, thickness, and surface topography of fabric affect the adhesion between TPU film and fabric [9]. The properties of fabric depend on the manufacturing technique, which divides the textiles into nonwoven, woven, and knitted textiles.

Nonwovens are fiber-based sheets and webs, which are formed by bonding the fibers without processing them first into yarns. The manufacturing process without the yarns simplifies the process into three main steps: web forming, web bonding,

and finishing process steps. The fiber matrix of nonwovens can be isotropic or anisotropic, and bonding is done mechanically, thermally, or chemically. The length of the fibers varies from a few mm-scale stable fibers to filaments. Also, materials vary between thermoplastics, thermosets, ceramics, carbon, and natural fibers. General applications for nonwovens are geotextiles, apparel, hygiene, and medical products. [105]

Woven fabrics are the most typically manufactured by biaxially interlacing two yarn structures together. The interlace patterns of longitudinal and cross directional yarns, the weft and warp yarns, correspondingly, are altered for different properties and dimensions. The simple plain weave pattern with a high amount of yarn interlacing forms stable and lightweight fabrics, while the satin pattern with a low amount of yarn interlacing with long unbonded lengths of yarn, forms dense and smooth fabrics. More complex patterns can be used for multi-layered fabrics for pockets and 3D fabrics. [101], [106] The woven fabrics can be considered unidirectionally stretchable in weft direction, where over 100 % elongations are achieved with stretchable yarns, e.g., with elastic polyurethane (PU) Lycra-yarns [107].

In the knitting, needles with hooks are used to make interlaced yarn loops, where the yarns run either in the weft or warp directions. The warp knitting is used for fine and complex structures, which stretchability is based on elastic yarns. The weft knitting allows inherent anisotropic stretchable fabrics, which is affected by the material of yarns and the structure; they stretch more in the horizontal direction than in the vertical yarn direction. With plain, double, and rib patterns, diverse stretchable seamless clothing is knitted. [102], [108] The plain knitted fabric can stretch over 100 %, and with PU-yarns, over 300 % stretchability has been achieved [109]. The stretchability of fabric allows the fabrication of dry electrodes from conductive yarns, which are used for ECG measurements in wearable electronics [108].

2.2 Module islands and joining methods

The intelligence of the stretchable electronics is implemented by the small and rigid PCB module islands, which stability allows the use of SMD components and their efficient packing on the board. The modules can include communication, processing, control, and other functions. The off-the-shelf ICs enable small and powerful modules, which currently cannot be fabricated by other manufacturing methods. For instance, 5,35 mm * 5,4 mm size ATtiny85 with 8 pins (by Atmel) and 7 mm * 7 mm

size ATmega32U4 with 32 pins (by Atmel) microcontrollers are used in wearable electronics [110], [111].

The module islands are prepared by standard electronics manufacturing methods. The process starts with a preparation of FR4 or PI substrate, which have a laminated copper foil on it. After cleaning and roughening the laminated copper surface, the surface is coated with a light-sensitive photoresist layer. The layer is exposed except for the desired pattern, and the undesired areas are etched away. After the etching, the remaining photoresist material on the pattern is removed, leaving the desired copper foil pattern on the substrate. Notably, the used lithography process allows precise patterning of copper layers, where the minimum dimensions are defined by a side etching phenomenon in Figure 9 in Chapter 2.3.1. With commercial materials and methods, 75 μm wide copper patterns are achieved with 12 μm thick copper foil [68]. The process is applied for one or two-sided PCBs. Finally, post-processing, such as cutting, drilling, encapsulation, and electrodeposition of silver on copper can be done. [44], [92]

The typical PCB is one or two-sided, where copper layers are on the top or top and bottom sides of the FR4 board along the components. For more complicated PCBs, a multi-layered PCB is made by the stacking. [44] The multi-layered PCBs allow more complex routing and a higher number of components. The single- and multi-layer PCB manufacturing process has been modified for the manufacturing of stretchable electronics with the SCB-process [15], [16]. Moreover, multiple 3D-printing methods for electronics, including interconnections, antennas, and sensor structures, have been commercialized, and are later discussed in Chapter 2.4.3.

In a stretchable electronics system, there are incompatibilities between rigid module islands and integrated electrical elements on deformable substrates. The components have mechanical differences, and for the electronics design, the rigid and stretchable electronic components have different design rules. Increasing the width of the printed stretchable interconnections improves maximum stretchability and decrease resistance at the expense of bigger space requirement [112]. On the contrary, the size of the etched copper foil interconnections on the module island is minimized to decrease the size of the module [44]. The difference in the density and size can cause challenges to combine mechanically and electrically the interconnections on the substrate and in the module. To solve the contradiction, for example, 3D-printed interposers [23], and 3D-printed stacked electronic structures are suggested [72].

2.2.1 Adhesion

The level of adhesion determines how well the modules are fixed on the TPU substrate. The components have mechanical and chemical composition mismatches, which hinder the forming of adhesion and promote multiple adhesion-forming mechanisms instead of a single prominent one [34]. The adhesion can be considered with a few simplified adhesion theories, where the adsorption theory, mechanical theory, and the diffusion theory have been used analyzing the bonding methods for stretchable electronics [113].

In the bonding methods, the joint interface is often considered a 2D area between two bodies. In some cases, especially with the mechanical and diffusion theories, a 3D interphase is used to describe the 2D interface and the volume around the interface [114]. The adhesion is based on the good contact between the bodies, which is achieved when the other body can flow, i.e., in the form of liquid, making the wetting of the solid surface by the liquid the major property of adhesion [115]. For example, the viscosity of the liquid and the surface roughness of the solid body affect the adhesion [116].

In the adsorption theory, wetting is in the critical role because the quantity of adhesion is directly proportional to the amount of interaction between the bodies. Based on the significance of the interactions, they can be divided into primary and secondary interactions. Hydrogen bonds, covalent bonds, and ionic bonds are strong and stable chemical bonds that form the primary adhesion between the bodies. In short, hydrogen bonds are bonds between a hydrogen atom and either oxygen, nitrogen, or fluorine atoms. Covalent bonds are formed when two atoms share their electrodes and ionic bonds are when opposite charged ions are attracted together. Furthermore, the secondary interactions, i.e. Van der Waals forces, are weak and unstable polar forces that are based on weak attraction forces and the movement of molecules. [116], [117] In addition to the inherent properties of the bodies, pre-treatments can be used to improve the chemical activity of surfaces. For instance, plasma treatments, corona discharge treatments, and chemical priming are used to improve surface properties prior to bonding. [118]

In mechanical theory, the adhesion of two bodies is considered via surface properties and topographies. Generally, poor adhesion of smooth surfaces can be improved by making the surface rougher. The effect of coarsening can be considered from different aspects. At the molecular level, a rough surface has a larger surface area for not fully bonded molecules compared to a smooth surface, which increases the surface free energy. Thus, at the substrate level, the total surface energy of the

coarsened body is higher. Mechanically, the coarsened body can transmit deformations more efficiently into the interphase and body, decreasing stresses in the interface. [116], [119] However, the coarsening works only a limited amount. Too much coarsening can weaken the constitution of the substrate, where soft substrates, such as polymers, are more sensitive to being damaged. A very rough surface can also trap air in the interphase during a bonding process, which decreases the wetting and durability of the joint. The cleaning of the surface is mandatory post-process to remove impurities from a manufacturing process and the coarsening. [118]

The diffusion theory discusses forming of adhesion between polymeric materials. When the bodies are above their Tg, their polymer chains can move and entangle. The entangled polymer chains act as binders in the interphase, adhering the bodies together. The amount of adhesion can be improved by enabling higher diffusion of polymer chains, which is done by altering the properties of polymers, for instance, increasing the level of amorphousness and the molecule weight. Moreover, the bonding settings, the temperature, pressure, and time of lamination, can be increased for higher diffusion of the polymers. [116], [120] Inherent properties of polymers affect the depth and duration of the diffusion mechanism. The polymers can be also incompatible, which causes weaker and more unstable diffusion. However, diffusion and adhesion can be improved by using copolymer compatibilizers [116].

2.2.2 Bonding methods

The rigid modules are fixed on deformable substrates with different methods. The aim is to fix mechanically the modules on the substrate and electrically connect the components of the module to the stretchable interconnections on the substrate. A good fixture keeps the module mechanically in place and the electrical connections between the module and the interconnections stable during the elongation of the substrate. Thus, the electrical connections need to be rigid while mechanical connections are allowed some degree of elasticity as long as mechanical strength and electrical connections are not damaged. Figure 5 presents examples of used bonding methods in stretchable wearable electronics.

The modules can be joined mechanically and electrically in separate processes or simultaneously in a single joining process. The discussed methods adapted from different fields are mechanical clamping [121], [122], snap buttons [37], soldering

[15], [123], gluing [124]–[126], lamination [11], [127], pressing [14], welding [128], [129], and sewing [110], [130].

Clamping (Figure 5a) is a bulky joining method, where two relatively rigid bodies are combined by compressing them together with snap-fit joints, screws, bolts, and rivets [121]. Two substrates with electronics can be electrically and mechanically connected via rivets [122] or snap buttons [37], where the snap buttons enable also easy unfastening. Clamping has been conventionally used in electronics to connect the top and bottom layers of PCB by clamping a hollow copper tube, called as a via, inside a drilled hole [131]. Moreover, detachable magnetic-based fixtures have been used in stretchable and wearable electronics [132].

Soldering (Figure 5b) is an electrically and mechanically stable joining method between metal substrates. The soldering materials are fusible metal alloys, which melting temperature, aka liquidus, varies between 90 °C – 450 °C [123]. For example, the melting points of traditional lead solder Sn37Pb and lead-free solder 96,5Sn3Ag0,5Cu (Sac305) are 183 °C and 221 °C, correspondingly [133], [134]. The soldering temperature needs to be higher than the melting point of the solder,

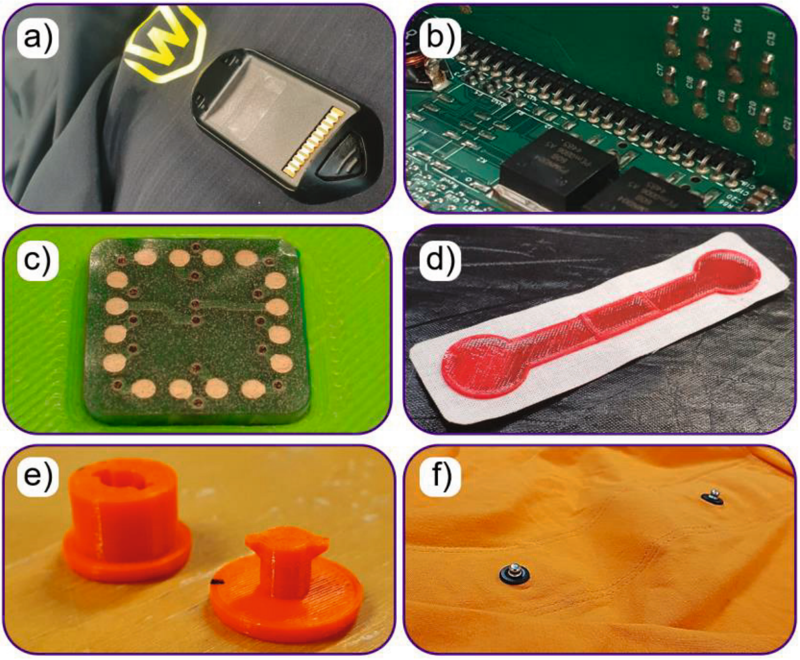

Figure 5. Bonding methods in wearable electronics: a) snap-fit joint, b) soldering, c) ACF, d) direct 3D printed plastic on textile, e) 3D printed fastener, and f) conventional snap buttons.

making the process temperatures too high for TPU-based stretchable electronics [123]. Low-temperature solders with lower melting points, such as 52In48Sn with 118 °C liquidus, can be used in stretchable electronics [15], [135].

Gluing is one of the most versatile methods to combine modules on a deformable substrate. The composition of adhesives varies considerably, which can be modified for specific applications. In electronics, epoxies have been widely used for underfill and encapsulation purposes because of their good thermal stability and gap-filling features [124]. The selection of adhesive depends on the joining type and substrates, where rigid-rigid and rigid-stretchable joints have different adhesives for optimum mechanical bonding [136], [137]. For this, also cyanoacrylate (CA), PU, and pressure-sensitive adhesives (PSA) can be considered [137]. Conventional non-conductive adhesives (NCAs) are used to bond modules on the substrate only mechanically or mechanically and electrically by locking the contact pads together. [125].

All NCAs, especially epoxies are used in isotropic conductive adhesives (ICAs), where the advantage of epoxies is to be able to maintain good adherence despite the high amount of fillers allowing a high load of conductive particles [124]. Materials and shape of conductive fillers affect the conductivity of ICAs. For instance, silver, gold, nickel, copper, and carbon fillers are used, from which silver is the most used despite its tendency to migrate in humid conditions [124], [138]. The fillers are shaped as different-sized flakes, spheres, cubes, and wires. The aspect ratio of particles is inversely proportional to the percolation threshold of the conductive filler network [126], [139]. The range of percolation threshold of conductive fillers is approximately 20 vol% – 40 vol% [126], [130].

In addition to NCAs and ICAs, anisotropic conductive adhesives (ACAs) and anisotropic conductive adhesive films (ACFs) (Figure 5c) are used to bond stretchable electronics [140]. ACFs have a relatively low amount of large conductive fillers, which can form electrical connections in the thickness direction (z-direction) when the ACF is compressed between two contact pads. The range of the amount of conductive fillers is 5 vol% – 20 vol%, which is not enough to form electrical connections planarly between the contact pads. Silver, gold, and nickel metal balls and metal-coated polymer spheres are used as conductive fillers. [125], [141] The fillers are covered with an adhesive matrix, and depending on the substrates to join, the adhesive matrix can be PDMS and nitrile rubber [140], [142]. Two substrates are bonded with ACF by pressing, which process parameters temperature, pressure, and time define the proper joining. With enough temperature and pressure, the non-conductive matrix flows and reveals the conductive fillers, and the sphere-shaped fillers are compressed and deformed slightly for better electrical contact. The

advantages of the ACF bonding process are its relatively low bonding temperatures, easiness, and suitability for fine-pitch electronics. [125], [141]

As also used with ACFs, pressing and lamination processes can be used versatilely to shape thermoplastic substrates and to join parts by melting them together. Stretchable electronic systems built on TPU substrate are laminated on textiles for wearable stretchable electronics [11], [127]. The lamination is adapted for other purposes, and instead of bonding planar substrates, a 2D substrate with electronics components is thermoformed into 3D by compressing the substrate between heated 3D-shaped molds [143]. The ACFs are used to bond two substrates together by pressing [141]. Bonding of electronics on copper structures on TPU film can be done also without conductive adhesives, solely by pressing [14]. Lamination and pressing methods have similarities, but typically it is considered that the lamination is used to join mechanically planar large area substrates, such as textiles and plastic films, while the pressing is done to bond mechanically and electrically small and more complex shaped objects on a large substrate, such as electronic components on plastic film.

Welding joins two similar materials, for example, plastic films or metal foils, by melting and diffusing them together. Complete or partial diffusion of the materials is done with various techniques. The materials are heated with direct contact with a heat source [144], exposition of intense pulsed light [128], or ultrasonic vibration [129]. Pressure has to be considered in contact welding methods, and in electronics patterning applications, the pressure is used to form metallic bonds between the stamp and metal coating of the substrate via cold welding [145]. Notably, welding is mainly used to bond electronic structures for electronic components, and dissimilar materials of stretchable electronic systems hinder the use of welding on a larger scale.

3D printing methods (Figure 5d) are also used to locally place molten plastic on textile or plastic films [146], [147]. Thermoplastic filaments or granulates are extruded via FFF, which enables at the same time the making of 3D objects and fixing it on a substrate [90], [148]. With plastics with conductive fillers, also electrical joints for low-temperature applications are possible [149]. SLA printing has been also used to prepare 3D objects on textiles from thermoset plastics [150]. However, the size of the substrate is very limited, and it needs to sustain the cleaning and curing steps of the SLA process. The 3D printed objects adhere directly to the substrate, and the 3D printing enables the manufacturing of fixtures directly on the substrate, such as functional latches, hooks, and other fasteners (Figure 5e) [151]. Moreover, fixtures from metal can be 3D printed separately and later assembled for wearable applications [152], or entire clothing can be 3D printed from metal [153].

In textiles, several methods to connect parts together have been used. Nonconductive and conductive yarns have been embroidered and sewn in textiles, adding interconnections in textiles and fixing PCB modules mechanically and electrically on textiles [130]. Embroidery and sewing have been also used for making sensors, antennas, and electrodes [45], [130], [154]. Buttons, snap fasteners (Figure 5f), zip fasteners, or other traditional clothing accessories are used to attach electronics to textiles [155]. Especially snap fasteners are widely used because they allow the removal of electronic modules before washing, and they are inherently conductive and durable.

Before the bonding of modules, the selected joining method depends on the size and number of contacts of the module. For example, a 5,35 mm * 5,40 mm size ATtiny85 microprocessor with two 1,6 mm * 0,8 mm size passive SMD components is used to manufacture round 20 mm size LilyTiny PCB modules, which can be sewn on the clothing using its 6 contact pads [110]. Also, 24CW1280X ICs (Microchip Technology) have been compressed with conductive fibers, which allow the manufacturing of yarns with > 1 mm diameter for memory storage and temperature measurements [7].

2.2.3 Stress concentration effect of the module

At the system level, mechanically heterogenous stretchable electronics systems can stretch because of the high stretchability of the substrate and interconnections, but at the component level, the stretching induces mechanical mismatches at interfaces between the rigid and stretchable components. The phenomenon is significant with adhered SMDs and PCB modules on stretchable substrates, which instead of deforming during stretching, act as rigid anchors which increase the amount of stress and elongation around them. The phenomenon, also called the stress concentration effect, can cause various damages to the system. For example, electrical failure of interconnections, delamination, and irreversible plastic deformations of the substrate. [34], [156] Notably, the stress concentration effect applies to every component that has a mechanical mismatch, and the phenomenon is also observed with meander-shaped copper interconnections on TPU substrate [157]. Figure 6 presents a finite element analysis (FEA) model and results of a straight copper element. After the failure and the formation of a crack that acts as the mechanical discontinuum point, over 50 times larger stresses are concentrated to the substrate between the copper element fragments [158].

The stress concentration induced by the rigid modules is decreased with two techniques. First, the mechanical difference between the rigid module and the stretchable substrate, the difference in Young's modulus of the components, is decreased. The modules and electronics can be made from softer materials [46], [159], or additional interposers between the module and the substrate can be used [23]. However, for more comprehensive design and long-term durability, there are other parameters, such as CTE and Tg to take into account with Young's modulus [14]. In principle, also stiffening the stretchable substrate decreases the mechanical difference between the modules and substrate, but it also decreases the stretchability of the system. To avoid universal stiffening, local stiffening modifications close to the stress concentration areas are feasible. For example, additional layers of TPU can be laminated [160], or 3D-printed on a TPU film for locally stiffer areas [147]. Moreover, TPU film can be locally removed for local stiffness tuning [34].

Secondly, to avoid premature failure, the elevated stresses can be controlled and directed to non-relevant areas of the stretchable system. Instead of decreasing the total amount of stress, it can be enough to make the interconnections and electronics areas deform homogeneously, preventing high-stress concentrations that can break the system electrically. This has done by protecting the area around the modules, which is realized during adhering of the modules [12], or in a later encapsulation

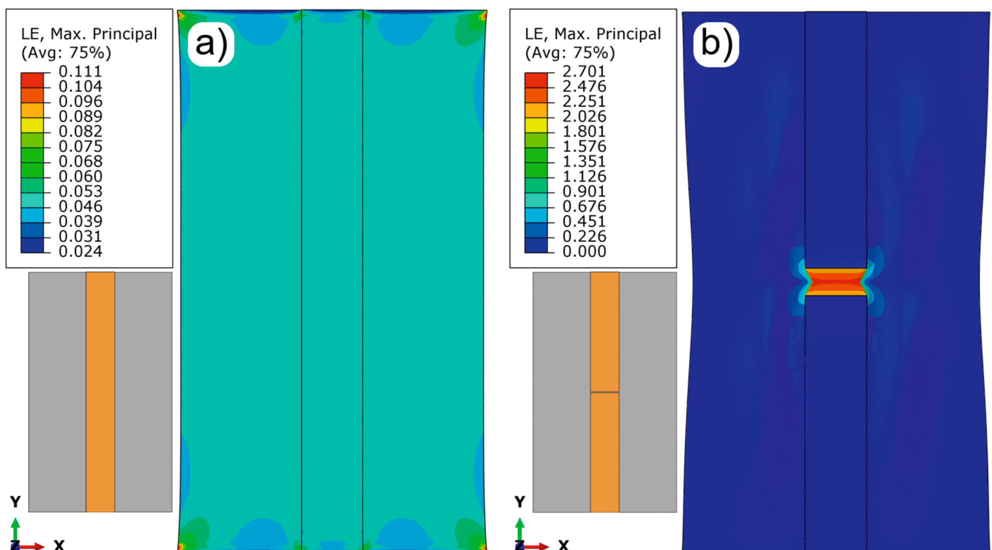

Figure 6. Role of the stress concentration at the failure of straight copper element: a) the elongation of the undamaged copper element, and b) the elongation of snapped copper element [158].

process [161]. Protective structures can be placed on the module-interconnection transition area [160], and weak points of shaped stretchable printed interconnections can be protected for more uniform elongation [147]. An option is also to change the geometries of interconnections [13], [162], or rigid modules [163].

After the stress concentration at the interface of module and substrate is considered, the next weak point of the stretchable system is the area with the second largest difference of Young's modulus, which highlights the usage of mechanical testing and FEA to predict the sufficient level of deformability [158]. FEA is a simulation method that under given conditions and set variables, predicts the physical behavior of models. In the simulation, the models are divided into meshes of smaller cells, which behavior is calculated with mathematical models. In addition to the mechanical behavior, with the right mathematical models, FEA can be used to predict the electrical properties of stretchable interconnections. [157], [164]

Depending on the integration level of the stretchable system (Figure 2), the stress concentration effect realizes differently. The discussed methods to decrease stress concentration apply to integration levels 2-4, where the rigid islands, stretchable interconnections, and substrate are used [12], [165], [166]. At integration level 1, which is based on single components, such as an electronic component, TPU film, and copper meander interconnection, FEA results are useful to determine the mechanical behavior of the component [157]. Still, notably, the hybrid systems of stretchable electronics can be analyzed more realistically only as a whole.

2.3 Stretchable interconnections

The module islands are electrically joined together with stretchable interconnections. In addition to the stretching, the interconnections undergo more complex deformations during stretching, which can include simultaneous stretching, compression, and twisting (Figure 3) [157]. The stretchable electronics have been developed by industries that have been active in wearable electronics, which has led to the wide variation of different stretchable interconnections. Because of this, stretchable electronics are fabricated with copper etching, printing, and textile manufacturing methods (Figure 7).

The manufacturing methods have their distinct features, which cause the differences between the stretchable interconnections. The SCB process is adapted from the traditional PCB manufacturing process, where photolithography [13], or

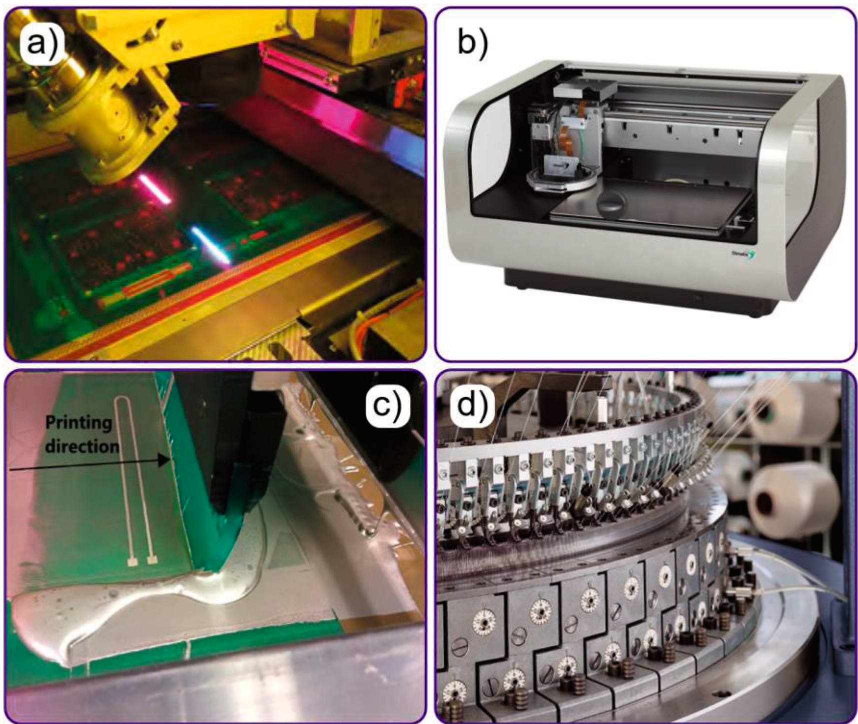

Figure 7. Manufacturing technologies of stretchable interconnections, a) laser direct imaging [167], b) Dimatix DMP-2850 inkjet-printer [168], c) screen-printing [18], and d) circular knitting machine [169].

laser direct imaging [127], are used for dry-film patterning to define etchable copper areas. The versatile laser direct imaging is also used in the solder mask imaging (Figure 7a) [167]. Conductive inks are printed with several printing methods, from which inkjet-printing (Figure 7b) and screen-printing (Figure 7c) are used for stretchable and flexible interconnections. Printing techniques are AM fabrication methods, where inks with silver and carbon fillers are mostly used [18], [170]. After final curing process step, the inks form conductive networks and conductive interconnections [18], [170]. In short, the inkjet-printing is accurate printing technique, which uses highly diluted inks for metallic interconnections [171]. The screen-printing uses a squeegee to push viscous ink through a patterned screen onto the substrate. The ink consisting of conductive fillers and deformable polymer matrix, is inherently stretchable and conductive [18]. In textile industry, several manufacturing methods are used to integrate conductive yarns in non-conductive textiles. Particularly, because of the elastic loop structure, knitting is often used for stretchable wearable electronics (Figure 7d). [172]

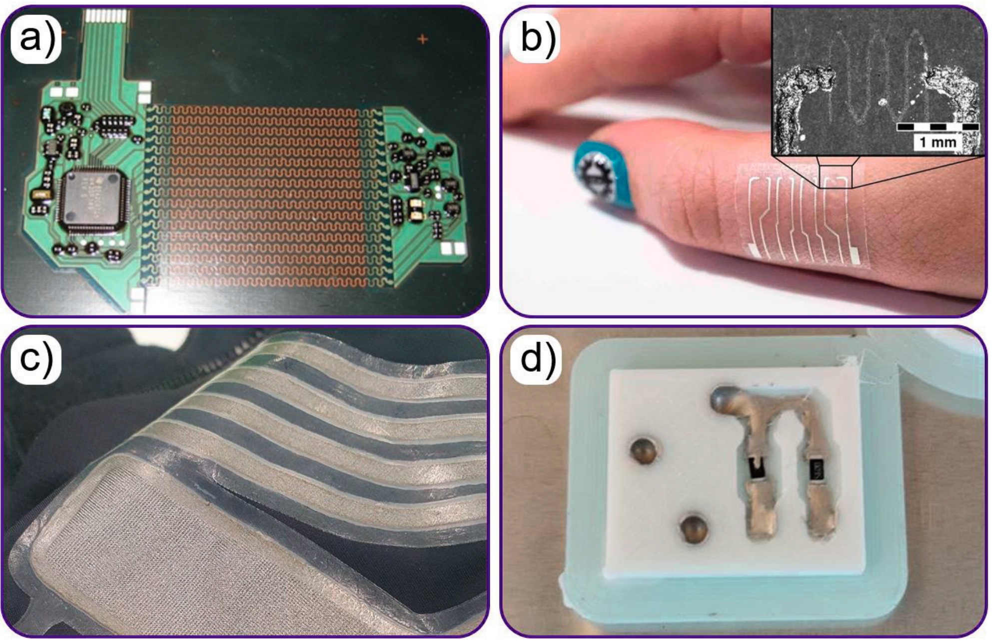

Figure 8. Stretchable interconnection examples: a) stretchable electronics system consisting copper meanders, made with SCB method [16], b) temperature sensor plaster, which consists inkjet-printed graphene/PEDOT:PSS temperature sensor between screen-printed silver ink interconnections [39], c) knitted interconnections and electrode from conductive silver coated yarn, and d) dispensed stretchable conductive ink interconnections in a 3D-printed board.

The examples of stretchable interconnections prepared by previously mentioned manufacturing methods are shown in Figure 8. For instance, the stretchability of the SCB copper foil meander-shaped interconnections is determined mainly by the meander-design, width, and thickness of the traces (Figure 8a) [11]. The thin and flexible inkjet interconnections can be made also stretchable by changing the ink composition and shaped design, or by pre-stretching the substrate [60], [173]. The screen-printed interconnections with stretchable polymer matrix are inherently stretchable [147], which can be combined with inkjet-printed graphene/PEDOT:PSS traces for temperature sensor plaster (Figure 8b) [39]. Knitting and weaving enable integrating of conductive yarns inside textiles [62], and for larger stretchable interconnections, thoroughly conductive knitted fabric can be cut and laminated on clothing for stretchable interconnections and electrodes (Figure 8c) [174].

Notably, the stretchable inks are also dispensed on 3D-printed TPU boards, which can be encapsulated with SMD components inside the 3D-printed object

(Figure 8d) [175]. The interconnections can be placed as planar [175], or 3D [43], which deform along the substrate of the 3D-printed object.

In addition to the multifunctional printing processes, different types of processes can be combined for the manufacturing of stretchable interconnections. Copper foil and printed interconnections are prepared on flexible or deformable film, which can be laminated further on conductive or non-conductive fabric [9]. A fabric can be directly screen-printed with conductive inks [8], or yarns with metal conductors and electronic components can be integrated and weaved inside fabrics [7]. Also, conductive inks can be printed on stretchable film that includes copper foil islands [158].

The most used conductive materials in stretchable interconnections, e.g., copper, silver, and carbon, are inherently rigid. This causes the imminent trade-off between their conductivity and stretchability. However, despite the rigid composition of the interconnections, they can be made more flexible by minimizing their thickness [176], and stretchable by using meander 2D spring patterns [127]. Additionally, 3D buckled interconnections are prepared by pre-stretching the substrate before fabrication of the interconnections, which stretching is afterwards released [17]. The shaping of interconnections enables rigid stretchable etched copper foil and inkjet-printed interconnections, where the 2D approach is well-studied.

2.3.1 Rigid shaped copper foil interconnections

Originally, the SCB technology is developed by Fraunhofer-TU Berlin and IMEC-Ghent research institutes, which prepare the etched copper structures on TPU and PDMS, correspondingly [16]. In the TPU-based SCB process, 35 μm thick electrodeposited (ED) copper foil is laminated on the TPU substrate. The laminated structure is processed the same way as traditional PCBs, which process includes the appliance of the photoresist mask, removal of non-exposed areas of the mask, etching, and removal of the rest of the photoresist mask. The bottom side of the ED copper foil is rough, approximately 3 – 5 μm, which improves the adhesion between the foil and the TPU substrate. The top side of the copper foil is smooth for electronic applications [127]. Similarly to PCBs, SCB boards are also compatible with post-processing and multi-layer designs [11].

As a subtractive manufacturing method, the etching enables precise shapes, where meanders with a minimum 100 µm width and undulation length have the highest stretchability [13], [127]. The copper foil has a relatively homogenous grain structure and thickness, which with a subtractive etching process step, enables precise control of electrical properties and dimensions of interconnections. The maximum developed accuracy of the SCB method is determined by the thickness of the copper foil and a side etching phenomenon (Figure 9), where the copper foil etches under a solder mask film unevenly [177]. Moreover, the process currently supports 60 cm * 40 cm sized boards, limiting the overall size of stretchable electronic systems.

The manufacturing methods of copper foil affect the mechanical properties of the meander-shaped copper traces. Generally, either rolled and annealed (RA) or ED copper foils are used in PCB manufacturing, from which ED foils are applied for the SCB process [11]. The RA foils are manufactured thermomechanically by rolling and annealing foils until desired thickness is achieved [178]. The rolling and annealing change the grain structure of the copper to be denser and more oriented towards the rolling direction, which provides a smooth surface finish and anisotropic mechanical properties [178], [179].

The ED foils are manufactured by depositing copper on a rotating drum in a copper electrolyte solution, where the drum acts as a cathode, and the anode is submerged into the copper electrolyte solution along the drum. The copper foil with a small and uniform grain structure grows on the drum, and because of the smooth surface of the drum, the other side of the foil is smooth, and the other side submerged into the electrolyte solution is rough. [180] Compared to the RA foils, the ED foils are more ductile, isotropic, and inexpensive. RA foils are more bendable for flexible applications, but the adhesion-promoting rough surface makes ED foil more suitable for the SCB process. [11], [179]

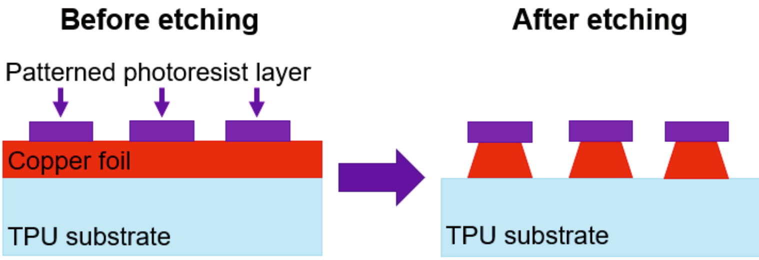

Figure 9. The side etching phenomenon of the meander-shaped copper foil interconnections.

Notably, copper and other metal foils can be shaped with pressure and elevated temperatures. Hot embossing with a heated mold and pressure is used to shape copper foils for detailed copper patterns [181], [182]. Furthermore, cold embossing is used to cut thin ~ 5 μm thick PI-supported silver layers for stretchable electronics [183]. Copper foil interconnections are also corrugated by feeding the foil between two gears, forming stretchable and vertically wavy traces [184].

2.3.2 Rigid printed interconnections

Inherently rigid stretchable interconnections are made additively by printing metallic interconnections on stretchable substrates and altering the interconnection design. The printing is done typically by inkjet printing, where a print head ejects ink droplets onto a substrate. The method can be divided into continuous inkjet and drop-on-demand inkjet printing, where the continuous inkjet has a lower printing resolution, a high need for maintenance, and limited usage in printed electronics because of the volatile solvents of the inks. The drop-on-demand method ejects droplets by piezo, heating, or electrolyte techniques, from which the piezo jet is the most used in industrial applications. In the piezo jet system, the vibration of the piezo crystal pushes the ink out from the nozzle. [185]

The width of the printed interconnection is defined by the drop diameter, which is defined by the drop volume, which varies between 0,5 – 500 pl. The typical drop diameter is set between 10 – 100 μm, for instance, the diameter of a 10 pl volume droplet is ~ 27 μm. [171] Viscosity is one of the key parameters of inkjet inks, which generally varies between 2 – 50 mPa·s [171]. The low viscosity sets the frames to conductive inks when their conductivity is optimized by modifying the four main components of the inks: solvent, metallic fillers, dispersant, and binder. The binder improves adhesion between the fillers and the substrate, which amount, however, is limited because of the viscosity increase. Also, the higher amount of fillers increases the viscosity. [186] After the printing, the inks are heat treated, which is a sintering process of metallic fillers. For instance, the commercial 736465 inkjet silver ink (by Sigma-Aldrich) is heat treated at 150 °C for 60 min [187]. The ready-sintered inkjet ink patterns are mainly composed of merged metallic particles, where an additional binder can be used [186].

The metallic inkjet-printed interconnections are made stretchable with a few methods. Similarly to the rigid copper foil interconnections, the inkjet interconnections can be prepared as planar meanders [60] or bridge-like buckled

traces [188]. Straight inkjet-printed interconnection can sustain less than 1,50 % elongation, and even the swelling of the polymer substrate during the sintering can be enough to break the interconnections [189]. The substrate can be pre-stretched to decrease the swelling of the substrate [189], but after the excess pre-stretching, the sintered inkjet-printed interconnections crack and fold, enabling stretchability at the expense of more uneven electrical properties [60].

2.3.3 Deformable printed interconnections

Soft conductive materials, which have low Young's modulus, are used for thoroughly stretchable interconnections. Elongation of such interconnections is governed by the deformations of the substrate, and for example, interconnections are made from screen-printed silver ink [39], liquid metal [190], and nm-scale thick gold film [191]. In the screen-printing, ink is added to a substrate by pushing it through a woven screen. The woven screen is composed of steel or polyester filament mesh, where the non-printable areas are covered with UV-hardened emulsion. The density of mesh structure and material and thickness of the yarn in the structure affect the thickness and amount of printed material on the substrate. [18]. For instance, polyester mesh with 79 threads per cm, a 55 μm thread diameter, and a 69 μm mesh opening enable theoretically screen-printed patterns with 26 μm wet thickness and 7 – 15 μm dry thickness with a silver ink CI-1036 (by ECM) [18], [161]. Furthermore, the parameters of the squeeze that is used to push the ink through the screen, e.g., the shape, hardness, and pushing pressure, affect the quality [192].

The composition of stretchable screen-printable conductive inks is based on a dissolved polymer matrix, which is diluted with a solvent. The polymer matrix binds nano- or micro-size conductive fillers, which material, shape, and size vary. Approximately 2 – 16 μm silver flakes [193], [194], < 20 μm graphite flakes with 45 nm spherical carbon black [170], and 3 – 8 μm long carbon nanotubes [195] are added in the screen-printable inks. Notably, also inks from conductive polymer PEDOT:PSS are fabricated, which do not have the distinct filler structure as the silver inks do [196]. The distribution and amount of conductive fillers affect the electrical and printability properties of the inks, which are modified to set the viscosity of the inks at least to 1000 mPa·s [170], [196]. Finally, after the screen-printing, the inks are heat treated at around 120 °C to remove the solvents [18], which is lower than the sintering conditions of inkjet metal particle inks.

Stretchable conductive inks are often used in single or roll-to-roll screen-printing processes [12], [197]. Moreover, functional inks are also applied for other printing processes, such as stencil printing [194], DIW [111], offset printing [198], and gravure printing [198]. The printing method affects considerably the cross-sectional area of the interconnections, which further influences the conductivity and stretchability of interconnections [112]. In some applications, instead of stretchable conductive inks, Gallium-based liquid metals are used for stretchable self-healing electronics [100]. However, the liquid metals are vulnerable to leaking, which requires precise process control and encapsulation. When exposed to air, gallium-based liquid metals form an oxide skin, which changes surface properties and decreases the flowability of the ink [100], [199].

2.3.4 Fiber-based interconnections

In general, fibers include a broad range of different types of fibers, materials, and applications for stretchable and wearable electronics. Non-conductive fibers and fabrics can be used as carriers for printed interconnections and laminated metal foils [9], [159]. Fibers can be made conductive with carbon, copper, silver, and other conductive materials [10]. The fibers are applied as conductive fillers in inks [200], functional carriers of conductive inks [98], stretchable interconnections in 3D-printed electronics [46], and conductive yarns and fabrics in wearable electronics [45].

The EU regulation defines the textile fiber means a unit of matter characterized by flexibility, fineness, and a high ratio of length to maximum transverse dimension, which renders it suitable for textile applications [201]. The fibers are made conductive, for instance, by silver-coating non-conductive fibers or making the fibers entirely from conductive material [202], [203]. Mm-scale and longer conductive fibers are used as fibers in non-woven processes, or processed into yarns for knitting, weaving, and embroidering applications [203], [204]. The long length of the fibers promotes good mechanical and electrical properties of fibers [203], [204]. The long conductive fibers are embedded into conventional textiles [45], or pieces of conductive knitted textiles can be encapsulated inside TPU for highly stretchable embedded interconnections [204]. Permeable carbon stable fiber cloth pieces can be integrated inside 3D-printed objects for stretchable interconnections and sensors [46].

Instead of textile applications, small μm and nm-scale conductive fibers are used as functional fillers in inks and plastics. When mixed with other sizes and shaped fillers, conductive fibers decrease the percolation threshold of the ink and increase the conductivity of interconnections [205]. For example, silver nanowires [205], and carbon nanotubes [195] are added in conductive inks. Carbon fibers are also combined with TPU for conductive films and filaments for FFF 3D printing, which can be categorized as conductive composites [206], [207].

2.3.5 Failure mechanisms of stretchable interconnections on a deformable substrate

Considering different types of stretchable interconnections, the very first manufacturing step is an AM process, for example, printing or lamination. After proper bonding of the conductive material to the stretchable substrate, the conductive material can be further processed with etching, sintering, or other process. Excluding liquid metal stretchable interconnections that are unstable without fully encapsulated inside a substrate [100], [190], etched copper foil meanders, inkjet and screen-printed traces, and embedded conductive yarns are widely used stretchable interconnections. The interconnection types have their own characteristic properties, and their usability is defined by their mechanical and electrical properties before and after the failure.

Universally, the resistance value of an interconnection depends on the material, length, and cross-sectional area of the interconnections [208]. The dimensions of the copper foil interconnection do not change, only the meanders open as 2D springs. The μm-scale thick copper foil structures are mechanically stable until concentrated and relatively fast mechanical failure (Figure 10a), which leads to the electrical failure of the system. The failure mechanism of the copper foil meanders on the deformable substrate is a multistage phenomenon [158]. At first, the substrate stretches, which induces stresses to the interface between the substrate and copper foil. Shape, interface area, copper foil thickness, and other parameters affect how high stresses the interface and the system endure [16]. Design decisions and electronics components can concentrate high local stresses, which cause premature damage and failure of the system [158]. The elevated stresses cause failure initiation, where the copper foil delaminates from the deformed substrate [209]. After the delamination, the unadhered copper foil area deforms more without the support of substrate, and a crack is initiated. The crack in the meander-shaped copper foil interconnection is

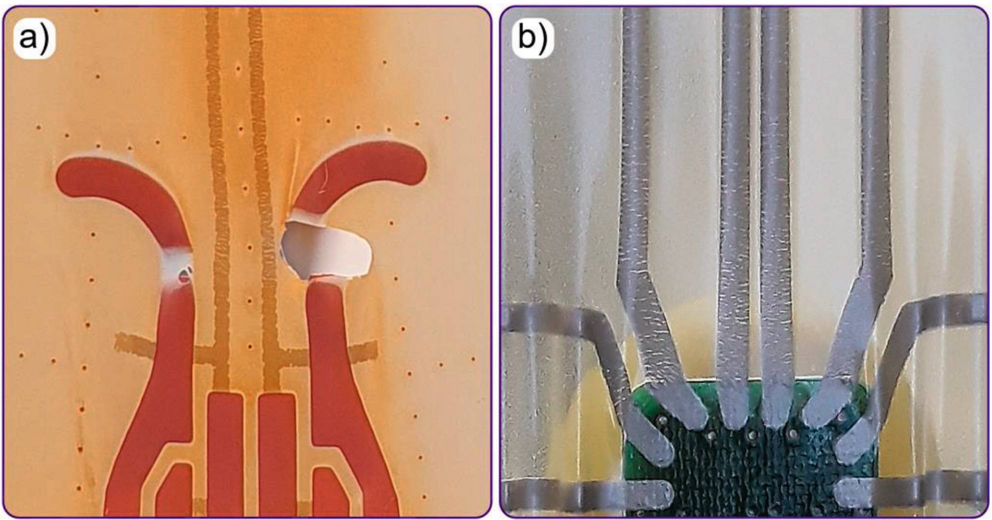

Figure 10. Example failures of different stretchable interconnection materials: a) shaped copper foil structures, and b) straight screen-printed silver interconnections.

formed at the location where the meander opens unless the crack has been already initiated during the delamination phase or from an external damage [157]. The initiated crack propagates perpendicularly to the elongation direction of the interconnection [209]. Thin 100 μm wide meanders are favored for their higher stretchability [127]. However, the small width of meanders also means the short distance for the cracks to propagate, making the failure of the copper foil meanders sudden and unpredictable [13]. After the failure, the copper foil interconnection can be considered as a switch - the cracked copper foil sides are electrically connected at 0 % elongation and disconnected when the elongation is > 0 % [158].

The failure mechanism of inkjet-printed interconnections resembles the failure of copper foil interconnections. The failure starts as the delamination at the interface between the sintered inkjet-printed interconnection and substrate. The printed interconnection structure consists of merged droplets and sintered conductive particles, making the structure more heterogenous than metal foils. Width and thickness variations can act as stress localization and delamination points in the printed interconnections [210]. The thinness and smallness of inkjet-printed interconnections mean that their failure requires less stress to realize, but also, the small dimensions decrease Young's modulus which defines the type of failure [191].

Differing from the inherently rigid interconnections on a stretchable substrate, the stretchable screen-printed interconnections comply thoroughly with the deformations of the substrate [196]. The printed patterns deform and form

microcracks along the substrate instead of sustaining elevated stresses until the fatal and sudden electrical failure of a single location in the interconnection (Figure 10b) [112]. Because the microcracks cause a systematic increase of resistance, an application-specific resistance level is decided to be the failure of the interconnection. Despite the shape of interconnection, the matrix of the ink is elongated along the elongation direction of the substrate and is compressed perpendicularly according to Poisson's effect [112]. This emphasizes simple designs, and the straight screen-printed interconnections are the most predictable ones, while additional shapes and angles need to be supported [147], [211]. The screen-printed interconnections work after reaching the failure level but depending on the amount of irreversible plastic deformation of substrate and ink, the microcracks do not fully close anymore and the resistance value at the undeformed stage remains higher than initially [18]. The micro-cracking, which is caused by the lower Young's modulus of the interconnection [191], can be considered to decrease the stress peaks in the interface between the interconnection and substrate, which further means the smaller delamination tendency of the printed traces.

The shape and orientation of the conductive yarns affect the failure mechanisms of textile-integrated stretchable interconnections. In general, electrical damages and failures are related to the physical damage of the conductive fibers. For example, conductive coating of stable fibers or filaments can be abraded [212], or completely snapped, causing the simultaneous electrical and mechanical failure of interconnection [213]. However, a cross-sectional area of yarns or nonwoven pieces consists of a large number of fibers, making the failure of a single fiber less significant.

2.4 3D printing of stretchable electronics

2.4.1 FFF 3D-printing method

FFF is the most widely used 3D printing method, which has been called with many names. Originally Stratasys Inc. developed the manufacturing method in the 1980s and trademarked it as fused deposition modeling (FDM) [214]. To avoid trademark issues, members of the RepRap project described a similar process as the FFF [215]. Later, the process in which a material is selectively dispensed through a nozzle or orifice is standardized as material extrusion (MEX) [216]. All the terms are used in

research, but in this work, the FFF is used to describe the selective dispensing of thermoplastic polymers (Figure 11).

FFF is a versatile 3D-printing method, which is applied for small tabletop machines (Figure 11a) and industrial-scale applications. FFF is based on semi-product thermoplastics, which are prepared in the form of filaments (Figure 11b).

Filaments are available in two sizes, with 1,75 mm and ~ 3,00 mm diameters. If the filaments are from the same material, the thicker filament is stiffer and requires a smaller movement of a feeder (Figure 11c) to push the material to the nozzle. The higher stiffness improves the printing of TPU and other soft plastics. The filament is directed through between two rolls of the feeder, which gives the force to the filament to overcome the resistance to the flow, induced by the print core (Figure 11d). Along the compression pressure between the rolls, grooved surfaces of another or both feeder rolls improve the grip of the filament. The too-low grip cannot push the filament through the nozzle, which can cause incomplete feeding and filament grinding. [217]–[219]

Ultimaker 3D printers have changeable print cores, which include the main structures of FFF print cores (Figure 11d): the heatsink, heat break, heater block, thermistor, heating cartridge, and nozzle. The filament is fed through the print core, which melts the head of the filament and directs the molten plastic through a nozzle. A tube-like heat break is connected between the heatsink and the heater block to

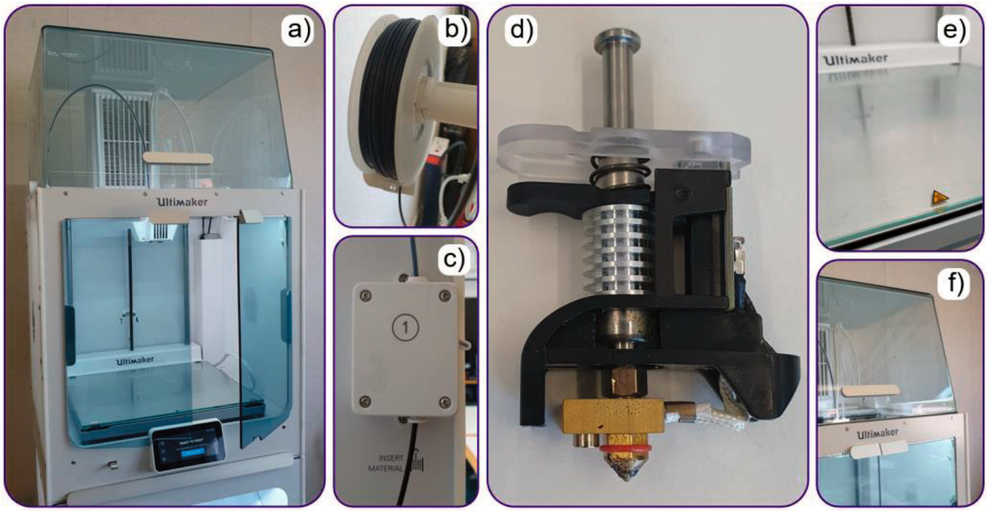

Figure 11. Ultimaker S5 3D-printer and the critical parts that affect the FFF process: a) Ultimaker S5 3D-printer, b) filament spool, c) feeding system, d) print core that includes a heat sink, heater block, and nozzle, e) building plate, and f) chamber.

distribute elevated temperatures from the heater block to the heatsink, which makes the filament melt only from the tip. The uneven melting of filament can cause clogging of the print core [219]. For tabletop 3D printers, a typical temperature area of the heater block is between 200 °C – 300 °C [91]. Industrial FFF printers are designed for more advanced plastics, such as polyetheretherketone (PEEK), which requires over 400 °C printing temperatures [59]. The size of the nozzle in the commercial FFF 3D printers varies between 0,2 mm – 1,0 mm, where the high nozzle size decreases the manufacturing time, and with fully filled structures, decreases the breaking force [220]. The small nozzle improves the accuracy of the 3D-printing, but slows the 3D-printing process, and increases the pressure drop of the system, hindering especially the extrusion of the soft plastics [221], [222]. Moreover, the width of the extruded molten plastic bead from the nozzle can be larger than the nozzle diameter because of the die-swelling phenomenon [218].

Molten plastic beads in FFF are printed on the building plate (Figure 11e) with a layer-by-layer technique. The extruding locations and amount of plastic are determined by a gcode program, which is generated from the 3D object that is processed in the slicer software. The settings of the first printing layer are optimized to improve adhesion between the plastic and the building plate. The building plate is also modified and post-processed for higher adhesion, and for example, coated plates, adhesives, and heating of the plate are used. Still, one of the most common failures of FFF is the delamination of unfinished 3D-printed objects from the building plate. Despite the first layer settings and building plate post-processes, the 3D-printed object can be delaminated because of the uneven thermal environment and uneven shrinking of plastic. The plastics have different amounts of shrinking, which is minimized by decreasing the thermal gradient between the object and the environment via an unheated or heated chamber (Figure 11f). [217]–[219]

The advantages of the FFF are the low material consumption compared to the subtractive manufacturing processes and the wide range of different materials. The 3D-printed objects are highly customizable and the production needs only a little amount of preparation, making the small and medium size production series feasible. [20] Nevertheless, the disadvantage is the relation between the printing time and accurateness, thus highly precise objects are slow to print [223]. Also, since the 3D-printing is a relatively new manufacturing method, it still needs further standardization, and testing of materials and methods is required [224].

2.4.2 Structure and stretchability of FFF 3D-printed objects

The objects 3D-printed with FFF have a unique structure, which can be modified for different purposes. The 3D structure (Figure 12) consists of four parts, I) a bottom part, II) walls, III) a top part, and IV) infill that fills the space made by I) – III) parts. [217], [223] Advanced slicer programs, such as Ultimaker Cura, have hundreds of settings, which are used to modify the whole 3D structure and the parts for desired applications. In this work, the 3D structure and the settings are introduced in the aspect of stretchability, and the assumed 3D-printing material is a TPU filament.

The main function of the bottom part (Figure 12a) is to adhere the object on the building plate, which is enhanced with multiple first layer settings, for instance, by increasing layer thickness and printing temperature and decreasing the printing speed [225], [226]. In the settings, a brim or raft can be made around the first layer to increase the area for higher adhesion [226]. Depending on the building plate material and sensor technology of the FFF printer, the thicker first layer also levels a possible unevenness of the plate [225]. Thin layers have higher stretchability than thick layers [54], but as the height of the FFF printed objects is in mm-scale, the role of the first layer in the general stretchability is very small. In addition to the first layer, the bottom part has a few solid layers, which numbers can be decreased to improve stretchability [226].

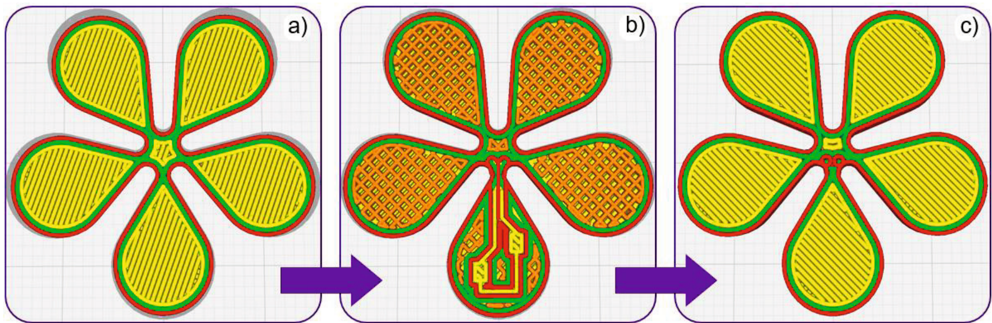

Figure 12. The screenshot from Ultimaker Cura slicer software (version 5.2.2), where the general structure of the 3D-printed module is shown: a) the bottom of the module, where the red line is the outer wall, the green line is the inner wall, and the yellow lines are the bottom areas, b) the middle of the module, where orange lines are the infill areas with 80 % infill ratio, and c) the top of the module.

The walls surround the outer and inner edges of a module (Figure 12b), which as printed in the direction of the edges, improve the strength and dimensional accuracy of the FFF object. Typically, two walls are used, but also a higher number of walls for higher strength and infill coverage are used. However, the higher amount of walls decreases the stretchability of the object. [217], [227] The stretchability can be improved by decreasing the planar thickness of the walls, which can be done in a precise manner by decreasing the size of the nozzle, or in an unprecise manner by only changing the setting values [228].

The top part of the object (Figure 12c) is made solid to hide the infill and to achieve even surface quality. The FFF printed surface always has at least a few microns of roughness, which can be further decreased with smaller layer thickness, the ironing feature of the software, or by post-processing the surfaces mechanically or chemically [218]. The top part consists of a few solid layers to improve the surface quality, and as with the number of walls, the top layer count can be decreased for higher stretchability [226].

Generally, the infill is the largest area of the FFF object (Figure 12b). The printing time, amount of material, and stiffness are decreased by lowering the infill ratio [217], [226]. Still, in case of good stability and the printing surface quality, the infill ratio is increased relatively high. In addition to the low infill ratio, the infill pattern can be optimized for stretchability [226], [229].

With universal settings, the stretchability of 3D-printed objects can be changed. There are multiple settings, for example, the nozzle size determines the size of the extruded plastic bead, and the smaller line width and layer thickness are achieved with smaller nozzles [228]. By lowering the layer thickness, the accuracy, and elongation are increased [54], [218]. Still, the relation between the infill ratio and the strength of the object must be considered because it increases when smaller nozzles are used [222]. Moreover, the printing temperature affects how well the extruded beads are diffused together, thus the stretchability can be increased by increasing the printing temperature [218], [226].

2.4.3 Electronics prepared by FFF

Similarly, to the stretchable interconnections, the plastic filaments in FFF are made thermally and electrically conductive by adding nano- and micro-scale conductive fillers inside the filaments. As cheaper filler materials, copper nanoparticles [230], graphene [149], carbon black [231], and CNTs [231] are mixed in the filaments. PLA-

based filaments are used with the fillers because it has very good printability, but also other low-temperature plastics are used [149]. The commercialized filaments are designed for currently used tabletop FFF printers, and they enable 3D printing of electronics with current fabrication limits. However, the long-term durability of filaments has to be studied further, since low-temperature plastics do not have as good thermal resistance as conventional PCB materials [230]. In addition, the extruded conductive filaments have high contact resistance [55], which has to be decreased by using conductive ink on the contacts [149], [232]. Moreover, fillers in the plastic hinder the extrusion process of the filament, and the 0,4 mm or larger nozzle diameters are generally recommended for commercial filaments to avoid clogging of the nozzle, which limits the minimum accuracy of the 3D-printed objects [230], [231].

Conductive features in FFF can be also added by integrating continuous carbon fiber filaments in the object [232]–[234]. A bundle of a few microns thick carbon fiber filaments is directly fed inside the print core of FFF along the 3D printing plastic filament [234], or they are integrated inside a prepreg carbon fiber filament, which polymer outer layer allows the 3D-printability [232], [233]. The advantage of continuous carbon fibers is the longer thermal and electrical pathways than nano- and micro-scale fillers, allowing higher conductive patterns [149], [232]. However, the challenges of the continuous carbon fiber systems for 3D-printed electronics applications are the breakage of the fibers during the 3D-printing process, the high anisotropic nature of mechanical and electrical properties, and the contact resistance as with conductive plastic filaments with fillers [232], [233]. Notably, the continuous fiber filaments are currently used to mechanically reinforce FFF parts, which are applied for various production levels by Markforged and Orbital Composites [235]. With the reinforcing feature, the carbon fibers allow structure self-monitoring [234], and shielding from electromagnetic interference [236].

The intelligence of conductive 3D-printed structures is increased by using off-the-shelf electronics components, for example, passive SMDs, LEDs, and sensors. The components are placed manually or with a pick-and-place machine inside the FFF object during the printing by pausing the process, and on surfaces, after the object is ready [237]. With the 3D-printing techniques, electronic components can be placed in various positions, for instance, on topside, downside, or sideways, allowing more packed modules than in the standard PCB modules [43], [237]. In addition to the pick-and-place device, printing devices, such as DIW, aerosol, and inkjet printers can be used along a modular FFF device for smaller and more conductive interconnections [61], [237], [238]. The interconnections are added inside

the channels, which are prepared during the designing of the object [237], or after the 3D printing, are routed for higher dimensional accuracy [239]. Neotech AMT and nScrypt companies have manufactured 5-axial 3D printing systems for electronics, where FFF, DIW, inkjet, and other devices can be versatilely mounted inside the system for complex 3D-printed electronics [43], [237], [240].

2.4.4 Electronics prepared by other 3D-printing techniques

In addition to the FFF, 3D-printed electronics are made by other methods. The UV-curable resin-based SLA 3D printing is combined with DIW to prepare structural 3D-printed electronics [72]. UV-curable inks are also used in multi-jet printing (MJP), in which an inkjet-printing head with UV-curing feature can do precise layer-by-layer printing. The MJP technique, developed by 3D Systems Inc., is used to make hollow objects that are filled with conductive silver ink. [241] Moreover, inkjet printing is adopted in DragonFly 3D-printer by Nano Dimension, where the machine is optimized for two inks, for the IR-curable conductive ink from silver nanoparticles and the UV-curable dielectric ink [242]. HP has also developed a multi-jet fusion (MJF) system, where the object is built by stacking polymer powder layers, which are fused by inkjet-printed fusing agents in the powder matrix. The fusion of polymer particles in the printed areas is activated with heating before making the next layer. The advantage of the MJF is the broad range of different fusing agents, which can be modified to make conductive, transparent, or soft areas. [243] Furthermore, aerosol jet printing is used by Optomec Inc. for the fabrication of printed electronics over 3D surfaces [244].

2.4.5 Stretchable electronics prepared by FFF

Electronic systems are made stretchable by using deformable materials or patterning rigid materials to stretchable shapes. Modularity and ability to use elastic thermoplastics make the FFF suitable technique for 3D-printed stretchable electronics [237], [240]. Currently, TPU filaments are used as stretchable material, which is modified with conductive fillers for conductivity, from which carbon fillers are the main options. Depending on the amount, size, and shape of the fillers, the hard conductive fillers stiffen the TPU filament in different amounts. The 3D-printing process also changes the stiffness of the filament, and with conventional 3D-printing settings, accuracy must be decreased to be able to 3D-print conductive

stretchable filaments. For instance, carbon black particles [221], [245], and MWCNTs [207], are mixed up to 18 wt.% and 5 wt.% in the TPU filament before the loss of elasticity, correspondingly. The relatively low limit of fillers restricts the conductivity of 3D-printed materials, and the filaments are mainly used for strain and pressure sensors, where relative resistance change is the main parameter. [207], [221], [245]

The continuous fibers are also used for 3D-printed stretchable electronics. Stretchable filaments are fabricated by forming a hollow stretchable filament from deformable plastics, which is filled with liquid metal [100], [246]. Continuous carbon fiber filaments are used for the 3D-printed electronics circuits [247], but still, the development has aimed at fiber reinforcing and structure stability monitoring [234], [235], and stretchable applications have not been focused yet. Other hard filaments are usable until they are shaped as meanders, and for example, conductive metal-based textile yarns could be integrated inside 3D-printed structures [104].

Additionally, stretchable conductive components can be integrated inside a 3D-printed stretchable matrix. Shaped pieces of carbon fiber nonwoven are inherently frail, but when they are integrated inside the TPU matrix, stretchable interconnections, and sensors are achieved [46]. The rigid conductive filaments can be shaped as meanders in a 3D-printed TPU matrix for strain sensors [248]. Conductive inks have been used inside rigid 3D-printed objects, and in the case of soft 3D-printed objects, stretchable conductive inks can be used for more robust electrical properties. As part of the stretchable electronics manufacturing process, FFF can be used to prepare additional structures on screen-printed stretchable electronics systems [147].

2.4.6 Stretchable electronics prepared by other 3D-printing techniques

Compared to 3D-printed electronics, there are no similarly commercial 3D printers dedicated to stretchable 3D-printed electronics. In addition to the FFF, stretchable 3D-printed electronics are fabricated by DIW, where functional inks are printed on a TPU substrate [40], and non-conductive and conductive TPU inks are printed by turns for multi-layer electronic systems [111]. Additionally, PDMS-based materials enable inherent deformable matrix to work with DIW printed electronics [22], [47], [249]. For instance, conductive silicone paste [22], carbon conductive grease [249], and liquid metal [47], are applied on PDMS substrate. 2D printed conductive traces can be printed in turns with non-conductive layers of PDMS [47], planarly printed

interconnections with 3D vias can be over-molded with PDMS [22], and conductive traces are dispensed on multiple levels inside a block of uncured PDMS [249]. Because of the versatile use of stretchable substrate materials and the similarity of DIW with conventional printing techniques, the difference between stretchable printed electronics and stretchable 3D-printed electronics can be vague.

3 RESULTS

In this work, the stretchable electronics system based on the three main components is studied and developed further. The high stiffness difference of the components concentrates stresses in the system unevenly, which can lead to premature mechanical and electrical failures. More robust designs are researched, and fabrication has also experimented with 3D printing. Moreover, 3D printing is used for making stretchable 3D-printed electronics. Figure 13 presents how the publications correlate with the topic.

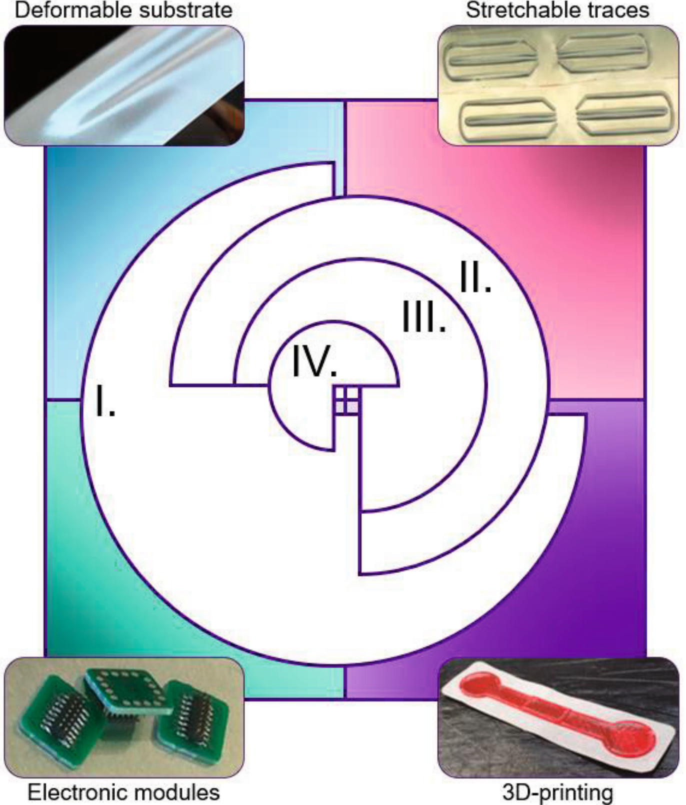

Figure 13. The four major areas of the Thesis with the overlapping pie chart, which marks the dealt areas in Publications I–IV.

First, in Section 3.1., the joining of rigid modules on the stretchable substrate is studied by adhering FR4 and 3D-printed PLA substrates on TPU film with different NCAs. The adhesion is measured by floating roller peel tests (modified SFS-EN 1464), and the failure mechanisms (described in EN ISO 10365) are defined by analyzing the peeled surfaces with Fourier-transform infrared spectroscopy (FTIR). Section 3.1 continues with a discussion of optimum shapes of the rigid modules, which designed reinforcing structures can be used to affect the elongation of the TPU film. The rigid islands based on copper foil are cyclic tested to determine mechanical failure phenomena, which lead to electrical failure.

Section 3.2. discusses screen-printed stretchable interconnections and their resistance increase behavior during the elongation of a substrate. The used screen-printed straight interconnections do not elongate as evenly as the meander-shaped traces that can be locally reinforced with 3D-printed areas. The 3D-printed TPU is directly extruded on TPU film, and the adhesion is studied with T-peel tests (modified SFS-EN ISO 11339). Finally, Section 3.3. deals with 3D-printed TPU matrix, where carbon fiber cloth (CFC) pieces of different thickness are integrated for 3D-printed electronics structures. The samples are tested via tensile and cyclic tests with 10000 cycles. The CFC layer can act as a stretchable interconnection or a sensor element inside the TPU matrix.

3.1 Rigid modules on deformable substrates

The intelligence for the stretchable system is implemented the most efficiently by traditional electronics, which makes the integration of small PCB islands or components on the stretchable substrate a crucial part of the design and manufacturing. The traditional electronics manufacturing methods and materials enable thin interconnections and dense packing of components on the FR4 board of the PCB island but also make the islands inherently rigid. By using the small enough PCB islands and spare placing of the islands, the overall elongation of the system is preserved. However, the islands cause local stress concentration that arise from the mechanical difference between the islands and the deformable substrate creating a weak point in the structure. In more detail, the adherence of the islands on the substrate and the stress concentration effect of the adhered islands on the substrate pose challenges, which are studied further.

3.1.1 Joining rigid islands on deformable substrate

One of the main issues in stretchable electronics is the attachment method of modules on a substrate. In **Publication I**, the suitability of available NCAs in the bonding of rigid and deformable stretchable electronic substrates is investigated. NCAs are promising choices because of their low costs, low curing temperatures, bonding speed, and wide range of materials and hardness levels [14], [125], [250]. With different NCA-based stretchable electronic joints (Table 1), peel test samples are prepared to compare the adhesion of NCAs. The peel test samples consist of two different rigid substrate: smooth FR4 with a solder mask (Coates XV501T) and rough 3D printed PLA substrate (by colorFabb). As the stretchable substrate, 100 μm thick Platilon U 4201 AU TPU film (by Covestro) is used. [137]

Table 1. Used NCAs with between rigid and deformable substrates. [137]

Name of adhesive	Composition	Hardness	Adhesive type
Permabond ET515	Epoxy	Semi-rigid	Structural
Permabond MT382	Epoxy	Semi-elastic	Structural
3M DP610	PU	Semi-elastic	Structural
Loctite 406	CA	Rigid	Structural
Loctite 406 with primer Loctite SF 7239	CA	Rigid	Structural
3M 8132LE	PSA tape	Elastic	Non-structural

The samples are tested with the floating roller peel test setup. The setup differs from the conventional test process as the TPU film elongates during peeling when the bond strength is high enough. The failure of the samples is studied with FTIR Optics Tensor 27 (by Bruker), which has a horizontal ATR unit GladiATR with a diamond crystal. In the failure analysis, three different classes of failure mechanisms were identified (Table 2), and the best results were achieved with a novel non-structural adhesive joint. The non-structural adhesive joints had a good average maximum bond strength (0,28 N/mm) with the FR4 substrate, which made the TPU film elongate considerably (85 %) during the peeling. [137]

The failure type I of epoxy and PU adhesives is realized as a single or two interface failure, which is affected by the rough surface topography of rigid substrates. The roughness increased the bond strength of epoxy adhesives which had poor adhesion,

Table 2. Identified failure mechanisms of the peel test samples. In embedded figures, green resembles the rigid FR4 and PLA substrates, light blue resembles the deformable TPU substrate (which was peeled from the rigid substrates), and dark blue resembles the adhesive layer. [137]

Peel test sample series (Rigid substrate)	Dominant failure mechanism	Average maximum bond strength	Failure type
Epoxy ET515 (FR4)		0,08 N/mm	I
Epoxy ET515 (3D-printed PLA)		0,12 N/mm	
Epoxy MT382 (FR4)		0,11 N/mm	
Epoxy MT382 (3D-printed PLA)		0,14 N/mm	
PU DP610 (FR4)		0,26 N/mm	
PU DP610 (3D-printed PLA)		0,19 N/mm	
CA Loctite 406 (FR4)		0,18 N/mm	II
CA Loctite 406 (3D-printed PLA)		0,26 N/mm	
CA primed Loctite 406 (FR4)		0,26 N/mm	
CA primed Loctite 406 (3D-printed PLA)		0,20 N/mm	
PSA tape 8132LE (FR4)		0,28 N/mm	III
PSA tape 8132LE (3D-printed PLA)		0,25 N/mm	

and vice versa decreased the bond strength of PU adhesive which had good adhesion. [137]

The failure type II of primed and non-primed CA samples occurred as the cohesive failure of the adhesive layer. For example, achieved good 0,26 N/mm average maximum bond strength and 28 % elongation of the TPU substrate with the primed CA and FR4 substrate. Generally, the adhesion of CA with substrates is good, and the strength of the samples is determined by the local evenness of the adhesive layer [136].

The failure type III of PSA tape is an adhesive failure between the rigid substrate and the PSA tape. The deformable PSA elongates along the TPU substrate, peels from the rigid surface steadily, and provides the best peel test results. After the peeling, the PSA remains tacky and can reattach to the peeled TPU substrate. [137]

The comparison of adhesives presented that the non-structural adhesives that are mechanically more similar to the deformable substrate than the rigid substrate provide more stable peeling behavior than structural adhesives. The CA adhesives

can also be used to bond rigid parts on the deformable substrate. However, as rigid adhesives, they promote the stress concentration effect of the stretchable system. [137]

3.1.2 Controlling the stress concentration around the rigid islands

Another main issue of stretchable electronics is the stress concentration effect of rigid islands on a stretchable substrate, which pushes the premature failure of routed stretchable interconnections on the stretchable substrate from the island. In **Publication IV**, hybrid stretchable electronics samples, prepared by the SCB process and screen-printing, are measured and compared to find the most optimum design with the least amount of stress concentrated on the printed interconnections. The two sets of samples, the tensile and cyclic test sample series, were prepared, where 100 μm thick Platilon U 4201 AU TPU film (by Covestro), silver ink CI-1036 (by ECM), and 35 μm thick PCB grade electrodeposited copper foil are used. [158]

Initially, the tensile test samples are printed with EKRA X5 (by EKRA Automatisierungssysteme GmbH) screen printer and elongated to 30 % with ESM303 tensile tester (by Mark-10 Corporation). The resistance of the printed interconnections is measured with a DMM6500 multimeter (by Keithley). The results show that protective structures around the sensitive copper foil – TPU film transition area reduce the resistance increase of the interconnection in the transition area from 640% to 12%. [158]

After the tensile tests, miniaturized cyclic test samples with five variations are designed, manufactured, and tested. The samples are tested with an ElectroPuls E10000 tester (by Instron), which elongates the samples 10000 times with a 1 Hz frequency to 10 %, 20 %, and 30 %. The elongation levels are selected by the tensile test parameters and initial cyclic test trials. The resistance of screen-printed interconnections is measured with a multiplexing resistance measurement device (Fraunhofer IZM, Berlin), where the transition areas and the loops are measured After the tests, further failure analyses (Figure 14) are done with the help of a scanning electron microscope Phenom XL G2 (by Thermo Fisher Scientific Inc.) and a FEA program ABAQUS (by Dassault Systèmes). [158]

The results show that the concentrated stresses can break the printed interconnection prematurely. By using protective structures in the copper – silver ink transition area, the concentrated stresses can be controlled (Figure 15a–b). The durability of the hybrid structures depends on the strength of the protective

structures, which fatigue damage can be measured from the printed interconnections as momentary decreasing resistance values (Figure 15c–d). The proper design of protective structures is in a critical role, where poorly designed structures can focus over 50 times larger stresses on the transition area and tear the deformable substrate in a few hundred cycles (Figure 14c). [158]

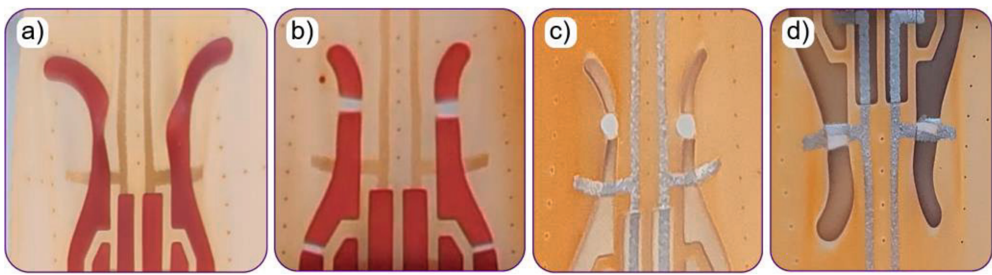

Figure 14. Deformations and damages of cyclic test samples: a) bending of protective structures, b) snapped protective structures because of fatigue damage, c) torn holes between snapped protective structures, and d) failed printed lines in the transition area of the sample. Adapted from [158]

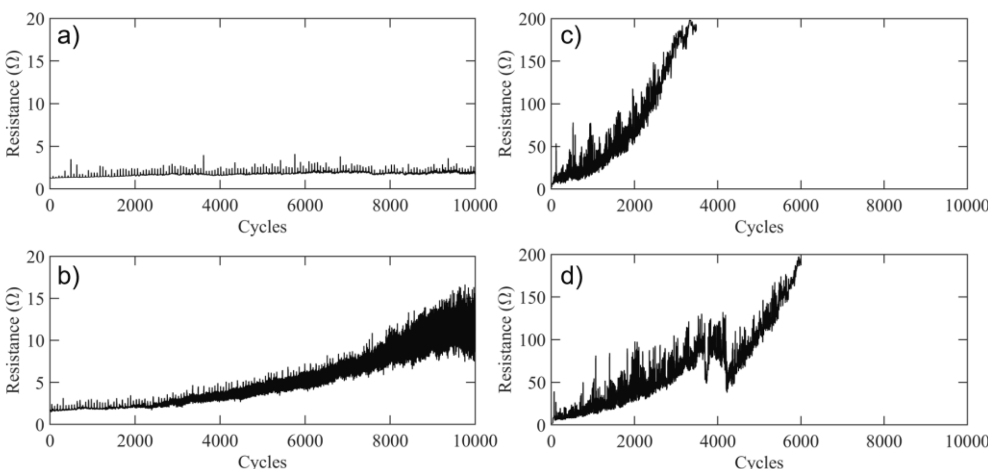

Figure 15. Resistance curves of the 20 % elongated cyclic test samples: a) the resistance of stable copper–printed silver transition area, b) the resistance of unstable transition area, c) the resistance of the printed interconnection without protective structure rupture, and d) the resistance of the interconnection with a rupture of protective structure. [158]

3.2 Stretchable interconnections on a deformable substrate

In a conductive ink the conductive particles are embedded in a soft matrix and therefore the printed interconnections can stretch on the substrate along the deformations of the substrate. Typically, the dimensions and directions of interconnections should be optimized according to the direction of expected deformations of the substrate. Still, in wearable applications, stretchable electronics can experience more complicated biaxial deformations. In practice, stretchable electronics do not only consist of straight interconnections, which have the most predictable electrical behavior during the uniaxial elongation. The presence of turns and biaxial deformation of substrate degrade faster the electrical properties of the interconnections. This can be minimized by using additional reinforcing structures, which can be prepared with various methods. In this study, 3D-printing is used.

3.2.1 Locally reinforced interconnections via 3D printing

The breakage of stretchable interconnections can cause the electrical failure of the stretchable electronics system, which can be prevented by decreasing the stress concentration close to the module islands. Also, corners and other irregular shapes of interconnections can induce uneven deformation, which decreases the amount of maximum elongation of the system. In **Publication II**, local alterations to the screen-printed meander-shaped silver ink interconnections are prepared by FFF 3D printing. The samples are printed with a DEK-248 screen printer (by DEK Printing Machines Ltd.), and the mechanical tests are done with a tensile test machine Tinius Olsen H5KT (by Tinius Olsen) while the resistance of the printed samples is measured with an iCraft ADC 4x 2-wire measurement system (by Icraft Oy). [147]

First, the adhesion of different directly 3D-printed plastics on 100 μm thick Platilon U U073 TPU film (by Covestro) is measured with T-peel tests. In the Ultimaker 3 (by Ultimaker BV) 3D printer, nGen copolyester filament (by colorFabb), PA filament (by Ultimaker BV), and TPU95A filament (by Ultimaker BV) are used. The peel tests conclude that the chemically most similar 3D-printing plastic adheres the best on the TPU film. Up to 260 °C heated directly 3D-printed TPU filament forms a strong ~ 1,9 N/mm bond strength with the TPU film (Figure 16), which is enough to melt the TPU film during printing and break the film after the start of the peeling. The high adhesion enables direct 3D printing of different mechanical structures on the TPU film, which can be used, for example, to modify

the mechanical and further the electrical properties of stretchable interconnections. [147]

The novel direct 3D-printing method is demonstrated by preparing support structures for the meander-shaped printed interconnections. The results show that the 1,0 mm wide and 0,3 mm thick supports changed the elongation distribution in the film, which affected the interconnections and their resistance (Figure 17). Compared to the plain samples without the supports (Figure 17a), the straight supports between the meanders increased the elongation of the tip of the meanders, accelerating the resistance increase by ~ 21 % (Figure 17b). Both straight supports outside the meanders and curved supports inside the meanders decrease the resistance increase by ~ 27 % (Figure 17c–d). However, the straight support did not cover the whole length of the meander, which caused more variation, thus the higher range to the resistance results. The results presented that FFF 3D printing can be used to prepare customized patterns in stretchable electronics systems. [147]

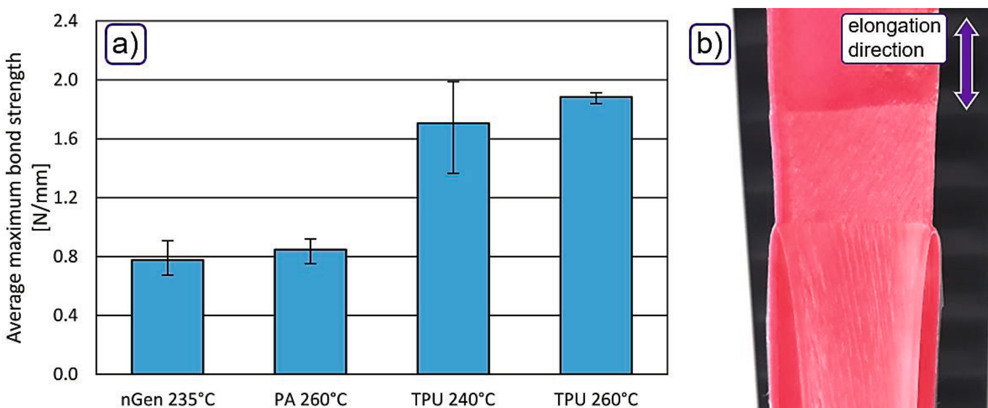

Figure 16. Directly 3D-printed plastics on the TPU film: a) average maximum bond strength of the sample series, and b) TPU 260 °C peel test sample before snapping of the film, which reveals the melted surface of the film. Adapted from [147]

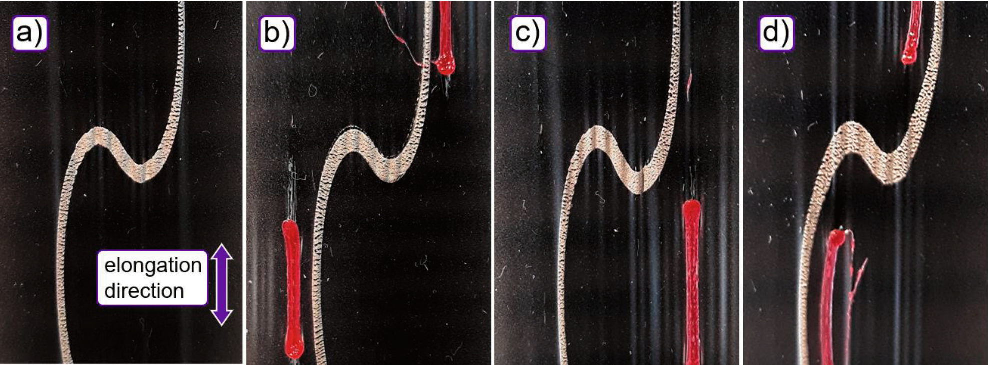

Figure 17. The transition area of screen-printed meanders, which deformations are modified differently by directly 3D-printed supports: a) plain sample without supports, b) straight supports between the meanders, c) straight supports outside the meanders, and d) curved supports inside the meanders. Adapted from [147]

3.3 3D printed structures in wearable electronics

FFF has been used to fabricate 3D-printed electronics, where conductive fillers have been mixed in plastic filaments for conductive patterns. However, the conductive filaments, as extruded through the nozzle, have a defined size and mixing ratio, which limits the conductivity and accuracy. Moreover, the high amount of fillers stiffens the 3D-printed structure, making the fabrication of stretchable 3D-printed electronics challenging. One of the possible methods to manufacture stretchable 3D-printed electronics is to integrate conductive materials inside a stretchable TPU matrix.

3.3.1 Stretchable 3D-printed structures for wearable electronics

There are currently three ways to add conductive fillers in an object that is 3D-printed with the FFF method. (1) micro and nano-sized fillers can be blended into the plastic filament which is extruded through the nozzle. Also, (2) continuous fiber filaments can be embedded in the melted plastic filament. In addition, (3) other materials and semi-products, such as inks and tows, have been integrated inside the 3D-printed object [237], [251]. However, the embedded fillers decrease the processability and mechanical properties of the filament, the continuous fiber filaments limit the 3D-printing process and reduce the accuracy, and materials and

semi-products inside the object have limited integration levels with the 3D-printed matrix. [46]

In **Publication III**, a new approach to preparing functional and deformable 3D-printed structures is experimented with by inserting permeable CFC inside a stretchable FFF 3D-printed matrix. The matrix is printed from the TPU95A filament (by Ultimaker BV) with Ultimaker S5 3D printer (by Ultimaker BV). Inside 10 mm wide and 1 mm thick samples, 8 mm wide CFC pieces are integrated simply by pausing the 3D printing in the middle of the process. Two different CFC plies with a thickness of ~ 53 µm and ~153 µm are used (by ACP Composites). Also, the thinner CFC ply is laminated into 2- and 3-layer plies. The samples are tested with tensile tests and cyclic tests with 10000 cycles, which are done with the ESM303 tensile tester (by Mark-10 Corporation) and a two-channel Arduino Uno -based resistance measurement device. The tensile test samples are elongated to 50 % and the cyclic samples are elongated to 10 % – 50 %. The samples are further studied with DIC analyses with the use of the stereo 3D DIC imaging system 3D StrainMaster Compact 5M (by LaVision GmbH). [46]

The results show that the integrated CFC layers create electrical properties in the TPU matrix. In the 3D-printing, the molten plastic flows through the CFC layer and compresses the fibers, bonding the fibers with the matrix and increasing the conductivity of the CFC layers. The conductivity depends also on the thickness and the number of interfaces between the laminated thin CFC plies. The samples with ~ 110 µm or thinner CFC layers have systematic elongation behavior, while the thicker CFC samples have more random resistance results (Figure 18). [46]

The samples with different amounts of carbon fibers deform mechanically and electrically differently, which highlights their different applications (Figure 19). With a thin CFC layer (53 µm), the TPU matrix retains its stretchability and remains conductive after 50 % cyclic elongation, which makes it usable in wearable sensing and heating applications where deformations are expected. A thick CFC layer (> 150 µm) is relatively stiff but also has the best electrical properties (5 Ω/10 mm), which promote its local use in stretchable electronics, where < 20 % elongation realizes. The results show that the electrical and mechanical properties are the most balanced in the samples with a 106 µm thick CFC layer, which resistance changes only 0,5 % in the cyclic tests after the orientation of the CFC layer. The stability of the structure allows the use of the samples as a 3D-printed strain sensor, which is lastly demonstrated in **Publication III**.

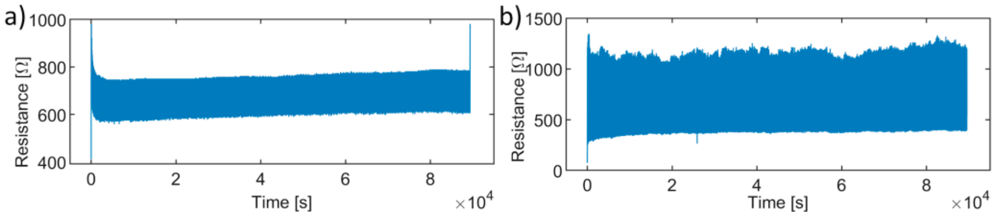

Figure 18. Raw data comparison of 3D-printed cyclic test samples with 30 % elongation: a) the sample with 1 thin CFC layer, which provides the systematic resistance variation between 600 Ω – 800 Ω, and b) the sample with a thick CFC layer laminated from 3 thin CFCs show varying resistance results between 350 Ω – 1250 Ω. Adapted from [46]

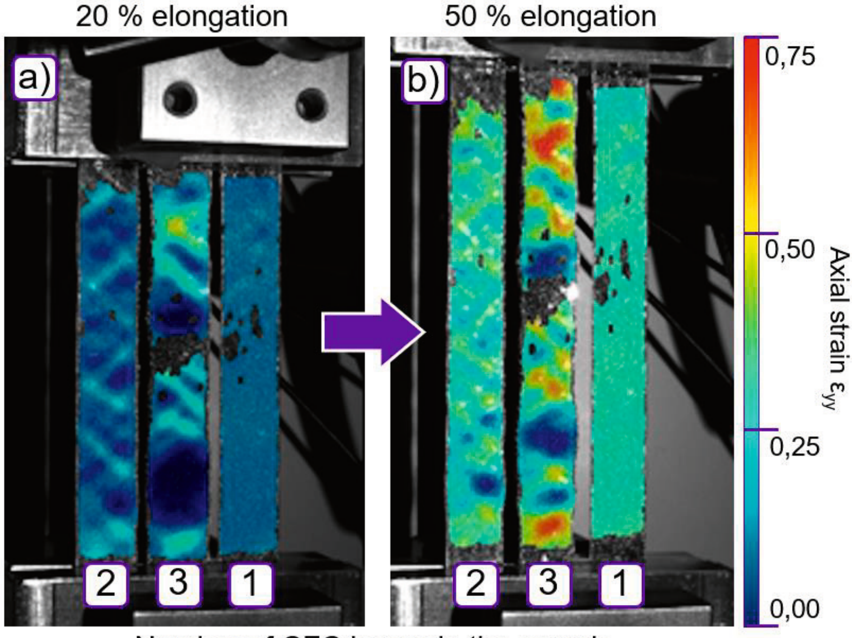

Figure 19. DIC results of 3D-printed samples with 2, 3, or 1 layers of thin CFC: a) in 20% elongation, and b) in 50% elongation. Adapted from [46]

4 DISCUSSION

A stretchable electronics system is a mechanically complex build-up, where the mechanical deformations and the electrical performance are coupled. The coupling affects to the electrical performance of stretchable system, which tends to be minimized. With the sensors, the relation is aimed at a specific level for sensitivity optimization. In this work, the implemented tests and novel results have provided insights into how the relation can be controlled for interconnection and sensor applications.

4.1 Compatible attachment of rigid islands on a deformable substrate

In the current stretchable electronics system, the most considerable mechanical contradiction realizes between the PCB module islands and the deformable substrate. The difference arises from the different material properties and fabrication methods. The high difference increases the stress concentration effect, which promotes electrical and mechanical failures of the system.

When the module islands are fixed on the TPU substrate, the main requirement is to attach the islands so that unexpected delamination does not happen. Second, the concentrated stresses around the islands should be minimized for the maximum electrical durability of the system. Often, the systems are unoptimized, and the joining decreases the functionality of the stretchable interconnections. The joining can be done with a lamination process or by using adhesives or other fixtures [11], [12], [37]. Based on the results, there are a few methods to optimize the joining process.

In the vertical (thickness) direction (z-direction), the stiffness of the adhesive layer between the island and the substrate affects how the elongation of the substrate advances through the substrate–adhesive interface, the adhesive layer, and the adhesive–island interface. In **Publication I**, in general, structural adhesives form the strong adhesive–rigid substrate interface, while the non-structural adhesive forms the strong deformable substrate–adhesive interface. The failure of structural

adhesives in the deformable substrate–adhesive interface and adhesive layer is unstable because the TPU film is repeatedly elongated and released during the peeling. With non-structural adhesive, the failure realizes in the adhesive–rigid substrate interface, which does not release the accumulated elongation of the TPU film. Thus the adhered stretchable electronic joint can be improved by using deformable adhesive, which at the same time, is stable and complies the stretching. [137] For further mechanical improvement, the thickness of the deformable adhesive layer can be increased [252]. Additionally, the thickness of the rigid substrate can be decreased for higher flexibility [253]. With the 3D-printing, the material of the module islands can be changed from rigid FR4 to TPU, which allows a more homogenous composition of the stretchable electronics system [175].

In addition to the z-direction modifications, the system can be optimized planarly (x-y-directions). The module island is shaped and rounded so that sharp corners are avoided, which otherwise can focus high stresses on the substrate [34]. The stretchable interconnections are routed from the islands, and the rigid-deformable transition area close to the islands is mechanically controlled with protective structures near the interconnections [127], [161]. The function of the protective structures can be embedded in the islands by using clover-shaped island design (Figure 12) [163], or the structures can be separate elements in the substrate [34]. Still, the planar structures are the most usable to direct stresses away from the interconnections, not to decrease the total amount of stresses in the stretchable system [160]. From **Publication IV.**, three design requirements for flexible planar protective structures can be suggested to improve electrical durability of stretchable interconnections. First, the width of the protective structures needs to be large enough to improve the fatigue resistance of the structure and to avoid the catastrophic failure of the system after the fatigue damage. Second, straight geometries aligned to the assumed elongation direction should be used to minimize the bending. Third, the sharp angles and other locations where the fatigue failure can be expected, are reinforced.

4.2 Relevance of stiffness to the stretchability of interconnections

Stretchable electronic systems have been manufactured with different kinds of stretchable interconnections. For instance, both meander-shaped copper foil interconnections and screen-printed interconnections have been used, which have very different compositions and material properties. There are many differences

between the interconnections, but in the aspect of the system durability, the differences can be generalized to the stiffness difference. [147], [191]

The stiffness difference between the interconnection and the deformable substrate under and around the interconnection is the dominant feature that determines the nature of the elongation of the interconnection. When the interconnection is considerably stiffer than the substrate, such as the 35 μm thick copper foil interconnections on TPU substrate, the interconnection is the load-carrying component, and the forces are focused locally on the weak areas of interconnection [13], [254]. If the stiffness of the interconnections is low, such as with the nm-thick deposited gold layers [191], and screen-printed interconnections on TPU substrate [147], the interconnection elongates thoroughly with the substrate.

The stiffness difference is closely related to the failure of the stretchable interconnections. The laminated meander-shaped copper foil interconnections with the high stiffness difference endure the stretching only when the foil remains adhered to the substrate, as with the copper foil protective structures in **Publication IV**. When the high local forces and strains are focused on the interconnection, the foil delaminates from the substrate [41]. The delaminated foil is prone to premature cracking without the mechanical support of the substrate [158]. The screen-printed interconnections elongate evenly, which allows the use of straight interconnections [18]. However, stretching of the interconnections is based on the deformations of the substrate, which makes the elongation of complex-shaped screen-printed interconnections complicated [147]. The deformable substrate has a high Poisson's ratio, which compresses the substrate perpendicularly to the elongation direction [132]. The compression in the width direction improves the conductivity and stretchability of the straight interconnections [112], but as seen in **Publication II**, the shaped printed interconnections have locations that fail prematurely [147].

Because of the fundamental differences of the stretchable interconnections, the durability of the interconnections is improved with different methods. The durability is related to the controlling of the stiffness on three levels:

1. Material-level,
2. Component-level, and
3. System-level.

At the material level, the stiffness is governed by the material properties of the interconnections. The screen-printing inks are heterogeneous liquids that have macroscale conductive fillers and a highly deformable polymer matrix [194]. The

polymer matrix complies with the deformation of the substrate, and by modifying the chemistry and decreasing the amount of fillers, the stretchability of the interconnections can be improved [255]. The copper interconnections are electrodeposited homogenous metal foils that have uniform thickness and grain size [11]. Between these, the inkjet technology uses conductive inks with nano- and macroscale metal fillers, which after sintering, form metallic interconnections [186]. Because of their thinness, the metallic interconnections are inherently flexible, and only with component-level design, are made stretchable [60], [184].

At the component level, the stiffness of the interconnections is changed by varying shapes and dimensions of interconnections. For instance, the durability of the stretchable meander-shaped copper foil interconnections can be improved by decreasing the width [254] or changing the shape of the meander [256]. The wider metallic interconnections are stiffer, which decreases their stretchability but improves their electrical properties. Also, the substrate can be pre-stretched prior to lamination or inkjet printing for wavy stretchable interconnections [60], [184]. The electrical properties of screen-printed interconnections also improve with wider interconnections [112], and because of the inherent stretchable polymer matrix composition, the stiffness increase is minimal. Still, increasing the size of interconnections is not feasible when small integrated stretchable wearables are desired.

At the system level, the stiffness of the system around the stretchable interconnections can be locally controlled by various methods. For example, between the meander-shaped copper foil interconnection and deformable substrate, a flexible meander-shaped PI film can be added to make the copper meanders elongate more uniformly [13]. This also decreases the delamination tendency of the copper foil, the main cause of the failure of the interconnection. With the screen-printed interconnections in **Publication II**, local support structures can be added on the TPU substrate next to the interconnection by 3D printing. 3D printing enables the placing and melting of 3D structures directly on the film, which increases the integration level of the system [147]. In addition, the printed interconnection can be covered with another layer of deformable substrate, which decreases the out-of-the-plane movement of conductive traces and distributes deformations on the larger area [161]. Moreover, holes and other cuts can also be used to change the deformation of the substrate [34], [160].

4.3 Possibilities of 3D-printing in stretchable electronics

The development of conductive materials in 3D printing has been advanced and there are commercial conductive materials available [149], [257]. Still, the commercial conductive materials have limitations, such as poor thermal stability [230], and rigidness [257]. One aspect is to consider the 3D-printed stretchable electronics as composite structures, and in **Publication III**, conductive fibers are integrated inside 3D-printed stretchable plastic [46]. When permeable carbon fiber cloths are placed in the plastic matrix, the higher amount of carbon fibers and the interfaces improve and stabilize the conductivity of the fiber layer. However, the high amount of fibers also increases the stiffness of the stretchable matrix. The electrical and mechanical properties are the most balanced in the matrix with a 106 μm thick fiber layer, which resistance changes only 0,5 % in the cyclic tests after the orientation of the CFC layer. The stability of the structure allows the use of the samples as a 3D-printed strain sensor, as demonstrated in **Publication III**.

Current FFF methods and materials are used mainly to prepare non-functional objects, such as fashion products and spare parts [152], [215]. Additionally, one of the benefits of FFF is that the parts can be prepared in a single process on a textile or plastic substrate instead of a multistage lamination or adhering process [146], [152]. The accurate dispensing of the molten plastic enables the combination of 3D printing and functional pre-printed plastic films, as tested in **Publication II**.

3D-printed objects are made functional with many methods. For instance, heating elements are made from intermediate conductive plastic filaments [55], and liquid metals are fed inside 3D-printed objects [100]. For the maximum efficiency of 3D printing, unlike conventional electronics, the electronics need to be designed non-planarly, where components are sideways, bottom side up, or in other directions [43]. The tighter packaging improves the integration level of the electronics, which however, is still limited in FFF because most commercial 3D printers have only three axes [227], [248], [258]. In the future, more complex structures can be prepared with modular and more sophisticated 5-axis systems [237], [257].

5 CONCLUSIONS AND FUTURE WORK

5.1 Conclusions

Stretchable electronics are enablers for intelligent and indistinguishable electronic systems that can be applied to clothing or other objects, which dimensions change during their use. The current limitations of stretchable electronics are their mechanical durability and electrical stability. In a system that consists of PCB modules, stretchable interconnections, and a deformable substrate, the mechanical and electrical features of the system are defined by their properties solely and after the joining of the components. The properties are affected by the material, manufacturing, and joining methods of the components, which are varied in this work.

First, different non-conductive adhesives are used to make stretchable electronics joints from stretchable TPU film and rigid FR4 and 3D-printed substrates (research question 1). The hard structural adhesives are more compatible with rigid substrates, where they cause inconsistent failure behavior. Peeling of the structural adhesives realizes in phases, which combined with the stretchability of the TPU film, makes the failures of PU-based adhesives unsystematic. Also, the uneven layer thickness of CA-based adhesives decreases reliability of the peeling. With non-structural PSA tape, the tape is elastic, thus it can follow the stretching of TPU and form a stable peeling profile. Moreover, PSA tape enables some degree of re-adherence of the joint after the stretching of the joint is removed, allowing the fabrication of re-bonding joints. Still, the evenness of the rigid substrate is highlighted, and with the uneven 3D-printed substrate, gluing is not the optimum joining method.

By using FDM 3D printing method to extrude molten TPU filament on stretchable TPU film, it is possible to diffuse two plastic objects together without adhesives (research question 2). The adherence of direct 3D-printed plastics on the film is improved by increasing the 3D-printing temperature. In stretchable electronics, the 3D-printed objects can be used to control the local elongation of the screen-printed stretchable interconnections. Meander-shaped screen-printed interconnections have uneven elongation, and with local 3D-printed supports, electrical properties of the interconnections are changed. The supports between the

meanders concentrate higher amount of elongation in the meanders, which increases their resistance. Inside or just outside the meanders, the supports improve elongation uniformity in the interconnections, which increase maximum elongation of stretchable interconnections.

3D printing can be used more extensively for stretchable electronics by integrating conductive fillers inside 3D-printed objects. As the novel fabrication method, carbon-based staple fiber cloth pieces are placed in the middle of the 3D-printed TPU matrix (research question 3). When the thickness of the cloth pieces is varied between ~ 53 μm – 153 μm, which together the 3D-printed TPU, forms stretchable 3D-printed composite structures. The high permeability of ~ 53 μm thick cloth pieces enables elastic and the steadiest mechanical behavior, while the thick ~ 150 μm cloth pieces have the highest conductivity and stiffness. The ~ 53 μm thick cloth pieces are also laminated together, where the interface area between two cloth layers boosts the conductivity. Also, the integration of the cloth pieces inside the 3D-printed TPU improves the electrical properties because of the compression of the fibers. Differing from the existing stretchable interconnections, the fibers resistance improves over cycles. At the initial cycles in the cyclic testing, the fibers orientate along the elongation direction, which causes the high resistance peak, which evens quickly to lower resistance levels.

As noted with 3D-printed supports and conductive fiber-reinforced matrix, the mechanical differences of the components in the stretchable system decrease the electrical and mechanical durability. The mechanical differences concentrate stresses to the interphase of elastic–rigid area, which is the first area to fail electrically. To study the controlling of the stress concentration, protective structures are prepared in the hybrid SCB stretchable electronics samples (research question 4). The resistance increase of screen-printed conductive traces over copper–TPU film transition area is limited efficiently by using straight protective structures outside the traces. The straight protective structures work the optimum way when they are parallel to the elongation direction. Curved top areas of the structures twisted during the elongation, which led to the cracking of the structures. The higher curvature accelerated the cracking. Also, the thickness of the protective structure affected the failure mechanisms, and with the thin 0,5 mm wide structures, the cracking realized faster and caused the tearing of the TPU film. The thick 1,0 mm structures were more stable, and cracking did not cause the complete mechanical failure of the samples.

The stretchable electronic systems include various materials, manufacturing methods, and joining techniques, which compatibility is determined by their

mechanical features, which further affects the electrical durability. In this work challenges and possible solutions to increase the general durability of stretchable electronic systems were presented.

5.2 Future work

The work has inspired the development of stretchable electronics further with two approaches. The current manufacturing methods, based on plastic, electronics, and textile approaches, can be merged more to develop new more integrated stretchable electronics. Also, the role of 3D printing as an alternative manufacturing method needs more research. Although the current 3D printing methods for complex materials, such as stretchable and conductive plastics, are still limited, the integrated permeable fiber matrices and stretchable conductive inks allow modified 3D printing processes for 3D-printed stretchable electronics.

The new manufacturing techniques create new products. The commercial applications of stretchable electronics have not been focused on this work, but with knowledge from this work, the application areas are considered in the future. The applications can be considered from aspects of manufacturers, service providers, and consumers. The three groups demand different properties from stretchable electronics. For example, stretchable electronics stand out for consumers often as wearable electronics, which are used in sports, healthcare, and gaming.

REFERENCES

[1] J. A. Rogers, T. Someya, and Y. Huang, 'Materials and Mechanics for Stretchable Electronics', *Science*, vol. 327, no. 5973, pp. 1603–1607, Mar. 2010, doi: 10.1126/science.1182383.

[2] L. Gillan, J. Hiltunen, M. H. Behfar, and K. Rönkä, 'Advances in design and manufacture of stretchable electronics', *Jpn. J. Appl. Phys.*, vol. 61, no. SE, p. SE0804, Jun. 2022, doi: 10.35848/1347-4065/ac586f.

[3] J. P. Collett, 'The history of electronics from vacuum tubes to transistors', in *Companion Encyclopedia of Science in the Twentieth Century*, J. Krige and D. Pestre, Eds., Routledge, United Kingdom: Taylor & Francis, 2003, pp. 253–274.

[4] M. Campbell-Kelly and D. D. Garcia-Swartz, 'The Internet Era', in *From mainframes to smartphones: a history of the international computer industry*, Cambridge, Massachusetts: Harvard University Press, 2015, pp. 155–208.

[5] S. Park, K. Chung, and S. Jayaraman, 'Wearables: Fundamentals, Advancements, and a Roadmap for the Future', in *Wearable Sensors*, E. Sazonov and M. R. Neuman, Eds., Elsevier, 2014, pp. 1–23. doi: 10.1016/B978-0-12-418662-0.00001-5.

[6] S. Park and S. Jayaraman, 'The wearables revolution and Big Data: the textile lineage', *J. Text. Inst.*, vol. 108, no. 4, pp. 605–614, Apr. 2017, doi: 10.1080/00405000.2016.1176632.

[7] G. Loke *et al.*, 'Digital electronics in fibres enable fabric-based machine-learning inference', *Nat. Commun.*, vol. 12, no. 1, p. 3317, Jun. 2021, doi: 10.1038/s41467-021-23628-5.

[8] B. Filipowska, B. Wiśniewski, and L. Zawadzka Michalak, 'Creation of electro-conductive paths and patterns by screen printing on textile bases', *Text. Res. J.*, vol. 88, no. 3, pp. 261–274, Feb. 2018, doi: 10.1177/0040517516679146.

[9] P. Veske, P. Bauwens, F. Bossuyt, T. Sterken, and J. Vanfleteren, 'Development and Washing Reliability Testing of a Stretchable Circuit on Knit Fabric', *Appl. Sci.*, vol. 10, no. 24, p. 9057, Dec. 2020, doi: 10.3390/app10249057.

[10] P. Bosowski, M. Hoerr, V. Mecnika, T. Gries, and S. Jockenhövel, 'Design and manufacture of textile-based sensors', in *Electronic Textiles*, T. Dias, Ed., Elsevier, 2015, pp. 75–107. doi: 10.1016/B978-0-08-100201-8.00005-9.

[11] F. Bossuyt and T. Löher, 'Technologies and Processes Used in Printed Circuit Board Fabrication for the Realization of Stretchable Electronics', in *Stretchable Electronics*, T. Someya, Ed., Weinheim, Germany: Wiley-VCH Verlag & Co. KGaA, 2013, pp. 187–205. [Online]. Available: https://doi.org/10.1002/9783527646982.ch1

[12] M. H. Behfar *et al.*, 'Fully Integrated Wireless Elastic Wearable Systems for Health Monitoring Applications', *IEEE Trans. Compon. Packag. Manuf. Technol.*, vol. 11, no. 6, pp. 1022–1027, Jun. 2021, doi: 10.1109/TCPMT.2021.3082647.

[13] J. Vanfleteren *et al.*, 'Printed circuit board technology inspired stretchable circuits', *MRS Bull.*, vol. 37, no. 3, pp. 254–260, Mar. 2012, doi: 10.1557/mrs.2012.48.

[14] P. Foerster, C. Dils, C. Kallmayer, T. Löher, and K.-D. Lang, 'First approach to cost-efficient fine pitch NCA flip-chip assembly on thermoplastic polyurethane printed circuit boards', in *2012 4th Electronic System-Integration Technology Conference*, Amsterdam, Netherlands: IEEE, Sep. 2012, pp. 1–6. doi: 10.1109/ESTC.2012.6542055.

[15] T. Löher, A. Ostmann, and M. Seckel, 'Stretchable and deformable electronic systems in thermoplastic matrix materials', in *IEEE CPMT Symposium Japan 2014*, Kyoto, Japan: IEEE, Nov. 2014, pp. 177–181. doi: 10.1109/ICSJ.2014.7009639.

[16] J. Vanfleteren *et al.*, 'SCB and SMI: two stretchable circuit technologies, based on standard printed circuit board processes', *Circuit World*, vol. 38, no. 4, pp. 232–242, Nov. 2012, doi: 10.1108/03056121211280440.

[17] J. Song and S. Wang, 'Theory for Stretchable Interconnects', in *Stretchable Electronics*, T. Someya, Ed., Weinheim, Germany: Wiley-VCH Verlag & Co. KGaA, 2013, pp. 1–29. [Online]. Available: https://doi.org/10.1002/9783527646982.ch1

[18] J. Suikkola *et al.*, 'Screen-Printing Fabrication and Characterization of Stretchable Electronics', *Sci. Rep.*, vol. 6, no. 1, p. 25784, May 2016, doi: 10.1038/srep25784.

[19] A. Pajkanovic, G. M. Stojanovic, and S. M. Djuric, 'Performance analysis of meander-type inductor in silicon and flexible technology', *Microelectron. J.*, vol. 56, pp. 57–64, Oct. 2016, doi: 10.1016/j.mejo.2016.07.016.

[20] M. Attaran, 'The rise of 3-D printing: The advantages of additive manufacturing over traditional manufacturing', *Bus. Horiz.*, vol. 60, no. 5, pp. 677–688, Sep. 2017, doi: 10.1016/j.bushor.2017.05.011.

[21] N. Asnafi, T. Shams, D. Aspenberg, and C. Öberg, '3D Metal Printing from an Industrial Perspective—Product Design, Production, and Business Models', *BHM Berg- Hüttenmänn. Monatshefte*, vol. 164, no. 3, pp. 91–100, Mar. 2019, doi: 10.1007/s00501-019-0827-z.

[22] P. Sun *et al.*, 'Directly Printed Interconnection Wires between Layers for 3D Integrated Stretchable Electronics', *Adv. Mater. Technol.*, vol. 7, no. 9, p. 2200302, Sep. 2022, doi: 10.1002/admt.202200302.

[23] S. Mondal, Mohd. I. Mohd. Ghazali, K. Wijewardena, D. Kumar, and P. Chahal, '3D Printed Interposer Layer for High Density Packaging of IoT Devices', in *2019 IEEE 69th Electronic Components and Technology Conference (ECTC)*, Las Vegas, NV, USA: IEEE, May 2019, pp. 1687–1692. doi: 10.1109/ECTC.2019.00273.

[24] X. Jin, G. Li, T. Xu, L. Su, D. Yan, and X. Zhang, 'Fully integrated flexible biosensor for wearable continuous glucose monitoring', *Biosens. Bioelectron.*, vol. 196, p. 113760, Jan. 2022, doi: 10.1016/j.bios.2021.113760.

[25] M. Mäntysalo, T. Vuorinen, V. Jeyhani, and A. Vehkaoja, 'Printed soft-electronics for remote body monitoring', in *Proceedings Volume 10366*, San Diego, California, United States: SPIE, Aug. 2017, pp. 1–7. doi: https://doi.org/10.1117/12.2275606.

[26] J. Jesionkowska, F. Wild, and Y. Deval, 'Active Learning Augmented Reality for STEAM Education—A Case Study', *Educ. Sci.*, vol. 10, no. 8, p. 198, Aug. 2020, doi: 10.3390/educsci10080198.

[27] M. C. Leue, T. Jung, and D. tom Dieck, 'Google Glass Augmented Reality: Generic Learning Outcomes for Art Galleries', in *Information and Communication Technologies in Tourism 2015*, I. Tussyadiah and A. Inversini, Eds., Cham: Springer International Publishing AG, 2015, pp. 463–476. doi: 10.1007/978-3-319-14343-9_32.

[28] Y. Adesida, E. Papi, and A. H. McGregor, 'Exploring the Role of Wearable Technology in Sport Kinematics and Kinetics: A Systematic Review', *Sensors*, vol. 19, no. 7, p. 1597, Apr. 2019, doi: 10.3390/s19071597.

[29] B. J. Stetter, S. Ringhof, F. C. Krafft, S. Sell, and T. Stein, 'Estimation of Knee Joint Forces in Sport Movements Using Wearable Sensors and Machine Learning', *Sensors*, vol. 19, no. 17, p. 3690, Aug. 2019, doi: 10.3390/s19173690.

[30] B. L. Smarr *et al.*, 'Feasibility of continuous fever monitoring using wearable devices', *Sci. Rep.*, vol. 10, no. 1, p. 21640, Dec. 2020, doi: 10.1038/s41598-020-78355-6.

[31] 'Talon International Inc. and KC Wearable Technologies Partner to launch New Innovations', *PR Newswire*, p. NA, Aug. 01, 2022.

[32] J. van den Brand *et al.*, 'Flexible and stretchable electronics for wearable health devices', *Solid-State Electron.*, vol. 113, pp. 116–120, Nov. 2015, doi: 10.1016/j.sse.2015.05.024.

[33] I. Wicaksono *et al.*, 'A tailored, electronic textile conformable suit for large-scale spatiotemporal physiological sensing in vivo', *Npj Flex. Electron.*, vol. 4, no. 1, p. 5, Apr. 2020, doi: 10.1038/s41528-020-0068-y.

[34] M. Mosallaei, D. Di Vito, B. Khorramdel, and M. Mäntysalo, 'Improvements in the electromechanical properties of stretchable interconnects by locally tuning the stiffness', *Flex. Print. Electron.*, vol. 5, no. 1, p. 015004, Jan. 2020, doi: 10.1088/2058-8585/ab68ae.

[35] D. J. Lipomi, 'Stretchable Figures of Merit in Deformable Electronics', *Adv. Mater.*, vol. 28, no. 22, pp. 4180–4183, Jun. 2016, doi: 10.1002/adma.201504196.

[36] R. S. Chandel, S. Sharma, S. Kaur, S. Singh, and R. Kumar, 'Smart watches: A review of evolution in bio-medical sector', *Mater. Today Proc.*, vol. 50, pp. 1053–1066, 2022, doi: 10.1016/j.matpr.2021.07.460.

[37] H. Ozkan, O. Ozhan, Y. Karadana, M. Gulcu, S. Macit, and F. Husain, 'A Portable Wearable Tele-ECG Monitoring System', *IEEE Trans. Instrum. Meas.*, vol. 69, no. 1, pp. 173–182, Jan. 2020, doi: 10.1109/TIM.2019.2895484.

[38] 'Product Data Sheet, AD Circus™ NFC ST25TN'. Avery Dennison Corp., 2022. Accessed: May 29, 2023. [Online]. Available: https://rfid.averydennison.com/en/home/product-finder/circus-nfc.html

[39] T. Vuorinen, J. Niittynen, T. Kankkunen, T. M. Kraft, and M. Mäntysalo, 'Inkjet-Printed Graphene/PEDOT:PSS Temperature Sensors on a Skin-Conformable Polyurethane Substrate', *Sci. Rep.*, vol. 6, no. 1, p. 35289, Oct. 2016, doi: 10.1038/srep35289.

[40] G. Costa *et al.*, '3D Printed Stretchable Liquid Gallium Battery', *Adv. Funct. Mater.*, vol. 32, no. 27, p. 2113232, Jul. 2022, doi: 10.1002/adfm.202113232.

[41] I. Chtioui, F. Bossuyt, M. de Kok, J. Vanfleteren, and M. H. Bedoui, 'Arbitrarily Shaped Rigid and Smart Objects Using Stretchable Interconnections', *IEEE Trans. Compon. Packag. Manuf. Technol.*, vol. 6, no. 4, pp. 533–544, Apr. 2016, doi: 10.1109/TCPMT.2015.2511077.

[42] O. Rusanen, T. Simula, P. Niskala, V. Lindholm, and M. Heikkinen, 'Injection Molded Structural Electronics Brings Surfaces to Life', in *2019 22nd European Microelectronics and Packaging Conference & Exhibition (EMPC)*, Pisa, Italy: IEEE, Sep. 2019, pp. 1–7. doi: 10.23919/EMPC44848.2019.8951795.

[43] G. T. Carranza, U. Robles, C. L. Valle, J. J. Gutierrez, and R. C. Rumpf, 'Design and Hybrid Additive Manufacturing of 3-D/Volumetric Electrical Circuits', *IEEE Trans. Compon. Packag. Manuf. Technol.*, vol. 9, no. 6, pp. 1176–1183, Jun. 2019, doi: 10.1109/TCPMT.2019.2892389.

[44] M. P. Groover, 'Electronics assembly and packaging', in *Fundamentals of modern manufacturing*, 7th ed., Singapore, Singapore: John Wiley & Sons Singapore Pte. Ltd., 2021, pp. 809–831.

[45] G. Ginestet *et al.*, 'Embroidered Antenna-Microchip Interconnections and Contour Antennas in Passive UHF RFID Textile Tags', *IEEE Antennas Wirel. Propag. Lett.*, vol. 16, pp. 1205–1208, 2017, doi: 10.1109/LAWP.2016.2628086.

[46] T. Salo, D. Di Vito, A. Halme, and J. Vanhala, 'Electromechanical Properties of 3D-Printed Stretchable Carbon Fiber Composites', *Micromachines*, vol. 13, no. 10, p. 1732, Oct. 2022, doi: 10.3390/mi13101732.

[47] J. Kang *et al.*, 'Modular and Reconfigurable Stretchable Electronic Systems', *Adv. Mater. Technol.*, vol. 4, no. 3, p. 1800417, Mar. 2019, doi: 10.1002/admt.201800417.

[48] Y.-C. Ma, Y.-P. Chao, and T.-Y. Tsai, 'Smart-clothes - Prototyping of a health monitoring platform', in *2013 IEEE Third International Conference on Consumer Electronics ¿ Berlin (ICCE-Berlin)*, IFA Fairground, Berlin, Germany: IEEE, Sep. 2013, pp. 60–63. doi: 10.1109/ICCE-Berlin.2013.6698063.

[49] M.-M. Laurila *et al.*, 'A Fully Printed Ultra-Thin Charge Amplifier for On-Skin Biosignal Measurements', *IEEE J. Electron Devices Soc.*, vol. 7, pp. 566–574, 2019, doi: 10.1109/JEDS.2019.2915028.

[50] K. L. Gandhi and W. S. Sondhelm, 'Technical fabric structures – 1. Woven fabrics', in *Handbook of Technical Textiles*, Elsevier, 2016, pp. 63–106. doi: 10.1016/B978-1-78242-458-1.00004-2.

[51] S. C. Anand, 'Technical fabric structures – 2. Knitted fabrics', in *Handbook of Technical Textiles*, Elsevier, 2016, pp. 107–162. doi: 10.1016/B978-1-78242-458-1.00005-4.

[52] M. Beltrão, F. M. Duarte, J. C. Viana, and V. Paulo, 'A review on in-mold electronics technology', *Polym. Eng. Sci.*, vol. 62, no. 4, pp. 967–990, Apr. 2022, doi: 10.1002/pen.25918.

[53] J. Kwon, J. Ock, and N. Kim, 'Mimicking the Mechanical Properties of Aortic Tissue with Pattern-Embedded 3D Printing for a Realistic Phantom', *Materials*, vol. 13, no. 21, p. 5042, Nov. 2020, doi: 10.3390/ma13215042.

[54] M. Kam, A. İpekçi, and Ö. Şengül, 'Investigation of the effect of FDM process parameters on mechanical properties of 3D printed PA12 samples using Taguchi method', *J. Thermoplast. Compos. Mater.*, vol. 36, no. 1, pp. 307–325, Jan. 2023, doi: 10.1177/08927057211006459.

[55] H. Kim and S. Lee, 'Characterization of Electrical Heating of Graphene/PLA Honeycomb Structure Composite Manufactured by CFDM 3D Printer', *Fash. Text.*, vol. 7, no. 1, p. 8, Mar. 2020, doi: 10.1186/s40691-020-0204-2.

[56] A. M. Bazargan, F. Sharif, S. Mazinani, and N. Naderi, 'A high quality ITO/PET electrode for flexible and transparent optoelectronic devices', *J. Mater. Sci. Mater. Electron.*, vol. 28, no. 3, pp. 2962–2969, Feb. 2017, doi: 10.1007/s10854-016-5881-7.

[57] G. Mattana, D. Briand, A. Marette, A. Vásquez Quintero, and N. F. de Rooij, 'Polylactic acid as a biodegradable material for all-solution-processed organic

electronic devices', *Org. Electron.*, vol. 17, pp. 77–86, Feb. 2015, doi: 10.1016/j.orgel.2014.11.010.

[58] J. A. Spechler, T.-W. Koh, J. T. Herb, B. P. Rand, and C. B. Arnold, 'A Transparent, Smooth, Thermally Robust, Conductive Polyimide for Flexible Electronics', *Adv. Funct. Mater.*, vol. 25, no. 48, pp. 7428–7434, Dec. 2015, doi: 10.1002/adfm.201503342.

[59] S. J. Park, J. E. Lee, J. Park, N.-K. Lee, Y. Son, and S.-H. Park, 'High-temperature 3D printing of polyetheretherketone products: Perspective on industrial manufacturing applications of super engineering plastics', *Mater. Des.*, vol. 211, p. 110163, Dec. 2021, doi: 10.1016/j.matdes.2021.110163.

[60] J. Abu-Khalaf, L. Al-Ghussain, and A. Al-Halhouli, 'Fabrication of Stretchable Circuits on Polydimethylsiloxane (PDMS) Pre-Stretched Substrates by Inkjet Printing Silver Nanoparticles', *Materials*, vol. 11, no. 12, p. 2377, Nov. 2018, doi: 10.3390/ma11122377.

[61] W. Zhou, F. A. List, C. E. Duty, and S. S. Babu, 'Fabrication of conductive paths on a fused deposition modeling substrate using inkjet deposition', *Rapid Prototyp. J.*, vol. 22, no. 1, pp. 77–86, Jan. 2016, doi: 10.1108/RPJ-05-2014-0070.

[62] I. Poupyrev, N.-W. Gong, S. Fukuhara, M. E. Karagozler, C. Schwesig, and K. E. Robinson, 'Project Jacquard: Interactive Digital Textiles at Scale', in *Proceedings of the 2016 CHI Conference on Human Factors in Computing Systems*, San Jose California USA: ACM, May 2016, pp. 4216–4227. doi: 10.1145/2858036.2858176.

[63] T. Liu and M. Devarajan, 'Influence of Prepreg Material Properties on Printed Circuit Board (PCB) Stack-up', in *2022 IEEE 72nd Electronic Components and Technology Conference (ECTC)*, San Diego, CA, USA: IEEE, May 2022, pp. 2244–2248. doi: 10.1109/ECTC51906.2022.00354.

[64] V. Kumar and M. Gupta, 'Comparative study of different natural fibre printed circuit board (PCB) composites', *Mater. Today Proc.*, vol. 44, pp. 2097–2101, 2021, doi: 10.1016/j.matpr.2020.12.182.

[65] J. F. J. Veldhuijzen van Zanten, G. A. Schuerink, A. H. J. Tullemans, R. Legtenberg, and W. W. Wits, 'Method to determine thermoelastic material properties of constituent and copper-patterned layers of multilayer printed circuit boards', *J. Mater. Sci. Mater. Electron.*, vol. 29, no. 6, pp. 4900–4914, Mar. 2018, doi: 10.1007/s10854-017-8449-2.

[66] C. Tulkoff and C. Hillman, 'Reliable Plated Through Via Design and Fabrication'.

[67] T. Sathishkumar, S. Satheeshkumar, and J. Naveen, 'Glass fiber-reinforced polymer composites – a review', *J. Reinf. Plast. Compos.*, vol. 33, no. 13, pp. 1258–1275, Jul. 2014, doi: 10.1177/0731684414530790.

[68] Multi Circuit Boards Ltd., 'Printed circuit boards - basic design rules'. May 2021. Accessed: Jun. 07, 2023. [Online]. Available: https://www.multi-circuit-boards.eu/fileadmin/user_upload/downloads/leiterplatten_design-hilfe/Multi-CB-Leiterplatten_Basic-Design-Rules_en.pdf

[69] S. Patermann and V. Altstädt, 'Lignin as renewable raw material for applications in electronics', presented at the PROCEEDINGS OF THE REGIONAL CONFERENCE GRAZ 2015 – POLYMER PROCESSING SOCIETY PPS: Conference Papers, Graz, Austria, 2016, p. 060003. doi: 10.1063/1.4965524.

[70] W. Pornwannachai, J. R. Ebdon, and B. K. Kandola, 'Fire-resistant natural fibre-reinforced composites from flame retarded textiles', *Polym. Degrad. Stab.*, vol. 154, pp. 115–123, Aug. 2018, doi: 10.1016/j.polymdegradstab.2018.05.019.

[71] J. R. Jian, T. Kim, J. S. Park, J. Wang, and W. S. Kim, 'High performance 3D printed electronics using electroless plated copper', *AIP Adv.*, vol. 7, no. 3, p. 035314, Mar. 2017, doi: 10.1063/1.4979173.

[72] A. J. Lopes, E. MacDonald, and R. B. Wicker, 'Integrating stereolithography and direct print technologies for 3D structural electronics fabrication', *Rapid Prototyp. J.*, vol. 18, no. 2, pp. 129–143, Mar. 2012, doi: 10.1108/13552541211212113.

[73] M. Adler, R. Bieringer, T. Schauber, and J. Günther, 'Materials for stretchable electronics compliant with printed circuit board fabrication', in *Stretchable Electronics*, T. Someya, Ed., Weinheim, Germany: Wiley-VCH Verlag & Co. KGaA, 2013, pp. 161–185. [Online]. Available: https://doi.org/10.1002/9783527646982.ch1

[74] X. Y. Chen, N. Tien-Binh, S. Kaliaguine, and D. Rodrigue, 'Polyimide Membranes for Gas Separation: Synthesis, Processing and Properties', in *Polyimides: synthesis, applications, and research*, C. Murphy, Ed., in Polymer science and technology. , New York: Nova Publishers, 2017.

[75] C. Feger and H. Franke, ‘Polyimides in High-Performance Electronics Packaging and Optoelectronic Applications’, in *Polyimides: Fundamentals and Applications*, 1st ed., M. Ghosh, Ed., Boca Raton, Florida, United States: CRC Press, 1996, pp. 759–814.

[76] H. A. Kang, I. S. Chung, M. Kakimoto, and S. Y. Kim, ‘Synthesis and Characterization of Polyimides from Unsymmetrical Diamine with Cyano Groups’, *Polym. J.*, vol. 33, no. 3, pp. 284–289, Mar. 2001, doi: 10.1295/polymj.33.284.

[77] DuPont de Nemours Inc., ‘DuPont Kapton Summary of Properties’. 2022. Accessed: Apr. 26, 2023. [Online]. Available: https://www.dupont.com/content/dam/dupont/amer/us/en/ei-transformation/public/documents/en/EI-10142_Kapton-Summary-of-Properties.pdf

[78] M. Loeblein *et al.*, ‘3D Graphene-Infused Polyimide with Enhanced Electrothermal Performance for Long-Term Flexible Space Applications’, *Small*, vol. 11, no. 48, pp. 6425–6434, Dec. 2015, doi: 10.1002/smll.201502670.

[79] V. Zardetto, T. M. Brown, A. Reale, and A. Di Carlo, ‘Substrates for flexible electronics: A practical investigation on the electrical, film flexibility, optical, temperature, and solvent resistance properties’, *J. Polym. Sci. Part B Polym. Phys.*, vol. 49, no. 9, pp. 638–648, May 2011, doi: 10.1002/polb.22227.

[80] M. Kujala, T. Kololuoma, J. Keskinen, D. Lupo, M. Mäntysalo, and T. M. Kraft, ‘Bending reliability of screen-printed vias for a flexible energy module’, *Npj Flex. Electron.*, vol. 4, no. 1, p. 24, Sep. 2020, doi: 10.1038/s41528-020-00087-4.

[81] A. Elamri, K. Zdiri, O. Harzallah, and A. Lallam, ‘Progress in Polyethylene Terephthalate Recycling’, in *Polyethylene Terephthalate: Uses, Properties and Degradation*, N. A. Barber, Ed., in Polymer science and technology. , Hauppauge, New York, USA: Nova Science Publishers, Inc., 2017, p. 22.

[82] S. Dwivedi and T. Kaneko, ‘Molecular Design of Soluble Biopolyimide with High Rigidity’, *Polymers*, vol. 10, no. 4, p. 368, Mar. 2018, doi: 10.3390/polym10040368.

[83] S. S. Kuhire, A. B. Ichake, E. Grau, H. Cramail, and P. P. Wadgaonkar, ‘Synthesis and characterization of partially bio-based polyimides based on biphenylene-containing diisocyanate derived from vanillic acid’, *Eur. Polym. J.*, vol. 109, pp. 257–264, Dec. 2018, doi: 10.1016/j.eurpolymj.2018.09.054.

[84] P. Suvannasara *et al.*, 'Biobased Polyimides from 4-Aminocinnamic Acid Photodimer', *Macromolecules*, vol. 47, no. 5, pp. 1586–1593, Mar. 2014, doi: 10.1021/ma402499m.

[85] Z. Fu, P. Tanninen, J. Keskinen, R. Lev, V. Leminen, and M. Mäntysalo, 'Wear reliability and failure mechanism of inkjet-printed conductors on paperboard substrate', *Flex. Print. Electron.*, vol. 8, no. 2, p. 025004, Jun. 2023, doi: 10.1088/2058-8585/accc9b.

[86] J. Liu *et al.*, 'Future paper based printed circuit boards for green electronics: fabrication and life cycle assessment', *Energy Env. Sci*, vol. 7, no. 11, pp. 3674–3682, 2014, doi: 10.1039/C4EE01995D.

[87] C. Wang *et al.*, '3D Printing of Lightweight Polyimide Honeycombs with the High Specific Strength and Temperature Resistance', *ACS Appl. Mater. Interfaces*, vol. 13, no. 13, pp. 15690–15700, Apr. 2021, doi: 10.1021/acsami.1c01992.

[88] J. Herzberger, V. Meenakshisundaram, C. B. Williams, and T. E. Long, '3D Printing All-Aromatic Polyimides Using Stereolithographic 3D Printing of Polyamic Acid Salts', *ACS Macro Lett.*, vol. 7, no. 4, pp. 493–497, Apr. 2018, doi: 10.1021/acsmacrolett.8b00126.

[89] R. Singh *et al.*, 'On 3D printing of low-cost sensors using recycled PET', *Sādhanā*, vol. 47, no. 4, p. 260, Nov. 2022, doi: 10.1007/s12046-022-02029-4.

[90] N. A. Fountas, I. Papantoniou, J. D. Kechagias, D. E. Manolakos, and N. M. Vaxevanidis, 'Modeling and optimization of flexural properties of FDM-processed PET-G specimens using RSM and GWO algorithm', *Eng. Fail. Anal.*, vol. 138, p. 106340, Aug. 2022, doi: 10.1016/j.engfailanal.2022.106340.

[91] J. Andrzejewski and L. Marciniak-Podsadna, 'Development of Thermal Resistant FDM Printed Blends. The Preparation of GPET/PC Blends and Evaluation of Material Performance', *Materials*, vol. 13, no. 9, p. 2057, Apr. 2020, doi: 10.3390/ma13092057.

[92] A. Hussain, 'Flexible Printed Circuit Boards', in *Introduction to Flexible Electronics*, Boca Raton, Florida, United States: CRC Press, 2021, pp. 165–174. [Online]. Available: https://doi.org/10.1201/9781003010715-14

[93] D. Avery, 'Copper Foil for Flexible Circuits', *Circuit World*, vol. 14, no. 2, pp. 16–20, Jan. 1988, doi: 10.1108/eb043948.

[94] B. Madadnia, F. Bossuyt, and J. Vanfleteren, 'Technological development for the reduction of out-of-plane deformation of metallic meander structures in thermoformed electronics', *Int. J. Adv. Manuf. Technol.*, vol. 119, no. 9–10, pp. 6649–6663, Apr. 2022, doi: 10.1007/s00170-022-08680-9.

[95] Y. Yanagihara, A. Suenaga, H. Kondo, and H. Saito, 'Structure and deformation recovery of the thermoplastic polyurethane spherulite', *J. Polym. Sci. Part B Polym. Phys.*, vol. 55, no. 21, pp. 1585–1594, Nov. 2017, doi: 10.1002/polb.24412.

[96] M. A. Hood, B. Wang, J. M. Sands, J. J. La Scala, F. L. Beyer, and C. Y. Li, 'Morphology control of segmented polyurethanes by crystallization of hard and soft segments', *Polymer*, vol. 51, no. 10, pp. 2191–2198, May 2010, doi: 10.1016/j.polymer.2010.03.027.

[97] Covestro Deutschland AG, 'Product information Platilon U'. 2017.

[98] R. Mikkonen, A. Koivikko, T. Vuorinen, V. Sariola, and M. Mäntysalo, 'Inkjet-Printed, Nanofiber-Based Soft Capacitive Pressure Sensors for Tactile Sensing', *IEEE Sens. J.*, vol. 21, no. 23, pp. 26286–26293, Dec. 2021, doi: 10.1109/JSEN.2021.3085128.

[99] A. Bhat, J. W. Ambrose, and R. C.-H. Yeow, 'Composite Soft Pneumatic Actuators Using 3D Printed Skins', *IEEE Robot. Autom. Lett.*, vol. 8, no. 4, pp. 2086–2093, Apr. 2023, doi: 10.1109/LRA.2023.3246841.

[100] Y. He *et al.*, 'Three-Dimensional Coprinting of Liquid Metals for Directly Fabricating Stretchable Electronics', *3D Print. Addit. Manuf.*, vol. 5, no. 3, pp. 195–203, Sep. 2018, doi: 10.1089/3dp.2017.0147.

[101] T. Kuroda, H. Takahashi, and A. Masuda, 'Woven Electronic Textiles', in *Wearable Sensors*, 1st ed., E. Sazonov and M. R. Neuman, Eds., San Diego, CA, USA: Academic Press, 2014, pp. 175–198. doi: 10.1016/B978-0-12-418662-0.00021-0.

[102] R. Paradiso, L. Caldani, and M. Pacelli, 'Knitted Electronic Textiles', in *Wearable Sensors*, 1st ed., E. Sazonov and M. R. Neuman, Eds., San Diego, CA, USA: Academic Press, 2014, pp. 153–174. doi: 10.1016/B978-0-12-418662-0.00003-9.

[103] J. Jang *et al.*, 'Knitted strain sensor with carbon fiber and aluminum-coated yarn, for wearable electronics', *J. Mater. Chem. C*, vol. 9, no. 46, pp. 16440–16449, 2021, doi: 10.1039/D1TC01899J.

[104] A. A. Simegnaw, B. Malengier, M. G. Tadesse, and L. Van Langenhove, 'Development of Stainless Steel Yarn with Embedded Surface Mounted Light Emitting Diodes', *Materials*, vol. 15, no. 8, p. 2892, Apr. 2022, doi: 10.3390/ma15082892.

[105] F. Kane, 'Nonwovens in smart clothes and wearable technologies', in *Smart Clothes and Wearable Technology*, J. McCann and D. Bryson, Eds., Cambridge, UK: Woodhead Publishing Limited, 2009, pp. 156–182. doi: 10.1533/9781845695668.2.156.

[106] L. Thomas, 'Woven structures and their impact on the function and performance of smart clothing', in *Smart Clothes and Wearable Technology*, J. McCann and D. Bryson, Eds., Cambridge, UK: Woodhead Publishing Limited, 2009, pp. 131–155. doi: 10.1533/9781845695668.2.131.

[107] N. Varghese and G. Thilagavathi, 'Development of woven stretch fabrics and analysis on handle, stretch, and pressure comfort', *J. Text. Inst.*, vol. 106, no. 3, pp. 242–252, Mar. 2015, doi: 10.1080/00405000.2014.914652.

[108] F. Saifee, 'The influence of knitwear on smart wearables', in *Smart Clothes and Wearable Technology*, J. McCann and D. Bryson, Eds., Cambridge, UK: Woodhead Publishing Limited, 2009, pp. 111–130. doi: 10.1533/9781845695668.2.111.

[109] T. Jovanović, Ž. Penava, and Z. Vrljičak, 'Impact of the Elastane Percentage on the Elastic Properties of Knitted Fabrics under Cyclic Loading', *Materials*, vol. 15, no. 19, p. 6512, Sep. 2022, doi: 10.3390/ma15196512.

[110] E. Lovell, L. Buechley, and J. Davis, 'The LilyTiny: A Case Study in Expanding Access to Electronic Textiles', in *CHI Conference on Human Factors in Computing Systems Extended Abstracts*, New Orleans LA USA: ACM, Apr. 2022, pp. 1–8. doi: 10.1145/3491101.3503579.

[111] A. D. Valentine *et al.*, 'Hybrid 3D Printing of Soft Electronics', *Adv. Mater.*, vol. 29, no. 40, p. 1703817, Oct. 2017, doi: 10.1002/adma.201703817.

[112] G. Cahn, O. N. Pierron, and A. Antoniou, 'Trace width effects on electrical performance of screen-printed silver inks on elastomeric substrates under

uniaxial stretch', *J. Appl. Phys.*, vol. 130, no. 11, p. 115304, Sep. 2021, doi: 10.1063/5.0056117.

[113] K. W. Allen, 'Theories of adhesion', in *Handbook of Adhesion*, 2nd ed., D. E. Packham, Ed., Chichester, West Sussex, England: John Wiley & Sons, Ltd, 2005, pp. 535–538.

[114] L. F. M. da Silva, A. Öchsner, and R. D. Adams, 'Introduction to Adhesive Bonding Technology', in *Handbook of Adhesion Technology*, 1st ed., L. F. M. da Silva, A. Öchsner, and R. D. Adams, Eds., Berlin, Germany: Springer-Verlag Berlin Heidelberg, 2011, pp. 1–7.

[115] J. F. Padday, 'Wetting and work of adhesion', in *Handbook of Adhesion*, 2nd ed., D. E. Packham, Ed., Chichester, West Sussex, England: John Wiley & Sons, Ltd, 2005, pp. 594–597.

[116] D. E. Packham, 'Theories of Fundamental Adhesion', in *Handbook of Adhesion Technology*, 1st ed., L. F. M. da Silva, A. Öchsner, and R. D. Adams, Eds., Berlin, Germany: Springer-Verlag Berlin Heidelberg, 2011, pp. 11–38.

[117] K. W. Allen, 'Adorption theory of adhesion', in *Handbook of Adhesion*, 2nd ed., D. E. Packham, Ed., Chichester, West Sussex, England: John Wiley & Sons, Ltd, 2005, pp. 38–40.

[118] G. Critchlow, 'General Introduction to Surface Treatments', in *Handbook of Adhesion Technology*, 1st ed., L. F. M. da Silva, A. Öchsner, and R. D. Adams, Eds., Berlin, Germany: Springer-Verlag Berlin Heidelberg, 2011, pp. 119–146.

[119] K. W. Allen, 'Mechanical theory of adhesion', in *Handbook of Adhesion*, 2nd ed., D. E. Packham, Ed., Chichester, West Sussex, England: John Wiley & Sons, Ltd, 2005, pp. 275–277.

[120] K. W. Allen, 'Diffusion theory of adhesion', in *Handbook of Adhesion*, 2nd ed., D. E. Packham, Ed., Chichester, West Sussex, England: John Wiley & Sons, Ltd, 2005, pp. 103–105.

[121] I. Singh, K. Debnath, and A. Dvivedi, 'Joining of Natural Fibre-reinforced Thermoplastic Composites', in *Biomass-based Biocomposites*, V. K. Thakur and A. S. Singha, Eds., Shawbury, Shrewsbury, Shropshire, UK: Smithers Rapra Technology Ltd, 2013, pp. 145–165.

[122] W. Hufenbach, F. Adam, I. Körner, A. Winkler, and D. Weck, 'Combined joining technique for thermoplastic composites with embedded sensor networks', *J. Intell. Mater. Syst. Struct.*, vol. 24, no. 10, pp. 1226–1232, Jul. 2013, doi: 10.1177/1045389X12471870.

[123] M. M. Schwartz, Ed., *Soldering: understanding the basics*. Materials Park, Ohio: ASM International, 2014.

[124] E. Sancaktar, 'Classification of Adhesive and Sealant Materials', in *Handbook of Adhesion Technology*, 1st ed., L. F. M. da Silva, A. Öchsner, and R. D. Adams, Eds., Springer-Verlag Berlin Heidelberg, 2011, pp. 261–290.

[125] S.-C. Kim and Y.-H. Kim, 'Review paper: Flip chip bonding with anisotropic conductive film (ACF) and nonconductive adhesive (NCA)', *Curr. Appl. Phys.*, vol. 13, pp. S14–S25, Jul. 2013, doi: 10.1016/j.cap.2013.05.009.

[126] Y. Tao, Z. Yang, X. Lu, G. Tao, Y. Xia, and H. Wu, 'Influence of filler morphology on percolation threshold of isotropical conductive adhesives (ICA)', *Sci. China Technol. Sci.*, vol. 55, no. 1, pp. 28–33, Jan. 2012, doi: 10.1007/s11431-011-4651-2.

[127] T. Löher *et al.*, 'Stretchable electronic systems: Realization and applications', in *2009 11th Electronics Packaging Technology Conference*, Singapore: IEEE, Dec. 2009, pp. 893–898. doi: 10.1109/EPTC.2009.5416416.

[128] I. Kim *et al.*, 'A photonic sintering derived Ag flake/nanoparticle-based highly sensitive stretchable strain sensor for human motion monitoring', *Nanoscale*, vol. 10, no. 17, pp. 7890–7897, 2018, doi: 10.1039/C7NR09421C.

[129] Y. Yin *et al.*, 'Stretchable and Tailorable Triboelectric Nanogenerator Constructed by Nanofibrous Membrane for Energy Harvesting and Self-Powered Biomechanical Monitoring', *Adv. Mater. Technol.*, vol. 3, no. 5, p. 1700370, May 2018, doi: 10.1002/admt.201700370.

[130] V. Mecnika, K. Scheulen, C. F. Anderson, M. Hörr, and C. Breckenfelder, 'Joining technologies for electronic textiles', in *Electronic Textiles*, T. Dias, Ed., Elsevier, 2015, pp. 133–153. doi: 10.1016/B978-0-08-100201-8.00008-4.

[131] 'PTH400 favorit through hole mechanical press operating instructions'. Fortex Engineering Limited, 2023. Accessed: Feb. 06, 2023. [Online]. Available: http://www.fortex.co.uk/product/favorit-through-hole-mechanical-plating/

[132] G. Kettlgruber *et al.*, 'Stretch-Safe: Magnetic Connectors for Modular Stretchable Electronics', *Adv. Intell. Syst.*, vol. 2, no. 8, p. 2000065, Aug. 2020, doi: 10.1002/aisy.202000065.

[133] Array Solders, 'Technical Data Sheet 63Sn/37Pb'.

[134] Array Solders, 'Technical Data Sheet Sac305 (Lead Free) (96,5Sn/3Ag/0,5Cu)'.

[135] Indium Corporation, 'Product Data Sheet Low-Temperature Solder'. 2018.

[136] P. Mazur, 'Evaluation of the quality of cyanoacrylate adhesive joints using the example of poly(methyl methacrylate) and polycarbonate', *Prod. Eng. Arch.*, vol. 14, no. 14, pp. 7–10, Mar. 2017, doi: 10.30657/pea.2017.14.02.

[137] T. Salo, A. Halme, M. Kanerva, and J. Vanhala, 'Bond Strength and Failure Mechanisms of Nonconductive Adhesives for Stretchable Electronics', *IEEE Trans. Compon. Packag. Manuf. Technol.*, vol. 10, no. 5, pp. 770–778, May 2020, doi: 10.1109/TCPMT.2020.2980121.

[138] Y. Li, D. Lu, and C. P. Wong, 'Isotropically Conductive Adhesives (ICAs)', in *Electrical Conductive Adhesives with Nanotechnologies*, Boston, MA: Springer US, 2010, pp. 121–225. doi: 10.1007/978-0-387-88783-8_4.

[139] D. Lu, Q. K. Tong, and C. P. Wong, 'Conductivity mechanisms of isotropic conductive adhesives (ICAs)', *IEEE Trans. Electron. Packag. Manuf.*, vol. 22, no. 3, pp. 223–227, Jul. 1999, doi: 10.1109/6104.795857.

[140] H. Hwang *et al.*, 'Stretchable anisotropic conductive film (S-ACF) for electrical interfacing in high-resolution stretchable circuits', *Sci. Adv.*, vol. 7, no. 32, p. eabh0171, Aug. 2021, doi: 10.1126/sciadv.abh0171.

[141] Y. Li, D. Lu, and C. P. Wong, 'Anisotropically Conductive Adhesives/Films (ACA/ACF)', in *Electrical Conductive Adhesives with Nanotechnologies*, Boston, MA: Springer US, 2010, pp. 227–278. doi: 10.1007/978-0-387-88783-8_5.

[142] 'tesa HAF 8412 Product datasheet'. tesa, 2017.

[143] C. Kallmayer, F. Schaller, T. Löher, J. Haberland, F. Kayatz, and A. Schult, 'Optimized Thermoforming Process for Conformable Electronics', in *2018 13th International Congress Molded Interconnect Devices (MID)*, Würzburg, Germany: IEEE, Sep. 2018, pp. 1–6. doi: 10.1109/ICMID.2018.8526929.

[144] D. Grewell and A. Benatar, 'Welding of Plastics: Fundamentals and New Developments', *Int. Polym. Process.*, vol. 22, no. 1, pp. 43–60, Mar. 2007, doi: 10.3139/217.0051.

[145] C. Kim, P. E. Burrows, and S. R. Forrest, 'Micropatterning of Organic Electronic Devices by Cold-Welding', *Science*, vol. 288, no. 5467, pp. 831–833, May 2000, doi: 10.1126/science.288.5467.831.

[146] M. Gorlachova and B. Mahltig, '3D-printing on textiles – an investigation on adhesion properties of the produced composite materials', *J. Polym. Res.*, vol. 28, no. 6, p. 207, Jun. 2021, doi: 10.1007/s10965-021-02567-1.

[147] T. Salo, A. Halme, J. Lahtinen, and J. Vanhala, 'Enhanced stretchable electronics made by fused-filament fabrication', *Flex. Print. Electron.*, vol. 5, no. 4, p. 045001, Dec. 2020, doi: 10.1088/2058-8585/abb931.

[148] M. Korey *et al.*, 'Recycling polymer composite granulate/regrind using big area additive manufacturing', *Compos. Part B Eng.*, vol. 256, p. 110652, May 2023, doi: 10.1016/j.compositesb.2023.110652.

[149] P. F. Flowers, C. Reyes, S. Ye, M. J. Kim, and B. J. Wiley, '3D printing electronic components and circuits with conductive thermoplastic filament', *Addit. Manuf.*, vol. 18, pp. 156–163, Dec. 2017, doi: 10.1016/j.addma.2017.10.002.

[150] T. Grothe, B. Brockhagen, and J. L. Storck, 'Three-dimensional printing resin on different textile substrates using stereolithography: A proof of concept', *J. Eng. Fibers Fabr.*, vol. 15, p. 155892502093344, Jan. 2020, doi: 10.1177/1558925020933440.

[151] E. Pei, J. Shen, and J. Watling, 'Direct 3D printing of polymers onto textiles: experimental studies and applications', *Rapid Prototyp. J.*, vol. 21, no. 5, pp. 556–571, Aug. 2015, doi: 10.1108/RPJ-09-2014-0126.

[152] Y. L. Yap and W. Y. Yeong, 'Additive manufacture of fashion and jewellery products: a mini review: This paper provides an insight into the future of 3D printing industries for fashion and jewellery products', *Virtual Phys. Prototyp.*, vol. 9, no. 3, pp. 195–201, Jul. 2014, doi: 10.1080/17452759.2014.938993.

[153] E. Landau, '"Space Fabric" Links Fashion and Engineering', *National Aeronautics and Space Administration*, Apr. 18, 2017. [Online]. Available:

https://www.nasa.gov/feature/jpl/space-fabric-links-fashion-and-engineering

[154] S. Y. Park and J.-H. Lee, 'Machine Embroidered Sensors for Limb Joint Movement-Monitoring Smart Clothing', *Sensors*, vol. 21, no. 3, p. 949, Feb. 2021, doi: 10.3390/s21030949.

[155] A. Tsolis, S. Bakogianni, C. Angelaki, and A. A. Alexandridis, 'A Review of Clothing Components in the Development of Wearable Textile Antennas: Design and Experimental Procedure', *Sensors*, vol. 23, no. 6, p. 3289, Mar. 2023, doi: 10.3390/s23063289.

[156] O. Van Der Sluis, Y. Y. Hsu, P. H. M. Timmermans, M. Gonzalez, and J. P. M. Hoefnagels, 'Stretching-induced interconnect delamination in stretchable electronic circuits', *J. Phys. Appl. Phys.*, vol. 44, no. 3, p. 034008, Jan. 2011, doi: 10.1088/0022-3727/44/3/034008.

[157] M. Gonzalez, Y.-Y. Hsu, and J. Vanfleteren, 'Modeling of printed circuit board inspired stretchable electronic systems', in *Stretchable Electronics*, T. Someya, Ed., Weinheim, Germany: Wiley-VCH Verlag & Co. KGaA, 2013, pp. 143–159. [Online]. Available: https://doi.org/10.1002/9783527646982.ch6

[158] T. Salo *et al.*, 'Mechanical properties of structured copper and printed silver hybrid stretchable electronic systems', *Flex. Print. Electron.*, vol. 8, no. 2, p. 025019, Jun. 2023, doi: 10.1088/2058-8585/acda46.

[159] N. Matsuhisa, X. Chen, Z. Bao, and T. Someya, 'Materials and structural designs of stretchable conductors', *Chem. Soc. Rev.*, vol. 48, no. 11, pp. 2946–2966, 2019, doi: 10.1039/C8CS00814K.

[160] D. Di Vito, M. Mosallaei, B. Khorramdel, M. Kanerva, and M. Mäntysalo, 'Mechanically driven strategies to improve electromechanical behaviour of printed stretchable electronic systems', *Sci. Rep.*, vol. 10, no. 1, p. 12037, Dec. 2020, doi: 10.1038/s41598-020-68871-w.

[161] M. Mosallaei, J. Jokinen, M. Kanerva, and M. Mäntysalo, 'The Effect of Encapsulation Geometry on the Performance of Stretchable Interconnects', *Micromachines*, vol. 9, no. 12, p. 645, Dec. 2018, doi: 10.3390/mi9120645.

[162] K.-S. Kim, K.-H. Jung, and S.-B. Jung, 'Design and fabrication of screen-printed silver circuits for stretchable electronics', *Microelectron. Eng.*, vol. 120, pp. 216–220, May 2014, doi: 10.1016/j.mee.2013.07.003.

[163] P. Iso-Ketola, J. Vanhala, and M. Mäntysalo, 'A stretchable structure comprising a conductive path and a method for manufacturing the structure', FI 127173 B

[164] D. Di Vito, M. Mosallaei, B. Khorramdel Vahed, M. Kanerva, and M. Mäntysalo, 'Deformability Analysis and Improvement in Stretchable Electronics Systems Through Finite Element Analysis', in *Proceedings of XXIV AIMETA Conference 2019*, in Lecture Notes in Mechanical Engineering. Cham: Springer International Publishing, 2020, pp. 755–763. doi: 10.1007/978-3-030-41057-5_61.

[165] R. Xu *et al.*, 'Fabric-based stretchable electronics with mechanically optimized designs and prestrained composite substrates', *Extreme Mech. Lett.*, vol. 1, pp. 120–126, Dec. 2014, doi: 10.1016/j.eml.2014.12.010.

[166] D. Di Vito, T. Salo, J. Vanhala, and M. Mäntysalo, 'Stretchable electronic devices for wearable and on-skin applications: effects of material anisotropy and extensibility in simple stretchable systems', in *2021 XXXIVth General Assembly and Scientific Symposium of the International Union of Radio Science (URSI GASS)*, Rome, Italy: IEEE, Aug. 2021, pp. 1–4. doi: 10.23919/URSIGASS51995.2021.9560273.

[167] 'X1000 series, flexible laser direct imaging solution for PCB inner- and outer layer and solder mask applications'. Limata GmbH, 2019. Accessed: Aug. 21, 2023. [Online]. Available: https://www.limata.com/wp-content/uploads/2019/11/Limata_Datasheet_X1000_series_2019.pdf

[168] 'Dimatix Materials Printer DMP-2850'. Fujifilm Dimatix, Inc., 2021. Accessed: Aug. 21, 2023. [Online]. Available: https://asset.fujifilm.com/www/us/files/2021-04/c80cdd17080a06095c34a26d6221c81a/PDS00085.pdf

[169] 'I2108'. Terrot GmbH, 2015. Accessed: Aug. 21, 2023. [Online]. Available: https://www.terrot.de/en/pdf/en/I2108.pdf

[170] M. Hatala, P. Gemeiner, M. Hvojnik, and M. Mikula, 'The effect of the ink composition on the performance of carbon-based conductive screen printing inks', *J. Mater. Sci. Mater. Electron.*, vol. 30, no. 2, pp. 1034–1044, Jan. 2019, doi: 10.1007/s10854-018-0372-7.

[171] G. D. Martin and I. M. Hutchings, 'Fundamentals of Inkjet Technology', in *Inkjet Technology for Digital Fabrication*, 1st ed., I. M. Hutchings and G. D. Martin, Eds., Wiley, 2012, pp. 21–44. doi: 10.1002/9781118452943.ch2.

[172] O. Atalay, W. R. Kennon, and E. Demirok, 'Weft-Knitted Strain Sensor for Monitoring Respiratory Rate and Its Electro-Mechanical Modeling', *IEEE Sens. J.*, vol. 15, no. 1, pp. 110–122, Jan. 2015, doi: 10.1109/JSEN.2014.2339739.

[173] L.-W. Lo, J. Zhao, H. Wan, Y. Wang, S. Chakrabartty, and C. Wang, 'An Inkjet-Printed PEDOT:PSS-Based Stretchable Conductor for Wearable Health Monitoring Device Applications', *ACS Appl. Mater. Interfaces*, vol. 13, no. 18, pp. 21693–21702, May 2021, doi: 10.1021/acsami.1c00537.

[174] K. A. Ohiri *et al.*, 'E-textile based modular sEMG suit for large area level of effort analysis', *Sci. Rep.*, vol. 12, no. 1, p. 9650, Jun. 2022, doi: 10.1038/s41598-022-13701-4.

[175] T. Salo, M. Luukko, A. Halme, and J. Vanhala, 'Additive Manufactured Compliant Surface Reflectance Sensor', in *2023 IEEE International Conference on Flexible and Printable Sensors and Systems (FLEPS)*, Boston, MA, USA: IEEE, Jul. 2023, pp. 1–4. doi: 10.1109/FLEPS57599.2023.10220374.

[176] K. D. Harris, A. L. Elias, and H.-J. Chung, 'Flexible electronics under strain: a review of mechanical characterization and durability enhancement strategies', *J. Mater. Sci.*, vol. 51, no. 6, pp. 2771–2805, Mar. 2016, doi: 10.1007/s10853-015-9643-3.

[177] D. Ball, 'Surface mechanics of fine-line etching', *Print. Circuit Fabr.*, vol. 21, no. 11, p. 3, 1998.

[178] H. D. Merchant, W. C. Liu, L. A. Giannuzzi, and J. G. Morris, 'Grain structure of thin electrodeposited and rolled copper foils', *Mater. Charact.*, vol. 53, no. 5, pp. 335–360, Dec. 2004, doi: 10.1016/j.matchar.2004.07.013.

[179] X.-Q. Yin *et al.*, 'Mechanical properties and microstructure of rolled and electrodeposited thin copper foil', *Rare Met.*, vol. 35, no. 12, pp. 909–914, Dec. 2016, doi: 10.1007/s12598-016-0806-4.

[180] N. Ikegawa, H. Hamada, and M. Yamanouchi, 'Evaluation of adhesion between glass/epoxy composite substrate and copper foil for printed circuit board applications', *Compos. Interfaces*, vol. 9, no. 3, pp. 235–245, Jan. 2002, doi: 10.1163/156855402320257320.

[181] M. Janka *et al.*, 'Use of microcutting for high throughput electrode patterning on a flexible substrate', *J. Micromechanics Microengineering*, vol. 24, no. 1, p. 015015, Jan. 2014, doi: 10.1088/0960-1317/24/1/015015.

[182] X. Li and J. Chen, 'Microembossed copper microchannel heat sink for high-density cooling in electronics', *Micro Nano Lett.*, vol. 14, no. 12, pp. 1258–1262, Oct. 2019, doi: 10.1049/mnl.2019.0198.

[183] G. Liu *et al.*, 'Embossing micro-fabrication-based epidermal electrode with a CNT-composed metal film as human–machine interface', *J. Mater. Sci. Mater. Electron.*, vol. 34, no. 16, p. 1254, Jun. 2023, doi: 10.1007/s10854-023-10599-0.

[184] M. Yamamoto, R. Karasawa, S. Okuda, S. Takamatsu, and T. Itoh, 'Long wavy copper stretchable interconnects fabricated by continuous microcorrugation process for wearable applications', *Eng. Rep.*, vol. 2, no. 3, Mar. 2020, doi: 10.1002/eng2.12143.

[185] A. Hudd, 'Inkjet Printing Technologies', in *The Chemistry of Inkjet Inks*, Singapore: World Scientific Publishing Co. Pte. Ltd, 2009, pp. 3–18.

[186] S. K. Tam, K. Y. Fung, G. S. H. Poon, and K. M. Ng, 'Product design: Metal nanoparticle-based conductive inkjet inks', *AIChE J.*, vol. 62, no. 8, pp. 2740–2753, Aug. 2016, doi: 10.1002/aic.15271.

[187] 'Product Specification, 736465'. Sigma-Aldrich.

[188] M. Pietsch, S. Schlisske, M. Held, P. Maag, and G. Hernandez-Sosa, 'Stretchable inkjet-printed electronics on mechanically compliant island-bridge architectures covalently bonded to elastomeric substrates', *Flex. Print. Electron.*, vol. 7, no. 2, p. 025007, Jun. 2022, doi: 10.1088/2058-8585/ac6c64.

[189] T. Liimatta, E. Halonen, H. Sillanpaa, J. Niittynen, and M. Mäntysalo, 'Inkjet printing in manufacturing of stretchable interconnects', in *2014 IEEE 64th Electronic Components and Technology Conference (ECTC)*, Orlando, FL, USA: IEEE, May 2014, pp. 151–156. doi: 10.1109/ECTC.2014.6897281.

[190] M. S. Kim *et al.*, 'Stretchable Printed Circuit Board Based on Leak-Free Liquid Metal Interconnection and Local Strain Control', *ACS Appl. Mater. Interfaces*, vol. 14, no. 1, pp. 1826–1837, Jan. 2022, doi: 10.1021/acsami.1c16177.

[191] T. Koshi and E. Iwase, 'Crack-Configuration Analysis of Metal Conductive Track Embedded in Stretchable Elastomer', *Micromachines*, vol. 9, no. 3, p. 130, Mar. 2018, doi: 10.3390/mi9030130.

[192] C. Phillips, D. Beynon, S. Hamblyn, G. Davies, D. Gethin, and T. Claypole, 'A Study of the Abrasion of Squeegees Used in Screen Printing and Its Effect on Performance with Application in Printed Electronics', *Coatings*, vol. 4, no. 2, pp. 356–379, Jun. 2014, doi: 10.3390/coatings4020356.

[193] T. Araki, M. Nogi, K. Suganuma, M. Kogure, and O. Kirihara, 'Printable and Stretchable Conductive Wirings Comprising Silver Flakes and Elastomers', *IEEE Electron Device Lett.*, vol. 32, no. 10, pp. 1424–1426, Oct. 2011, doi: 10.1109/LED.2011.2161663.

[194] V. Scenev *et al.*, 'Low-Temperature Processible Highly Conducting Pastes for Printed Electronics Applications', *Adv. Eng. Mater.*, vol. 24, no. 9, p. 2101752, Sep. 2022, doi: 10.1002/adem.202101752.

[195] H. Menon, R. Aiswarya, and K. P. Surendran, 'Screen printable MWCNT inks for printed electronics', *RSC Adv.*, vol. 7, no. 70, pp. 44076–44081, 2017, doi: 10.1039/C7RA06260E.

[196] U. Linderhed, I. Petsagkourakis, P. A. Ersman, V. Beni, and K. Tybrandt, 'Fully screen printed stretchable electrochromic displays', *Flex. Print. Electron.*, vol. 6, no. 4, p. 045014, Dec. 2021, doi: 10.1088/2058-8585/ac3eb2.

[197] O.-H. Huttunen, T. Happonen, J. Hiitola-Keinänen, P. Korhonen, J. Ollila, and J. Hiltunen, 'Roll-To-Roll Screen-Printed Silver Conductors on a Polydimethyl Siloxane Substrate for Stretchable Electronics', *Ind. Eng. Chem. Res.*, vol. 58, no. 43, pp. 19909–19916, Oct. 2019, doi: 10.1021/acs.iecr.9b03628.

[198] W. Yuan and Z. Cui, 'Printing Technology for Fabrication of Flexible and Stretchable Electronics', in *Flexible and Stretchable Electronics*, 1st ed., R.-W. Li and G. Liu, Eds., Jenny Stanford Publishing, 2019, pp. 295–344. doi: 10.1201/9780429058905-9.

[199] T. Liu, P. Sen, and C.-J. Kim, 'Characterization of Nontoxic Liquid-Metal Alloy Galinstan for Applications in Microdevices', *J. Microelectromechanical Syst.*, vol. 21, no. 2, pp. 443–450, Apr. 2012, doi: 10.1109/JMEMS.2011.2174421.

[200] J. Liang, K. Tong, and Q. Pei, 'A Water-Based Silver-Nanowire Screen-Print Ink for the Fabrication of Stretchable Conductors and Wearable Thin-Film Transistors', *Adv. Mater.*, vol. 28, no. 28, pp. 5986–5996, Jul. 2016, doi: 10.1002/adma.201600772.

[201] 'Regulation (EU) No 1007/2011 of the European Parliament and of the Council of 27 September 2011 on textile fibre names and related labelling and marking of the fibre composition of textile products and repealing Council Directive 73/44/EEC and Directives 96/73/EC and 2008/121/EC of the European Parliament and of the CouncilText with EEA relevance', p. 64.

[202] H. Kim, H. Moon, D. Lim, and W. Jeong, 'Process Optimization for Manufacturing PAN-Based Conductive Yarn with Carbon Nanomaterials through Wet Spinning', *Polymers*, vol. 13, no. 20, p. 3544, Oct. 2021, doi: 10.3390/polym13203544.

[203] X. Chen *et al.*, 'Passive Moisture Sensor Based on Conductive and Water-Soluble Yarns', *IEEE Sens. J.*, vol. 20, no. 18, pp. 10989–10995, Sep. 2020, doi: 10.1109/JSEN.2020.2994449.

[204] Dils, Werft, Walter, Zwanzig, von Krshiwoblozki, and Schneider-Ramelow, 'Investigation of the Mechanical and Electrical Properties of Elastic Textile/Polymer Composites for Stretchable Electronics at Quasi-Static or Cyclic Mechanical Loads', *Materials*, vol. 12, no. 21, p. 3599, Nov. 2019, doi: 10.3390/ma12213599.

[205] J.-T. Wu, S. Lien-Chung Hsu, M.-H. Tsai, Y.-F. Liu, and W.-S. Hwang, 'Direct ink-jet printing of silver nitrate–silver nanowire hybrid inks to fabricate silver conductive lines', *J. Mater. Chem.*, vol. 22, no. 31, p. 15599, 2012, doi: 10.1039/c2jm31761c.

[206] N. Duan, Z. Shi, J. Wang, G. Wang, and X. Zhang, 'Strong and Flexible Carbon Fiber Fabric Reinforced Thermoplastic Polyurethane Composites for High-Performance EMI Shielding Applications', *Macromol. Mater. Eng.*, vol. 305, no. 6, p. 1900829, Jun. 2020, doi: 10.1002/mame.201900829.

[207] J. F. Christ, N. Aliheidari, A. Ameli, and P. Pötschke, '3D printed highly elastic strain sensors of multiwalled carbon nanotube/thermoplastic polyurethane nanocomposites', *Mater. Des.*, vol. 131, pp. 394–401, Oct. 2017, doi: 10.1016/j.matdes.2017.06.011.

[208] S. Merilampi, T. Björninen, V. Haukka, P. Ruuskanen, L. Ukkonen, and L. Sydänheimo, 'Analysis of electrically conductive silver ink on stretchable substrates under tensile load', *Microelectron. Reliab.*, vol. 50, no. 12, pp. 2001–2011, Dec. 2010, doi: 10.1016/j.microrel.2010.06.011.

[209] N. Lu, X. Wang, Z. Suo, and J. Vlassak, 'Metal films on polymer substrates stretched beyond 50%', *Appl. Phys. Lett.*, vol. 91, no. 22, p. 221909, Nov. 2007, doi: 10.1063/1.2817234.

[210] R. Mikkonen, P. Puistola, I. Jönkkäri, and M. Mäntysalo, 'Inkjet Printable Polydimethylsiloxane for All-Inkjet-Printed Multilayered Soft Electrical Applications', *ACS Appl. Mater. Interfaces*, vol. 12, no. 10, pp. 11990–11997, Mar. 2020, doi: 10.1021/acsami.9b19632.

[211] M. A. Yokus, T. Songkakul, V. A. Pozdin, A. Bozkurt, and M. A. Daniele, 'Wearable multiplexed biosensor system toward continuous monitoring of metabolites', *Biosens. Bioelectron.*, vol. 153, p. 112038, Apr. 2020, doi: 10.1016/j.bios.2020.112038.

[212] N. Y. K. Lam, J. Tan, A. Toomey, and K. C. J. Cheuk, 'Washability and abrasion resistance of illuminative knitted e-textiles with POFs and silver-coated conductive yarns', *Fash. Text.*, vol. 9, no. 1, p. 39, Nov. 2022, doi: 10.1186/s40691-022-00313-9.

[213] H. Probst, K. Katzer, A. Nocke, R. Hickmann, M. Zimmermann, and C. Cherif, 'Melt Spinning of Highly Stretchable, Electrically Conductive Filament Yarns', *Polymers*, vol. 13, no. 4, p. 590, Feb. 2021, doi: 10.3390/polym13040590.

[214] S. S. Crump, 'Apparatus and method for creating three-dimensional objects', 5,121,329, 1992

[215] R. Jones *et al.*, 'RepRap – the replicating rapid prototyper', *Robotica*, vol. 29, no. 1, pp. 177–191, Jan. 2011, doi: 10.1017/S026357471000069X.

[216] Finnish Standards Association, 'Additive manufacturing. General principles. Fundamentals and vocabulary. SFS-EN ISO/ASTM 52900:2021:en.' 2021.

[217] I. Gibson, D. Rosen, and B. Stucker, 'Extrusion-Based Systems', in *Additive Manufacturing Technologies*, New York, NY: Springer New York, 2015, pp. 147–173. doi: 10.1007/978-1-4939-2113-3_6.

[218] B. N. Turner, R. Strong, and S. A. Gold, 'A review of melt extrusion additive manufacturing processes: I. Process design and modeling', *Rapid Prototyp. J.*, vol. 20, no. 3, pp. 192–204, Apr. 2014, doi: 10.1108/RPJ-01-2013-0012.

[219] S. Aranda, *3D printing failures: how to diagnose & repair all desktop 3D printing issues*. Lexington, KY: CreateSpace, 2017.

[220] W. Kiński and P. Pietkiewicz, 'Influence of the Printing Nozzle Diameter on Tensile Strength of Produced 3D Models in FDM Technology', *Agric. Eng.*, vol. 24, no. 3, pp. 31–38, Sep. 2020, doi: 10.1515/agriceng-2020-0024.

[221] H. Ren *et al.*, 'Smart structures with embedded flexible sensors fabricated by fused deposition modeling-based multimaterial 3D printing', *Int. J. Smart Nano Mater.*, vol. 13, no. 3, pp. 447–464, Jul. 2022, doi: 10.1080/19475411.2022.2095454.

[222] N. A. Sukindar, M. K. A. Ariffin, B. T. H. T. Baharudin, C. N. A. Jaafar, and M. I. S. Ismail, 'Analyzing the effect of nozzle diameter in fused deposition modeling for extruding polylactic acid using open source 3D printing', *J. Teknol.*, vol. 78, no. 10, Sep. 2016, doi: 10.11113/jt.v78.6265.

[223] I. Gibson, D. Rosen, and B. Stucker, 'Introduction and Basic Principles', in *Additive Manufacturing Technologies*, New York, NY: Springer New York, 2015, pp. 1–18. doi: 10.1007/978-1-4939-2113-3_1.

[224] I. Gibson, D. Rosen, and B. Stucker, 'Development of Additive Manufacturing Technology', in *Additive Manufacturing Technologies*, New York, NY: Springer New York, 2015, pp. 19–42. doi: 10.1007/978-1-4939-2113-3_2.

[225] E. S. Heras, F. B. Haro, J. M. de A. del Burgo, and M. E. I. Marcos, 'Plate auto-level system for fused deposition modelling (FDM) 3D printers', *Rapid Prototyp. J.*, vol. 23, no. 2, pp. 401–413, Mar. 2017, doi: 10.1108/RPJ-06-2015-0065.

[226] J. Wang *et al.*, 'Research of TPU Materials for 3D Printing Aiming at Non-Pneumatic Tires by FDM Method', *Polymers*, vol. 12, no. 11, p. 2492, Oct. 2020, doi: 10.3390/polym12112492.

[227] G. Ćwikła, C. Grabowik, K. Kalinowski, I. Paprocka, and P. Ociepka, 'The influence of printing parameters on selected mechanical properties of FDM/FFF 3D-printed parts', *IOP Conf. Ser. Mater. Sci. Eng.*, vol. 227, p. 012033, Aug. 2017, doi: 10.1088/1757-899X/227/1/012033.

[228] B. N. Turner and S. A. Gold, 'A review of melt extrusion additive manufacturing processes: II. Materials, dimensional accuracy, and surface roughness', *Rapid Prototyp. J.*, vol. 21, no. 3, pp. 250–261, Apr. 2015, doi: 10.1108/RPJ-02-2013-0017.

[229] C. C. Vu, T. T. Nguyen, S. Kim, and J. Kim, 'Effects of 3D Printing-Line Directions for Stretchable Sensor Performances', *Materials*, vol. 14, no. 7, p. 1791, Apr. 2021, doi: 10.3390/ma14071791.

[230] D. Mitra *et al.*, 'Conductive Electrifi and Nonconductive NinjaFlex Filaments based Flexible Microstrip Antenna for Changing Conformal Surface Applications', *Electronics*, vol. 10, no. 7, p. 821, Mar. 2021, doi: 10.3390/electronics10070821.

[231] G. Stano, A. Di Nisio, A. M. Lanzolla, M. Ragolia, and G. Percoco, 'Fused filament fabrication of commercial conductive filaments: experimental study on the process parameters aimed at the minimization, repeatability and thermal characterization of electrical resistance', *Int. J. Adv. Manuf. Technol.*, vol. 111, no. 9–10, pp. 2971–2986, Dec. 2020, doi: 10.1007/s00170-020-06318-2.

[232] J. Galos, Y. Hu, A. R. Ravindran, R. B. Ladani, and A. P. Mouritz, 'Electrical properties of 3D printed continuous carbon fibre composites made using the FDM process', *Compos. Part Appl. Sci. Manuf.*, vol. 151, p. 106661, Dec. 2021, doi: 10.1016/j.compositesa.2021.106661.

[233] Q. Hu, Y. Duan, H. Zhang, D. Liu, B. Yan, and F. Peng, 'Manufacturing and 3D printing of continuous carbon fiber prepreg filament', *J. Mater. Sci.*, vol. 53, no. 3, pp. 1887–1898, Feb. 2018, doi: 10.1007/s10853-017-1624-2.

[234] Z. Wang, C. Luan, G. Liao, X. Yao, and J. Fu, 'Mechanical and self-monitoring behaviors of 3D printing smart continuous carbon fiber-thermoplastic lattice truss sandwich structure', *Compos. Part B Eng.*, vol. 176, p. 107215, Nov. 2019, doi: 10.1016/j.compositesb.2019.107215.

[235] S. M. F. Kabir, K. Mathur, and A.-F. M. Seyam, 'A critical review on 3D printed continuous fiber-reinforced composites: History, mechanism, materials and properties', *Compos. Struct.*, vol. 232, p. 111476, Jan. 2020, doi: 10.1016/j.compstruct.2019.111476.

[236] L. Yin, X. Tian, Z. Shang, X. Wang, and Z. Hou, 'Characterizations of continuous carbon fiber-reinforced composites for electromagnetic interference shielding fabricated by 3D printing', *Appl. Phys. A*, vol. 125, no. 4, p. 266, Apr. 2019, doi: 10.1007/s00339-019-2566-0.

[237] M. Ankenbrand, Y. Eiche, and J. Franke, 'Programming and Evaluation of a Multi-Axis/Multi-Process Manufacturing System for Mechatronic Integrated Devices', in *2019 International Conference on Electronics Packaging (ICEP)*, Niigata, Japan: IEEE, Apr. 2019, pp. 273–278. doi: 10.23919/ICEP.2019.8733548.

[238] S. Jambhulkar, D. Ravichandran, B. Sundaravadivelan, and K. Song, 'Hybrid 3D printing for highly efficient nanoparticle micropatterning', *J. Mater. Chem. C*, vol. 11, no. 13, pp. 4333–4341, 2023, doi: 10.1039/D3TC00168G.

[239] D. Espalin, D. W. Muse, E. MacDonald, and R. B. Wicker, '3D Printing multifunctionality: structures with electronics', *Int. J. Adv. Manuf. Technol.*, vol. 72, no. 5–8, pp. 963–978, May 2014, doi: 10.1007/s00170-014-5717-7.

[240] U. Robles, E. Bustamante, P. Darshni, and R. C. Rumpf, 'High-frequency filters manufactured using hybrid 3D printing method', *Prog. Electromagn. Res. M*, vol. 84, pp. 147–155, 2019, doi: 10.2528/PIERM18102603.

[241] S.-Y. Wu, C. Yang, W. Hsu, and L. Lin, '3D-printed microelectronics for integrated circuitry and passive wireless sensors', *Microsyst. Nanoeng.*, vol. 1, no. 1, p. 15013, Jul. 2015, doi: 10.1038/micronano.2015.13.

[242] D. Sokol, M. Yamada, and J. Nulman, 'Design and Performance of Additively Manufactured In-Circuit Board Planar Capacitors', *IEEE Trans. Electron Devices*, vol. 68, no. 11, pp. 5747–5752, Nov. 2021, doi: 10.1109/TED.2021.3117934.

[243] J. A. Wittkopf, K. Erickson, P. Olumbummo, A. Hartman, H. Tom, and L. Zhao, '3D Printed Electronics with Multi Jet Fusion', *NIP Digit. Fabr. Conf.*, vol. 35, no. 1, pp. 29–33, Sep. 2019, doi: 10.2352/ISSN.2169-4451.2019.35.29.

[244] P. Njogu, B. Sanz-Izquierdo, A. Elibiary, S. Y. Jun, Z. Chen, and D. Bird, '3D Printed Fingernail Antennas for 5G Applications', *IEEE Access*, vol. 8, pp. 228711–228719, 2020, doi: 10.1109/ACCESS.2020.3043045.

[245] A. Georgopoulou, T. Sebastian, and F. Clemens, 'Thermoplastic elastomer composite filaments for strain sensing applications extruded with a fused deposition modelling 3D printer', *Flex. Print. Electron.*, vol. 5, no. 3, p. 035002, Jul. 2020, doi: 10.1088/2058-8585/ab9a22.

[246] Y. Wang, Z. Wang, Z. Wang, T. Xiong, P. P. Shum, and L. Wei, 'Multifunctional Electronic Textiles by Direct 3D Printing of Stretchable

Conductive Fibers', *Adv. Electron. Mater.*, vol. 9, no. 4, p. 2201194, Apr. 2023, doi: 10.1002/aelm.202201194.

[247] S. Swaminathan, K. B. Ozutemiz, C. Majidi, and S. E. Hudson, 'FiberWire: Embedding Electronic Function into 3D Printed Mechanically Strong, Lightweight Carbon Fiber Composite Objects', in *Proceedings of the 2019 CHI Conference on Human Factors in Computing Systems*, Glasgow Scotland Uk: ACM, May 2019, pp. 1–11. doi: 10.1145/3290605.3300797.

[248] M. Alsharari, B. Chen, and W. Shu, '3D Printing of Highly Stretchable and Sensitive Strain Sensors Using Graphene Based Composites', in *EUROSENSORS 2018*, MDPI, Dec. 2018, p. 792. doi: 10.3390/proceedings2130792.

[249] J. T. Muth *et al.*, 'Embedded 3D Printing of Strain Sensors within Highly Stretchable Elastomers', *Adv. Mater.*, vol. 26, no. 36, pp. 6307–6312, Sep. 2014, doi: 10.1002/adma.201400334.

[250] Y. Li, D. Lu, and C. P. Wong, 'Non-conductive Adhesives/Films (NCA/NCF)', in *Electrical Conductive Adhesives with Nanotechnologies*, Boston, MA: Springer US, 2010, pp. 279–301. doi: 10.1007/978-0-387-88783-8_6.

[251] X. Yao, C. Luan, D. Zhang, L. Lan, and J. Fu, 'Evaluation of carbon fiber-embedded 3D printed structures for strengthening and structural-health monitoring', *Mater. Des.*, vol. 114, pp. 424–432, Jan. 2017, doi: 10.1016/j.matdes.2016.10.078.

[252] R. D. S. G. Campilho, D. C. Moura, M. D. Banea, and L. F. M. Da Silva, 'Adhesive thickness effects of a ductile adhesive by optical measurement techniques', *Int. J. Adhes. Adhes.*, vol. 57, pp. 125–132, Mar. 2015, doi: 10.1016/j.ijadhadh.2014.12.004.

[253] A. Hussain, 'Physics of Flexible Electronics', in *Introduction to Flexible Electronics*, Boca Raton, Florida, United States: CRC Press, 2021, pp. 9–22. [Online]. Available: https://doi.org/10.1201/9781003010715-3

[254] A. Grams, S. Kuttler, T. Löher, H. Walter, O. Wittier, and K.-D. Lang, 'Lifetime modelling and geometry optimization of meander tracks in stretchable electronics', in *2018 19th International Conference on Thermal, Mechanical and Multi-Physics Simulation and Experiments in Microelectronics and Microsystems (EuroSimE)*, Toulouse, France: IEEE, Apr. 2018, pp. 1–5. doi: 10.1109/EuroSimE.2018.8369887.

[255] N. Anderson, N. Szorc, V. Gunasekaran, S. Joshi, and G. Jursich, 'Highly sensitive screen printed strain sensors on flexible substrates via ink composition optimization', *Sens. Actuators Phys.*, vol. 290, pp. 1–7, May 2019, doi: 10.1016/j.sna.2019.02.028.

[256] J. A. Fan *et al.*, 'Fractal design concepts for stretchable electronics', *Nat. Commun.*, vol. 5, no. 1, p. 3266, May 2014, doi: 10.1038/ncomms4266.

[257] M. Li, Y. Yang, F. Iacopi, J. Nulman, and S. Chappel-Ram, '3D-Printed Low-Profile Single-Substrate Multi-Metal Layer Antennas and Array With Bandwidth Enhancement', *IEEE Access*, vol. 8, pp. 217370–217379, 2020, doi: 10.1109/ACCESS.2020.3041232.

[258] S. Lage-Rivera, A. Ares-Pernas, J. C. Becerra Permuy, A. Gosset, and M.-J. Abad, 'Enhancement of 3D Printability by FDM and Electrical Conductivity of PLA/MWCNT Filaments Using Lignin as Bio-Dispersant', *Polymers*, vol. 15, no. 4, p. 999, Feb. 2023, doi: 10.3390/polym15040999.

PUBLICATION
I

Bond Strength and Failure Mechanisms of Nonconductive adhesives for Stretchable Electronics

Salo T., Halme A., Kanerva M., Vanhala J.

IEEE Transactions on Components, Packaging and Manufacturing Technology,
vol. 10, no. 5, pp. 770-778
https://doi.org/10.1109/TCPMT.2020.2980121

Publication is licensed under a Creative Commons Attribution 4.0 International License CC-BY-NC-ND

Bond Strength and Failure Mechanisms of Nonconductive Adhesives for Stretchable Electronics

Teemu Salo, Aki Halme, Mikko Kanerva, and Jukka Vanhala, *Member, IEEE*

***Abstract*— Over the past few years, there has been an increasing demand for techniques that allow the forming of stretchable electronics systems from the combination of rigid printed circuit board (PCB) modules and stretchable substrates. The durability issues between the module and interconnects have been solved by optimizing the module's geometry. However, the limiting factor is a reliable attachment method of the module on the substrate. The use of nonconductive adhesives (NCAs) for bonding is one of the most potential techniques due to their low costs and ability to form bonds fast and without a high-temperature cure. In this article, we focused on the testing of different stretchable electronics joints from readily available NCAs and different rigid module materials. The joint samples were tested by using a peel test setup. The fracture surface analysis was carried out by applying the Fourier transform infrared spectroscopy (FTIR). Three different classes of failure mechanisms were identified. The best results were achieved with a novel nonstructural adhesive joint. The nonstructural adhesive joints had a good (0, 28 N/mm) average maximum bond strength with the rigid and smooth FR4 substrate, which made the stretchable substrate elongate considerably (85%) during the peeling. The joint samples from structural adhesives, traditionally used in the electronics industry, were suboptimal.**

***Index Terms*— Adhesive strength, failure analysis, Fourier transform infrared spectroscopy (FTIR), stretchable electronics.**

NOMENCLATURE

ATR	Attenuated total reflection.
CA	Ethylene cyanoacrylate.
FTIR	Fourier transform infrared spectroscopy.
IR	Infrared.
PCB	Printed circuit board.
PLA	Polylactic acid.
PSA	Pressure-sensitive adhesive.
PU	Polyurethane.
NCA	Nonconductive adhesive.
TPU	Thermoplastic polyurethane.

Manuscript received September 16, 2019; revised December 31, 2019 and January 29, 2020; accepted February 15, 2020. This work was supported in part by the European Union Regional Development Fund (ERDF), Satakunta Regional Council and City of Kankaanpää through the Project A73741 SOFT3L under the Grant 2947/31/2018. Recommended for publication by Associate Editor D. Lu upon evaluation of reviewers' comments. *(Corresponding author: Teemu Salo.)*

Teemu Salo, Aki Halme, and Jukka Vanhala are with the Faculty of Information Technology and Communication Sciences, Tampere University, FI-33014 Tampere, Finland (e-mail: teemu.salo@tuni.fi).

Mikko Kanerva is with the Faculty of Engineering and Natural Sciences, Tampere University, FI-33014 Tampere, Finland.

Color versions of one or more of the figures in this article are available online at http://ieeexplore.ieee.org.

Digital Object Identifier 10.1109/TCPMT.2020.2980121

I. INTRODUCTION

TRADITIONAL electronic circuits are powerful yet inherently rigid. The rigidity restricts the formability and deformation during operation, which further limits the usability of rigid circuits in complex applications. The problem is solved with stretchable electronics that can accommodate very high strains and comply with deformations simply by elongating them [1]. Furthermore, the behavior of the elongation is reliable and provides for compatibility, enabling new implementations of these electronics, such as wearable applications and multisite instrumentation typical of the Internet of Things [2].

Of the many ways to produce stretchable electronics, one way is to attach small intelligent islands on a highly elastic substrate. The islands are, for example, PCBs that hold standard electronic components [2], [3]. The islands are electrically connected by stretchable interconnections on the compliant substrate. The interconnections are shaped and optimized per composition so that they intrinsically elongate until they reach very high maximum strains [4]. The islands form an intelligent network with the interconnections, in which functional operations are distributed to several islands.

The advantage of the island network is that the concept can be implemented with standard manufacturing methods using off-the-shelf components. Well-established manufacturing processes make the stretchable electronics reliable and cost effective to produce [2]. This kind of manufacturing approach is supported by the development of electronics components, which will increase the functional capacity of the islands and decrease their size. The size and shape of islands considerably affect how individual islands interfere with the elongation of the highly compliant substrate. Based on existing work, circular islands—with diameters as high as 18 mm—permit a stretchable system [5].

Stretchable electronics include three types of components: rigid islands, stretchable interconnections, and a highly compliant substrate. Stretchable interconnections have been intensively studied, and 600% elongations have been achieved for interconnections [6], but the connections to a component typically break at 20%–50% [7]. The solutions described previously are difficult to implement when they involve delicate local modification of the substrate or embedded guard structures.

The durability issues between the module and interconnects have been studied extensively [4], [8], [9]. One potential solution is to optimize the module's geometry [4], [10].

This work is licensed under a Creative Commons Attribution 4.0 License. For more information, see https://creativecommons.org/licenses/by/4.0/

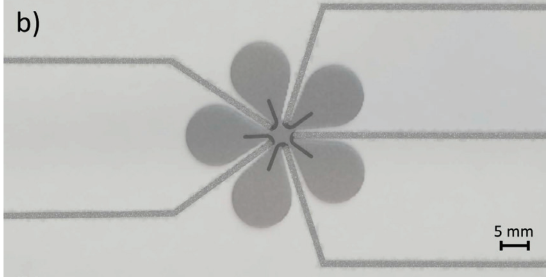

Fig. 1. (a) Proposition for stretchable electronics module design. Clover-shaped module directs deformations away from printed interconnections [10], and compliant (black) PSA tape decreases the stress concentration effect between the module and the substrate. (b) Illustration on how the interconnections turn under the clover-shaped module.

The optimization is based on inwardly curved edges, which form tapered channels through which the interconnections are routed (see Fig. 1). This guides the stress away from the critical area of the component edge and guards the connection between the interconnections and the component.

However, the optimized modules need a proper attachment method to work as stress release. Currently, the limiting factor is the adherence method of the modules on the substrate. In this article, we have investigated the applicability of available adhesives with the materials of stretchable electronics to find the optimal combination for the assembly of the stretchable circuit board.

NCAs have been reported for the use of adhering the components and the islands during the preparation of stretchable conductive joints, focusing on electric properties. The mechanical quality and the durability have received little attention, although long-term durability is a primary challenge in these systems [3]. In this article, the adhesion and the weakest links of various bonds of stretchable electronics joints are studied by means of testing and material characterization. Alternative testing methods and more durable stretchable joint designs are pursued with the cross-disciplinary methods.

II. Theory

A. Methods to Attach Islands on Substrate

When the islands, such as PCBs, and the substrate with the interconnections are joined, they are designed to form electrical and mechanical contacts. The electrical contacts are created between the islands and stretchable interconnections, which form an intelligent stretchable network. The mechanical contacts are made between nonconductive areas of the islands and substrate to protect the electrical contacts from mechanical stresses and corrosion. The islands can be adhered on a substrate with adhesives, mechanical interlocking, or solders.

Adhesives with fillers such as silver flakes and carbon nanotubes are generally versatile and the conductive fillers make the joints conductive. The conductivity depends on the amount and type of the conductive fillers in the adhesive. A high amount of the fillers, i.e., above the percolation threshold, allow isotropic conductivity. A low amount of fillers, i.e., below the percolation threshold, allow anisotropic conductivity (or no conductivity). Both kinds of conductive adhesives, isotropic conductive adhesives and anisotropic conductive adhesives, are used in stretchable electronics. NCA can be added to the conductive adhesive joints; this improves the joints' mechanical strength and decreases the amount of costly conductive adhesive [9].

An alternative option to attach the islands on a highly compliant substrate is the compression joint method, which is especially used in smart textiles. The compression bonds are made by fastening the parts mechanically—that is, by applying pressure to the contacts. The compression joints can be permanent, like rivets [11] or adhesives, or removable, like snap fasteners [12]. When using fasteners, this approach tends to be complicated and expensive to manufacture.

As a third option, solders can be used to create the electrical contacts. Low-temperature solders containing bismuth and/or indium have to be used because of the low thermal softening range of the substrates [13]. NCAs are often used with solders as underfills and later as encapsulators to improve the mechanical strength [3]. However, specialized low-temperature solders are expensive. In addition, reliable contacts to the printed stretchable traces on compliant (and compressive) substrate are difficult to achieve with solders.

NCAs can be used as underfills or as the bonding method to form stretchable electronics joints in all previously described attachment methods. NCAs are used to clamp joints together mechanically and electrically [8], [9], such that the clamping pressure, along with the hardening shrinkage of the NCA, leads to compressive forces at the joint, which maintain the contacts. The formed contacts are also affected by the geometry of the contacts [9]. Using solely NCAs in stretchable electronics is attractive because of the cost-effectiveness and the ability to form bonds fast and at low temperatures. Reduced assembly costs are a result of shorter overall assembly time and adhesives with no additional expensive conductive fillers [8]. However, each attachment method is influenced both by the compatibility between the specific substrates and the NCA and by how the formed joint deforms and fails under stresses. The compatibility depends on various parameters, and this article aims to provide new information about the compatibility of common stretchable electronics substrates and widely used NCAs.

B. Phenomena in the System

The primary requirement for choosing a proper NCA for stretchable electronics is that it needs to fix the surfaces of the

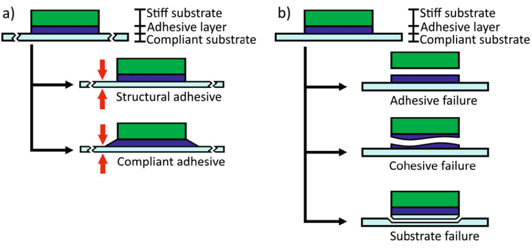

Fig. 2. (a) Behavior of stiff and highly deformable adhesive under uniaxial stretching. (b) Basic failure modes of an adhesive joint.

rigid PCB islands and a highly compliant substrate together. The NCA needs to comply with the deformation differences of materials and, at the same time, maintain adhesion.

Generally, adhesion can be defined as an action when two bodies stick together [14]. In theory, the bond surfaces of the bodies form a common 2-D interface, where adherence of surfaces can be thought to happen. In some cases, depending on the properties of surfaces and expected deformation mechanisms of the joint (e.g., in the stretchable electronics joints), the 2-D interface is better represented by a 3-D interphase. The interphase consists of the interface and the bulk surrounding it, forming the volume for adhesion phenomena, such as mechanical mixing and diffusion, to occur [15].

When NCA is used to attach a PCB island on the substrate, NCA has two different interfaces to adhere to: an interface between the island and the adhesive and an interface between the substrate and the adhesive. The adhesive must wet the surfaces upon preparation to establish interfacial bonds on solid surfaces at the interfaces. Wetting and the flow deformation of an adhesive are affected by the temperature, pressure, and composition [15].

The wetting is also influenced by the properties of the solid surfaces, such as roughness, permeability, and composition. Theoretically, rough surfaces can increase adhesion via a higher surface area, which enables a higher amount of interfacial bonds and mechanical interlocking. However, a too high roughness might lead to voids, which can weaken the joint [15].

Two kinds of NCAs can be used, based on the designed deformation mechanisms in the stretchable electronics joint. The so-called structural adhesives are relatively stiff and can withstand high loads, although the stretchable substrate deforms [16].

Viscoelastic adhesives, such as PSAs, are highly deformable and can follow the substrate under loading [17], [16]. Fig. 2(a) shows the behavior of a structural and a highly deformable adhesive layer.

Adhesives have several parameters that affect the actual bonding strength of the joint. The optimum thickness of the adhesive layer depends on the nature of the adhesive. The cohesive strength of a thick adhesive layer can be less than that of the substrate. Likewise, a variation in the thickness of the adhesive layer offers initiation points for fractures [18]. Furthermore, the exact composition, temperature, humidity, and possible curing agents influence the chemical bond formation within the adhesive [16].

In principle, there are three ways for a joint to fail, which Fig. 2(b) shows. Basically, an adhesive joint can fail in either an adhesive or a cohesive manner. The adhesion failure happens when the adhesive layer does not form sufficient adhesion to bondable surfaces, and the failure occurs cleanly along an interface. The cohesive failure of the adhesive layer happens when the adhesive layer forms a bond stronger than its constitution, and the adhesive layer itself breaks. Moreover, the cohesive failure can occur in the substrate, which causes a type of substrate failure. The substrate failure can occur in the form of substrate delamination or breakage [15], [19].

The strength of the substrate-PCB island system also depends on the local stress–strain gradients [3]. Steep stress–strain gradients typically lead to damage initiation. The failure is caused by a stress concentration effect due to the components having a high mismatch in terms of initial stiffness and stress–strain behavior at high strains [3], [20]. The disadvantageous features of the stress concentration effect can be adjusted by optimizing the islands' shape [10] or by smoothening the deformation differences by gradually stiffening areas around the islands [20], [21]. Additionally, the stress concentration effect can be influenced by the adhesive selection. The selection must also meet the primary requirement of working as a static contact, which might be difficult to achieve using only highly deformable, nonstructural NCAs [8].

C. Modeling as a Part of Designing Interconnections

The testing of various bonding concepts and adhesive products is a laborious activity but is typically necessary up to a certain point. Numerical simulations with validated material models can be used to optimize the geometries of conductive paths (inks), interconnections of PCB modules and the substrates so that electronics in the future could match better deformation of skin and human motion [22], [23]. Valid simulations of strains in the conductive parts of stretchable electronics are the first step on the way to estimate the loading and ultimate failure of adhesive bonds [4]. Furthermore, the modules and possible encapsulation must be accurately modeled [24], [25]. The mode of failure and the properties of the adhesive(s) must be known for the damage of the actual bonding to be properly characterized. The first experiments of the bonding failure can be used as benchmark tests to fit and adjust the numerical models for further optimization routines. Typical methods for these experiments are various tests of adhesion, such as peel tests and pull-off tests. The failure mode observed in a real test provides the knowledge of the damage site, i.e., the model must include a damage model for the specific material or interface that breaks. The behavior of the damage propagation during experimentation can be used to decide whether or not inertia plays a role in the simulation of the test. Finally, a proper combination of tests is needed to fit a 2-D or even a 3-D model with the critical fracture mechanics parameters, such as fracture energy or fracture toughness. Methods on a finite element basis are necessary, especially for the 3-D models.

TABLE I
SUBSTRATE MATERIALS USED IN FOR SAMPLE PREPARATION

Property	Platilon U 4201 AU film	Solder masked FR4 board	3D-printed board
Composition	TPU	Glass fibre reinforced epoxy composite	PLA
Thickness	0.1 mm	1.6 mm	1.8 mm
Nature	Compliant	Stiff	Stiff
Surface	Solid and smooth	Solid and smooth	Permeable and corrugated

TABLE II
SAMPLE TEST SERIES FOR PEEL TESTING

Series	Polymer	Trade name, provider	Time to adhesive achieve handling strength
1	Epoxy	Permabond ET515	0.5 h
2	Epoxy	Permabond MT382	2 h
3	Polyurethane	3M DP610	2 h
4	Cyanoacrylate	Loctite 406	10 s
5	Cyanoacrylate with primer	Loctite 406 with Loctite SF 7239	10 s
6	Pressure-sensitive	3M 8132LE	20 s / 50 °C

III. METHODS

A. Sample Preparation

All of the samples have a 100-μm thick TPU film (Platilon U 4201 AU, by Covestro) representing the highly compliant substrate in the stretchable joint. The length of each film piece is 210 mm (50-mm longer than the "stiff" substrates) so that the film can be fixed to the lower jaw of the tensile test machine. Two kinds of stiff substrates are used: 1) a smooth and solid solder mask-covered (Coates XV501T) green FR4 board; and 2) a rough and permeable 3-D-printed PLA substrate board. The 3-D-printed samples are made with a 0.2-mm layer thickness, and the direction of printing on the surface layer is parallel to the lengthwise direction of the sample. Table I lists the substrates. The bond surfaces of the substrates are cleaned with isopropyl alcohol before applying any of the adhesive candidates.

Table II presents all of the six sample series with the studied adhesive candidates and related times of adhesives to achieve handling strength. We studied four different structural adhesives. Epoxy adhesives are used in the manufacture of traditional electronics and stretchable electronics [21]. Therefore, two kinds of two-component epoxy adhesive systems are used in the specimen preparation: semiflexible toughened ET515 [26] and a modified MT382 for sealing and bonding applications [27], both by Permabond. The other, less conventional structural adhesives for electronics manufacturing are a compliant two-component PU adhesive system Scotch-Weld DP610 (3M) [28] and a one-component CA adhesive system 406 for plastics and elastomeric materials by Loctite [29]. Loctite 406, also Loctite SF 7239 primer that is designed for difficult plastic substrates [30], is used. In total, there are five different structural adhesive candidates.

The samples are prepared by spreading the adhesive (paste) on the substrate pieces and by pressing a substrate piece and

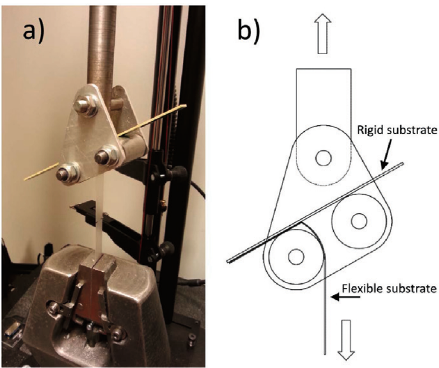

Fig. 3. (a) Floating roller peel test setup with the 45° peel angle used in this article. (b) Schematic diagram of floating roller peel test jig.

TPU film together for a specified time. The duration of the pressing depends on the reported time, which is required for adhesives to acquire sufficient handling strength. The pressing pressure for all the samples is 1.4 kPa. The process was conducted the same way for all the samples in each series to ensure even bond line thickness of parallel samples. In this article, the effect of bond line thickness to adhesion was not studied.

As a candidate for compliant adhesives, PSA tape 8132LE (3M) is used. 8132LE tape is 58-μm thick and has support films on both sides prior to bonding [31]. The PSA tape included samples prepared by applying the PSA tape over the substrate pieces, then attaching them on to the TPU film. The adherence of the tape is enhanced by pressing the samples in a press with a 500-kPa pressure for 20 s. The heated plate supporting the sample in the press is heated to 50 °C (the heated plate on the film side).

After all the bonding preparations, all of the six sample series are dried in ambient laboratory conditions for seven days. After the dehydration period and before the peel tests, the specimens are conditioned for 24 h at a temperature of 23 °C and 50% relative humidity (RH).

B. Peel Tests

The behaviors of five NCAs in the assembly of stretchable electronics joints are studied with the floating roller peel test method. The floating roller peel test can be used to determine the bond strength of a sample under a constant peeling speed (50 mm/min) at a 45° peel angle. Here, the peel tests are carried out by using an Instron 5967 tensile test machine with a 2-kN load cell. The floating roller instrument is attached to the movable upper screwhead. Each sample is tested until sample failure or the tensile test machine's limit, which is 300 mm. Fig. 3 shows the peel test setup used.

The value of the momentary adhesion depends on the direction of the peel force, the width of the sample, and the measured force, following the equation below:

$$G_p = F/b(1 - \cos\theta) \tag{1}$$

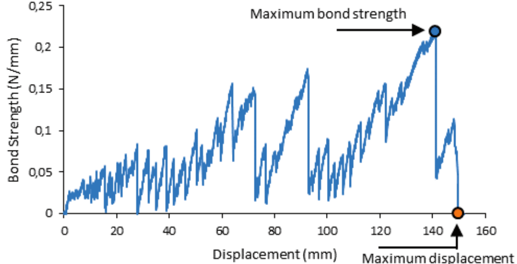

Fig. 4. Typical peel test result and the determined strength values.

where G_p is the momentary peel strength (N/mm), F is the measured force (N), b is the width of the sample (mm), and θ is the angle of peel. In this case, the width of the sample is 12 mm and the angle of the peel is 45°. It should be noted that (1) is a simplified form where plastic deformation of the peeled substrate is ignored [32]. In this article, the size of the peel test sample is 160 × 12 mm, in which the peelable length is 140 mm after the gripping and onset of peeling. Six samples per each sample series are tested in order to calculate average and standard deviation values per series.

C. FTIR

By comparing the surfaces of the unused substrates (film and stiff substrates) and the peeled substrates, it is possible to recognize adhesive residues by using a composition-sensitive technique [33].

The peel-tested samples are studied by using a microscope and FTIR device Optics Tensor 27 (Bruker) to determine the microscale quality of the joints and the failure mechanisms at the interfaces. The device has a horizontal ATR unit GladiATR, provided with a diamond crystal. The ATR system used is compatible with the mid-region IR spectrum (4000–400 cm^{-1}) [34]. Background noise is removed by scanning each surface 128 times with a 4-cm^{-1} resolution. The data collected by using the FTIR technique are related to matter at a 1–10-μm depth from the measured surface.

IV. Results

Fig. 4 shows a typical peel test result where the illustrated curve has the indicated maximum (max) bond strength and max displacement values. Additionally, the shapes of the peel test curves are considered with the determined failure mechanisms to conclude with the performance of the NCAs.

A. Determined Bond Strength per Sample Series

Fig. 5 compares the average max bond strengths of the sample series. The highest average max bond strength value is 0.28 N/mm, and the lowest value is 0.08 N/mm. The highest bond strength of 0.28 N/mm is achieved by 8132LE adhesive and the lowest with a value of 0.08 N/mm by ET515—both result with the FR4 substrate. The standard deviations show the result distribution among the six parallel samples, where a

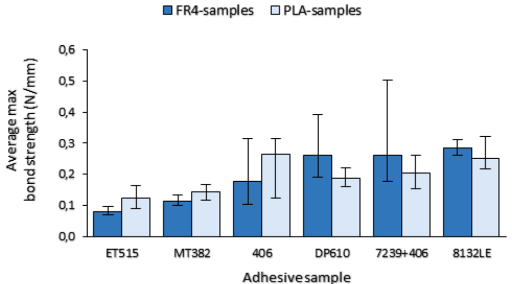

Fig. 5. Average maximum bond strength of the peel test series.

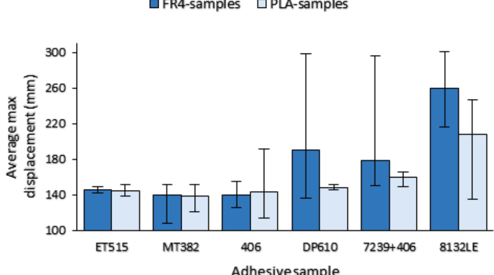

Fig. 6. Average maximum displacement of peel samples.

low deviation indicates an even debonding process and a high deviation indicates an uneven debonding process.

B. Maximum Displacement During the Peel Tests

The average max displacement recorded until the breakage or test machine limit gives an indication in Fig. 6 of high bond strength (high force required to elongate the TPU film) and stability of the debonding process. Low max displacement indicates poor adhesion. Very high limit strains are desirable for stretchable joints in real products, and the high strains manifest themselves as high displacement in the peel tests. The average max displacement of the tests with the PSA tape and the smooth FR4 substrate is 85% and with the PSA tape and the rough PLA substrate 48% higher than the original peelable length of the samples (140 mm).

Moreover, also with the structural adhesives, the average max displacement in the tests with the PU adhesive DP610 and the FR4 substrate is 38% higher than the peelable length. Likewise, with the primed Loctite 406 and the FR4 substrate, the max displacement is 28% higher than the peelable length.

Figs. 5 and 6 show that peel tests are more complicated when the flexible peel arm is also stretchable. In the sample series, which have high average bond strength, the stretchability of the TPU film (and thus displacement of the tests) is not directly proportional. Typically, when samples have low bond strength, the TPU film does not elongate much. However, each test results in a force-displacement curve, i.e., average or peak values do not resemble all of the behavior. The displacement

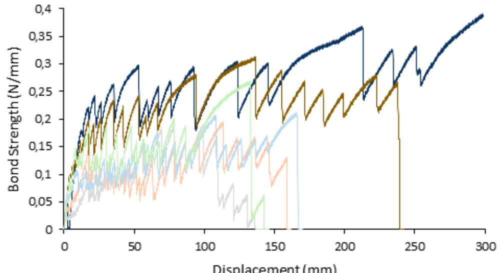

Fig. 7. Peel curves of PU adhesive DP610 with solder masked FR4 substrate. Dark colors indicate samples that had dual interface failure, and light colors represent samples that had adhesive failure on the interface between the adhesive layer and the TPU substrate.

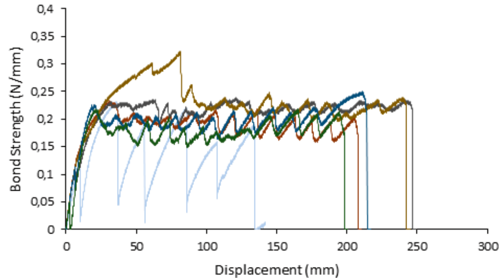

Fig. 8. Peel curves of 8132LE PSA tape with 3-D printed substrate. Dark colors indicate samples, which had adhesive failure on the interface between the tape and the rigid PLA substrate. Light colors represent samples, which had adhesive failure on the interface between the tape and the TPU substrate.

rate is simply a constant (control parameter), but the force is dependent on the dynamic behavior of the nonlinear crack tip-peel arm system.

C. Peel Test Behavior for Structural and Nonstructural Compliant Adhesives

The structural adhesives and the nonstructural, compliant adhesives lead to very different peeling behavior. The peeling occurs in steps with the structural adhesives, which represent stick-slip behavior typical in adhesive joints. Stick-slip behavior indicates development of the plastic crack tip and a subsequent change in the energy dissipation by a shifting of the failure mode. Fig. 7 shows a typical stick-slip behavior in the curves as sudden jumps of values.

In Fig. 7, the samples peel inherently accompanied by random stick-slip behavior. The two samples that have a high average bond strength (over 0.3 N/mm) peel with a failure locus shifting between adhesive substrate and adhesive film interface (determined visually during the tests and later with FTIR-ATR, see Section IV-D). The other four samples with a lower bond strength have simple adhesive failure on the interface between the adhesive layer and the TPU substrate.

The PSA tape including samples generally have a more constant peeling behavior than do the structural adhesive samples. However, the roughness of the 3-D-printed PLA substrate presumably caused regular unevenness and loci of failure initiation, as is seen for most of the sample curves in Fig. 8. An exceptional peeling behavior is observed for one of the samples (8132LE PSA tape), which is explained by a different observed failure mechanism. When the other samples (8132LE PSA tape) mainly have adhesion failure at the interface between the adhesive layer and PLA substrate, the deviate sample has adhesion failure on the interface between the adhesive layer and TPU film.

D. Failure Mechanisms of Peel Samples

Fig. 9 shows typical FTIR results of a substrate (Loctite 406 adhesive-bonded sample). The IR spectrums indicate different absorbance of IR energy, which directly indicates that the chemical compositions of these surfaces differ. Thus, the peeled surface has adhesive residues left after peel testing.

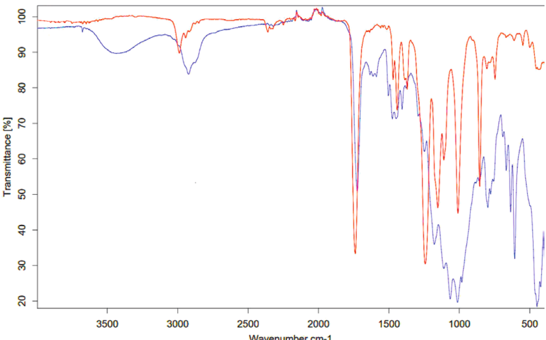

Fig. 9. FTIR-ATR analysis of the reference FR4 substrate (blue) and the FR4 substrate from the Loctite 406 adhesive-bonded sample (red).

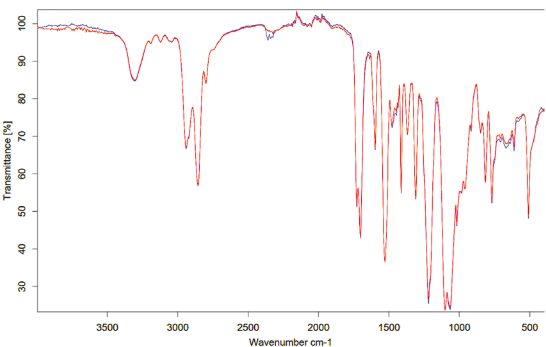

Fig. 10. FTIR-ATR analysis of the reference TPU film (red) and the TPU substrate from the sample DP610 PU adhesive with the FR4 substrate (blue).

The IR spectrums for the samples in this article are either clearly different, representing two different polymers, or identical, as Fig. 10 shows (the variation around 2350 cm^{-1} is caused by moisture and carbon dioxide [35]). Since the “identical” curves also represent the composition of the original surfaces (prior bonding), these samples do not have adhesive residues.

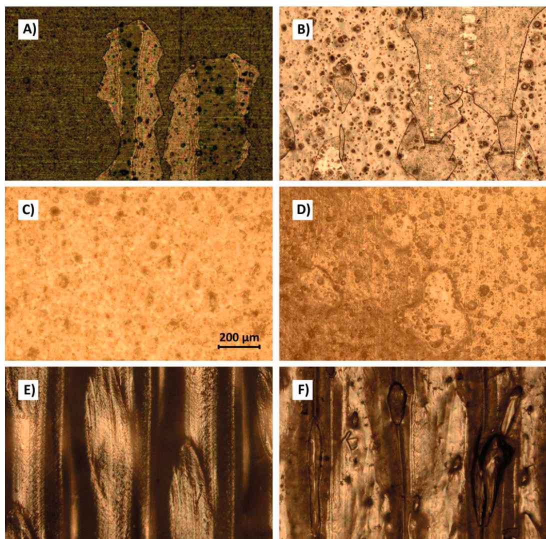

Fig. 11. Microscope images of samples. The peeling direction in the photographs of failed samples is downward. (a) FR4 substrate of the DP610 PU adhesive sample that had dual interface failure. Areas of clean FR4 and the adhesive layer are recognizable. (b) TPU substrate of the same DP610 PU adhesive sample with surfaces of clean TPU substrate and torn adhesive layer. (c) Unpeeled reference TPU substrate. (d) TPU substrate of 406 CA sample that had cohesive failure. Despite the uncolored adhesive, the presence of the adhesive residues can be seen as irregularities on the surface. (e) 3-D-printed PLA substrate of PSA tape sample that had adhesive failure. The tape has peeled cleanly from corrugated 3-D-printed surface. (f) TPU substrate of the same PSA tape sample. The tape on the substrate has deformed and taken the shape of the PLA substrate.

In addition to FTIR, peeled substrates are also studied with microscope imaging and are shown in Fig. 11. Fig. 11(a) and (b) shows the DP610 sample that had a dual interface failure. Fig. 11(c) shows the reference TPU substrate, which visually differs from the TPU substrate of Fig. 11(d), which has irregular adhesive residues on it. Fig. 11(e) introduces a 3-D-printed substrate from a peeled PSA tape sample. The tape has cleanly peeled from the rigid substrate and has remained on the TPU substrate in Fig. 11(f).

The dominant failure mechanism per sample series can be identified and established after visual inspection, microscope examination, and FTIR inspections. The results are categorized into three failure mode groups, which are presented in Table III.

From the observed failure modes, the epoxy adhesive-bonded and PU adhesive-bonded samples tend to have the adhesive failure on a single interface between the adhesive layer and the TPU substrate when the FR4 substrate is used. For the samples with the rough PLA substrate, adhesion failure occurred in a random manner at both interfaces of the adhesive layer.

The second failure mode pattern can be seen for the Loctite 406 CA adhesive-bonded samples with or without the primer Loctite SF 7239. Failure occurs as a cohesive failure in the adhesive layer in all the four series, despite the determined high standard deviation in the series results (of peel strength).

TABLE III
DOMINANT FAILURE MODES OF PEEL TEST SAMPLES

Adhesive	Substrate	Dominant failure mechanism	Failure type
ET515 epoxy	Solder masked FR4		
ET515 epoxy	3D-printed PLA		
MT382 epoxy	Solder masked FR4		
MT382 epoxy	3D-printed PLA		I
DP610 PU	Solder masked FR4		
DP610 PU	3D-printed PLA		
Loctite 406 CA	Solder masked FR4		
Loctite 406 CA	3D-printed PLA		
primed Loctite 406 CA	Solder masked FR4		II
primed Loctite 406 CA	3D-printed PLA		
8132LE PSA tape	Solder masked FR4		
8132LE PSA tape	3D-printed PLA		III

For all the test series, TPU film is peeled from the substrate.

The sample series with the PSA tape stand out from the structural adhesive series and lead to mainly adhesive failure at the interface between the tape and the stiff substrates that are typically deemed as unacceptable in adhesive joints. While the compliant adhesive totally remains on the TPU substrate, the strength values represented promising results. The PSA tape samples have high resistance against peeling, high bond strength, and steady debond process. The PSA tape on the fracture surface actually remains sticky after the peel testing, and it has an ability to reattach back to the surfaces.

V. DISCUSSION

The peel tests were successfully performed and carefully analyzed to understand the behavior and bond quality of different film–substrate combinations. A high elongation of the TPU film-substrate increases the elastic energy stored in the test setup during the testing. Since the TPU film primarily deforms in an elastic manner, the peel strength values are essentially anticipated correctly. However, any plastic dissipation in the film could be subtracted to provide more accurate fracture energy values, for example, for modeling purposes [32], [33]. The elasticity of the peel arm (film) is seen in Fig. 7 from the recorded peel curves. It can be assumed that the first linear increase in the curves is caused by the reversible elastic deformations in the TPU substrate [33], which changes to less steep because the elastic deformations change to irreversible plastic deformation [36].

The properties of the adhesive layers, i.e., thickness, area, and geometry, influence the load distribution in real application joints. The floating roller peel tests are clearly more demanding for the stretchable joints than their actual applications because the crack tip stresses are induced in a single planar direction. Furthermore, the TPU substrate in wearable

applications is usually laminated on a textile or other substrate, which stiffens the stretchable joint and may also increase its durability. It should be noted that there are different approaches for peel testing [32], [33]. Here, the standard preparing conditions of the samples were applied to ensure comparable results from all the sample series, but the air humidity could have affected the adhesives differently [16]—the results are specific to the selected test condition (50% RH).

A. Analysis of Failure Type I Samples

The dominant failure mode of the epoxy adhesive and the PU adhesive samples with the solder masked FR4 substrates is adhesion failure at the interface between the adhesive layer and the TPU substrate. In turn, the failure of the samples with the 3-D-printed PLA substrates is the randomly located adhesive failure on both interfaces of the adhesive layer.

The epoxy adhesives formed poor adhesion on the TPU substrate and are not a good choice for stretchable electronics joints. Between the samples, the PLA substrate samples have a slightly higher average bond strength than the FR4 substrate samples, which is explained by the failure mechanisms. The epoxy adhesive samples have the same degree of adhesion when the adhesion failure occurred along a single interface that increased when the adhesive layer was torn and the failure occurred simultaneously at both interfaces. Tearing of the adhesive layer was the phenomenon that consumed additional energy and was caused by the thickness variations of the adhesive layer.

The PU adhesive-bonded samples have a higher average bond strength than the epoxy adhesive-bonded samples, which is caused by a higher amount of adhesion between the adhesive and the TPU substrate. There were also challenges in the preparation of the PU adhesive DP610, including samples. The adhesive required seven days in total to fully dry after the manufacturer-specified time to achieve handling strength [28]. The adhesive is also sensitive to moisture [16], which causes bubbles inside the adhesive layer during curing.

B. Analysis of Failure Type II Samples

As seen in Table III, cohesive failure is the dominant failure mode of the CA adhesive-bonded samples. The conclusion is confirmed by the FTIR analysis on a microscale. Generally, cyanoacrylates cure rapidly at room temperature [16], [29]. Despite the time window of CA adhesive to achieve handling strength, the cure of the CA adhesive might have already begun before the clamping, which increases any variations in the quality of the adhesive layer. Additionally, the primer can work as an activator and accelerate the CA curing [30]. The surface topography of the stiff substrates also causes variations to the local microscale thickness of the adhesive layer. A thin adhesive layer is generally considered durable with cyanoacrylates [37].

The fast curing reaction of the CA adhesive is a disadvantage for manual bonding but can be an advantage for industrial mass production. The results indicate that the CA adhesive adheres very well on both TPU film and the stiff substrates. The adhesive could be used in the stretchable electronics joints, especially when the adhesive layer's thickness is optimized.

C. Analysis of Failure Type III Samples

The results of the samples with PSA tape stand out when comparing the structural adhesives and the failure modes. The mechanical properties of the PSA tape are closer to the properties of the TPU film than the other tested adhesives. The dominant failure mode occurs in the form of adhesive failure at the interface between the adhesive layer and the stiff substrate. However, these samples have satisfactory average bond strength values with a low standard deviation and high max displacements.

The failure mechanism allowed regular peeling of the TPU film from the PSA tape-treated samples because the PSA tape elongates rather equally with the TPU film. The challenge, in reality, with this type of result is that the peel test performance with a very high elongation does not represent well the biaxial (or even tri-axial) loadings amid real PCBs. For a real planar design, the PCB surroundings must be redesigned to allow for enhanced compliance, imitating the free edges of the slender specimens in the peel test. Fig. 1(a) shows a proposition for stretchable electronics modules design to improve the applicability and full potential of the excellent peel test results. The design uses clover-shaped PCBs, which decrease deformations of printed interconnections [10], and compliant PSA tape, which decreases the mismatch between the rigid PCB and the highly compliant substrate.

In real applications, the PSA tape can reattach after failure but cannot alone support high-quality electrical connections in the stretchable electronics joint (after bond failure). The clover-shaped module allows the contacts to be routed to each "leaf" like arm, shown in Fig. 1(b), where the PSA tape does not elongate as much at the module's edges. Moreover, compliant adhesive joints could be gradually stiffened by using the same stiffening methods that are used currently in the stretchable electronics [1], [20], [38].

VI. Conclusion

Conventional NCAs, when used in the manufacturing of rigid electronics, are not suitable as durable adhesives in stretchable electronics. NCAs are still an attractive attachment method for the stretchable electronics because of their cost-effectiveness and simplicity. In this article, the debond onset and the process of different NCAs are studied with six different adhesive test series and two different rigid-type substrates.

The results emphasize the completely different bond formation by structural adhesives and the more compliant "elastic" adhesives in the stretchable joints. The epoxy and PU structural adhesives lead to stick-slip behavior and mixed-mode failure at the glue line. An optimal level of dual interfacial failure gives the highest bond strength values for these adhesives. Moreover, the CA structural adhesives induced cohesive failure in the glue line despite highly varying bond strength values during the tests. The bond strength could be increased and made more consistent for these systems by optimizing the thickness and processing of the adhesive layer.

In contrast to the structural adhesives that resemble more rigid substrates after curing, the compliant adhesive PSA tape behaves (from the mechanical point of view) like the TPU film in the peel tests. The compatibility with the TPU film enhanced the bond strength and allowed the optimal failure process for stretchable joints. The main failure mechanism type of these samples was adhesive failure, yet the peel strength and displacement of the compliant adhesive series were among the best of the total test series.

The compliant adhesive joints, with different levels of target deformability, could be used to increase the elongation of a stretchable electronics structure. PSA tape-type adhesives can be used to bond rigid islands with clover-shaped modules to apply the full potential of highly compliant interfaces and the results by standard peel testing. Clearly, the overall planar shaping of PCB joints is needed to increase the durability of joints with extensive deformations.

ACKNOWLEDGMENT

The authors would like to thank researchers O. Orell and S. Siljander for their assistance with the testing activities.

REFERENCES

[1] N. Matsuhisa *et al.*, "Printable elastic conductors with a high conductivity for electronic textile applications," *Nature Commun.*, vol. 6, no. 1, Nov. 2015, Art. no. 7461.

[2] F. Bossuyt, T. Vervust, and J. Vanfleteren, "Stretchable electronics technology for large area applications: Fabrication and mechanical characterization," *IEEE Trans. Compon., Packag., Manuf. Technol.*, vol. 3, no. 2, pp. 229–235, Feb. 2013.

[3] T. Someya, Ed., *Stretchable Electronics*. Weinheim, Germany: Wiley, 2012, p. 462.

[4] M. Mosallaei *et al.*, "Geometry analysis in screen-printed stretchable interconnects," *IEEE Trans. Compon., Packag., Manuf. Technol.*, vol. 8, no. 8, pp. 1344–1352, Aug. 2018.

[5] R. Vieroth *et al.*, "Stretchable circuit board technology and application," in *Proc. Int. Symp. Wearable Comput.*, Linz, Austria, Sep. 2009, pp. 33–36.

[6] T. Araki, M. Nogi, K. Suganuma, M. Kogure, and O. Kirihara, "Printable and stretchable conductive wirings comprising silver flakes and elastomers," *IEEE Electron Device Lett.*, vol. 32, no. 10, pp. 1424–1426, Oct. 2011.

[7] A. Jahanshahi, P. Salvo, and J. Vanfleteren, "Stretchable biocompatible electronics by embedding electrical circuitry in biocompatible elastomers," in *Proc. Annu. Int. Conf. IEEE Eng. Med. Biol. Soc.*, San Diego, CA, USA, Aug. 2012, pp. 6007–6010.

[8] P. Foerster, C. Dils, C. Kallmayer, T. Loher, and K.-D. Lang, "First approach to cost-efficient fine pitch NCA flip-chip assembly on thermoplastic polyurethane printed circuit boards," in *Proc. 4th Electron. Syst.-Integr. Technol. Conf.*, Amsterdam, The Netherlands, Sep. 2012, p. 6.

[9] C. Goth, "Connection mediums," in *Three-Dimensional Molded Interconnect Devices (3D-MID)*, J. Franke, Ed. Munich, Germany: Carl Hanser Verlag GmbH & Company KG, 2014, pp. 143–148.

[10] P. Iso-Ketola, J. Vanhala, and M. Mäntysalo, "Extensible construction comprising a conductive path and method of manufacturing the structure," Google Patent FI 127 173 B, Dec. 29, 2017.

[11] W. A. Hufenbach, F. Adam, T. Möbius, D. Weck, and A. Winkler, "Experimental investigation of combined electrical and mechanical joints for thermoplastic composites," in *Proc. Tech. Conf. Exhib. (ANTEC)*, Las Vegas, NV, USA, Apr. 2014, pp. 592–595.

[12] A. Mehmann, M. Varga, and G. Tröster, "Reversible contacting for smart textiles," in *Smart Textiles*, S. Schneegass and O. Amft, Eds. Cham, Switzerland: Springer, 2017, pp. 185–198.

[13] E. E. M. Noor, H. Zuhailawati, and O. J. Radzali, "Low temperature In-Bi-Zn solder alloy on copper substrate," *J. Mater. Sci., Mater. Electron.*, vol. 27, no. 2, pp. 1408–1415, Feb. 2016.

[14] R. J. Good, "Semantic physics of adhesion," in *Treatise on Adhesion and Adhesives*, vol. 5, R. L. Patrick, Ed. New York, NY, USA: Marcel Dekker, 1981, p. 295.

[15] F. M. da Silva, A. Öchsner, and R. D. Adams, Eds., *Handbook of Adhesion Technology*. Berlin, Germany: Springer, 2011, p. 1554.

[16] F. C. Campbell, "Adhesive bonding," in *Joining—Understanding the Basics*, F. C. Campbell, Ed. Ohio, OH, USA: ASM International, 2011, pp. 243–277.

[17] M. M. Feldstein, E. E. Dormidontova, and A. R. Khokhlov, "Pressure sensitive adhesives based on interpolymer complexes," *Progr. Polym. Sci.*, vol. 42, pp. 79–153, Mar. 2015.

[18] D. A. Dillard, "Stress distribution: Bond thickness," in *Handbook of Adhesion*, D. E. Packham, Ed., 2nd ed. Chichester, U.K.: Wiley, 2005, pp. 494–496.

[19] *Adhesives. Designation of Main Failure Patterns*, document SFS-10365, Finnish Standards Association, Helsinki, Finland, 1995.

[20] I. M. Graz, D. P. J. Cotton, A. Robinson, and S. P. Lacour, "Silicone substrate with *in situ* strain relief for stretchable thin-film transistors," *Appl. Phys. Lett.*, vol. 98, no. 12, Mar. 2011, Art. no. 124101.

[21] I. Chtioui, F. Bossuyt, and M. H. Bedoui, "Thermo-plastically stretchable electronic and sensor circuits," in *Proc. 17th Int. Conf. Electron. Packag. Technol. (ICEPT)*, Wuhan, China, Aug. 2016, pp. 1396–1400.

[22] H. Joodaki and M. B. Panzer, "Skin mechanical properties and modeling: A review," *Proc. Inst. Mech. Eng., H, J. Eng. Med.*, vol. 232, no. 4, pp. 323–343, Apr. 2018.

[23] J. M. Benítez and F. J. Montáns, "The mechanical behavior of skin: Structures and models for the finite element analysis," *Comput. Struct.*, vol. 190, pp. 75–107, Oct. 2017.

[24] M. Mosallaei, J. Jokinen, M. Kanerva, and M. Mäntysalo, "The effect of encapsulation geometry on the performance of stretchable interconnects," *Micromachines*, vol. 9, no. 12, p. 645, Dec. 2018.

[25] H. Varner, J. Mahaffey, T. Marinis, and C. DiBiasio, "Encapsulation of microelectronic assemblies for use in harsh environments," in *Proc. Int. Symp. Microelectron.*, no. 1, Oct. 2017, Art. no. 000292.

[26] *Permabond ET515 Technical Datasheet*, Permabond LLC, Pottstown, PA, USA, Oct. 2016.

[27] *Permabond MT382 Technical Datasheet*, Permabond LLC, Pottstown, PA, USA, Feb. 2018.

[28] *Scotch-Weld EPX Clear Adhesive DP610 Product Data Sheet*, Suomen 3M Oy, Espoo, Finland, 2011.

[29] *Loctite 406 Technical Data Sheet*, Henkel, Düsseldorf, Germany, Feb. 2012.

[30] *Loctite SF 7239 Technical Data Sheet*, Henkel, Düsseldorf, Germany, Oct. 2015.

[31] *3M Adhesive Transfer Tape 8132LE*, 3M, Saint Paul, MN, USA, 2019.

[32] B. A. Morris, "Fracture mechanics analysis of peel test," in *Science and Technology of Flexible Packaging*, B. A. Morris, Ed. Oxford, U.K: William Andrew, 2017, pp. 354–360.

[33] M. Nase, B. Langer, and W. Grellmann, "Fracture mechanics on polyethylene/polybutene-1 peel films," *Polym. Test.*, vol. 27, no. 8, pp. 1017–1025, Dec. 2008.

[34] J. S. Gaffney, N. A. Marley, and D. E. Jones, "Fourier transform infrared (FTIR) spectroscopy," in *Characterization of Materials*, E. N. Kaufmann, Ed., 2nd ed. New York, NY, USA: Wiley, 2012, pp. 1104–1135.

[35] J. M. Chalmers, "Mid-infrared spectroscopy: Anomalies, artifacts and common errors," in *Handbook of Vibrational Spectroscopy*, J. M. Chalmers and P. R. Griffiths, Eds. Hoboken, NJ, USA: Wiley, 2006, pp. 2327–2347.

[36] A. J. Kinloch and J. G. Williams, "The mechanics of peel tests," in *Adhesion Science and Engineering*, vol. 1, D. A. Dillard, A. V. Pocius, and M. Chaudhury, Eds. Amsterdam, The Netherlands: Elsevier, 2002, pp. 273–301.

[37] B. Goss, "Cyanoacrylates," in *Practical Guide to Adhesive Bonding of Small Engineering Plastic and Rubber Parts*, B. Goss, Ed. Shawbury, U.K.: ISmithers, 2010, pp. 1–8.

[38] N. Karyu, M. Noda, S. Fujii, Y. Nakamura, and Y. Urahama, "Effect of adhesive thickness on the wettability and deformability of polyacrylic pressure-sensitive adhesives during probe tack test," *J. Appl. Polym. Sci.*, vol. 133, no. 27, p. 11, Jul. 2016.

PUBLICATION
II

Enhanced stretchable electronics made by fused-filament fabrication

Salo T., Halme A., Lahtinen J., Vanhala J.

Flexible and Printed Electronics, vol. 5, no. 4, 045001
https://doi.org/10.1088/2058-8585/abb931

Publication is licensed under a Creative Commons Attribution 4.0 International License CC-BY-NC-ND

IOP Publishing Flex. Print. Electron. 5 (2020) 045001 https://doi.org/10.1088/2058-8585/abb931

Flexible and Printed Electronics

OPEN ACCESS

RECEIVED
28 May 2020

REVISED
3 September 2020

ACCEPTED FOR PUBLICATION
16 September 2020

PUBLISHED
9 October 2020

Original content from this work may be used under the terms of the Creative Commons Attribution 4.0 licence.

Any further distribution of this work must maintain attribution to the author(s) and the title of the work, journal citation and DOI.

PAPER

Enhanced stretchable electronics made by fused-filament fabrication

Teemu Salo, Aki Halme, Juhani Lahtinen and Jukka Vanhala

Information Technology and Communication Sciences, Tampere University, Tampere, Finland

E-mail: teemu.salo@tuni.fi

Keywords: 3D printing, printed electronics, stretchable electronics, wearable electronics

Abstract

3D printing is widely used for manufacturing complex non-functional parts, and recently, the fabrication of electronics has also attracted research attention. The commercialized process of fused-filament fabrication (FFF), which is still evolving,has been used in the preparation of basic electronic conductors and sensors but only a few studies of more complex structures with integrated circuits and passive components have been reported. Notably, the usage of FFF in wearable stretchable electronics has not been studied previously. We demonstrate that the combination of FFF printing and commonly used stretchable electronics materials and methods enables new wearable stretchable electronics. In this study, thermoplastics were extruded directly onto a stretchable substrate and their adhesion was measured using T-peel tests. The test results were further used in the fabrication of supports for meander-shaped screen-printed interconnects. The elongation of the interconnects with the supports were studied by tensile tests with simultaneous measurements of the electrical conductivity. The results were good, and the adhesion exceeded the constitution of the substrate when the filament and the substrate were of the same material type. The average bond strength was $\sim$2 N mm^{-1}. Support structures placed close to the meander-shaped interconnects changed the interconnects' deformation under elongation. The average maximum elongation of the interconnects was improved by $\sim$27% when the supports directed stresses away from the interconnects' weak areas. Conversely, the results were $\sim$21% lower when the supports directed stresses towards the weak areas. This study demonstrates that it is possible to use direct 3D printing onto highly stretchable substrates. Currently, commercial FFF materials and methods can be used to manufacture supports, frames and other non-functional parts on wearable electronics substrates in a single process step. We believe that in the future, FFF will become a valuable tool in the manufacture of inexpensive and reliable wearable electronics.

1. Introduction

In a normal process flow for manufacturing rigid and flexible PCBs, screen printing is used to pattern interconnects and dielectric layers onto a substrate. In addition to normal rigid and flexible substrates, interconnections are now also fabricated on highly stretchable substrates [1]. However, the use of stretchable substrates has introduced new adhesion and stress concentration issues [2]. In particular, the attachment of rigid electronic modules and components to highly stretchable plastic substrates has proved difficult [3]. In addition, the stress concentrations at the interconnections and the electrical contacts between the conductor and the modules cause reliability problems [4].

In this paper, we show how manufacturing methods based on 3D printing can be used to improve the realiability of stretchable electronics. 3D printing allows the easy fabrication of complex module geometries and support structures for interconnects. The available literature describes many approaches for 3D-printed electronics, but no practical application in the domain of wearable stretchable electronics with fused-filament fabrication (FFF) has been presented [5–10].

© 2020 The Author(s). Published by IOP Publishing Ltd

1.1. 3D-printed electronics

At present, sensors and electrical structures are successfully integrated into pliable polydimethylsiloxane and thermoplastic polyurethane (TPU) systems by the direct ink writing (DIW) method [5, 6]. The structures fabricated in this way have high maximum elongations but the method is not suitable for pliable multilayered elements and the components require an additional heat treatment to solidify the inks and elastic materials.

In addition, stereolithography (SLA) is used in the fabrication of 3D printed electronics. Micro-sized components, such as coils, can be prepared by a modified two-photon SLA method [7]. SLA is also combined with the DIW method to produce multichip modules [8]. These methods can produce accurate and rigid 3D printed electronics on rigid substrates, which could be used as modules in stretchable electronics.

Totally new 3D-printing setups have also been prepared for 3D printed stretchable electronics. For example, gallium-based liquid metal is coprinted with flexible silicon material to make elastic conductors and components [9]. Inflatable silicone membranes, which can work as elastic substrates for stretchable electronics, can be printed on an air-permeable mandrel [10]. However, these setups are still at the development stage; working with liquid metal is inconvenient, components are bulky and inert silicon materials can make the assembly of stretchable systems difficult.

1.2. Direct 3D printing

In this paper, we propose a novel direct 3D printing method for attaching polymer-based supports, PCB islands and other similar structures to a stretchable substrate, which utilizes the widely used FFF method and common additive manufacturing materials. In this method, an FFF machine is used to place a molten polymer material directly onto a stretchable substrate. With this method, the supports for interconnects, frames and mountings for rigid PCB islands can be made easily and cost-effectively using existing non-conductive polymers. Also, multimaterial FFF printing, which can be applied for single-step fabrication of PCB islands on a stretchable substrate, has been used to create bendable wearable electronics [11]. This method is straightforward compared to most other current stretchable electronics manufacturing methods, and takes advantage of the versatility of additive manufacturing processes to form complex 3D structures instead of common planar designs [10].

There are several things which we believe this method will accomplish:

(a) The adhesion between the melted printing material and the stretchable substrate must be strong enough. In the optimal case, the bonding strength would be better than the constitution of the substrate itself.
(b) The placement of structures on the substrate must be accurate and reliable. For example, damage to screen-printed interconnects must be avoided when placing structures on the substrate.
(c) This method allows the fabrication of complex geometries to tackle stress concentration issues on the substrate.

As described in this paper, peel tests were used to test the adhesion between the substrate and direct printed materials. The placement of structures by an FFF printer was also tested by printing support structures for shaped stretchable interconnects. Furthermore, different shapes of support structures were prepared to study how they affect the reliability of the interconnects.

1.3. Support structures for stretchable interconnects

There are two common ways to prepare stretchable interconnects on a highly stretchable substrate: screen printing with stretchable conductive ink and using methods from flexible PCB manufacturing to pattern copper foil onto a stretchable substrate. Screen printing with conductive ink enables simple and short interconnects that can have high elongations [12]. The structures and shapes of ink interconnects crack and induce high relative resistance changes due to strain, which prevents their use in sensitive measurement applications such as bioimpedance lead wires. As the whole structure of the interconnect elongates, the shapes of the interconnects can induce stress concentration and irregular deformations, finally decreasing maximum elongations [13].

The other way to make strechable interconnects is to adhere copper film onto a stretchable substrate and etch it to create meander-shaped interconnects [14]. The copper interconnects have a small and stable resistance increase under elongation because the meander opens and twists, and the conductor itself does not elongate. However, copper interconnects do not elongate as much as ink interconnects and their multi-stage preparation process is complicated.

Thanks to the direct 3D-printing method, it is possible to combine the best properties of the ink and copper interconnects and produce supported meander-shaped silver ink interconnects. The support structures are directly and additively manufactured alongside the interconnects and guide deformations for more regular stretchability.

2. Methods

2.1. Materials

In this work, 100 μm-thick TPU film is used as a substrate. Initially, a TPU film (Platilon® U 4201AU by

Table 1. 3D-printed materials and the printing temperatures of the peel samples.

Trade name and manufacturer	Polymer	Nozzle temperature (°C)
nGen, colorFabb	copolyester (CPE)	235
Nylon, Ultimaker BV	polyamide (PA)	260
TPU95A, Ultimaker BV	TPU	240
TPU95A, Ultimaker BV	TPU	260

Covestro) was tested and found to be suitable. However, in practice, the temperature of the heated building plate of the 3D printer affected the TPU film and caused softening and swelling of the film. The softening improves the formation of adhesion between the film and the 3D-printed polymer, but the swelling makes the film unevenly wavy and unsuitable for the process. Therefore, a carrier film is needed to keep the TPU film even and stable in the printing process. A TPU film (Platilon® U U073 by Covestro), which has a 100 μm thick TPU film with a carrier film is used as the substrate. Furthermore, the original polyethylene (PE) carrier film is replaced by a thermally stable polyethylene terephthalate film.

The four materials directly 3D printed onto TPU films are presented in table 1, which introduces the 3D-printing filaments used, their compositions and process temperatures (nozzle temperatures).

Copolyester (CPE) and polyamide (PA) filaments are common 3D-printing plastics which have good mechanical properties and are used for more demanding applications. Also, TPU95A is a natural choice for the direct printing because it is based on the same polymer as the film. The recommended printing temperature for TPU95A is 240 °C, but 260 °C can also be used for better adhesion.

In addition to the direct 3D printing, meander interconnects are screen printed onto the film by a screen printer (DEK 248) using conductive silver ink (CI-1036 by ECM). For each sample, the screen printer squeezes the ink twice through the screen using 14 kg of pressure. The ink is heat treated in an oven (30 min at 125 °C) following the screen printing to make the ink conductive [1, 13].

2.2. Preparation of samples

All the test samples are direct printed on the TPU film with an FFF printer (Ultimaker 3 by Ultimaker BV). The film is placed on a heated build plate (80 °C), whose temperature straightens the film, adheres the film temporarily to the build plate and assures sufficient bonding between the film and 3D printed polymer. The thickness of the film is taken into account by setting the z offset value to 0.17 mm in the slicer program used (Cura v. 4.0.0. by Ultimaker BV). Moreover, a 0.4 mm nozzle and a 0.15 mm layer thickness is used in the samples' printing.

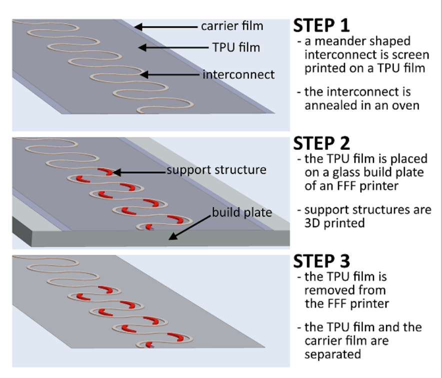

Figure 1. The three preparation steps of the support structure sample.

The T-peel test samples are based on the SFS-EN ISO 11 339 standard. The length of the samples is 210 ± 1 mm and the width is 25 ± 1 mm. The samples consist of two substrates, the film and the directly 3D-printed bar, which together have 160 ± 1 mm of bonded area and 50 ± 1 mm of separated area. The separated area is made by adding Kapton tape to the TPU film before printing. The thickness of the 3D-printed bar is 0.5 mm, which varies slightly because of the different properties of polymers. The bar is 3D printed with 100% infill density with a rectilinear 45° infill pattern.

In addition, support structures for screen-printed interconnects are 3D printed on the film. The length of the samples is 150 ± 1 mm and the width is 40 ± 1 mm. The meander-shaped interconnects are 1 mm wide, 140 mm long (straightened length ~310 mm) and have a 30° turn between meanders. The 0.3 mm-thick support structures are 3D printed with TPU filament (Ultimaker TPU95A) using a 260 °C nozzle temperature, in order to produce stiff but still pliable supports. The measured initial resistance of the interconnects before the tensile tests is 10.7 ± 1.3 Ω. Various factors, such as the interconnects' thickness and process steps, affect the resistance. In screen printing, the thickness of the interconnects depends on the heat treatment and the roughness of the substrate. A small (±3 μm) thickness variation can be present for smooth substrates such as plastic films [15]. In the tests, the screen-printed interconnects can also be affected by the 3D-printing process and the removal of the carrier film after the 3D printing. For example, an average increase of 3.2% of the resistance was observed after the carrier film was removed in the final preparation step. Figure 1 presents the preparation steps of the tensile test samples.

Altogether four series of meander samples (with six parallel samples) are tested, one unsupported and three supported, as presented in figure 2. The support

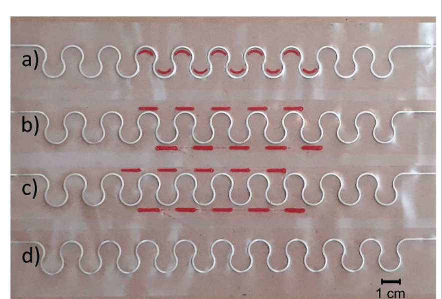

Figure 2. Direct 3D-printed support structures on the screen-printed TPU film. (a) Curved support inside the meanders. (b) straight support outside the meanders. (c) straight support in the space between the meanders. (d) unsupported meanders.

structures in figures 2(a) and (b) are designed to toughen the meanders' peaks and figure 2(c) to stiffen the unprinted TPU between the meanders. During the interconnects' elongation, stress concentrates on top of the meanders [16], and it is assumed that the support structures close to the meanders' peaks decrease the stress concentration effect and improve the maximum elongation of interconnects.

For comparison, two conventionally shaped straight interconnect samples (2 mm wide and 140 mm long) are also screen printed and tested to see the electrical differences due to the different interconnect shapes. The initial resistance of the straight interconnects is 2.8 Ω.

2.3. Peel tests

In the tests, a tensile test machine with a 500 N force cell is used (Tinius Olsen H5KT). The machine measures the force (N) and the displacement of the upper grip during the tests (mm). The peel test samples are tested using the tensile test machine with 100 mm min^{-1} speed, 70 mm gauge length and a 1.0 N preload. The displacement limit of the peel tests was 450 mm, which was defined by the height of the tensile test machine. The machine is equipped with 50 mm-wide tacky-film jigs, which prevent the samples from slipping during the tests.

The results of the peel tests provide the bond strength of the samples (N/mm), which was calculated as the measured force divided by the width of the samples. The test series consisted of five parallel samples, and in the comparison, the average maximum bond strength of each test series and the failure mechanisms are analyzed.

2.4. Tensile tests of reinforced printed interconnects

The effect of shaped support structures on the maximum elongation of the interconnects is tested using the tensile test setup, which is presented in figure 3. In the tests, the test speed used was 100 mm min^{-1}, the gauge length was 100 mm and the extension limit was 200 mm. While the tensile test machine measured mechanical properties of the samples, a two-wire measurement system (iCraft ADC 4x by iCraft Oy, Tampere, Finland) measured the electrical properties of the interconnects. The system used a 24-bit A/D channel and measured the voltage across the samples to calculate the resistance of the interconnects. The tensile tests were carried out until the resistance of the samples increased rapidly, which indicated critical failure of the interconnects. The system was calibrated to have less than a ±2% error over the whole measurement range of 0–3000 Ω. The sample was compressed between two PCBs in order to form a stable low-resistance connection.

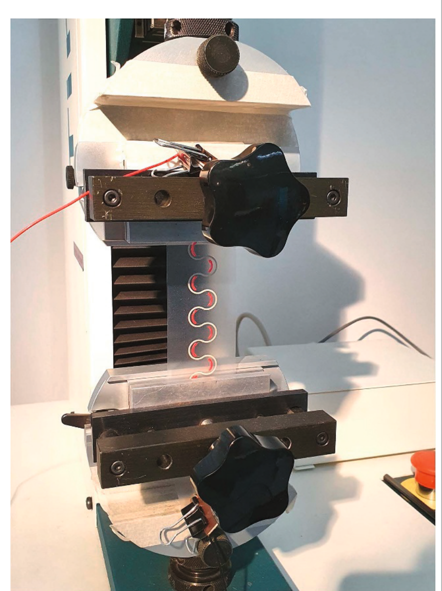

Figure 3. The tensile test setup. The upper and lower sides of the sample are connected to probes with two PCBs and clamps. The probes are connected to the iCraft measurement system, which measures the electrical behaviour of the sample.

3. Results

3.1. Peel tests

The results of the T-peel tests are presented in table 2 and figure 4, where the CPE and PA sample series have lower average maximum bond-strength values (under 1 N mm^{-1}) compared to the TPU95A sample series values (between 1.5–2.0 N mm^{-1}). The bond-strength values are complemented by the prevailing failure mechanisms and peeling behaviors of the sample series, which are visualized in figure 5.

In the adhesion failure of the peel test samples, the TPU film peels from the direct 3D-printed bar, which is the most typical failure mechanism in the CPE, PA

Table 2. Peel tests' results.

Sample series	Average maximum bond strength and standard deviation (N mm^{-1})	Dominant peeling behavior	Dominant failure mechanism
CPE (235 °C)	0.78 ± 0.08	Steady	Adhesion failure
PA (260 °C)	0.85 ± 0.05	Jerky	Adhesion failure
TPU95A (240 °C)	1.70 ± 0.21	Steady	Adhesion failure
TPU95A (260 °C)	1.88 ± 0.03	Steady	Substrate failure (of TPU film)

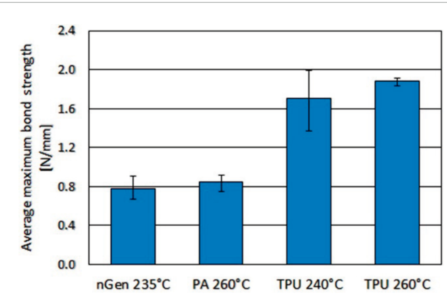

Figure 4. Average maximum bond strength (N/mm) and range of the T-peel samples.

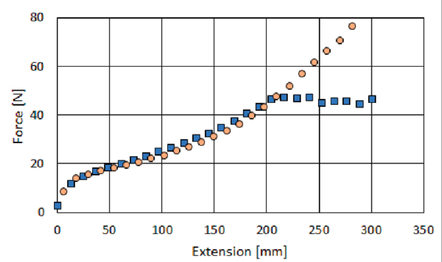

Figure 6. Comparison of a TPU95A peel test (square blue curve) and a tensile test of the TPU film (round orange curve). The curves' points represent every thirtieth measurement point.

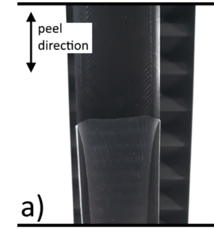

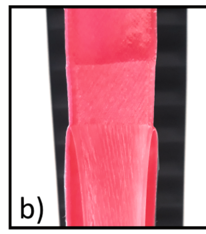

Figure 5. T-peel test samples in the peel tests. (a) PA peel sample that has low adhesion between the TPU film and the direct printed PA bar. The TPU film has pale stripes, which reveal locally higher elongations and adhesion forces in the peeling. (b) TPU95A (260 °C) peel sample before breaking of the film. The film and substrate have distinctly deformed.

and TPU95A (240 °C) sample series. After the start of peeling, the peeling is steady in the CPE and TPU95A (240 °C) sample series. The PA sample series peels unevenly in jerks, which leaves deformed pale stripes in an otherwise clear TPU film figure 5(a).

The TPU95A (260 °C) sample series has the highest average maximum adhesion with 1.88 N mm^{-1} of bond strength and an unpredictable failure mechanism. The TPU film is tightly bonded to the 3D-printed bar and at some point in the peeling process, the film breaks instead of continuing to peel. figure 5(b) shows the TPU95A (260 °C) sample before the breaking of the film, when the surface of the 3D-printed bar is ripped and the TPU film is deformed and elongated. The breaking of the film indicates that the strength of the 3D-printed TPU filament is higher than the constitution of the TPU film, thus the bond area of the components is stronger than the TPU film itself.

The TPU film elongates during the peeling, which especially affects the peeling of the more durable TPU95A sample series. To verify the elongation's effect, the beginnings of the peel curves are compared to a tensile test of a bare TPU film, with a gauge length of 35 mm (the length of the TPU film in the peel tests) in figure 6.

As figure 6 shows, the beginning of the peel test of the TPU95A sample series has a gradual increase of force, which resembles the tensile test of the TPU film. In other words, the TPU95A samples have a high enough adhesion to first make the TPU film elongate before the peeling starts.

3.2. Tensile tests

In the tensile test results of the reinforced printed interconnect samples in figure 7, the effects of the different support structures on the interconnects' elongation can be seen. The unsupported meander interconnect samples have, on average, a 35.4% maximum elongation before electrical failure takes place. When bar-shaped supports are added between the meanders (figure 2(c)), the average maximum elongation drops to 29.1%, which is 20.7% lower than the unsupported samples. Correspondingly, the bar supports outside the meanders (figure 2(b)) increase the average maximum elongation to 42.9%, but they also increase the range between the samples. Also, the curved support samples (figure 2(a)) improve the elongation, and the series has an average maximum elongation of 45.3% with a small range. Compared to the unsupported

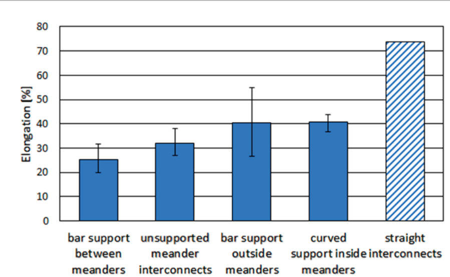

Figure 7. The average maximum elongation (%) and the ranges of the tensile test samples before interconnect failure. As a comparison with the meander interconnects, the patterned column shows the straight interconnects' results.

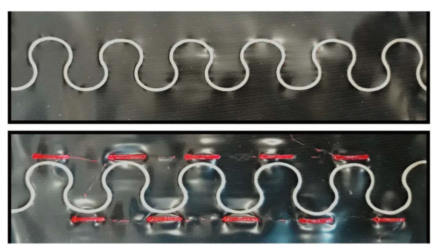

Figure 9. The unstretched unsupported meander interconnect versus the stretched supported interconnect. As the unstretched interconnect is 6 meanders long, the stretched interconnect is 5,5 meanders long. The stretched sample has elongation residues, which are seen from the length of the interconnect and wrinkled film around the 3D-printed supports.

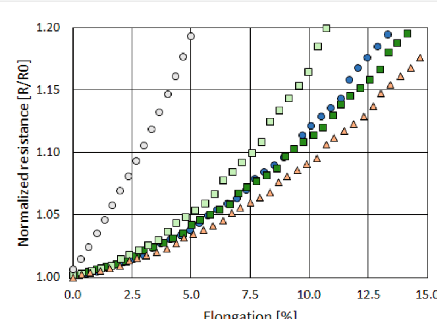

Figure 8. Initial resistance development of tensile test samples. The curves' points present every fifth measurement point. The curves from the largest normalized resistance change to the smallest are: the straight interconnects (light gray circles), bar support between meanders (light green squares), the unsupported meander interconnects (dark blue cirrcles), bar support outside meanders (dark green squares) and curved support inside meanders (light red triangles).

sample series, the bar supports outside the meanders have 26.2% and the curved support samples have 27.3% higher average maximum elongation.

figure 7 also presents the scale of difference between straight and meander-shaped interconnects. The meander interconnects' average maximum elongation is 35.4%, and the straight interconnects' average elongation is 73.7%. The difference between interconnects can also be seen in figure 8.

3.3. Resistance development of interconnects

figure 8 presents the interconnect support samples' initial resistance changes in the tensile tests. The results for the meander-shaped interconnects follow the average maximum elongation results (figure 7). The series with bar supports outside the meander (figure 2(b)) and the curved support (figure 2(a)) sample series have a lower resistance increase than the unsupported samples (figure 2(d)), which indicates a more even elongation of interconnects. The series with bar support between the meanders (figure 2(c)) has a higher resistance increase than the unsupported series, which points to unstable elongation of the shaped interconnects.

figure 8 also shows the resistance increase of the straight interconnects, which differs from the meander interconnects. The straight interconnects' resistance increase has a distinctly steeper positive curve than the unsupported meanders', despite the high maximum elongation in figure 7.

It should be noted that the straight interconnects have a distinctly lower initial resistance than the meander-shaped interconnects, which is caused by the larger width and shorter length of the interconnects.

3.4. Interconnects' deformations under elongation

The sample series have different resistance developments under elongation, which are presented in figures 7 and 8. This phenomenon is caused by deformations in the TPU film and the interconnects, which are shown in figures 9 and 10.

During the tensile test, the TPU film and the interconnect on it elongates unevenly, due to stiffer support structures. figure 9 presents the unelongated unsupported sample and the elongated supported sample, which differ distinctly. The TPU film of the unsupported sample is smooth, but the elongated support sample has wrinkles around the supports, which are caused by residual strain. The wrinkles indicate that the TPU film and the meander interconnect have elongated less closer to the supports.

As the meanders' elongation is based on the stretching and cracking of the conductive ink, the supports' effect on the interconnect's elongation can be seen as divergent cracking of the conductive ink, which is shown in figure 10.

figure 10 presents close-ups from areas between two meanders from all the elongated test series that are shown in figure 2. figure 10(a) shows the unsupported test series, and figure 10(b) presents the sample series with straight supports between the

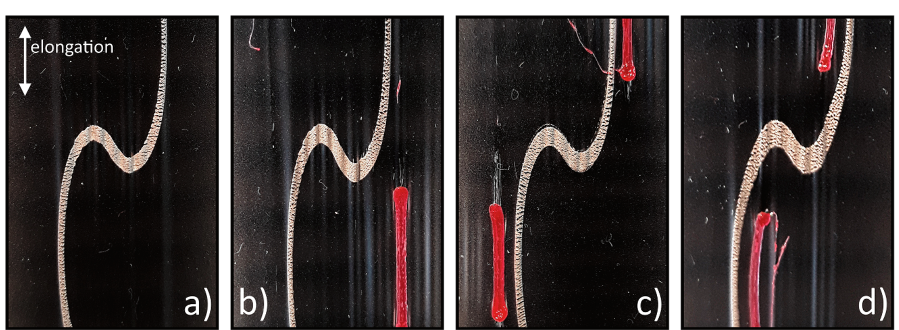

Figure 10. The area between two elongated meanders of the interconnect samples. (a) The unsupported meanders have elongated evenly from the tips of the meanders. (b) Bar supports between the meanders induce higher elongations in the meanders' tips. (c) Bar supports outside the meanders have changed the meanders' elongation. Close to the middles of the supports, the interconnects are denser and closer to the supports' edges and the interconnects have cracked more and thus elongated more. (d) Curved supports smooth the elongation of the interconnects and change the shapes of the elongated interconnects a little bit.

meanders. figure 10(c) shows the straight-support test series with supports just outside the meanders. Finally, figure 10(d) presents the curved-support test series, which had the highest maximum average elongation.

4. Discussion

4.1. Peel tests

Good adhesion between the additively manufactured materials and the stretchable film is a basic requirement for direct 3D-printed stretchable electronic structures. As figures 4, 5 and table 2 present, the TPU95A filament can form a proper bond with the TPU film, which leads to the TPU film's failure before the joint's failure. The filament's adhesion is on the same scale as a laminated copper film's adhesion with the TPU film, which makes the direct 3D-printed structures also usable with laminated- copper interconnects [14].

The bonding of 3D-printed plastic on a plastic film is mainly affected by same factors that influence multi-material FFF printing. In multi-material 3D printing, the material properties, process settings, geometry and environment affect the formation of an interface between two plastics [17]. In particular, diffusion and mechanical interlocking adhesion theories should be applied, which can be improved by increasing the thermal energy radiated and optimizing the surface roughness and geometries of the printing process [17].

In direct 3D printing on a 'semi-manufactured' stretchable substrate, the main method for adhering a 3D printed plastic to a film is based on diffusion theory and the polymer chain mobility at the interface between two polymers. The amount of diffusion is easily controlled in 3D printing by varying the time and temperature of the 3D printing process.

In addition, the first layer of the printed pattern shapes the TPU film, and the pattern can be optimized according to mechanical interlocking theory.

Conventionally solid structures are fabricated on stretchable films using adhesives. The majority of adhesives form a polymeric composition after curing [18]. Different kinds of adhesives have been studied for use in stretchable electronics joints, and the durable bonding of rigid and highly pliant substrates has been found challenging [19]. The removal of the requirement for adhesive is a major benefit of the direct 3D-printing method, which considerably simplifies the fabrication process and improves the stretchability of the system.

4.2. Tensile tests

The tensile tests of supported interconnects showed that directly 3D-printed structures close to screen-printed interconnects can be used to affect the durability of interconnects. Based on the results, the interconnects start to crack from the meanders' tops, and the cracks propagate towards intersections of the meanders. 3D-printed support structures can be used to create stiffened areas on the stretchable film, and they can be placed close to the meanders' tops to make the film's unsupported areas elongate first. The supports can be placed either outside or inside the meanders to stiffen the meanders' top areas. Under elongation, the meanders straighten, which induces tensile stresses in the inside areas and compressive stresses in the outside areas of the meanders. The high stiffness difference between an interconnect material and the stretchable substrate promotes stresses in the meanders, which should particularly be considered in the case of laminated-metal interconnects [20]. Based on the tensile test results, it is more effective to place 3D printed supports inside meanders to prevent tensile stresses in the interconnects.

Overall, the elongations of screen-printed meander-shaped interconnects were lower than assumed, and the unsupported meanders' average maximum elongation was 35.4%. For future work, it would be interesting to prepare curved support structures inside the meanders for optimized meander interconnects with 0° turns [21]. The optimized screen-printed meander interconnects' properties would be somewhere in between the commonly used screen printed unshaped interconnects and laminated-metal-film meander interconnects. The screen printed meander interconnects have a low relative resistance change in figure 8, which makes them a good option for sensing applications, compared to non-shaped screen-printed interconnects or laminated-metal-film interconnects.

It should also noted that the support structures were fabricated with simple planar designs as a proof of concept. Currently, most preparation methods in stretchable electronics use planar designs, which can be replaced with 3D printing. The thicknesses, shapes and locations of direct 3D-printed structures on a stretchable substrate can easily be modified, which makes local control of the elongation of the stretchable substrate possible. As conductive plastics and inks are developed and used, 3D printing can combine several process steps and 3D-printed electronic modules can be made on a stretchable substrate by a single-step method. With recent inventions, such as clover-shaped modules, new customizable and durable wearable electronics can be created [22].

4.3. Interconnects' deformations under elongation

In figure 10, elongated interconnect areas can be seen between two meanders in the four tensile test series. figure 10(a) shows the unsupported meander interconnect, which has a typical elongation mechanism. The interconnect cracks from the tips of the meanders, and the cracks progress evenly towards the transition area of the meanders. The meanders flatten and become thinner when the elongation increases, and finally the cracks in the tips of the meanders break the interconnect.

figure 10(b) presents the bar support between the meanders, which decreased the interconnects' elongation. The bar-shaped supports locally decrease the elongation of the TPU film around them, but, on the contrary, the space between the supports has large elongations induced. The supports are placed so that the meanders' tips are just between them, which stretches and straightens the meanders more than in the unsupported sample.

Straight support samples just outside the meanders affected the cracking of the meanders in figure 10(c). The supports blocked elongation in the tips of the meanders, and they have minimum cracking. However, the length of the supports was not enough to protect the whole meander, and they started to crack close to the supports' ends. This local cracking of meanders can cause random failures of interconnects, which explains the high variation of the test series in figure 7.

Curved supports inside the meanders are shown in figure 10(d). The cracking of the meanders is uniform, but the shape of the interconnect has changed a little. As the TPU film elongates more between the supports, the elongation is concentrated in the thicker transition areas of the meanders, which increases the durability of the meanders.

5. Conclusions

In the field of wearables and stretchable electronics, there are various benefits of using an FFF printer to manufacture direct printed structures on a stretchable substrate. This study introduced an easy alternative method for producing deformable supports and frames. Eventually, this work will lead to complex additively manufactured multilayer circuit boards using the multimaterial FFF method. Most importantly, the results demonstrated that the adhesion between 3D-printed TPU material and a stretchable substrate is excellent and can exceed the constitution of the substrate, which is a basic requirement for directly printed supports and other structures. In addition, the direct printing method allows the easy additive manufacture of complex geometries and accurate placement of small shapes without adhesives. Furthermore, the direct printing method is compatible with the most common materials and manufacturing methods used for stretchable electronics. The direct printed structures could be also used as platforms for electronics components.

We demonstrated the approach by direct printing several kinds of support structures for screen-printed stretchable interconnects. With the support structures, the stretchability of the interconnects improved by up to 27.3%. The support structures enable the use of meander-shaped screen-printed interconnects, which have a more stable resistance increase under elongation than traditional straight interconnects; this makes them more suitable for sensing applications, where resistance fluctuations are potential error sources.

We believe that this method will enable cost-effective manufacture for new applications in the fields of smart textiles, wearable healthcare products and automotive interior design. In the future, the authors will continue to develop direct 3D-printing methods for the fabrication of stretchable electronics for wearable applications.

Acknowledgments

This work was funded by the European Union Regional Development Fund (ERDF) and the city of Kankaanpää under the project SOFT3L (Project

A73741) and by Business Finland under the project Elastronics (Grant Nos. 2947/31/2018).

ORCID iD

Teemu Salo https://orcid.org/0000-0001-7746-0564

References

[1] Mosallaei M, Jokinen J, Kanerva M and Mäntysalo M 2018 The effect of encapsulation geometry on the performance of stretchable interconnects *Micromachines* **9** 645

[2] Graz I M, Cotton D P J, Robinson A and Lacour S P 2011 Silicone substrate with in situ strain relief for stretchable thin-film transistors *Appl. Phys. Lett.* **98** 124101

[3] Bossuyt F and Löher T 2013 Technologies and processes used in printed circuit board fabrication for the realization of stretchable electronics *Stretchable Electronics* ed T Someya (Weinhheim: VCH) pp 187–205

[4] Vanfleteren J, Gonzalez M, Bossuyt F, Hsu -Y-Y, Vervust T, De Wolf I and Jablonski M 2012 Printed circuit board technology inspired stretchable circuits *MRS Bull.* **37** 254–60

[5] Li K, Wei H, Liu W, Meng H, Zhang P and Yan C 2018 3D printed stretchable capacitive sensors for highly sensitive tactile and electrochemical sensing *Nanotechnol.* **29** 185501

[6] Valentine A D, Busbee T A, Boley J W, Raney J R, Chortos A, Kotikian A, Berrigan J D, Durstock M F and Lewis J A 2017 Hybrid 3D printing of soft electronics *Adv. Mater.* **29** 1703817

[7] Ha C W, Prabhakaran P and Son Y 2019 3D-printed polymer/metal hybrid microstructures with ultraprecision for 3D microcoils *3D Printing and Additive Manufacturing* **6** pp 165–70

[8] Bahr R, Tehrani B, Tentzeris M M and Byers K 2018 A novel integration of stereolithography and inkjet printing for multichip modules with high frequency packaging applications *IEEE 68th Electronic Components and Technology Conf.* 2498–504

[9] He Y, Zhou L, Zhan J, Gao Q, Fu J, Xie C, Zhao H and Liu Y 2018 Three-dimensional coprinting of liquid metals for directly fabricating stretchable electronics *3D Printing and Additive Manufacturing* vol **5** pp 195–203

[10] Coulter F B, Coulter B S, Marks J R and Ianakiev A 2018 Production techniques for 3D printed inflatable elastomer structures: part I-fabricating air-permeable forms and coating with inflatable silicone membranes via spray deposition *3D Printing and Additive Manufacturing* vol **5** pp 5–15

[11] Kwok S W, Goh K H H, Tan Z D, Tan S T M, Tjiu W W, Soh J Y, Ng Z J G, Chan Y Z, Hui H K and Goh K E J 2017 Electrically conductive filament for 3D-printed circuits and sensors *Appl. Mater. Today* **9** 167–75

[12] Merilampi S, Björninen T, Haukka V, Ruuskanen P, Ukkonen L and Sydänheimo L 2010 Analysis of electrically conductive silver ink on stretchable substrates under tensile load *Microelectron. Reliab.* **50** 2001–11

[13] Mosallaei M, Jokinen J, Honkanen M, Iso-Ketola P, Vippola M and Vanhala J 2018 Geometry analysis in screen-Printed stretchable interconnects *IEEE Trans. Compon. Packag. Manuf. Technol.* **8** 1344–52

[14] Löher T, Seckel M and Ostmann A 2010 Stretchable electronics manufacturing and application *IEEE 3rd Electronics System Integration Technology Conf.* 693–8

[15] Merilampi S, Laine-Ma T and Ruuskanen P 2009 The characterization of electrically conductive silver ink patterns on flexible substrates *Microelectron. Reliab.* **49** 782–90

[16] Chen S H, Shan X C, Tang W L R, Mohaime B M, Goh M H, Zhong Z W and Wei J 2017 Mechanical and electrical characteristics of screen printed stretchable circuits on thermoplastic polyurethane *IEEE 19th Electronics Packaging Technology Conf.* 1–4

[17] Freund R, Watschke H, Heubach J and Vietor T 2019 Determination of influencing factors on interface strength of additively manufactured multi-material parts by material extrusion *Appl. Sci.* **9** 1782

[18] Cope B C 2008 Adhesive classification *Handbook of Adhesion* 2nd edn ed E D Packham (New York: Wiley) pp 25–28

[19] Salo T, Halme A, Kanerva M and Vanhala J 2020 Bond strength and failure mechanisms of nonconductive adhesives for stretchable electronics *IEEE Trans. Compon. Packag. Manuf. Technol.* **10** 770–8

[20] Gonzalez M, Hsu -Y-Y and Vanfleteren J 2013 Modeling of printed circuit inspired stretchable electronic systems *Stretchable Electronics* ed T Someya (Weinheim: VCH) pp 143–59

[21] Zhong Z W, Tang R W L, Chen S H and Shan X C 2019 A study of screen printing of stretchable circuits on polyurethane substrates *Microsyst. Technol.* **25** 339–50

[22] Iso-Ketola P, Vanhala J and Mäntysalo M2017A stretchable structure comprising a conductive path and a method for manufacturing the structure*Finland Patent* FI 127173 B

PUBLICATION
III

Electromechanical Properties of 3D-Printed Stretchable Carbon Fiber Composites

Salo T., Di Vito D., Halme A., Vanhala J.

Micromachines, vol. 13, no. 10, 1732
https://doi.org/10.3390/mi13101732

Publication is licensed under a Creative Commons Attribution 4.0 International License CC-BY-NC-ND

Article

Electromechanical Properties of 3D-Printed Stretchable Carbon Fiber Composites

Teemu Salo *, Donato Di Vito, Aki Halme and Jukka Vanhala

Faculty of Information Technology and Communication Sciences, Tampere University, 33720 Tampere, Finland
* Correspondence: teemu.salo@tuni.fi

Abstract: The addition of fillers has been implemented in fused filament fabrication (FFF), and robust carbon fillers have been found to improve the mechanical, electrical, and thermal properties of 3D-printed matrices. However, in stretchable matrices, the use of fillers imposes significant challenges related to quality and durability. In this work, we show that long carbon staple fibers in the form of permeable carbon fiber cloth (CFC) can be placed into a stretchable thermoplastic polyurethane (TPU) matrix to improve the system. Four CFC sample series (nominally 53–159-µm-thick CFC layers) were prepared with a permeable and compliant thin CFC layer and a highly conductive and stiff thick CFC layer. The sample series was tested with single pull-up tests and cyclic tensile tests with 10,000 cycles and was further studied with digital image correlation (DIC) analyses. The results showed that embedded CFC layers in a TPU matrix can be used for stretchable 3D-printed electronics structures. Samples with a thin 53 µm CFC layer retained electrical properties at 50% cyclic tensile deformations, whereas the samples with a thick >150-µm CFC layer exhibited the lowest resistance (5 Ω/10 mm). Between those structures, the 106-µm-thick CFC layer exhibited balanced electromechanical properties, with resistance changes of 0.5% in the cyclic tests after the orientation of the samples. Furthermore, the suitability of the structure as a sensor was estimated.

Keywords: stretchable electronics; 3D printing; carbon fibers; electromechanical testing; strain sensor

Citation: Salo, T.; Di Vito, D.; Halme, A.; Vanhala, J. Electromechanical Properties of 3D-Printed Stretchable Carbon Fiber Composites. *Micromachines* **2022**, *13*, 1732. https://doi.org/10.3390/mi13101732

Academic Editors: Libo Gao and Zhuoqing Yang

Received: 29 September 2022
Accepted: 11 October 2022
Published: 13 October 2022

Publisher's Note: MDPI stays neutral with regard to jurisdictional claims in published maps and institutional affiliations.

Copyright: © 2022 by the authors. Licensee MDPI, Basel, Switzerland. This article is an open access article distributed under the terms and conditions of the Creative Commons Attribution (CC BY) license (https://creativecommons.org/licenses/by/4.0/).

1. Introduction

Additive manufacturing (AM) is widely used in several manufacturing sectors. Fused filament fabrication (FFF), especially, has advantages such as simplicity and cost-effectiveness [1]. For example, strain sensors [2], multiaxial force sensors [3], and batteries [4] have already been fabricated with this single-step FFF process. FFF can also be adopted in the textile field by printing plastics directly on textile substrates [5] or by printing the whole textile composition [6]. Moreover, it has been demonstrated that FFF with deformable plastics and substrates can be used in manufacturing stretchable electronics, which can be further laminated on textiles for wearable electronics [7].

Recently, 3D-printed stretchable and wearable electronics have gained more attention, and rigid [4] and stretchable wearables [8] have been successfully fabricated. Still, stretchable electronics that are practically integrable into clothing have not yet been manufactured via 3D printing. For integrable stretchable and wearable electronics, carbon-filled polymers are an especially promising alternative for the creation of mechanically complex and thermally and electrically conductive structures [2,9]. These polymers can be modified using carbon-based additives with different form factors and dimensions, such as carbon fibers [10], carbon nanotubes (CNTs) [2,3,9], carbon black [11], graphene [12], and others [13], with a wide variety of outcomes in terms of properties such as strength, thermal and electrical conductivity, piezoresistive behavior, and many others [14–16]. These modified materials enable the fabrication of sensors, wearables, and other end-products, e.g., by providing higher strength, fire retardancy, or electrical properties. However, FFF polymers with fillers generally require a high nozzle diameter to prevent clogging, decreasing the

printing quality [2] and causing highly anisotropic printing results [17]. Fillers also rapidly increase the Young's modulus of the polymers, leading to a trade-off between stiffness and conductivity [2].

In FFF polymers, the shape and size of carbon fillers influence the formation of the fillers' conductive network, percolation threshold, and overall conductivity. For example, when the results from previous studies are converted into conductivity values, acrylonitrile butadiene styrene (ABS) filament consisting of 15 wt% nano-scale carbon black has 0.025 S/m conductivity [11], and 5.6 wt% graphene flakes with a lateral size of 3–5-µm [12] provide 0.001 S/m. CNTs were mixed into thermoplastic polyurethane (TPU) filaments (with a CNT content of 4 wt%) of in 9.5 nm diameter and 1.5 µm in length, providing 32 S/m conductivity after the 3D-printing process (with a 0.6 mm nozzle) [2]. Furthermore, Tzounis et al. blended TPU and CNTs (5 wt%, 9.5 nm diameter, 3.0 µm length), which resulted in higher conductivity, approximately 100 S/m, but this required a less accurate 0.8 mm nozzle [17]. Spoerk et al. 3D-printed polypropylene (PP) filaments filled with short carbon fibers (7 µm in diameter and 250 µm in length) at proportions of up to 10 wt% with a 0.6 mm nozzle [18] for thermally conductive structures. Even longer millimeter-scale fibers can be added during the filament manufacturing process, but these are chopped to the micrometer-scale during the process [10].

Furthermore, continuous carbon fiber filaments are used in FFF by feeding them into molten-state polymers during extrusion [19,20], increasing an object's carbon fiber content. However, this process requires a larger nozzle [19,20]. Another alternative is to impregnate carbon fiber filaments before printing, enabling more complex [21] and precise [22] printing with filaments.

Feeding carbon fillers and carbon filaments through a 3D printer's nozzle makes them compatible with readily available FFF printers. Furthermore, carbon semi-products, such as laminates and inks, can be integrated into the 3D printing process semi-automatically or automatically by pausing the process. Carbon fiber sheets can be laminated on top of objects to form durable and lightweight composite structures [23] or inside them to address porosity and layer adhesion issues [13]. Moreover, integrated carbon fiber tows can be used to monitor a matrix's structural health via the tows' resistance changes [24]. Other electrical and thermal properties can be created by spray-depositing the 3D-printed surface with CNTs, and a 19-nm layer thickness on the smoothened surface is possible [25,26]. Furthermore, the direct ink writing (DIW) method can be combined with FFF to print carbon black ink electrodes for 3D printed supercapacitors [27]. The FFF process even allows the manual or automatic integration of printed circuit board (PCB) components inside an object [8], which, along with other placement methods, enables versatile 3D-printed electronics.

In this study, stretchable and wearable 3D-printed electronics components were made by adding sparse carbon fiber cloths (CFCs) inside a TPU matrix made with FFF. The advantages of this process are that CFCs with mechanical and electrical properties were (1) integrated inside the matrix without cavities or other 3D printing design modifications, and (2) adhesives were not required for their placement—it was sufficient to change the general 3D printing settings. Furthermore, CFCs embedded in this way inside the structure (3) do not decrease the adhesion between the TPU layers, and (4) they can be cut into different shapes, which can be used as functional elements in fabricating stretchable and wearable electronics. Furthermore, integrated CFCs can create (5) more isotropic and detailed objects than those created through FFF with carbon fiber filaments.

To the authors' knowledge, permeable CFC has never been used to improve the electrical and mechanical properties of FFF objects. The measured properties of CFC compare favorably to those of carbon-filler filaments and can be used to provide stretchable and conductive composite matrices. The obtained results prove that matrices with CFC can sustain large numbers of deformation cycles with minimal changes in their resistance behavior, thanks to the combined mechanical and adhesion properties of the materials involved. We studied the characteristics and advantages of this new method by conducting

quasi-static and cyclic electromechanical tests, which we further analyzed using digital image correlation (DIC) techniques to attain information about the local deformation field in the samples. Finally, the properties of the structure for sensor applications were estimated.

2. Materials and Methods

CFCs with centimeter-scale fibers are traditionally used in composite manufacturing to increase the Young's modulus of materials with a minimal increase in density, i.e., to improve the specific modulus of materials. As well as mechanical features, CFCs are thermally and electrically conductive, thus having the potential to be used in wearable electronics. The stretchability that wearable electronics require was achieved by combining sparse CFCs and a highly stretchable TPU matrix. Single pull-up tests were first used to study the mechanical properties of the CFC matrices. Then cyclic tensile tests were conducted to measure the electromechanical features. Finally, the samples' behavior was further analyzed with DIC.

2.1. Composition and Preparation of Samples

The CFCs used in this work were provided by ACP Composites [28], and the reported average single carbon fiber length was 25.4 mm. The carbon fibers were processed from polyacrylonitrile (PAN) to promote their electrochemical properties [29]. CFCs with two grades of nominal thicknesses, 0.0021″ (53 μm) and 0.006″ (153 μm), were tested. Thin CFCs were also tested as two- and three-layered plies to further improve their electrical conductivity. The single-layer CFCs and the two- and three-layered plies were laminated to make them flat and fixed together for the 3D printing process, which can decrease the nominal thicknesses of CFCs. Furthermore, plain zero samples without CFCs were tested for comparison. The composition of the carbon fiber and its nominal thickness in the electromechanical samples are presented in Table 1.

Table 1. Studied CFC compositions based on the manufacturer's data.

Series	Thickness (μm)	Weight (g/m^2)	N of Layers	Grade
1	-	-	0	-
2	53	6.8	1	800015i
3	106	13.6	2	800015i
4	159	20.3	3	800015i
5	153	17	1	800020i

A TPU filament was used as a 3D-printed backbone for the fabricated structure. TPU is a widely used material in 3D printing and stretchable electronics because of its high deformability and stability [2,3,7]. For example, TPU-based stretchable films have also been used in wearable and printed electronics in combination with screen-printable conductive silver inks. Using TPU filaments is a convenient choice for developing 3D-printed stretchable and wearable electronics because of the ease of integration in these types of systems. Blue Ultimaker TPU 95A filament (Ultimaker B.V., Utrecht, The Netherlands) by Ultimaker B.V. (nominal diameter: 2.85 mm) was used in the tests, as it is more reliable to 3D print compared to the thinner 1.75 mm diameter FFF filaments, which are prone to bend and jam during 3D printing.

A commercial Ultimaker S5 FFF printer (Ultimaker B.V., Utrecht, The Netherlands) with an official air management unit accessory, with the Cura slicer program (version 4.4.0, Ultimaker B.V., Utrecht, The Netherlands) from Ultimaker B.V., was used in the 3D printer setup. The nozzle diameter was 0.4 mm, and the layer thickness was 0.15 mm. The nozzle temperature was 240 °C and the bed temperature was 60 °C, enabling good adhesion on a clean glass building plate. The printing speed was 25 mm/s, and the cooling fan was off. The number of walls was two, the infill ratio was 100%, and the infill shape was 45° lines. Furthermore, the infill was printed before the walls so that the CFC piece was smoothly fixed on the printed surface. As well as the typical printing settings, a script was added in

the middle of the printing program to pause the printing automatically to manually insert the CFC piece. Furthermore, a prime tower feature was used before printing on top of the applied CFC piece to avoid uncontrolled leaking of the molten TPU from the nozzle onto the sample.

FFF was used to fabricate samples, of which the target dimensions were 10 mm wide, 200 mm long, and 1 mm thick. In the middle of the samples, an 8-mm-wide and 230-mm-long piece of CFC was placed longitudinally. CFCs were cut in the machine direction orientation (MDO), their loose ends serving as electrical contacts. Then, the CFC was fixed with two strips of Kapton tape to avoid using an adhesive and to reinforce the electrical contacts. The placed CFCs affected the samples' dimensions, measured with a digital Vernier caliper with ± 0.01 mm measurement resolution. The sample preparation steps, drawn in Solidworks 3D design software (version 2021, Dassault Systèmes SolidWorks Corporation, Waltham, MA, USA), are presented in Figure 1.

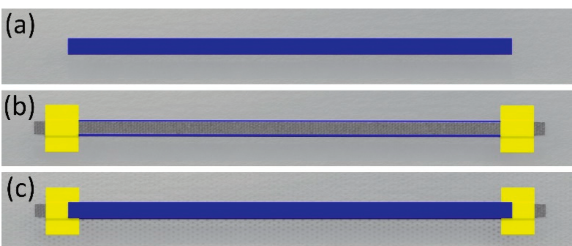

Figure 1. Preparation steps of the samples as modeled in Solidworks: (**a**) 3D printing of the sample's bottom half-layer, (**b**) placement of the CFC piece with the use of Kapton tape, and (**c**) continuing the 3D printing until the sample was ready.

2.2. Electrical Measurement of the Samples

The CFC pieces were electrically conductive. Based on the amount of carbon fibers they contained, they provided different levels of electrical conductivity in the 3D-printed matrix. In the sample preparation, the resistance of the CFC pieces was measured twice: before their placement inside the sample and after the 3D printing process. The resistance was measured using a Fluke 183 multimeter (Elfa Distrelec Oy, Helsinki, Finland) by firmly pressing the multimeter probes on the CFC pieces to achieve a stable reading (<5 Ω variation). The distance between the probes was 220 mm. The comparability of the results to those of previous studies was enabled by converting resistance to conductivity. The conductivity was calculated with the equation

$$\sigma = 1/((RA)/L), \quad (1)$$

where σ is the conductivity in S/m, R is the resistance in Ω, A is the cross-sectional area of CFC in m^2, and L is the distance between probes in m. The cross-sectional area was calculated based on the nominal width and thickness of CFCs, as reported in Table 1. Note that the conductivity here does not refer to the carbon fiber's conductivity but to the average conductivity of the macroscopic sample's CFC material.

2.3. Mechanical Tests

The mechanical behavior of the 3D-printed samples and the effect of the quantity of the integrated CFCs on the failure behavior was evaluated with an ESM303 tensile tester (Mark-10 Corporation, Copiague, NY, USA), equipped with a 500 N load cell. The distance of the clamps was 50 mm; the movement speed of the upper clamp was 25 mm/min. From each sample series, two samples were elongated 50% (25 mm) with a single pull-up test.

Because clothing-integrated stretchable and wearable components endure thousands of stretching cycles during their lifetime [30], cyclic tensile loading was chosen as a more realistic testing method. The cyclic electromechanical behavior of the samples was tested

with the simultaneous use of the tensile tester and a custom-built resistance measurement system (Tampere University, Tampere, Finland). In the cyclic electromechanical tests, the movement speed of the upper clamp was 240 mm/min.

A custom-built resistance measurement system was constructed using an Arduino Uno board. The system used Arduino Uno's 10-bit AD converter for two-wire measurements to calculate real-time voltage values over the samples, which were converted to resistance values and recorded. The system had three measurement channels that used 3470 Ω resistors as a reference. Based on the reference resistor values, the system's accuracy was ±3 Ω. A threshold of 3000 Ω was used to indicate the total sample failure. The probes of the resistance measurement system were fixed to the samples' contacts with anisotropic conductive adhesive film (ACF), and were further clamped to ensure stable electrical connections.

Since the conducting material's structure is not homogeneous but is rather an interconnected network of fibers with small contact points between the fibers, the current density may influence the sample's resistance. Nevertheless, no such effect was observed with the low (less than 100 mA) measured DC currents. With higher frequencies (in MHz range) or high currents (several A), the influence of current density on the resistance would probably be observed, in alignment with previously reported results [31].

In the cyclic tests, three samples from the same category were fixed together in the 50-mm-wide clamps and simultaneously stretched 10,000 times. During testing, the tensile tester measured the average force and displacement of three samples, and the resistance measurement system measured each sample's resistance. For every sample series in Table 1, five degrees of tensile deformations were tested (10%, 20%, 30%, 40%, and 50%), and 25 cyclic tests were conducted. Figure 2 presents the clamped cyclic test samples with background light. After the cyclic tests, a strain sensor test was carried out with the cyclic test setup and a previously tested (50% elongated) cyclic test sample with a 153 µm nominally thick carbon fiber layer. The sample was elongated repeatedly up to 10% with a speed of 0.5 mm/min.

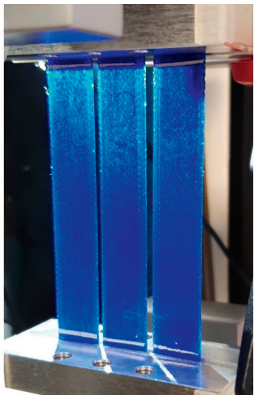

Figure 2. Clamped cyclic test samples in the ESM303 tensile tester. The samples were inspected with a background light, which revealed the integrated CFCs inside the 3D-printed TPU matrix.

The cyclic test analysis was performed using Matlab (version R2021b, MathWorks, Inc., Natick, MA, USA). Maximum and minimum resistance values during cyclic loading were extracted from the test data by averaging the steady-state results obtained after the first thousand cycles, and a high variation in the sample resistance was observed, presumably due to fiber reorientation in the CFC layer. The change in the samples' resistance was then calculated based on the two parameters extracted above. Furthermore, the average change in the resistance of the cyclically loaded samples was calculated by dividing the testing time into ten cycle periods and calculating the average resistances of each period. After that,

the average resistance data from the last 5000 cycles, with which the increase in resistance versus the cycle could be linearized, were fitted using a linear relationship through the polyfit Matlab function ($n = 1$) to obtain the average resistance change per cycle.

2.4. DIC Analyzes

To further analyze the electromechanical properties of the samples, DIC was used for separate cyclic tests to inspect surface deformations of the samples in 100 early cycles, in which the largest resistance changes typically occur. The surfaces of the samples were studied and compared in the first, 50th, and 100th cycles. For this purpose, the deformation of the samples during loading was recorded using the stereo 3D DIC imaging system 3D StrainMaster Compact 5M (LaVision GmbH, Göttingen, Germany) and analyzed using DaVis software (version 10.2.1, LaVision GmbH, Göttingen, Germany). The strain measure used through the DIC analyses—and thus the one shown in the figures in this work—was the logarithmic (Hencky) strain. For DIC, the speed of the upper clamp was 50 mm/min, and the maximum elongation of the samples was 50% (25 mm).

The CFC pieces were studied with DIC without the 3D-printed TPU matrix to observe the mechanical limits of the fabricated CFC pieces more closely. In these samples, each CFC piece was laminated between two clear TPU films (Platilon U 4201 AU by Covestro). The thickness of the films was 100 µm, width 10 mm, and length 200 mm. The film was transparent and notably more deformable under the same load levels compared to the 1-mm-thick 3D-printed TPU matrix, enabling the evaluation of the deformation of the CFC pieces.

3. Results

3.1. Preparation of the Samples

The dimensions of the designed samples were 10 mm in width, 1 mm in thickness, and with a cross-sectional area of 10 mm^2. Table 2 shows the measured average dimensions of the sample series that underwent cyclic electromechanical testing, classified by amount and type of reinforcement. The sample series contained 15 parallel samples.

Table 2. Studied CFC compositions based on the manufacturer's data, and the target and measured average dimensions of the sample series.

Series	Average Width (mm)	Average Thickness (mm)	Average Area (mm^2)
Target dimensions	10	1	10
Without CFC	9.97	1.02	10.15
1 thin CFC (53 µm)	10.09	1.03	10.41
2 thin CFCs (106 µm)	10.12	1.04	10.56
3 thin CFCs (159 µm)	10.21	1.06	10.83
1 thick CFC (153 µm)	10.11	1.04	10.49

The area of the unreinforced sample series was 1.5% larger than the target dimensions. With one layer of thick CFC, the average area increased by 4.9%. With 1–3 layers of thin CFC, the average area increased by 4.1%, 5.6%, and 8.3%, correspondingly.

Figure 3 shows the resistance measurements of the CFC pieces of the samples before 3D printing, compared with the same measurements after the process. From these data, it is evident that CFCs' electrical performance improved after their integration into the 3D-printed matrix, since their resistance decreased. This differs, for example, from the currently used carbon filler filaments, which have better electrical properties before 3D printing. The resistance of the samples with thick CFC decreased by 27% after 3D printing, making the average conductivity of the sample series approximately 1000 S/m. In the sample series with one thin CFC, the resistance decreased by 33%, whereas the sample series with two thin CFCs and three thin CFCs exhibited a 38% decrease in resistance. The

calculated conductivity of all thin CFC sample series was at the level of 1500 S/m, which is not a drastic variation, despite their differing thicknesses and several interfaces.

In addition to the decrease in the resistance, Figure 3 shows the scattering of the resistance values in the CFC pieces. The series with one thin CFC showed the highest dispersion of results, which decreased when more CFC plies were laminated on each other. Furthermore, although the thickness of the sample with one thick CFC and that of the sample with three thin CFCs samples were nominally similar, the resistance values and scattered results of the series with one thick CFC were at the level of the series with two thin CFCs.

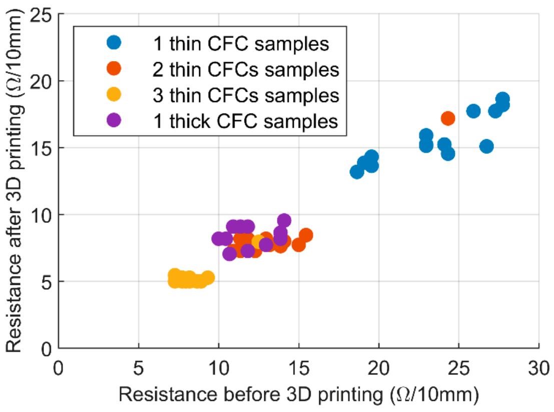

Figure 3. CFC layers' resistance per 10 mm before and after the 3D printing process. The sample series contained 15 parallel samples.

3.2. Mechanical Tests

First, the samples were elongated by 50% in the single pull-up tests; the results are shown in Figure 4. In Figure 4a, it is possible to note that in the initial elastic phase, before any crack formation in the samples, the increased amounts of CFCs added to the samples resulted in larger slopes in the elastic region of the force-displacement curve. The high amount of CFCs affected the elastic phase end, with the deformation developing into a permanent plastic phase, the transition area becoming irregular, and random force drops appearing. After the elastic phase, the decline in the force of the samples with one thick CFC was about 20 N (20%) and it was approximately 5 N (6%) in the samples with three thin CFCs. Furthermore, Figure 4b shows that the force results of the samples approached certain levels, with the force of the plain samples and the samples with one thin CFC approaching 70 N. In the samples with two thin CFCs and with three thin CFCs, the force levels were around 90 N, whereas the force in the samples with one thick CFC varied between 90 and 100 N.

After the single pull-up tests, the samples' long-term durability was examined through cyclic tensile tests. The raw data concerning resistance over time showed that three phases could be identified for each cyclic test. Data from one sample from the sample series with two thin CFCs (50% elongation) are shown in Figure 5. Initially, there was (1) a cycle in which a high increase in the sample's resistance was observed, followed by (2) a few more cycles with decreasing resistance values, which finally (3) stabilized to a specific level. In phase 3, the resistance behavior over the cycle was predictable and stable, or it varied unpredictably and accumulated damage, as shown in Figure 6.

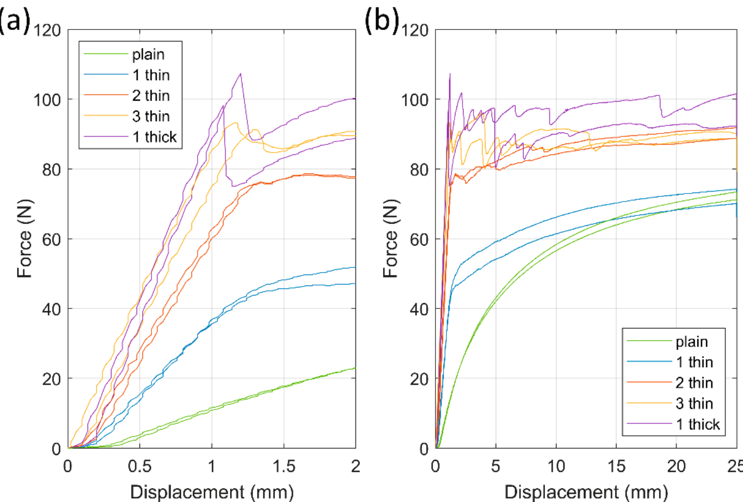

Figure 4. Force–displacement curves of the 3D-printed samples. (**a**) Results focusing on the initial 2 mm displacement (4% elongation), presenting the increase in stiffness caused by CFCs, (**b**) the samples' total displacement was 25 mm (50% elongation).

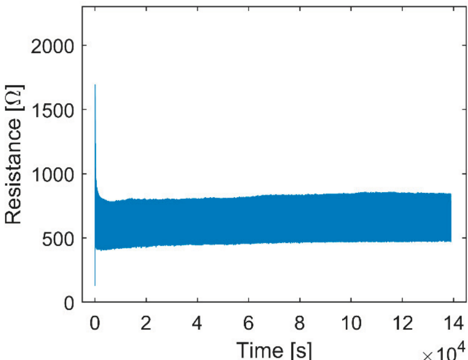

Figure 5. Raw data of a sample from the sample series with two thin CFCs, elongated 50% 10,000 times. The data show the high increase in resistance in the first cycle and the decrease in resistance and stabilization that occurred within a few cycles.

The samples' resistance varied differently depending on the CFC layer's thickness, structure, and tensile deformation level. The samples with a thin CFC layer and a low degree of elongation were more likely to have a more stable resistance variation in phase 3 (Figure 6a) than the samples with a thick layer of CFCs and high elongation (Figure 6b). In some cases, the resistance values in phase 3 exceeded the measurement limits of the test setup (3000 Ω), indicating the electrical failure of the sample.

In addition to the resistance behavior, the samples with different CFC layers exhibited different elongation and failure behavior (Figure 4). The samples with 1–2 layers of thin CFCs elongated uniformly, but those with a stiffer CFC layer elongated more locally. Thinner CFC layers tended to show delocalized damage and deformation along the whole sample through the TPU matrix; in the thicker samples, the deformation was localized where the CFC layers started forming cracks, leading to high local strains in the matrix, greatly affecting the samples' electromechanical properties.

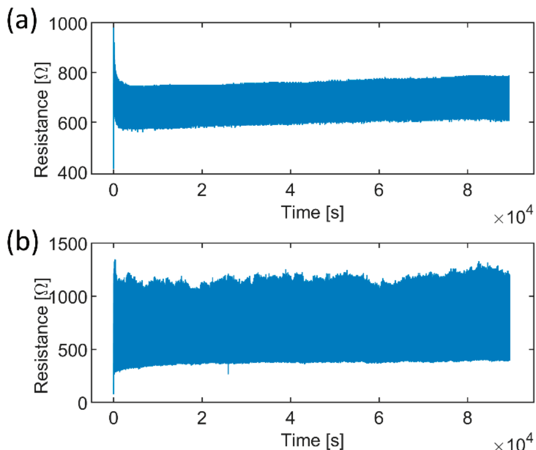

Figure 6. Cyclic behavior comparison of the samples elongated 30%. (**a**) The sample with 1 thin CFC exhibited repetitive electrical behavior in the 600 Ω–800 Ω range, whereas (**b**) the sample with 3 thin CFCs exhibited varying properties in the 350 Ω–1250 Ω range.

Figure 7 shows the resistance ranges of the cyclic sample series, with the electromechanical behavior of each measured sample regarding its resistance properties is displayed as a vertical line. The results of the three parallel samples are grouped, and the endpoints of the lines show the maximum and minimum resistances, whereas the line's length displays the resistance change during stable cyclic loading. As depicted in Figure 7a, the sample series with one thin CFC showed a moderate, gradual increase in its resistance range before the final 50% deformation level, which increased the samples' resistance range and variation. Figure 7b shows the modest resistance behavior of the series with two thin CFCs, with similar resistance values at the 30% and 40% deformation levels; at the 50% deformation level, the resistance range was less than 500 Ω.

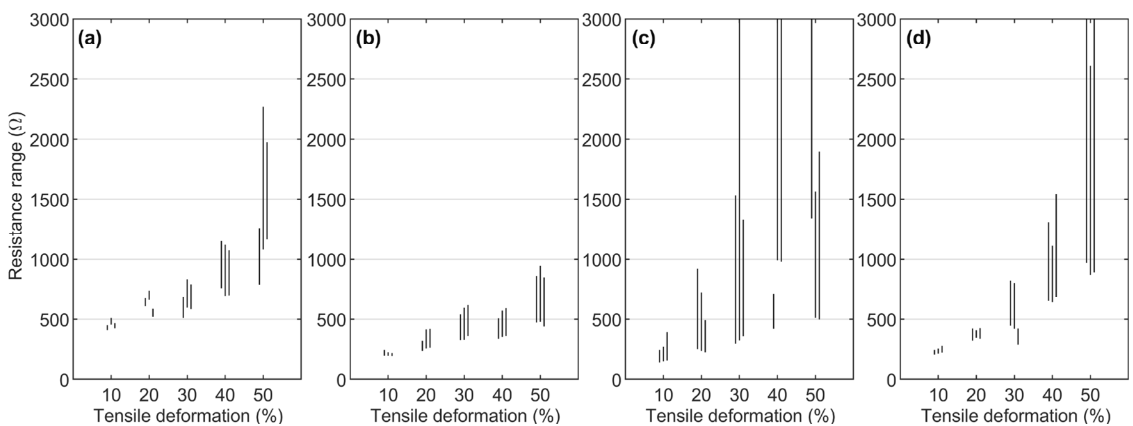

Figure 7. Resistance range lines of cyclic sample series, where three parallel samples are grouped together. The bottom and top endpoints of the lines show the minimum and maximum resistance values of the samples: (**a**) series with 1 thin CFC, (**b**) series with 2 thin CFCs, (**c**) series with 3 thin CFCs, and (**d**) series with 1 thick CFC.

As illustrated in Figure 7c, the stiff series with three thin CFCs showed more scattered results regarding the maximum resistance and resistance range values, whereas the min-

imum resistance level still exhibited a recognizable gradual increase. Finally, as shown in Figure 7d, the series with one thick CFC behaved similarly to the series with one thin CFC. However, the resistance was lower at the 10–20% deformation levels because of the greater thickness of the CFC layer. Conversely, this sample series showed higher resistance changes at the deformation levels of 40% and 50% because of its stiffness.

Like Figure 7, Figure 8 shows the changes in the average resistance in the samples per 5000 cycles, which indicates how much the resistance changed in the stable cyclic deformation phase of the cyclic samples (previously defined as phase 3). The failed samples that reached the 3000 Ω failure limit in Figure 7 are absent from Figure 8.

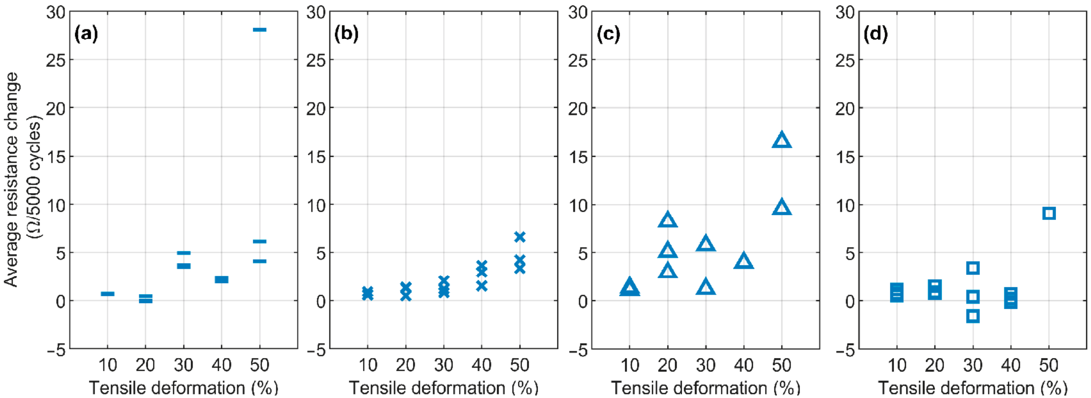

Figure 8. Average resistance changes between cycles in the last 5000 test cycles: (**a**) series with 1 thin CFC, (**b**) series with 2 thin CFCs, (**c**) series with 3 thin CFCs, and (**d**) series with 1 thick CFC.

In Figure 8a, the series with 1 thin CFC exhibited a change of approximately 5 Ω (1%) or smaller throughout 5000 cycles, except for a 50% tensile deformation level. The more random 50% tensile deformation level indicates the possible electrical limits of the sample series. In Figure 8b, the change in resistance increased as the tensile deformation increased; in the 10–30% tensile deformations, the average resistance change was always lower than 3 Ω (0.5%). At the 40–50% level, the resistance change was still small, but the low resistance range in Figure 7b increased the percentual resistance change and the results were approximately 5 Ω (lower than 1%).

In Figure 8c, the scattered resistance values show that the samples with three thin CFCs were not deformed evenly. Moreover, several samples (one sample from the 30% deformation level, two from the 40%, and one from the 50% level) were removed as failures. Despite this, the samples' percentual resistance change was lower than 1%; even with two unstable samples at 20% and 50% deformation levels, the change was approximately 2% and 1.5%, correspondingly.

Figure 8d depicts the results of the series with 1 thick CFC, which differed from the rest of the sample series in Figure 8 and which exhibited small negative resistance changes (lower than −0.3%) at the 30% and 40% tensile deformation levels. In the samples, the resistance decreased throughout the cycles, which can be explained, e.g., by the alignment of the carbon fibers. Furthermore, the average resistance changes were small at the 10–40% levels and were always less than 4 Ω (1%) due to the high thickness of the CFC layer. This, however, changed at the 50% deformation level, where the CFC layer's stiffness was high enough (compared to one of the TPU matrices) that the sample continued accumulating damage, resulting in only one intact sample at the end of the cyclic test that showed an average resistance change equal to 10 Ω per 1000 cycles.

3.3. A Strain Sensor Demonstration

Finally, the usage of 3D-printed samples with an integrated carbon fiber layer as a strain sensor was tested, with results shown in Figure 9. As an interconnection, the samples lasted well up to 50% elongation, but for sensor applications, a smaller 10% dynamic range was used after the initial 10,000 cycles, with a maximum elongation of 50%.

In the tests, rapid changes caused a dynamic error, and the response to a step change stabilized in about 200 s. The test in Figure 9a was carried out with a stretching speed of 0.5 mm/min and a maximum elongation of 10%. Figure 9a shows a linear increase in resistance, which is optimal for sensing applications. However, there was some drift in the output signal, similarly to what can be seen in the cyclic test in Figure 5. The drift stabilized after about 100 cycles.

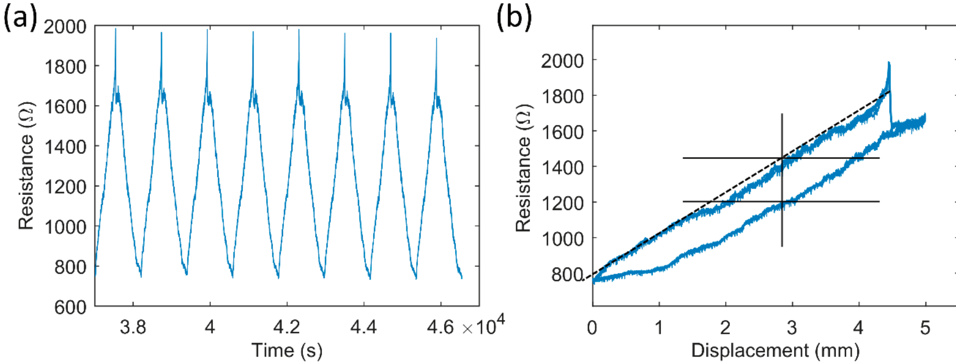

Figure 9. Sensor properties of tested cyclic test samples (153-µm-thick CFC, 10,000 cycles, 50% elongation, 240 mm/min speed). (**a**) Raw data with 10% elongation and 0.5 mm/min speed, and (**b**) a resistance-displacement curve of the first 4 cycles from (**a**).

As shown in Figure 9b, the practical dynamic range of the sensor was 750 Ω–1800 Ω. The system shown in Figure 9b was not strictly linear. The nonlinearity error and noise were <5% of the full scale. The sensor's output after the structure stabilized was repeatable, and the nonlinearity could be compensated for using software.

Figure 9b also shows hysteresis and sensitivity. The maximum difference during the hysteresis cycle was 220 Ω, which corresponds to ~10% of the full scale. The sensitivity of the sensor structure was ~200 Ω/mm.

3.4. DIC Analyses

The 3D-printed samples are also studied with DIC to identify local deformations to supplement the mechanical test results. The results of DIC analyses for the different sample series are presented in Figure 10.

Figure 10 shows that samples with different embedded CFC layers also exhibited different levels of local deformations. The non-reinforced plain sample (b1) and those with one thin CFC (a3 and b3) elongated uniformly without visual signs of deformation in the vertical direction. The stiffening effect of one thin CFC did not affect the overall surface deformation of the TPU matrix, nor did it create stress concentration areas. Instead, the sample with two thin CFCs (a1) showed multiple oblique failure bands that followed the shape of a 45° infill pattern over the entire length of the sample. Moreover, the high strain peaks observed here differed from the bulk level of deformations by only 20%.

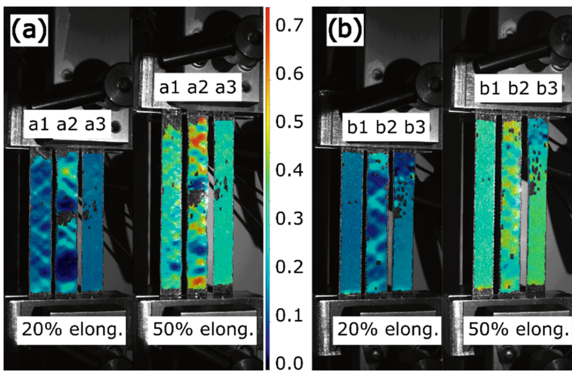

Figure 10. DIC *y*-axial Hencky strain results of 3D-printed samples in 20% and 50% elongations: (**a**) the a1 sample with 2 thin CFCs, the a2 sample with 3 thin CFCs, and the a3 sample with 1 thin CFC; (**b**) the b1 sample without CFCs, the b2 sample with 1 thick CFC, and the b3 sample with 1 thin CFC. The scale bar shows the level of local deformations compared to the initial undeformed phase of the samples.

The stiffest samples (a2 with three thin CFCs and b2 with one thick CFC) showed prominent failure bands, where failure was concentrated on the CFC layer. At 50% elongation, it is possible to note that some areas in the sample with three thin CFCs were almost undeformed (5%), whereas other areas exhibited axial deformation reaching over 70% due to the complete local failure of the CFC layer. The sample with one thick CFC also displayed a visible failure with a 40% deformation difference between the undeformed and failure areas.

As well as the 3D-printed samples, the deformation of CFC pieces embedded between thin and highly elastic TPU films is presented in Figure 11. In these cases, the stiffness of the CFCs and the TPU films differed considerably, making the CFC piece the load-carrying component and the TPU films only the binders of the CFC piece.

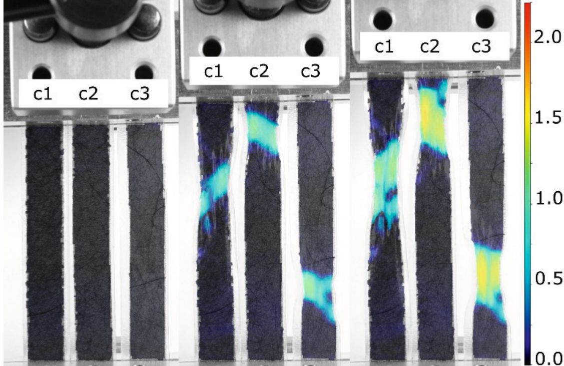

Figure 11. DIC *y*-axial Hencky strain analyses of the elongation of laminated CFC samples, where the c1 sample had 1 thin CFC, the c2 sample had 2 thin CFCs, and the c3 sample had 3 thin CFCs between the transparent TPU films. The deformation was mostly localized in the failure locations, whereas the rest of the sample exhibited almost no deformation under the load. The scale bar shows the level of local deformations compared to the initial undeformed phase of the samples.

The DIC examination, shown in Figure 11, indicated that the failure of the CFC piece occurred at the same deformation level for samples with different thicknesses and structures. Generally, when a failure was localized at one point on the CFC piece, the

elongation was focused on that area. For instance, in the highly elongated samples shown in Figure 11, the dark-colored CFC areas were elongated by less than 10%, whereas the elongation in the cracked areas could reach over 150%. The results showed that the highly deformable TPU films around the CFC piece did not distribute loads across the CFC piece and required a stiffer TPU matrix, which can be made through FFF.

4. Discussion

4.1. Effect of CFCs on the 3D Printing Process

Adding CFCs into FFF had both negative and positive effects on the process and the prepared object. The object's dimensions changed when CFCs were added inside an object without a cavity (Table 2). The samples' dimensions increased when the amount of CFCs increased since the carbon fibers replaced molten polymer on the layer, forcing it to flow elsewhere. However, when considering FFF's general accuracy, the calculated volume increases were small, and these changes can be considered in the design phase.

In the preparation of the samples, integrating CFC pieces into the TPU matrix changed the CFC layer's electrical properties. The 3D-printed molten plastic on the CFC piece compressed the fibers on the previously printed layer in the z-direction, improving the CFCs' electrical properties by decreasing the resistance by about 30%. Furthermore, the shrinkage of the molten plastic during cooling may have compressed the CFC layers even more in the x- and y-directions, improving their electrical properties more. The measured sample series had different amounts of integrated CFC layers, and the series with one thin CFC (a nominally 53-µm-thick CFC layer) showed scattered resistance results, as shown in Figure 3. When the CFC layer's nominal thickness was at least 100 µm, the sample's final resistance value was more consistent and predictable. Moreover, the series with two thin CFCs series and that with one thick CFC had approximately the same measured electrical behavior despite their 50 µm difference in thickness, indicating that lamination and the inclusion of an interface between the two CFC plies even out the electrical properties of randomly oriented CFCs efficiently.

The conductivities of the thin and thick CFC pieces were about 1500 S/m and 1000 S/m, correspondingly. The lamination of two or three thin CFCs plies together did not change the conductivity despite its effect on the resistance values. Notably, the nominal thicknesses of the CFC plies were used in the conductivity calculations. In case of the possible compression of the plies, a lower thickness would mean even higher conductivity. Furthermore, in measuring the initial resistances (used for the conductivity calculations), the accuracy of the resistance measurements was affected by the contact resistance and surface topography of the permeable fiber matrices. The inaccuracy was the same in the case of the CFC pieces ($<5\ \Omega$). Nevertheless, sample conductivity obtained using this method was two orders of magnitude higher than that of the methods currently used to incorporate carbon particles into FFF-generated objects, which justifies the use of CFCs in FFF matrices.

Also notable is that adhesion of the TPU matrix and the CFC piece was solid, showing no traces of delamination. The CFCs were placed on the additive manufactured surface without adhesives, and the flowing molten TPU fixed the CFC pieces inside the matrix's TPU infill structure. It is also likely that the molten TPU did not fully penetrate the thick CFC piece but still encapsulated the CFC layer inside the sample.

4.2. Electromechanical Behavior of the Samples

All the integrated CFC sample series were produced using the same 3D printing process, but their electromechanical properties varied. Independently, the CFC plies had different electrical properties because of their thicknesses and fabrication procedures, which, however, did not affect properties such as their elongation at break (Figure 11). Furthermore, considering the results of the plain TPU samples, one can claim that the samples' electromechanical properties came from the unique combination of the 3D printed TPU and CFCs.

The cyclic tensile test samples exhibited three phases in their tensile deformations (Figure 4), in which the first cycles might be explained through the rearrangement of the carbon fibers in the material. During the first loading cycles, carbon fibers embedded in the 3D-printed material may experience high enough local deformation, which may break part of the conduction network; as this induces an increase in resistance, some of the fibers that are now free to move to rearrange themselves due to the highly directional deformation applied, thus creating new (and more stable) paths that lead to a substantial decrease in the overall resistance. However, this phenomenon is not fully explained and requires more analysis.

The third phase is related to the electromechanically stabilized area that is observed after the orientation of the fibers. The regularity of phase 3 is affected by the amount of tensile deformation, thickness, and the number of interfaces in the CFC piece. Moreover, phase 3′s erratic behavior commonly affects only the maximum resistance values per cycle, whereas the minimum value stays at the same level. In the series with one thin CFC, phase 3 was even, but the resistance range in the cycles was extensive. In the series with three thin CFCs series and that with one thick CFC, phase 3 was unstable because of increased damage accumulation in the CFC layer. The most promising was the series two thin CFCs, where phase 3 was stable, and the resistance varied only 500 Ω between the maximum and the minimum during cycling at 50% tensile deformation.

4.2.1. Plain Sample Series and Series with One Thin CFC

In the plain sample series and that with one thin CFC, the deformations of the samples were determined by the properties of the TPU matrix. The plain sample series exhibited smooth force-displacement curves, as shown in Figure 4, which are typical for rubber-like materials. Adding one thin CFC into the matrix changed the curves, so that there were (1) linear elastic and (2) settling plastic deformation areas. The samples with one thin CFC elongated evenly, and their force approached the same level as that of the plain samples, meaning that the thin CFC influenced the samples' initial stiffness and the TPU matrix carried a load further at higher elongations. The 53-μm-thin CFC's minimal effect on the long-term deformation of the TPU matrix can also be seen in the DIC results in Figure 10, where the plain sample series and that with one thin CFC exhibited well-distributed deformations.

The low density of fibers in the samples with one thin CFC allowed molten TPU to penetrate the fiber layer, encapsulating the fibers inside the matrix and enhancing the samples' mechanical properties, also affecting their electrical properties. The electrical properties of the series with one thin CFC were governed by the TPU's mechanical deformations, resulting in a nonlinear relationship with the average resistance, as shown in Figure 7a. At 10–40%, tensile deformations—the one thin CFC encapsulated inside the TPU matrix—the electrical connection between carbon fibers was maintained, and this was improved by the fibers' length (25.4 mm). At 50% tensile deformation, the fibers partially detached from each other, increasing the resistance range values, as shown in Figure 7a, and causing scattering, as shown in Figure 8a. Furthermore, the great increase in resistance could be caused by the random orientation of the fibers and the local thickness variations of the thin CFC, which can make parts of CFC more electrically sensitive to mechanical deformations.

4.2.2. Sample Series with Two Thin CFCs

In the sample series with two thin CFCs, the combination of the TPU matrix and CFCs was mechanically balanced, which can also be seen in the series' good electrical properties. Compared with the samples with one thin CFC, the stiffness of the samples with two thin CFCs doubled (Figure 4a), and the samples showed a small force fluctuation at the start of the plastic deformation phase (Figure 4b), indicating minor reorientation or tearing of the CFC layer. The series' closely balanced mechanical properties are also shown in Figure 10a, where the CFC layer was stiff enough to form 45° failure bands in the sample, which, however, were distributed along the samples' length, and their deformation level

was only 20% higher than in the undeformed areas. The stretchability of TPU with the long length of the carbon fibers meant that the 20% deformation level of the failure bands did not negatively affect the samples' electromechanical properties.

The electrical properties of the sample series were stable. In Figure 7b, the resistance range stayed at the same level with 30–40% tensile deformations and with 50% tensile deformations of 500–1000 Ω. This stable behavior can be explained by the local failure bands, where tensile deformations were "absorbed". Furthermore, the two laminated CFC plies and the interface between them could form an impermeable layer; the molten TPU did not completely bind with the lower CFC ply. In that case, the lower CFC ply can move and be further subjected to higher tensile deformations. However, only a specific degree of movement can improve the electrical properties by preserving the conductive fiber network under the movement of the TPU matrix. In contrast, too great a movement can detach and reconnect the fibers and lead to unstable electrical properties, which likely occurred in the series with three thin CFCs. With these features, the series with two thin CFCs showed the most balanced and stable electrical properties, which can be considered for the development of stretchable interconnects or sensors for wearable applications.

4.2.3. Sample Series with Three Thin CFCs and with One Thick CFC

In the samples with three thin CFCs and those with one thick CFC, the CFC layer was rigid, surpassing the stiffness of the TPU matrix governing the deformations in the samples. The tensile deformations oriented and tore the CFC layer, leading to uneven mechanical results and further varying the samples' electrical properties at high levels of tensile deformation.

As shown in Figure 4, the failure of the sample series with three thin CFCs and that of the samples with one thick CFC resembled each other, although the samples consisting of three thin CFCs had about 10 N lower maximum tensile strength than the samples with one thick CFC. Moreover, as shown in Figure 10, the samples with three thin CFCs showed a 70% difference between the least and most elongated areas, whereas the samples with one thick CFC showed a deformation difference of 40%. These results indicate that the two interfaces of the thin CFCs negatively affected the matrix's mechanical durability and restricted the transmission of forces in the CFC layer.

During 3D printing, molten TPU likely cannot penetrate deeply into the CFC layer, although decreasing resistance due to the compression effect of TPU can be observed. The CFC and the infill area were encapsulated inside the sample, but CFC adhered only on one side, affecting the samples' mechanical and electrical properties. This partial adherence promoted the effect of the interface areas in the CFC layers, allowing them to act as the weaker points for failures and resulting in the lower tensile properties of the samples with three thin CFCs compared to those with one thick CFC, as shown in Figure 4.

Among the entire sample series, the electrical properties of the series with three thin CFCs were the lowest in regard to resistance. The samples showed low and predictable resistance values, as shown in Figure 3, with the two interface areas between the three thin CFCs making the CFC layer conductivity very even. Still, this sample series could only sustain 10–20% tensile deformations before random failures occurred, as shown in Figures 7c and 8c. Depending on the application, however, this can still be sufficient, since each sample must be subjected to an external load of approximately 100 N before reaching higher deformation levels, enabling one to use structures with three thin CFCs in low-level stretchable electronics for wearable sensor pads.

The electrical behavior of the sample series with one thick CFC and that with one thin CFC showed similar features. The difference was that the thick CFC was thicker and stiffer, making it more conductive at lower tensile deformations. However, after the breaking point, the samples exhibited higher resistance ranges because of the 45° failure bands. In fact, distributed local elongation points can orient the fibers in the tensile direction, even after thousands of cycles—whenever a failure band is formed—which can cause the resistance range to decrease, as in Figure 8d.

4.3. Sensor Properties of the Samples

Figure 9 shows the use of the already cyclically tested sample as a sensor. Despite the fact it had been elongated up to 50% 10,000 times, the sample exhibited a repeatable resistance curve at 10% elongation. The practical dynamic range was at least 10%, and the sensitivity was good, at approximately 10 Ω per 1% change of the full scale (~200 Ω/mm). Furthermore, the low amount of noise, drift, and the small nonlinearity error enables the application of the matrix in sensors. However, its high hysteresis decreases its accuracy and could limit its use.

In the sensor testing, the properties of the TPU matrix and sample dimensions also likely affected the resistance values. At the start of the testing process, the sample exhibited similar drift values to those of the cyclic test samples (Figure 5), which stabilized when the number of cycles increased. Fast mechanical deformations can cause dynamic errors; therefore, the 3D-printed matrix with the current dimensions exhibits the best performance when measuring slow changes.

5. Conclusions

Adding CFCs into the 3D printing process of a deformable TPU matrix represents a new way to make electrically conductive, stretchable, and wearable 3D-printed electronic devices. This method differs from current methods due to the possibility of creating structures with stretchability, excellent conductivity, printing accuracy, and isotropic layers. After studying the sample series during their fabrication phase, with single pull-up tests, electromechanical cyclic tests, and finally by analyzing them with DIC, the benefits of the addition of CFCs into the 3D-printed deformable matrix are obvious.

The results showed that the TPU matrix with just one nominally 53-μm-thin CFC layer provided 1500 S/m of conductivity—a result which has not been achieved with other carbon additives in the FFF process. When the thickness and number of interface areas were increased, the resistance of the CFC layers decreased to 5 Ω/10 mm, which has been conventionally achieved in the stretchable electronics field only with the use of metal-based materials.

The electromechanical properties of the CFC samples varied according to the thickness and structure of the CFC pieces, enabling versatile applications. The use of a thin and permeable CFC piece could support more stable and durable mechanical features, enabling the structure to deform based on the properties of the 3D-printed TPU matrix. The thick and multilayered CFC piece exhibited better electrical properties with low resistance and good mechanical stability, and the CFC's stiffness governed the structure's deformation. Between these extremes, the sample series with two thin CFCs and one interface area between the CFC plies demonstrated more balanced electromechanical properties. Small 45° failure bands with long carbon fibers absorbed tensile deformations while maintaining stable electrical properties.

These results show the potential of this novel production method to create 3D-printed stretchable electronics that can withstand high levels of deformation in a single pulling experiment and in numerous cycles. The use of one thin CFC increased the stiffness of the elastic phase but did not affect the plastic phase of 3D printed samples. The use of a high amount of CFCs increased the stiffness considerably and resulted in an irregular plastic phase, in which a 20% force decline was possible. In the cyclic testing, the samples with one thin CFC or two thin CFCs layers could reach even higher elongation than that measured at 50% for 10,000 cycles. This fabrication approach is easy to incorporate into current 3D printing practices, enabling the preparation of 3D-printed stretchable and wearable electronics with commercially available materials and methods. Varying the thickness and number of CFCs added into the 3D-printed matrix allows one to optimize the structures' properties for different purposes. Additive-manufactured deformable CFC electronics can be used, for example, in sensors, interconnects, and circuit boards.

The use of CFCs inside 3D-printed structures has advantages, for example, using one thin CFC in several layers in FFF so that every printing layer adheres to only one

layer of a thin CFC can be implemented to make highly reinforced structures that elongate steadily and which have intermediate electrical conductivity. Moreover, the CFCs on multiple layers can be shaped differently, enabling simple 3D PCBs that are stretchable and wearable. However, the manufacturing parameters of 3D-printed TPU matrices and CFCs of differing thicknesses require further optimization for sensor applications. Furthermore, the placement method of CFCs needs to be automated, for instance, with the use of a modified pick-and-place machine.

Author Contributions: Conceptualization, A.H., T.S. and J.V.; methodology, A.H. and T.S.; software, D.D.V.; validation, A.H. and T.S.; formal analysis, D.D.V. and T.S. investigation, T.S.; resources, A.H. and D.D.V.; data curation, D.D.V. and J.V.; writing—original draft preparation, T.S.; writing—review and editing, D.D.V., T.S. and J.V.; visualization, D.D.V. and T.S.; supervision, J.V.; project administration, T.S. and J.V.; funding acquisition, J.V. All authors have read and agreed to the published version of the manuscript.

Funding: This research was partially funded by the European Union Regional Development Fund (ERDF) and city of Kankaanpää under the project SOFT3L (A73741), of which the official authority is Satakunta Regional Council under Grant 2947/31/2018. Furthermore, this research was partly funded by the Academy of Finland under the project REEL, decision number 334175.

Institutional Review Board Statement: Not applicable.

Informed Consent Statement: Not applicable.

Data Availability Statement: Not applicable.

Conflicts of Interest: The authors declare no conflict of interest.

References

1. Singh, S.; Singh, G.; Prakash, C.; Ramakrishna, S. Current status and future directions of fused filament fabrication. *J. Manuf. Process.* **2020**, *55*, 288–306. [CrossRef]
2. Hohimer, C.J.; Petrossian, G.; Ameli, A.; Mo, C.; Pötschke, P. 3D printed conductive thermoplastic polyurethane/carbon nanotube composites for capacitive and piezoresistive sensing in soft pneumatic actuators. *Addit. Manuf.* **2020**, *34*, 101281. [CrossRef]
3. Kim, K.; Park, J.; Suh, J.; Kim, M.; Jeong, Y.; Park, I. 3D printing of multiaxial force sensors using carbon nanotube (CNT)/thermoplastic polyurethane (TPU) filaments. *Sens. Actuators A Phys.* **2017**, *263*, 493–500. [CrossRef]
4. Reyes, C.; Somogyi, R.; Niu, S.; Cruz, M.A.; Yang, F.; Catenacci, M.J.; Rhodes, C.P.; Wiley, B.J. Three-Dimensional Printing of a Complete Lithium Ion Battery with Fused Filament Fabrication. *ACS Appl. Energy Mater.* **2018**, *1*, 5268–5279. [CrossRef]
5. Ahrendt, D.; Romero Karam, A. Development of a computer-aided engineering–supported process for the manufacturing of customized orthopaedic devices by three-dimensional printing onto textile surfaces. *J. Eng. Fibers Fabr.* **2020**, *15*, 1558925020917627. [CrossRef]
6. Uysal, R.; Stubbs, J.B. A New Method of Printing Multi-Material Textiles by Fused Deposition Modelling (FDM). *TEKSTILEC* **2019**, *62*, 248–257. [CrossRef]
7. Salo, T.; Halme, A.; Lahtinen, J.; Vanhala, J. Enhanced stretchable electronics made by fused-filament fabrication. *Flex. Print. Electron.* **2020**, *5*, 045001. [CrossRef]
8. Stuart, T.; Kasper, K.A.; Iwerunmor, I.C.; McGuire, D.T.; Peralta, R.; Hanna, J.; Johnson, M.; Farley, M.; LaMantia, T.; Udorvich, P.; et al. Biosymbiotic, personalized, and digitally manufactured wireless devices for indefinite collection of high-fidelity biosignals. *Sci. Adv.* **2021**, *7*, 1–18. [CrossRef]
9. Ly, S.T.; Kim, J.Y. 4D printing–fused deposition modeling printing with thermal-responsive shape memory polymers. *Int. J. Precis. Eng. Manuf. Technol.* **2017**, *4*, 267–272. [CrossRef]
10. Tekinalp, H.L.; Kunc, V.; Velez-Garcia, G.M.; Duty, C.E.; Love, L.J.; Naskar, A.K.; Blue, C.A.; Ozcan, S. Highly oriented carbon fiber-polymer composites via additive manufacturing. *Compos. Sci. Technol.* **2014**, *105*, 144–150. [CrossRef]
11. Zhang, J.; Yang, B.; Fu, F.; You, F.; Dong, X.; Dai, M. Resistivity and Its Anisotropy Characterization of 3D-Printed Acrylonitrile Butadiene Styrene Copolymer (ABS)/Carbon Black (CB) Composites. *Appl. Sci.* **2017**, *7*, 20. [CrossRef]
12. Wei, X.; Li, D.; Jiang, W.; Gu, Z.; Wang, X.; Zhang, Z.; Sun, Z. 3D Printable Graphene Composite. *Sci. Rep.* **2015**, *5*, 11181. [CrossRef]
13. Jahangir, M.N.; Billah, K.M.M.; Lin, Y.; Roberson, D.A.; Wicker, R.B.; Espalin, D. Reinforcement of material extrusion 3D printed polycarbonate using continuous carbon fiber. *Addit. Manuf.* **2019**, *28*, 354–364. [CrossRef]
14. Al-Saleh, M.H.; Sundararaj, U. Review of the mechanical properties of carbon nanofiber/polymer composites. *Compos. Part A Appl. Sci. Manuf.* **2011**, *42*, 2126–2142. [CrossRef]
15. Forintos, N.; Czigany, T. Multifunctional application of carbon fiber reinforced polymer composites: Electrical properties of the reinforcing carbon fibers—A short review. *Compos. Part B Eng.* **2019**, *162*, 331–343. [CrossRef]

16. Li, Y.; Huang, X.; Zeng, L.; Li, R.; Tian, H.; Fu, X.; Wang, Y.; Zhong, W.H. A review of the electrical and mechanical properties of carbon nanofiller-reinforced polymer composites. *J. Mater. Sci.* **2019**, *54*, 1036–1076. [CrossRef]
17. Tzounis, L.; Petousis, M.; Grammatikos, S.; Vidakis, N. 3D printed thermoelectric polyurethane/multiwalled carbon nanotube nanocomposites: A novel approach towards the fabrication of flexible and stretchable organic thermoelectrics. *Materials* **2020**, *13*, 2879. [CrossRef]
18. Spoerk, M.; Savandaiah, C.; Arbeiter, F.; Traxler, G.; Cardon, L.; Holzer, C.; Sapkota, J. Anisotropic properties of oriented short carbon fibre filled polypropylene parts fabricated by extrusion-based additive manufacturing. *Compos. Part A Appl. Sci. Manuf.* **2018**, *113*, 95–104. [CrossRef]
19. Yin, L.; Tian, X.; Shang, Z.; Wang, X.; Hou, Z. Characterizations of continuous carbon fiber-reinforced composites for electromagnetic interference shielding fabricated by 3D printing. *Appl. Phys. A.* **2019**, *125*, 266. [CrossRef]
20. Wang, Z.; Luan, C.; Liao, G.; Yao, X.; Fu, J. Mechanical and self-monitoring behaviors of 3D printing smart continuous carbon fiber-thermoplastic lattice truss sandwich structure. *Compos. Part B Eng.* **2019**, *176*, 107215. [CrossRef]
21. Hu, Q.; Duan, Y.; Zhang, H.; Liu, D.; Yan, B.; Peng, F. Manufacturing and 3D printing of continuous carbon fiber prepreg filament. *J. Mater. Sci.* **2018**, *53*, 1887–1898. [CrossRef]
22. Yu, T.; Zhang, Z.; Song, S.; Bai, Y.; Wu, D. Tensile and flexural behaviors of additively manufactured continuous carbon fiber-reinforced polymer composites. *Compos. Struct.* **2019**, *225*, 111147. [CrossRef]
23. Türk, D.-A.; Ebnöther, A.; Zogg, M.; Meboldt, M. Additive Manufacturing of Structural Cores and Washout Tooling for Autoclave Curing of Hybrid Composite Structures. *J. Manuf. Sci. Eng.* **2018**, *140*, 105001. [CrossRef]
24. Yao, X.; Luan, C.; Zhang, D.; Lan, L.; Fu, J. Evaluation of carbon fiber-embedded 3D printed structures for strengthening and structural-health monitoring. *Mater. Des.* **2017**, *114*, 424–432. [CrossRef]
25. Falco, A.; Petrelli, M.; Bezzeccheri, E.; Abdelhalim, A.; Lugli, P. Towards 3D-printed organic electronics: Planarization and spray-deposition of functional layers onto 3D-printed objects. *Org. Electron.* **2016**, *39*, 340–347. [CrossRef]
26. Abdelhalim, A.; Abdellah, A.; Scarpa, G.; Lugli, P. Fabrication of carbon nanotube thin films on flexible substrates by spray deposition and transfer printing. *Carbon N. Y.* **2013**, *61*, 72–79. [CrossRef]
27. Fieber, L.; Evans, J.D.; Huang, C.; Grant, P.S. Single-operation, multi-phase additive manufacture of electro-chemical double layer capacitor devices. *Addit. Manuf.* **2019**, *28*, 344–353. [CrossRef]
28. ACP Composites. Carbon Fiber Tissue. Product Data Sheet. 2014. Available online: https://store.acpcomposites.com/carbon-fiber-veil?quantity=1&weight=1 (accessed on 20 September 2022).
29. Hagberg, J.; Leijonmarck, S.; Lindbergh, G. High Precision Coulometry of Commercial PAN-Based Carbon Fibers as Electrodes in Structural Batteries. *J. Electrochem. Soc.* **2016**, *163*, A1790–A1797. [CrossRef]
30. Persons, A.K.; Ball, J.E.; Freeman, C.; Macias, D.M.; Simpson, C.L.; Smith, B.K.; Burch, V.R.F. Fatigue testing of wearable sensing technologies: Issues and opportunities. *Materials* **2021**, *14*, 4070. [CrossRef]
31. Guadagno, L.; Vertuccio, L.; Naddeo, C.; Raimondo, M.; Barra, G.; De Nicola, F.; Volponi, R.; Lamberti, P.; Spinelli, G.; Tucci, V. Electrical current map and bulk conductivity of carbon fiber-reinforced nanocomposites. *Polymers* **2019**, *11*, 1865. [CrossRef]

PUBLICATION
IV

Mechanical properties of structured copper and printed silver hybrid stretchable electronic systems

Salo T., Werft L., Adams B., Di Vito D., Halme A., Scenev V., Walter H., Löher T., Vanhala J.

Flexible and Printed Electronics, vol. 8, no. 2, 025019
https://doi.org/10.1088/2058-8585/acda46

Publication is licensed under a Creative Commons Attribution 4.0 International License CC-BY-NC-ND

Flexible and Printed Electronics

OPEN ACCESS

RECEIVED
15 March 2023

REVISED
25 April 2023

ACCEPTED FOR PUBLICATION
31 May 2023

PUBLISHED
8 June 2023

Original content from this work may be used under the terms of the Creative Commons Attribution 4.0 licence.

Any further distribution of this work must maintain attribution to the author(s) and the title of the work, journal citation and DOI.

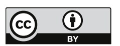

PAPER

Mechanical properties of structured copper and printed silver hybrid stretchable electronic systems

Teemu Salo[1,*], Lukas Werft[2], Basel Adams[2], Donato Di Vito[3], Aki Halme[1], Vitalij Scenev[2], Hans Walter[2], Thomas Löher[2] and Jukka Vanhala[1]

[1] Information Technology and Communication Sciences, Tampere University, Tampere, Finland
[2] Fraunhofer Institute for Reliability and Microintegration IZM, Berlin, Germany
[3] Tactotek Oy, Oulu, Finland
[*] Author to whom any correspondence should be addressed.

E-mail: teemu.salo@tuni.fi

Keywords: stretchable electronics, printed electronics, fatigue testing, stress concentration effect, failure analysis

Abstract

Stretchable electronics can be realized using different manufacturing methods and hybrids thereof. An example of the latter is the combination of stretchable circuit boards with screen-printing, which will be discussed in this work. The hybrid stretchable electronics structures are based on photolithographically structured and rigid copper islands and screen-printed silver ink interconnections. This enables the assembly of components with a high number of contacts onto the copper islands and deformable silver ink lines between islands. The transition area between islands and lines is critical due to local stress concentration. The effect and potential mitigations were studied by measuring the electrical resistance of test interconnections under mechanical loading. The first set of samples was elongated up to 30% in tensile tests. The second set of samples was elongated 10%, 20%, and 30% in cyclic tests up to 10 000 cycles. After the tests, extensive failure analysis, e.g. scanning electron microscope, and finite element analysis were conducted. In tensile tests at maximum load, the interconnections either snap apart or their resistance increases by 640% in the transition area. Adding protective structures around the transition area, the resistance increase can be reduced to 12%. Stress concentration in the transition area can be controlled with the layout of the structures, as shown in the cyclic tests. Depending on a layout, the structures protect interconnections in the transition area (resistance $<4\ \Omega$ at 10% and 20% throughout 10 000 cycles, and up to 5000 cycles at 30% elongation), or with particular designs, cause fatal damage of the circuitry and fail early. The identified failure mechanism is typically fatigue damage caused by the repeated bending of the protective structure. The observed resistance increase at the interface was closely related to the crack propagation phase in the protective structures.

1. Introduction

The availability of flexible and stretchable electronics has enlarged the field of electronics by enabling new wearable applications, such as smart band-aids [1], electrocardiogram monitoring circuits [2], electronic tattoos [3], and strain and capacitive pressure sensors [4, 5]. The current development of stretchable electronics is a very broad field with very different material/fabrication approaches and realized build-ups. Depending on the used manufacturing method, stretchable electronics have specific advantages and disadvantages. This is most prominent when different stretchable interconnection types are compared, which each have their respective characteristics [6, 7], and thus makes the combination of different manufacturing methods complicated.

1.1. Stretchable electronics based on structured copper foil

Conventional printed circuit board (PCB) manufacturing and component assembly are well-established and can be adapted for stretchable electronics fabrication. For example, copper-etching, soldering, and other related process steps are used in stretchable circuit board (SCB) fabrication, developed by Fraunhofer IZM and TU Berlin (Germany), where rigid substrates (glass-reinforced epoxy laminate FR4

© 2023 The Author(s). Published by IOP Publishing Ltd

boards) are replaced by stretchable thermoplastic polyurethane (TPU) film [1, 2, 6, 8]. Contrasting the rigid and flexible PCBs, the electronic system is stretchable on the TPU carrier and components are connected by meandering copper tracks [1, 2]. The copper foil thickness in a typical SCB-build-up is 17 μm or 35 μm, like it is used in the conventional PCB manufacturing. Straight copper interconnection on this basis would typically allow elastic deformations in the order of 1% before plastic deformation sets in and the structure eventually ruptures [9]. Larger deformations without tearing up can be reached by meandering designs of the interconnects, which elongate like two-dimensional springs [1, 2, 8]. Generally, the weakest points of the interconnections and the vulnerability of the stretchable system are the tips of the meanders and the area close to the rigid component on the deformable substrate, where stresses concentrate [1, 2, 6, 8]. In this study, the area close to the rigid component is called a transition area. The copper meanders can be mechanically optimized by (i) decreasing the track width, (ii) increasing the radius, and (iii) adding protective structures to distribute the deformations [2]. Furthermore, the rigid-stretchable transition area can be also shaped to implement a gradual stiffening of that area. Combining all optimization potentials an interconnect can be realized which can be elongated up to 200% before rupture [1, 2].

Still, after design optimization of the deformable system the copper tracks are torn apart at some elongation level in a stretch-to-failure experiment [1]. The rupture in such experiment occurs rather spontaneous, i.e. there are no indicators for the imminent rupture. That is because the total copper interconnections' length and resistance do not change during elongation, only the meanders open under elongation. The accumulated stress in the meanders is then released in a short time snapping of the interconnection [8]. By contrast, under repeating cyclic deformation at much lower deformation levels eventually fatigue fracture occurs, the number of cycles until break is inversely dependent on the elongation level [6].

Technical benefits of stretchable electronics fabricated with conventional PCB manufacturing processes, like SCB, are the stable conductivity until fatigue failure and established process capabilities enabling track width down to 30 μm [6, 8]. Although benefitting from the well-established fabrication technology there are drawbacks to this approach. Since in many applications for stretchable electronics, components of such systems are distributed over large areas with relatively few interconnections between them, making stretchable printed circuit relatively costly. Also, the amount of waste is rather high considering that most of the copper is etched off the substrate. Finally, typical fabrication boards in PCB manufacturing are in the range of 1/4 m^2 which is too small to fabricate really large area system (e.g. in the range of square meters) as a monolithic block [8]. To tackle these problems, a hybrid approach is promising which combines fine-structured SCB substrates onto which electronic components are assembled (component islands) and an additive manufacturing method like printing to bridge larger distances between the component islands.

1.2. Printed stretchable electronics

Screen-printing, inkjet printing, fused filament fabrication (FFF), and other additive manufacturing methods are used to fabricate deformable electronics [5, 10–12]. Inkjet printing is a widely used printing method for on-skin and wearable sensors and actuators [5, 13]. Here system designs with patterns down to 10 μm line/space are possible using conductive inks with nanoscale particles. After a sintering process such interconnection structures are flexible [5, 13], while some-degree stretchability can be achieved by pre-stretching a substrate at expense of accuracy and stability [14]. Moreover, inkjet printing is adapted into the FFF process for more complex additive manufactured electronics [12].

Besides other additive manufacturing methods, screen-printing is especially used in the fabrication of inherently deformable electronics for wearable applications [3, 7, 11, 15]. In this case, the ink is squeezed through a screen onto a substrate, which enables the use of large conductive fillers and high polymer binder content in the inks [16]. By using local stiffeners, the deformations in critical areas of the screen-printed circuitry can be engineered so that the overall system allows a higher stretchability [11].

Differing from the copper interconnections, the screen-printed interconnections show a non-linear resistance increase under elongation, which is caused by the separation of the conductive particles in the elastic polymer matrix [7, 10]. Several factors affect the resistance dependence on the elongation of the interconnections. First, the geometry of the interconnections affects how evenly the interconnection starts to crack and the resistance changes under uniaxial elongation. The straight-line interconnections have a more pronounced resistance increase than meander-shaped interconnections [11]. Second, the non-linear stress–strain properties and Poisson's ratio of the substrate make the printed interconnections deform non-linearly [10, 17]. Third, close to the rigid islands, a stress concentration at certain parts of the interconnects can cause the premature electrical failure of stretchable electronic system [15].

The advantages of printed electronics are (1) the application of material only where needed (no disposal of material, like etching) and (2) the versatility in the combination of inks and substrates for specific application cases [5, 13, 15]. Furthermore, screen-printing allows large-area (potentially roll-to-roll)

and cost-efficient fabrication of stretchable and wearable electronics [7]. However, these inks have lower conductivity than bulk copper [18], and the inherent non-linear resistance has to be considered in the design of the respective electronic system [11].

In this study, SCB substrates and screen-printing are used to fabricate a hybrid-technology stretchable build-up. The aim is to manufacture the hybrid structures that benefit from the advantages of both manufacturing methods while minimizing the imminent mechanical stress concentration and its effect on the electrical properties of interconnections. The hybrid structure is studied to understand possibilities to manufacture new cost-efficient, scalable, and highly stretchable electronic structures.

The test-system consists of the SCB-type copper islands and overlapping screen-printed silver interconnections reaching from the islands into the more stretchable parts of the substrate with no copper structures (see figure 1). One single electronic component, a commercial connector to connect test probes for resistance measurement, is mounted onto each SCB island. The printed interconnections are for test purposes straight lines.

Since the SCBs and the screen-printed interconnections have been already well-studied and defined individually [1, 2, 7], the authors focus on the transition area between the rigid copper contacts, the deformable substrate, and the stretchable printed silver tracks. The stress in the substrate concentrates close to the copper contact pads, which can damage and break the screen-printed interconnections during cyclic deformation [10]. With additional protective copper structures, the stress concentration effects can be mitigated.

2. Methods

2.1. Sample fabrication

Two sets of the SCB-samples, tensile test samples (sample series A) and cyclic test samples (sample series B) are fabricated (see figure 1). The tensile test samples are used to confirm the level of the stress concentration and the possibility to minimize it with protective structures. The second set of test samples are used to study cyclic elongation loading. The different designs are used to inspect the failure mechanisms of the islands and derive the optimum design.

The fabrication sequence is as follows: first, 35 μm thick copper foil is laminated on a 100 μm thick TPU film (Walopur Platilon U 4201 AU). The copper foil is PCB grade electrodeposited foil with one rough side (average roughness value 4 μm) which is laminated towards the TPU film, which results in an excellent adhesion at the interface of up to $\sim$2 N mm^{-1} [1, 19]. The exposed copper side after lamination is smooth. Subsequently the copper is structured by photolithography. Finally, a surface finish of electroless silver (70 nm) is deposited on the copper. Onto these substrates stretchable silver ink (CI-1036, ECM) is screen-printed, and it overlaps the copper at designated contact areas on the SCB-islands.

The sample series A is screen-printed with an EKRA X5 screen-printer. The ink is heat treated at 125 °C for 30 min. The width of the samples is 25 mm, and the length (distance between the clamps) is 50 mm, set by slippage preventing top and bottom square-shaped copper areas.

The sample series B is screen-printed manually. The ink is heat treated at 125 °C for 10 min, which after the connector is mounted onto the samples with isotropic conductive adhesive (ICA) (Dualbond IC343, Delo) and heat treated again at 100 °C for 10 min. The width of the samples is 15 mm, and the length of the samples is set similarly like the sample series A.

2.2. Sample design and test setup of sample series A

Figure 1(a) presents the tensile test samples, where the transition area has different designs. The width of the contact pads is 1,75 mm, and they are separated by 0,5 mm. The width of the protective structures is 4 mm. In the samples series A1 and A2 the protective structures are below or at the same level as the contact pads, thus not overlapping the transition area between printed and copper structures. In samples A3 to A5 the protective structures extend from the transition by 3,5 mm, 6,5 mm, or 8,5 mm, correspondingly. In the sample A4 a 45° tilted tip after a 3,5 mm straight area was implemented. All copper structures have a 0,5 mm radius rounding at the corners. Loop-shaped screen-printed interconnection are printed onto these substrates with a width of 1,0 mm and a length of 75 mm (2 × 37,5 mm) and are overlapping the copper contact pads by 6,5 mm. Electrically, the samples are connected with alligator clips from an extra copper area under the bottom clamp.

The samples are stretched with a Mark-10 tensile tester and simultaneously the resistance was monitored with a Keithley DMM6500 multimeter. The tensile tester has a 500 N force cell and rubber-coated clamps to minimize slippage and to insulate the clamps and the samples from each other. The test speed is 50 mm min^{-1}, and the distance between the clamps is 50 mm.

The multimeter is used in four-terminal sensing (Kelvin sensing) method. The range of the resistance measurements is 100 Ω and the accuracy is ±0,012% of reading, reported by the manufacturer. The four-terminal measurement targets on the transition of copper pads and printed interconnections. Furthermore, the loop of the printed interconnections is measured with a two-terminal resistance measurement at 30% elongation. The sample series A1–A5 have five parallel samples, where the average resistances are calculated at 0% and 30% elongations.

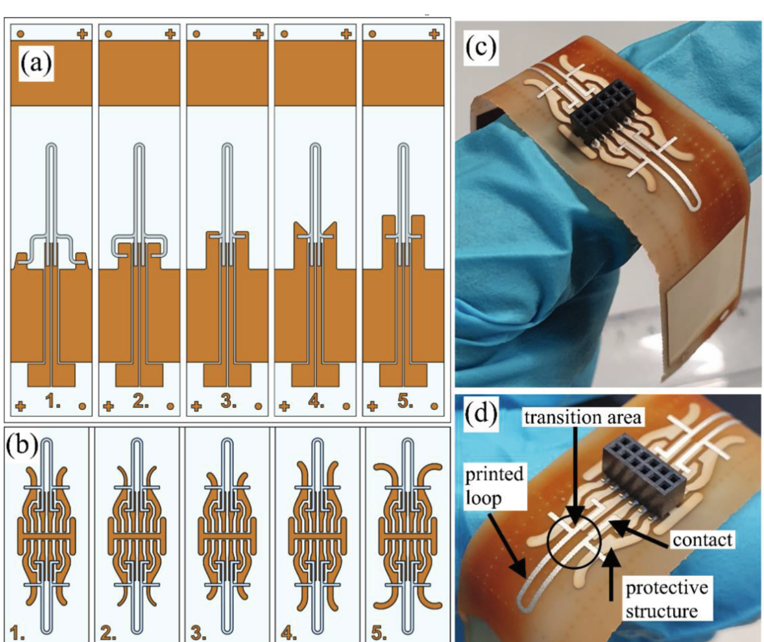

Figure 1. (a) Sample series A designs A1–A5. (b) Sample series B designs B1–B5, where the top and bottom side of the contacts are identical with contacts 1–6 from left to right. (c) A prepared sample B1. (d) The pointed-out transition area, contact and protective structure of the sample B1.

2.3. Sample design and test setup of sample series B

Figure 1(b) presents the smaller cyclic test sample designs. The samples have 1,0 mm wide contacts, which are protected with curvy protective structures. The copper areas are separated 0,5 mm from each other. The sample B1 is used as the base design, where the straight part of the protective elements after the contacts is 2,0 mm, and the top part has a 60° turn with a 2 mm radius circle. The total length of the protective structure is 4,4 mm. The width of the printed interconnection loop is 0,5 mm and the length is 45 mm (2 × 13,0 mm), which are overlapping the middle copper contact pads by 3,5 mm. The inner part of the system is designed so that the surface mount connector (M50-3120 645, HARWIN) with 1,27 mm pitch spacing, and 12 contacts fits in the middle and is mechanically protected with an additional 'H'-shape stiffener structure. The connectors are fixed onto the substrate using ICA. In figure 1(c), the sample B1 is shown. Table 1 summarizes the main characteristics of the five different sample types B1–B5. The sample parts that are referred as the transition area, a contact, a printed loop, and a protective structure are highlighted in figure 1(d).

One sample per design is initially tested mechanically with the Mark-10 tensile tester, where the test speed 50 mm min^{-1} and the distance between the clamps 50 mm settings are used.

For the cyclic loading of the samples, the ElectroPuls E10000 by Instron with the 10 kN force cell and 1,0 Hz frequency is used. The samples are tested up to 10 000 cycles. The samples were cyclically stretched to 10%, 20%, and 30% maximum elongations. The elongation levels are determined by the results of sample series A, and initial trials of the sample series B.

Notably, in the tests, the elongation refers to the total elongation of the samples, which is calculated from the distance between the clamps of the test machines. In the samples, local elongations are not divided evenly. When comparing the plain deformable TPU substrate area and the rigid copper area in the samples, the plain TPU substrate elongates more than the copper area. From the initial tests of sample B1, it is estimated that the plain TPU substrate elongates 1,5–2 times more than the reported total elongation.

Table 1. The sample series B variations that are designed based on the sample B1.

Protective structures' properties	Type B1	Type B2	Type B3	Type B4	Type B5
Width (mm)	1,0	0,5	1,0	1,0	1,0
Length of the linear part (mm)	2,0	2,0	1,0	3,0	2,0
Angle of the top part (°)	60	60	60	60	120

The resistance of the sample series B is monitored with a two-terminal resistance measurement system, which allows multiplexing between six measurement channels. The system measures contacts that are next to each other, enabling monitoring samples' transition area with four channels and the loop with two channels. The measurement time of each channel is 70 ms during which three resistance values are measured before switching to measure the next channel. The cut-off resistance value of the transition area and the loop were set to 20 Ω and 200 Ω, correspondingly, which were also the rupture points of the interconnections. The measured resistance results are processed by filtering the cut-off resistance values from the measurements and calculating average resistance values from consecutively recorded values (figure 6). Moreover, the reported average resistance values at specified cycle numbers are calculated from resistance values that are measured between 50 cycles around the points (figure 7).

From each sample type and the chosen elongation values, two parallel samples are measured. In total, 30 samples have been tested.

3. Results

The results show that the transition area of the samples deforms under mechanical loading, which changes the mechanical and electrical properties of the samples. In the analysis, the transition area can be understood from the mechanical aspect, where the transition area is the unfixed TPU area between the protective structures of the samples. This is called plainly the transition area. From the electrical aspect, there is the electrical interconnection transition area, where the silver ink passes the copper contact's boundary to the TPU surface. The interesting area for electrical properties can be delimited more precisely. For example, to the direction of the track 1 mm on the copper contact and 5 mm on the TPU, and perpendicularly to the track 2 mm to each side of the track.

3.1. Sample series A results

The calculated average resistances of the samples at 0% and 30% elongations are presented in table 2. Notably, two samples in series A1, and one sample in series A2 were electrically broken at 30% elongation.

In the samples, there was no visible damage due to the mechanical loading. From figure 1(a) and table 2, it can be seen, that length of printed interconnection between the measured two left-most contacts has only a minor effect on the initial four-terminal resistance values. Still, at the 30% elongation, the samples A1 and A2 have the highest and the most increased resistance values because of the long and unprotected interconnections together with the exposed electrical interconnection transition area, which also shows a high coefficient of variation.

Figures 2(a) and (b) shows the elongated samples, where the deformed interconnections can be seen. Figures 2(c)–(e) present the samples A3, A4, and A5 at 30% elongation, correspondingly. In the samples, the copper protection structures besides the contact pads largely prevent the elongation in the electrical interconnection transition area.

The longer the structure is, the smaller the resistance changes in the transition area and the loop (table 2). This can be also seen in figure 2 by visually comparing samples A3 and A5. The transition area and the printed loop do not deform between the copper protections. Especially in figure 2(d), the area between the copper areas is not affected by the Poisson's effect of the TPU film, and the sample deforms minimally in the transition area, as reflected in the resistance changes in table 2.

3.2. Sample series B results

The initial tensile test comparison of the cyclic test samples is shown in figure 3. The results show that the design variations of the protective structure affect only slightly the stretchability of the samples. The differences are smaller than 1 N, where the thinnest protective structure design (sample B2) stiffens the sample the least (6,3 N after 5 mm displacement), and the longest protective structure design (sample B4) stiffens the sample the most (7,2 N after 5 mm displacement).

3.2.1. Failure mechanisms

Photolithographically defined copper structures and screen-printed silver ink have pronouncedly different mechanical properties, which need to be considered in the results and analysis of the samples. The copper structures have stable electrical properties until sudden fatigue failure, while the silver ink has high stretchability, mechanical robustness, and dynamical variation or resistivity during extension. Also, the general mechanical properties of the copper and its use in meander-shaped interconnections have been studied [1, 6, 8], but its usage as structured copper islands with silver ink has not been studied previously. Because of this, it is important to focus on the rupture of the copper structures in the islands, which main failure types are presented in figure 4.

In figure 4(a), the complicated movement of the TPU film deforms the copper protection structure beyond a certain level. The structure is deformed in the elongation direction (y-axis) by opening the curve, and because of Poisson's effect on the film (x-axis), the copper buckles out of plane (z-axis). The repeated buckling results eventually in a fracture of the curved copper structure as shown in figure 4(b). After cracking of the structure, the substrate no longer buckles out of plane.

Depending on the elongation level and the width of the copper structures, the TPU film at the cracked copper protective structures deforms differently. At

Table 2. The four-terminal and two-terminal measurement results of sample series A.

Sample series	Average resistance at 0% elongation (Ω)	Average resistance (and resistance increase) at 30% elongation (Ω)	Average resistance at 30% elongation, compared to the sample A5	Coefficient of variation	Average two-terminal resistance of the loop at 30% (Ω)
Sample A1	0,102	6,14 (60,4)	74,6	29,1	90,7
Sample A2	0,0853	3,01 (35,2)	36,5	33,3	85,2
Sample A3	0,0806	0,272 (3,37)	3,30	7,24	82,4
Sample A4	0,0834	0,217 (2,60)	2,63	8,39	80,7
Sample A5	0,0736	0,0824 (1,12)	1	7,70	77,0

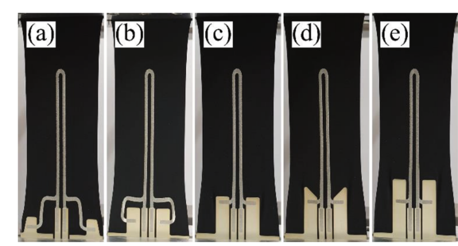

Figure 2. The samples series A at 30% elongation. (a) Sample A1. (b) Sample A2. (c) Sample A3. (d) Sample A4. (e) Sample A5.

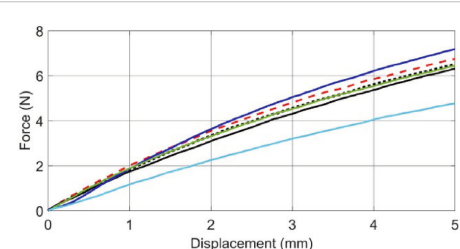

Figure 3. The initial tensile test results of cyclic test samples. From the top downwards, the displacement–force curves show the results of sample B4 (dark blue solid line), sample B1 (red dashed line), sample B3 (black dotted line), sample B5 (green solid line), sample B2 (black solid line), and plain TPU film (light blue solid line).

low elongation levels (10%–20%) and with 1,0 mm copper width, the damage in the TPU does not advance and the next rupture in the sample happens in the lower part of the copper structure, which is seen in figure 4(b). If the sample undergoes high elongation (30%) and has 0,5 mm wide copper, the TPU film tears and forms holes between the cracked copper parts in figure 4(c), which grows during the cyclic testing and causes the snapping of the whole sample. Figure 4(d) presents the electrical failure of the horizontal interconnection areas because of the cracking of the copper area. It is likely, that the silver ink has affected the initiation locations of the cracks. Table 3 shows the dominant failures of the sample types.

Notably, in all samples, only the outermost copper structures were damaged during the cyclic testing, and the middle copper areas remained undamaged.

Furthermore, in figure 5, the observed failure mechanisms are studied in more detail from initially tested samples with a scanning electrode microscope (SEM) Phenom XL G2 Desktop SEM by Thermo Scientific. Figure 5(a) shows the silver ink on the electrical interconnection transition area of the middle copper contact (3rd copper contact) from the sample B3 after 50 k cycles with 20% maximum elongation. The electrical interconnection transition area has been protected by the protective structures and the layered silver flakes of the ink form still a uniform matrix. From the same sample B3, figure 5(b) presents the cracked middle part of the copper protective structure, which location can be also seen in figure 4(b).

Figure 5(c) shows damage in the horizontal interconnection, where a longitudinal crack propagates in the silver ink on the border of the copper area (sample B5, the TPU substrate failed under 3000 cycles outside the studied area with 50% maximum elongation). Figure 5(d) shows the cracked cross-section area of the same sample B5. Figure 4(c) describes the observed failure mechanism of the sample in figure 5(d). The copper has partially delaminated from the TPU film.

3.2.2. Finite element (FE) analysis of copper structures

To support the hypotheses of the observed failure mechanisms in the cyclic test samples, a FE analysis was performed using commercial software ABAQUS. The models were constituted by simple TPU strips with different layouts of copper on the samples (as can be seen in the details of figure 6); both models were subjected to a uniaxial tensile stretch with 10% elongation. While in the first model the copper constitutes a single strip of material going across the sample, in the second one the strip presents a crack in the center of the sample, to represent a crack forming in the copper layer on the sample.

Results obtained in these simulations show that the copper structures, while undamaged, have a specific mechanical role during elongation in the

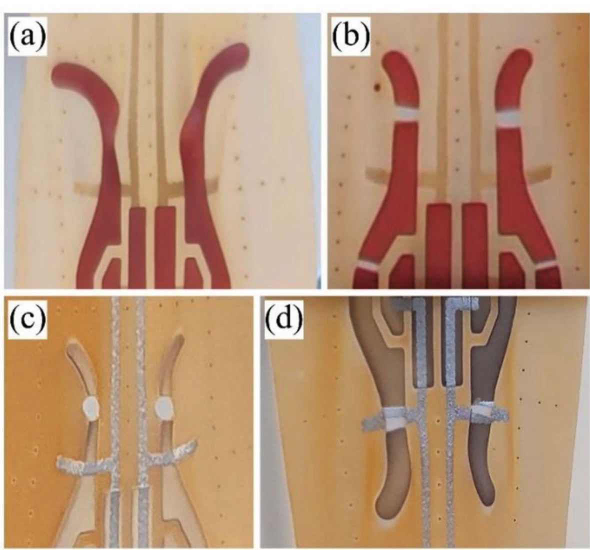

Figure 4. Deformations and ruptures of the samples. (a) The copper protective structure is bending under elongation (sample type B5). (b) The protective structure has snapped after the curved head and from the lower part of the structure (sample B4). (c) The revealed TPU under the snapped copper area has torn and formed a hole (sample B2). (d) The protective structure has cracked below the horizontal silver ink tracks (sample B1).

Table 3. The dominant failures of the sample series B.

Sample series	Sample B1	Sample B2	Sample B3	Sample B4	Sample B5
10% elongation					
20% elongation					
30% elongation					

samples. In fact, they reinforce the transition area and even out the deformations.

However, as soon as cracking in this stiff layer occurs, deformation localizes in the TPU layer that was previously protected by copper. The difference in the two systems can be seen in the plot in figure 6(b), where the presence of a crack in the copper layer increases the local maximum deformation in the TPU layer from a value of roughly 5% to a value of 270% (an increase of over 50 times). This strain concentration in TPU, in turn, will cause the formation and propagation of crack in the substrate. In contrast, when the copper is uncracked as in figure 6(a), deformation in the deformable substrate is evenly distributed.

3.2.3. Electrical measurement results

The measured electrical resistance during the sample series B show the effect of different protective structures on the transition area, which durability or weakness affected the measured resistance.

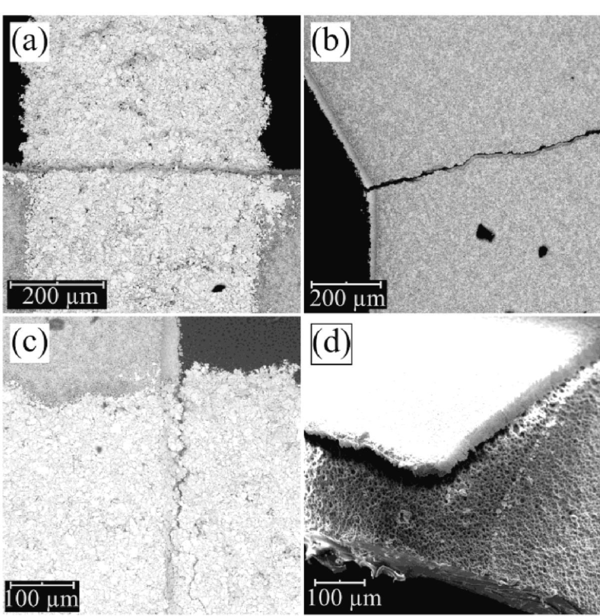

Figure 5. SEM images of observed failure mechanisms of initially tested sample series B samples. (a) An electrical interconnection transition area of the silver ink and the copper contact after 50 k cycles with 20% elongation (sample B3). (b) The cracked middle part of the copper structure after 50 k cycles with 20% elongation (sample B3). (c) A longitudinal crack in the horizontal interconnection area (sample B5, failed before 3000 cycles with 50% elongation). (d) A ruptured surface of the sample, where the copper has partially delaminated from the TPU (sample B5, failed before 3000 cycles with 50% elongation).

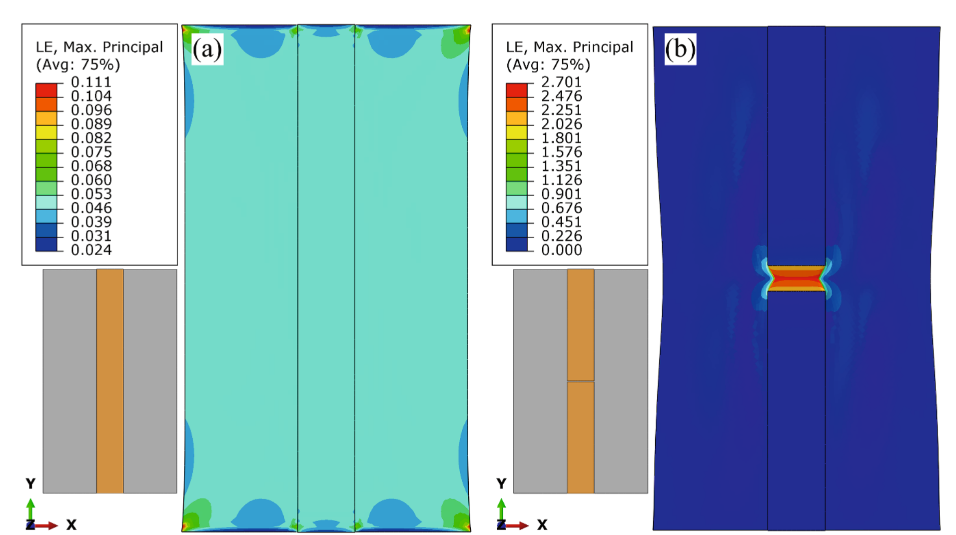

Figure 6. FE analysis for a straight copper structure on the TPU substrate. (a) An undamaged copper structure. (b) Ruptured copper structure.

Figure 7 shows the example results of channels from different samples in the 20% elongation cyclic tests. In the cyclic test results, the typical sawtooth phenomenon of stretchable printed interconnections because of conductive filler network deformations can be seen [20, 21]. The results of the protected interconnections in the transition area depend on the design of protective structure, where the samples B4 with the long copper structure has more stable resistances (figure 7(a)) than the samples B3 with short copper structures (figure 7(b)). The failure time and location of the protective structures (table 3) affect

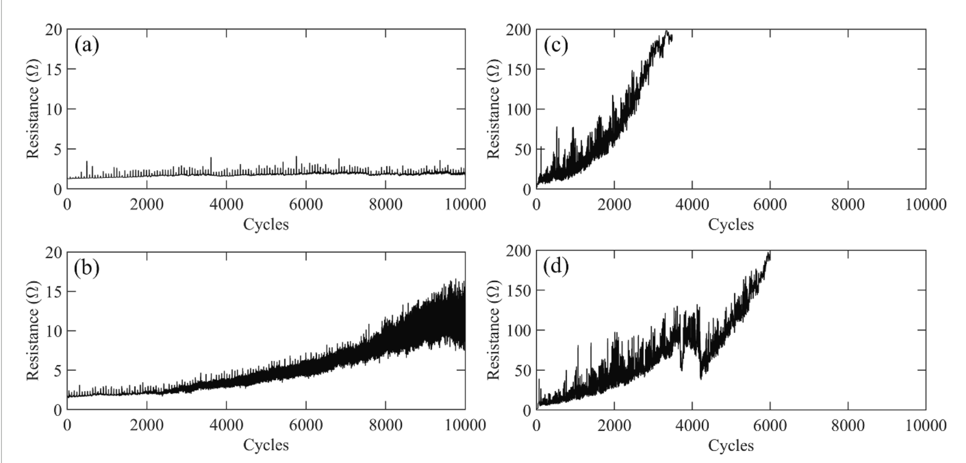

Figure 7. Resistance curves of cyclic test samples. The maximum number of cycles is 10 000, the elongation is 20%, and the maximum resistances in the measurements of transition area and the loop are 20 Ω and 200 Ω, correspondingly. (a) The resistance curve of stable electrical interconnection transition area (sample B4). (b) The resistance curve of unstable electrical interconnection transition area (sample B3). (c) The resistance curve of the loop without the effect from the rupture of protective layer (sample B2). (d) The resistance curve of the loop with the effect of protective structure rupture (sample B4).

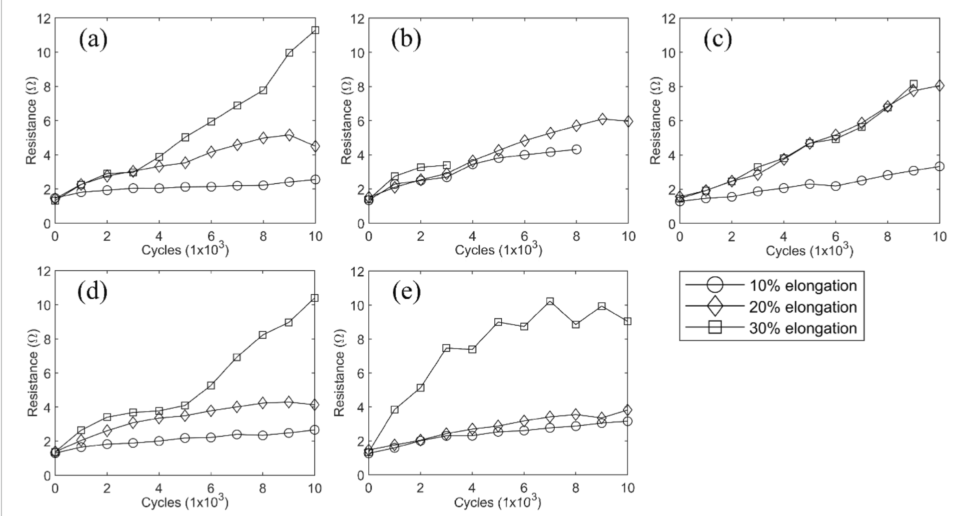

Figure 8. Average resistance results of the samples series B. The average resistance values are calculated from the resistance values of 50 cycles around the data points. (a) The sample B1. (b) The sample B2. (c) The sample B3. (d) The sample B4. (e) The sample B5.

the amount of deformation in the electrical interconnection transition area. Moreover, the failure of the structures can be seen in the resistance results of loops. The damage in the printed loops accumulates over cycles, and in the sample B2 with thinner protective structures, the resistance increase follows a typical behavior of printed interconnections in figure 7(c) and increases over the maximum value (200 Ω) [7, 11]. However, in figure 7(d), the resistance of the loop in the sample B4 decreases between 3000–4000 cycles, which is the time window of the failure of the protective structure.

After the failure of the structure, the resistance of the loop increases more steeply.

From the results of the samples, the average resistance values of the transition areas of the sample types at different elongations are calculated and presented in detail in figure 8, which is further summarized in table 4. In figure 8, the results of the loops are excluded because they generally reached 200 Ω early and failed prematurely (figure 7), preventing the relevant comparison between the sample types. The high resistance increase of the loop is caused by the small width of the interconnections (0,5 mm) [22].

Table 4. Summary of the calculated resistance results of the sample series B. In addition to the resistance values, the last cycle number for the prematurely failed samples is reported.

Average resistance results	Type B1	Type B2	Type B3	Type B4	Type B5
Average resistance at 10% elongation (Ω)	<3,0	<4,5 (8000)	<3,5	<3,0	<3,5
Average resistance at 20% elongation (Ω)	<5,5	<6,5	<8,5	<4,5	<4,0
Average resistance at 30% elongation (Ω)	<11,5	<3,5 (3000)	<8,5 (9000)	<10,5	<10,5

Figure 8 and table 4 present that the samples with 1,0 mm wide protection structures endured the cyclic 10% elongation well. The protective structures of the reference sample design in figure 8(a) limited the resistance until 5000 cycles (20% elongation) and 3000 cycles (30% elongation) before the structures ruptured and allowed higher deformations in the electrical interconnection transition area. Such phenomenon is not seen in figure 8(c) where the short protective structures reinforced the transition area less at higher deformations. In figure 8(d), on the contrary, the longer protective structures constrained the resistance 2000 cycles longer at 30% cyclic elongation.

Other design changes affected the resistance results considerably. The thinner protective structures in figure 8(b) and table 4 are more unreliable. Typically, they do not have as high resistance values as other samples, because the thinner structures snap or ruptures the whole sample before fatigue damage in the silver ink accumulates and increases the resistance. The more curved structures in figure 8(e) emphasized spring-like movement of the structures, which snaps the protective structures early (before 500 cycles) and spread the stresses of the transition area, which together minimized the resistance changes at 20% elongation, but accelerated the resistance increase at 30% elongation.

4. Discussion

4.1. Analysis of sample series A

The sample series A shows the function of the protective structures. The unprotected electrical interconnection transition area of samples can already fail at 30% elongation, while the well-protected samples can have only 12% resistance increase in the transition area. Also, the long protective structures can protect the interconnections from the horizontal Poisson effect, which can be useful to control the local biaxial deformations of interconnections. The non-square design (sample A4) improves the leveling of the stress concentration, but in the tensile testing, had a small influence on the resistance of the transition area. However, in cyclic loading, the re-direction of stresses in the stretchable substrate can be crucial for long-term durability.

Despite the good results of sample series A, the most efficient protective structure can be modified. The structure is relatively large (8,5 × 4 mm, with 0,5 mm rounding), which needs to be reduced for smaller stretchable electronics systems.

4.2. Analysis of sample series B

The smaller sample series B have more intricate designs and display a more complex mechanical and electrical behaviors compared to the sample series A. They can be divided into primary and secondary deformations, which happen before and after snapping of the copper protective structures, correspondingly.

In sample series A and B, the TPU substrate elongates, which is the primary deformation that affects the resistance of the transition area. The elongation of the TPU film transfers the mechanical load simultaneously to the copper structures and the silver ink, which deform differently at different stages of the deformation process because of their contrasting mechanical properties. Generally, in the sample series B, after the primary deformation (up to 10%), the samples break by snapping of protective structures. After the breakage, the secondary deformation (>10%) sets in, which includes more complicate damage of the electronic system.

At 10% elongation, 1,0 mm wide protective structures can endure the 10 000 cycles without a rupture. In case of the rupture, the 1,0 mm wide structures can still protect the electrical interconnection transition area, and the elongation level is enough to damage (and increase resistance) only the electrical interconnection transition area of thinner 0,5 mm wide structures.

The resistance changes in the samples due to the elongation of the silver ink causes the filler particles to detach from each other and thereby reduce electronic pathways in the ink. The observed damage seems to locally accumulate in the silver ink and leads to transverse cracks in the lines. The damage is distinct in the printed loops, where the resistance increases (beyond 200 Ω) with the number of cycles. The damage is minimum in the transition area between the copper protections as they prevent the ink deformation.

At higher elongation levels (20% and 30%), the samples are elongated by the testing machine, which is the main reason for the resistance changes of the samples. In addition, the protective structures rupture and change the deformation distribution in the transition area, which can be said to be secondary deformations that affect the resistance of the samples.

Thus, the protective structure designs affected considerably the resistance results. The rupturing of the structure changed the resistance of the loop which first decreases, and then increases faster. It is likely, that after the crack initiates outside the structure (because of Poisson's effect), the crack propagates and makes the structure more bendable from that point, allowing re-distribution of stresses in the loop, decreasing maximum local elongation of the silver ink particles, which further decreases the resistance in the loop. After the snapping of the structure, the failed area has the stress concentration effect, which damages locally the printed loop and transition area.

Moreover, the copper and the silver ink have different electrical behavior after failure. After rupture the copper structures act as an unreliable on/off switch. The fractured copper areas can be connected at 0% elongation and will be disconnected at >0% elongation. The failure of the silver ink still enables the stretchability of the system, despite the damage in the ink can permanently increase the resistance values.

4.2.1. Failure stages of the protective structures

From the identified failures of the sample series B, general failure stages of the hybrid stretchable electronics structures can be defined. Before failure, the samples elongate and the deformations of the TPU substrate induce forces to the copper–TPU interface. The large and simple-shaped copper areas do not deform, but more complex protective structures can have spring-like movements that cause tensile and compressive forces to the structures. Also, at higher elongations, Poisson's effect on the TPU substrate makes the structures twist three-dimensionally, which causes additional forces to the copper–TPU interface.

When the forces on the copper–TPU substrate interface increase over the strength of the interface, the failure of the system starts. The failure of the copper structure realizes first as (1) the delamination of the copper and TPU substrate (figure 5(d)). In the protective structures, if the delamination area is located on the top of the structure, the delamination is the peeling of the copper and the TPU substrate. If the delamination is in the middle, (3) the crack initiates on the side of the structure, where the tensile forces have been induced. Further forces and cycles advance (4) the crack propagation, which changes the spring-like movement of the structure. The movement changes can affect the electrical properties of printed interconnections that are close to the deforming copper areas (figure 7(d)). After the crack has (5) snapped the copper structure, (6) the revealed TPU substrate between the fractured parts undergoes the high stress concentration effect (figure 6(b)). If the stresses are concentrated in a small area (the width of the fractured parts is 0,5 mm, for example), (7) the TPU substrate can be torn and cause quickly the total failure of the system (figure 4(c)).

4.2.2. Effect of sample design on the failure

The sample design B4 with long protective structures decreased the damage accumulation in the transition area in the optimal way. Still, the protective structures snapped, which after the secondary deformations affected the printed interconnection and the electrical interconnection transition area, which makes the design further improvable.

First, the width of the structures affected the failure of the system. The 0,5 mm wide structures snapped early, and under the high elongation (30%), the revealed 0,5 mm wide TPU substrate area between the fractured copper sides concentrated high forces into the TPU substrate and left a hole in the substrate. The wider 1,0 mm structures endured better the low elongation (10%), and after the snapping, the stresses in the fractured area are distributed over a larger area, and the TPU substrate is not torn.

Also, the angle of the protective structures' top part affected the cracking. The curved head of the structure mainly defined the location of the crack, which was formed after 2D-spring-like movement and out of plane buckling. Also, the silver ink overprinted on the copper affected the location of the crack initiation. The amount of angle affected the amount of twisting and durability, where 60° curved structures lasted multiple times longer than 120° curved structures.

Moreover, the length of the structures affected mainly to the electrical properties of the transition area. The longer structures decreased movement of the substrate in the transition area, and at 30% elongation, 1 mm longer structures made the electrical interconnection transition area stable 2000 cycles longer (figures 8(a) and (d)).

Furthermore, only the protective structures of the samples snapped, and all the other copper areas remained intact.

4.2.3. Design improvements

Based on the results of the sample series A and B, a more optimal design can be suggested. The sample series B design can be improved by (1) increasing the width of the protective structures, (2) using straight geometries that do not bend out of the elongation direction, and (3) the possible copper areas, where local tensile forces and crack initiation can be expected, are reinforced.

Also, in future designs, the areas for the electronic components need to be stiffened more. In the samples, the 'H'-shape stiffener under the connector is meant to prevent movement of the connector, but in the tests, the 0,5 mm wide TPU area between the 'H'-stiffener and contact pads could elongate enough to detach the connector from the sample. In the optimum design, the size of the 'H'-stiffener is larger,

or the TPU substrate is locally reinforced with pieces of PI film [2].

5. Conclusions

The stretchable electronics system can be improved by using hybrid stretchable structures, which have the electrically optimal rigid electronics islands (SCB islands) and stretchable interconnections (screen-printed silver ink interconnections). However, the well-known stress concentration effect influences the mechanical properties of the structure, which can be controlled by the design of the protective structures in the SCB island. With tensile tests, we demonstrated the damage in the SCB—stretchable interconnection transition area, which is caused by the stress concentration effect. The damage can be prevented with protective structures, which can limit the resistance increase of the transition area at 30% elongation to 12%. Based on the results, the miniaturized sample designs with the transition area and the printed loop were prepared and tested in cyclic stretch tests with 10 000 cycles. The samples broke and the designed protective structures with curved heads snapped, which changed the mechanical response of the samples and induced over 50 times higher stresses between the fractured copper parts. The snapping was detected in the resistance measurements of the printed loop, which decreases at the crack propagation phase. Otherwise, because of the high resistance increase of the loops, the results from them are limited. The long protective structures (sample B4) reinforce the printed loop the most, limiting the transition area resistance to <4,5 Ω at 10 000 cycles with 20% elongation and 5000 cycles with 30% elongation. The thin and highly curved protective structures (samples B2 and B5, correspondingly) damage the loop the most. Notably, after the breakage of the thin structures, the TPU substrate between the fractured copper parts was torn, which advanced to the total failure of the samples.

In the miniaturized SCB islands, curved protective structures should be avoided. Due to curvature of the thin structures, they bend under elongation and fold because Poisson effect. Together with repeated cyclic deformations, the protective structures break typically by snapping between the curved head and the straight middle area. For future applications, the curved protective structures cannot be recommended, and the straight structures parallel to the elongation direction is more rational.

The hybrid stretchable electronics made from SCB copper islands and printed stretchable interconnections are able to combine the advantages of both fabrication methods and enable more scalable and efficient manufacturing of stretchable electronics for e.g. wearables and automotive industries. In the future, studying the design parameters and failure mechanisms of hybrid stretchable electronics in detail will enable a broader usage of these structures in complex stretchable electronic systems.

Data availability statements

The data cannot be made publicly available upon publication because they are not available in a format that is sufficiently accessible or reusable by other researchers. The data that support the findings of this study are available upon reasonable request from the authors.

Acknowledgments

The authors acknowledge Manuel Seckel for helping with sample designing and Evelyn Wegner for helping of SCB process. Also, the authors acknowledge Maija Luukko for assisting with tensile tests.

This work was funded by the Academy of Finland under the project REEL, Decision Number 334175.

ORCID iDs

Teemu Salo https://orcid.org/0000-0001-7746-0564
Thomas Löher https://orcid.org/0000-0003-2941-3311

References

[1] Löher T, Seckel M, Vieroth R, Dils C, Kallmayer C, Ostmann A, Aschenbrenner R and Reichl H 2009 Stretchable electronic systems: realization and applications *11th Electronics Packaging Technology Conf. (EPTC)* (*Singapore, 9–11 December 2009*) pp 893–8
[2] Vanfleteren J, Löher T, Gonzalez M, Bossuyt F, Vervust T, De Wolf I and Jablonski M 2012 SCB and SMI: two stretchable circuit technologies, based on standard printed circuit board processes *Circuit World* **38** 232–42
[3] Huttunen O-H, Behfar M H, Hiitola-Keinänen J and Hiltunen J 2022 Electronic tattoo with transferable printed electrodes and interconnects for wireless electrophysiology monitoring *Adv. Mater. Technol.* **7** 2101496
[4] Salo T, Di Vito D, Halme A and Vanhala J 2022 Electromechanical properties of 3D-printed stretchable carbon fiber composites *Micromachines* **13** 1732
[5] Mikkonen R, Koivikko A, Vuorinen T, Sariola V and Mäntysalo M 2021 Inkjet-printed, nanofiber-based soft capacitive pressure sensors for tactile sensing *IEEE Sens. J.* **21** 26286–93
[6] Grams A, Kuttler S, Löher T, Walter H, Wittier O and Lang K-D 2018 Lifetime modelling and geometry optimization of meander tracks in stretchable electronics *19th Int. Conf. on Thermal, Mechanical and Multi-Physics Simulation and Experiments in Microelectronics and Microsystems (Eurosime)* (*Toulouse, France, 15–18 April 2018*) pp 1–5
[7] Suikkola J, Björninen T, Mosallaei M, Kankkunen T, Iso-Ketola P, Ukkonen L, Vanhala J and Mäntysalo M 2016 Screen-printing fabrication and characterization of stretchable electronics *Sci. Rep.* **6** 25784
[8] Bossuyt F, Guenther J, Löher T, Seckel M, Sterken T and de Vries J 2011 Cyclic endurance reliability of

stretchable electronic substrates *Microelectron. Reliab.* **51** 628–35
[9] Yu H, Zhao X and Kong C 2022 Mechanical properties of rolled copper foils in cryogenic and room-temperature environments *Adv. Eng. Mater.* **24** 2100830
[10] Mosallaei M, Jokinen J, Honkanen M, Iso-Ketola P, Vippola M, Vanhala J, Kanerva M and Mäntysalo M 2018 Geometry analysis in screen-printed stretchable interconnects *IEEE Trans. Compon. Packag. Manuf. Technol.* **8** 1344–52
[11] Salo T, Halme A, Lahtinen J and Vanhala J 2020 Enhanced stretchable electronics made by fused-filament fabrication *Flex. Print. Electron.* **5** 045001
[12] Mangoma T N, Yamamoto S, Malliaras G G and Daly R 2022 Hybrid 3D/inkjet-printed organic neuromorphic transistors *Adv. Mater. Technol.* **7** 2000798
[13] Laurila M-M *et al* 2019 A fully printed ultra-thin charge amplifier for on-skin biosignal measurements *IEEE J. Electron Devices Soc.* **7** 566–74
[14] Abu-Khalaf J M, Al-Ghussain L and Al-Halhouli A 2018 Fabrication of stretchable circuits on polydimethylsiloxane (PDMS) pre-stretched substrates by inkjet printing silver nanoparticles *Materials* **11** 2377
[15] Behfar M H, Di Vito D, Korhonen A, Nguyen D, Amin B M, Kurkela T, Tuomikoski M and Mäntysalo M 2021 Fully integrated wireless elastic wearable systems for health monitoring applications *IEEE Trans. Compon. Packag. Manuf. Technol.* **11** 1022–7
[16] Scenev V, Szalapak J, Werft L, Hoelck O, Jakubowska M, von Krshiwoblozki M, Kallmayer C and Schneider-Ramelow M 2022 Low-temperature processible highly conducting pastes for printed electronics applications *Adv. Eng. Mater.* **24** 2101752
[17] Walter H, Grams A, Seckel M, Löher T, Wittler O and Lang K D 2018 Determination of relevant material behavior for use in stretchable electronics *19th Int. Conf. on Thermal, Mechanical and Multi-Physics Simulation and Experiments in Microelectronics and Microsystems (Eurosime)* (*Toulouse, France, 15–18 April 2018*) pp 1–5
[18] Jablonski M, Lucchini R, Bossuyt F, Vervust T, Vanfleteren J, De Vries J W C, Vena P and Gonzalez M 2015 Impact of geometry on stretchable meandered interconnect uniaxial tensile extension fatigue reliability *Microelectron. Reliab.* **55** 143–54
[19] Neggers J 2013 Ductile interfaces in stretchable electronics: multi-scale mechanics and inverse methods *PhD Thesis* Technische Universiteit, Eindhoven (https://doi.org/10.6100/IR761382)
[20] Boda U, Strandberg J, Eriksson J, Liu X, Beni V and Tybrandt J 2023 Screen-printed corrosion-resistant and long-term stable stretchable electronics based on AgAu microflake conductors *ACS Appl. Mater. Interfaces* **15** 12372–82
[21] Behfar M H, Khorramdel B, Korhonen A, Jansson E, Leinonen A, Tuomikoski M and Mäntysalo M 2021 Failure mechanisms in flip-chip bonding on stretchable printed electronics *Adv. Eng. Mater.* **23** 2100264
[22] Cahn G, Pierron O N and Antoniou A 2021 Trace width effects on electrical performance of screen-printed silver inks on elastomeric substrates under uniaxial stretch *J. Appl. Phys.* **130** 115304